

# **Imaging simulation of atmospheric turbulence based on phase screen methods**

Zur Erlangung des akademischen Grades eines  
DOKTORS DER NATURWISSENSCHAFTEN  
von der KIT-Fakultät für Physik des  
Karlsruher Instituts für Technologie (KIT)

genehmigte

DISSERTATION

von

**Daniel Wegner**  
aus Wörth am Rhein

Tag der mündlichen Prüfung:	14.01.2022
Referent:	Prof. Dr. Peter Braesicke
Korreferent:	Priv.-Doz. Dr. Michael Höpfner



## Zusammenfassung

Im Rahmen dieser Arbeit wird ein Ansatz zur bildbasierten Simulation von Luftturbulenzstörungen vorgestellt. Es wird aufgezeigt, wie durch einen bestehenden Ansatz aus experimentellen Kameradaten Parameter von aktuellen Turbulenzmodellen abgeschätzt werden können. Diese Parameter werden dann für vergleichbare Simulationen genutzt und mit experimentellen Daten verglichen.

Eine weit verbreitete Methode ist das sogenannte "Split-step"-Strahlpropagationsverfahren, welches die Ausbreitung eines Lichtsignals durch ein turbulentes Medium simulieren kann. Hierbei werden Phasenstörungen des elektromagnetischen Felds verursacht durch Turbulenz als zweidimensionale Phasenschirme in mehreren Abständen zwischen Lichtquelle und Kamerasensor modelliert und simuliert.

Anhand aktueller Turbulenzmodelle werden zwei Methoden zur Phasenschirmerzeugung hinsichtlich Genauigkeit und Rechenzeit verglichen. Zum einen ist das als Goldstandard die inverse Fouriertransformation von gefiltertem Rauschen mit Hinzufügen von subharmonischen Frequenzen. Zum anderen ist das die "Sparse Spectrum"-Methode zur Erzeugung von korrelierten Phasenschirmen durch Überlagerung von planaren Wellen mit zufälligen Ausrichtungen.

Phasenschirme stellen 2D-Abbilder von zufälligen räumliche Schwankungen des Brechungsindex von Luft dar, die zu meist unerwünschten Störeffekten bei der Übertragung von Lichtsignalen führen. In der Kamerabildgebung äußern sich diese Störeffekte durch räumliche und zeitliche Schwankungen der Bildschärfe und Position ("Image dancing") einzelner Bildausschnitte. Diese Schwankungen entstehen durch Induktion turbulenter Luftströmungen durch Sonneneinstrahlung verbunden mit der Temperatur- und Druckabhängigkeit des Brechungsindex von Luft. Da exakte fluiddynamische Simulationen zeit- und rechenaufwendig sind und die Kenntnis vieler Randbedingungen, z.B. der Bodenbeschaffenheit voraussetzen, werden diese Brechungsindexschwankungen oft durch Rauschleistungsspektren als Turbulenzmodelle beschrieben.

Mithilfe der Phasenstrukturfunktion als häufig genutztes Validierungskriterium wird gezeigt, dass erzeugte Phasenschirme korrekte, zu erwartende räumliche Korrelationen aufweisen.

Für beide Methoden werden zweidimensionale Ausbreitungsprofile von Lichtpunktquellen berechnet und mit gängigen Metriken validiert. Dies sind zum Beispiel Langzeit- und Kurzzeitmodulationstransferfunktionen ("long-exposure/short-exposure"), das Strehlverhältnis und der aperturgemittelte Szintillationsindex. Das Strehlverhältnis setzt zwei Maximalwerte für eine räumliche, ensemble-gemittelte optischen Intensitätsverteilung ins Verhältnis, einem Maximalwert für eine gegebene Turbulenzstärke und dem Maximalwert für den turbulenzfreien Fall. Durch zunehmende Turbulenzstärke werden die optischen Intensitätsverteilungen im Allgemeinen breiter. Dadurch sinken diese Maximalwerte und dadurch

auch das Strehlverhältnis. Das Punktbildprofil auf dem Sensor ergibt sich dann durch Fourieroptik aus der Feldverteilung an der Apertur. Diese Punktbildprofile repräsentieren die Turbulenzstörung einzelner Lichtpunktquellen für bestimmte Sichtlinien. Durch Verschiebung der Phasenschirme senkrecht zur Ausbreitungsrichtung lassen sich Punktbildprofile für unterschiedliche Sichtlinien zum Sensor berechnen. Dadurch ergeben sich räumlich variierende und korrelierte Punktbildprofile. Es lassen sich regelmäßige Gitter solcher Punktbildprofile berechnen, und zur ungleichmäßigen Filterung über beliebige Bilder als Eingangsszenen nutzen. Zur experimentellen Validierung werden in mehreren Feldversuchen vergleichbare Messungen mit LED-Matrizen als Gitter von Punktquellen durchgeführt. Durch Verwendung von zwei Arten von LEDs von geringfügig unterschiedlichen mittleren Wellenlängen wird untersucht, ob und inwieweit sich der erwartete Unterschied in der Bildunschärfe der LED-Projektion zur Verbesserung der Abschätzung von Turbulenzmodellparametern eignet. Aus gemessenen Bildern der LED-Matrizen werden außerdem differentielle Neigungsvarianzen berechnet. Die differentielle Neigungsvarianz als Maß für die räumliche Korrelation der Zentroidverschiebungen dieser Punktbildprofile ist analytisch beschreibbar und wird deshalb auch zur Validierung genutzt. Durch Anpassung theoretischer Ausdrücke an diese lassen sich die wahrscheinlichsten Parameter von aktuellen Turbulenzmodellen abschätzen. Basierend auf diesen Parametern werden turbulent gestörte Punktgitter simuliert und daraus abgeleitete Neigungsvarianzen mit experimentellen Daten verglichen. Ebenso werden Verteilungen der Turbulenzmodellparameter über alle Messtage aufgezeigt sowie ihrer Anisotropie zwischen horizontaler und vertikaler Richtung. Dies kann als Datengrundlage für zukünftige bildgebenden Turbulenzsimulationen genutzt werden, zum Beispiel zur Bewertung von Kameras oder der Entwicklung und Verbesserung von turbulenzkompensierenden Bildverarbeitungstechniken. Die aufgefundenen Verteilungen von Turbulenzmodellparametern können außerdem zur Validierung von Simulationen und Messungen von kleinskaligen atmosphärischen Phänomenen in Bodennähe genutzt werden.





## Abstract

In this thesis, an approach to image-based simulation of air turbulence disturbances is presented. It is shown how an existing approach can be used to estimate parameters of current turbulence models from experimental data. These parameters are subsequently used for independent simulations and compared to experimental data.

A widely used method is the so-called "split-step" beam propagation method, which simulates the propagation of a light signal through a turbulent medium. Phase perturbations of the electromagnetic field caused by atmospheric turbulence are modeled and simulated as 2D phase screens at several distances between light source and camera sensor.

Using current turbulence models, two methods for phase screen generation are compared in terms of accuracy and computation time. The first one is the inverse Fourier transform of filtered noise with addition of subharmonic frequencies. The second one is the sparse spectrum method for generating correlated phase screens by superposition of planar waves with random orientations.

Phase screens represent 2D projections of random spatial fluctuations of the refractive index of air which lead to mostly undesired perturbation effects in the transmission of light signals. For camera imaging applications these perturbation effects are manifested by spatiotemporal fluctuations of image blur and positions ("image dancing") of single image sections. These fluctuations are caused by induction of turbulent air flows by solar radiation and the dependency of the refractive index on temperature and pressure. Since exact fluid-dynamic simulations are time-consuming and computationally expensive and require the knowledge of many boundary conditions, e.g. soil properties, these refractive index fluctuations are often described by noise power spectra as turbulence models.

Using the phase structure function as a frequently used validation criterion, it is shown that generated phase screens have correct, expected spatial correlations.

A commonly used validation criterion for phase screens is the phase structure function. For both methods, propagated 2D profiles of point sources are computed and validated with common metrics. These are e.g. long-exposure and short-exposure modulation transfer functions, the Strehl ratio and the aperture-averaged scintillation index. The Strehl ratio puts into relation the peak level of average spatial optical intensity distributions for some turbulence strength and the peak level of intensity distribution for the case of no turbulence. For increasing turbulence strength the intensity distribution gets wider, the peak level decreases and thus also the Strehl ratio. The so-called point spread function, i.e. the profile in the sensor plane, results from Fourier optics from the field distribution at the aperture. These point spread functions represent the turbulence perturbation of individual point sources for specific lines of sight.

By shifting the phase screens perpendicular to the direction of propagation, point image profiles can be calculated for different lines of sight to the sensor. This results in spatially varying and correlated point profiles. Regular grids of such point image profiles can be calculated and used for non-uniform filtering over images as input scene. The differential tilt variance as measure for the spatial correlation of the centroid shifts of these point spread functions can be described analytically and is therefore also used for validation. For experimental validation, comparable measurements are performed in several field experiments using LED matrices as grids of point sources. By using two types of LEDs with slightly different mean wavelengths, it is investigated whether and to what extent the expected difference of image blur of the LED projections is suitable for an improvement of model parameter estimation. Then, differential tilt variances can also be calculated from the measured images. By fitting theoretical expressions to these, the most likely parameters of current turbulence models can be estimated. Based on these parameters, point source grids degraded by turbulence are simulated and the differential tilt variances derived from them are compared with experimental data. Likewise, distributions of turbulence model parameters over all recording days are shown as well as their anisotropy between horizontal and vertical direction. This can be used as a data basis for future imaging turbulence simulations, e.g. for performance assessment of cameras or the development and enhancement of techniques for turbulence mitigation

The diagnosed distributions of model parameters may also be used for the validation of simulations and measurements of microscale atmospheric phenomena near ground.

# Contents

<b>Zusammenfassung</b>	<b>i</b>
<b>Abstract</b>	<b>v</b>
<b>1 Introduction</b>	<b>1</b>
<b>2 Turbulence models</b>	<b>7</b>
2.1 Generalized modified atmospheric spectrum . . . . .	11
2.2 Generalized modified von Kármán spectrum . . . . .	12
2.3 Height dependency of atmospheric turbulence . . . . .	13
<b>3 Theory</b>	<b>17</b>
3.1 Point spread function (PSF) and optical transfer function (OTF) . . . . .	17
3.2 Figures of merit . . . . .	20
3.2.1 Spatial covariance . . . . .	20
3.2.2 Structure function . . . . .	21
3.2.3 Wave structure function $D(\rho)$ . . . . .	21
3.2.4 Fried parameter $r_0$ . . . . .	23
3.2.5 Strehl ratio . . . . .	23
3.2.6 Isoplanatic angle . . . . .	24
3.2.7 Rytov variance $\sigma_R^2$ . . . . .	24
3.2.8 Scintillation index . . . . .	25
3.2.9 Differential tilt variance . . . . .	26
3.2.10 Long-exposure and short-exposure optical transfer function . . . . .	28
3.3 Convergence of numerical integration . . . . .	31
<b>4 Methods</b>	<b>35</b>
4.1 Wave propagation by split-step beam propagation . . . . .	35
4.1.1 Paraxial wave equation . . . . .	36
4.1.2 Split-step beam propagation method . . . . .	37
4.2 Generation of uncorrelated 2D phase screens . . . . .	40
4.2.1 Addition of subharmonics . . . . .	41

4.2.2	Phase structure function of uncorrelated 2D phase screens . . . . .	43
4.2.3	Validation of phase screens . . . . .	43
4.3	Generation of correlated 2D phase screens . . . . .	53
4.3.1	3D random fields . . . . .	53
4.3.2	Correlated 2D phase screens . . . . .	54
4.3.3	Phase structure function of correlated 2D phase screens . . . . .	55
4.3.4	Validation of phase screens . . . . .	57
4.4	Calculation of point spread function . . . . .	67
4.5	Turbulence simulation via non-uniform filtering . . . . .	70
4.5.1	Generation of local point spread functions . . . . .	71
4.5.2	Rescaling of point spread functions to sensor units . . . . .	74
<b>5</b>	<b>Evaluation of simulated images</b>	<b>75</b>
5.1	Uncorrelated 2D phase screens . . . . .	75
5.1.1	Validation of modulation transfer function . . . . .	75
5.1.2	Validation of differential tilt variance . . . . .	80
5.1.3	Validation of scintillation index . . . . .	84
5.1.4	Validation of Strehl Ratio . . . . .	85
5.2	Correlated 2D phase screens . . . . .	86
5.2.1	Validation of modulation transfer function . . . . .	87
5.2.2	Validation of differential tilt variance . . . . .	90
5.2.3	Validation of scintillation index . . . . .	92
5.2.4	Validation of Strehl ratio . . . . .	92
5.3	Implementation and benchmarks . . . . .	93
5.4	Comparison: Inverse Fourier method with subharmonics versus sparse spectrum (SS) method . . . . .	94
<b>6</b>	<b>Evaluation of observed degraded images</b>	<b>97</b>
6.1	Experimental acquisition of turbulence degraded imagery . . . . .	97
6.1.1	Experimental settings . . . . .	101
6.1.2	Image evaluation on regions of interest . . . . .	102
6.1.3	Calculation of LED footprint MTF . . . . .	104
6.1.4	Calculation of modulation transfer function (MTF) ratios . . . . .	106
6.1.5	Calculation of centroids . . . . .	109
6.1.6	Mechanical stability of experimental setup . . . . .	111
6.1.7	Calculation of differential tilt variance (DTV) . . . . .	113
6.2	Estimation of the most likely turbulence model parameters . . . . .	115
6.3	Cummulative distribution functions of turbulence parameters . . . . .	133

6.3.1	Generalized modified von Kármán spectrum . . . . .	133
6.3.2	Generalized modified atmospheric spectrum . . . . .	136
6.4	Correlation between turbulence parameters . . . . .	140
6.5	Turbulence parameters versus date . . . . .	142
<b>7</b>	<b>Summary and outlook</b>	<b>147</b>
<b>A</b>	<b>Bibliography</b>	<b>151</b>
<b>B</b>	<b>List of Figures</b>	<b>159</b>
<b>C</b>	<b>List of Tables</b>	<b>167</b>
	<b>Symbols</b>	<b>169</b>
	<b>Acronyms</b>	<b>175</b>
	<b>Acknowledgements</b>	<b>177</b>



# 1. Introduction

Optical turbulence effects in the atmosphere of earth pose a problem in a variety of application areas to name but a few astronomy, imaging, remote sensing, free space optical communication and laser radar systems (Andrews and Phillips [2005]).

The cause for these perturbation effects lies in the fact that the sun heats the rough earth surface and the atmosphere in different ways. This temperature difference generates convective air currents which lead to spatiotemporal fluctuations of temperature and air pressure in the atmosphere. Hence the refractive index of air is also fluctuating spatially and temporally, since it depends on temperature and pressure. For optical wave propagation these variations of refractive index result in wave front distortions leading to various undesired phenomena limiting the performance of various applications.

Depending on turbulence strength beams are spreaded beyond pure diffraction. There are random variations of the position of the beam centroid denoted as beam wander. Irradiance fluctuations often denoted as scintillation occur due to random redistributions of beam energy within the cross section of the propagating beam. In ground-based astronomy this can be observed as twinkling of stars. For imaging applications aperture-averaged wave front phase distortions result in local image dancing and non-uniform blur, i.e. there are spatially and temporally varying local shifts of individual image patches and the sharpness of these image areas is also temporally fluctuating.

For some applications advanced adaptive optics (AO) systems are used to counteract these degradational effects. For wave-front sensing a variety of different types of wave-front sensors have been developed within the last decades such as the Shack-Hartmann wave-front sensor (Platt and Shack [2001]) or the curvature sensor (Roddier [1988]). In ground-based astronomy objects of interest are often subject to faint fields. Then artificial guide stars (Foy and Labeyrie [1985]) in the vicinity of the object of interest are formed by scattered laser light. As the projection of the object of interest is then subject to wave front distortions similar to those of the guide star, images of the object of interest can be enhanced by sensing and correcting wave front distortions from the guide star. Deformable mirror arrays are used to correct sensed turbulence-induced aberrations. Various types of deformable mirror arrays have been proposed and developed such as the bimorph mirrors (Samarkin et al. [2002]), which use two thin piezo-ceramics plates with locally varying surface curvature. Bending of a mirror surface is achieved by mechanical tension caused by applied electrical voltages (inverse piezoelectric effect). Stacked-actuator mirrors (Laslandes et al. [2015]) use sophisticated electrode layouts optimized for low residual wavefront aberrations with minimum number of separate electrodes. Compared to plain imagers AO systems are

in general more extensive due to the required wavefront sensor and corrector. Data processing between wavefront sensor and corrector is also specific for the used device.

For imaging applications, several digital turbulence mitigation techniques have been proposed. These methods use series of turbulence-degraded images to reconstruct single enhanced images. Lucky region fusion (Vorontsov and Carhart [2001]) forms a running average of frames within a video sequence weighted by a local sharpness metric. However, for using appropriately sized image patches, this method requires knowledge about turbulence conditions which is in general not available from series of turbulence-degraded images with arbitrary image content. Bispectral speckle imaging (Carrano [2002]) uses averaged spectra of image frequencies for series of captured images to form reconstructions near the diffraction limit. Space-variant blind deconvolution (Zhu and Milanfar [2013]) uses an image registration technique, which estimates a motion field of local displacements for every image of a series of turbulence-degraded images. By inverse shifting of image patches turbulence-induced image dancing is corrected. Then a near diffraction-limited image is reconstructed by selecting locally sharpest image patches from the entire image series. A single-image global deconvolution process compensates for degradations caused by the used imager itself and gives the final image. Another work (Nieuwenhuizen and Schutte [2019]) shows that deep models trained on image sequences with simulated turbulence with known turbulence strength can reconstruct mitigated images with enhanced quality from image sequences with real turbulence and unknown turbulence strength.

However, field trials with cameras for aggregating turbulence-degraded imagery are time-consuming and expensive. Also atmospheric turbulence depends on a variety of environmental conditions such as temperature, daytime, wind, cloudiness, ground condition, air humidity, etc. Most of these conditions are not deliberately controllable and therefore difficult to reproduce. Furthermore, the measurement of these conditions is aggravated by spatial and temporal inhomogeneity. Another problem can be nonstationary stabilization errors of cameras due to wind effects and displacements in the experimental setup. Hence, for assessing imager performance of multiple imagers under same conditions especially of those using unknown embedded turbulence mitigation techniques it is preferable to have an experimental setup in the laboratory consisting of a part for scene projection and the devices under test. As the effects of atmospheric turbulence on scenes with objects of interest then have to be replaced by artificial video sequences representing projected scenes, a realistic image-based simulation of turbulence effects is required.

An algorithm for image-based turbulence simulation using non-uniform Gaussian blur and inverse mapping for local displacement was proposed (Repasi and Weiss [2008], Bosq and Repasi [2015]). Blur kernel widths and displacements were derived from edge width end position variations of checkerboard patterns captured in a field trial. This approach was enhanced by a data-constrained algorithm for the generation of long-range turbulence-degraded videos (Miller et al. [2019]). A main focus of this work has been real-time application in order to generate much image data in short time for assessment of machine learning algorithms, whose performance highly depends on the availability of large amounts of data. 2D random maps for non-uniform blur and local image displacement based on power law noise spectra are

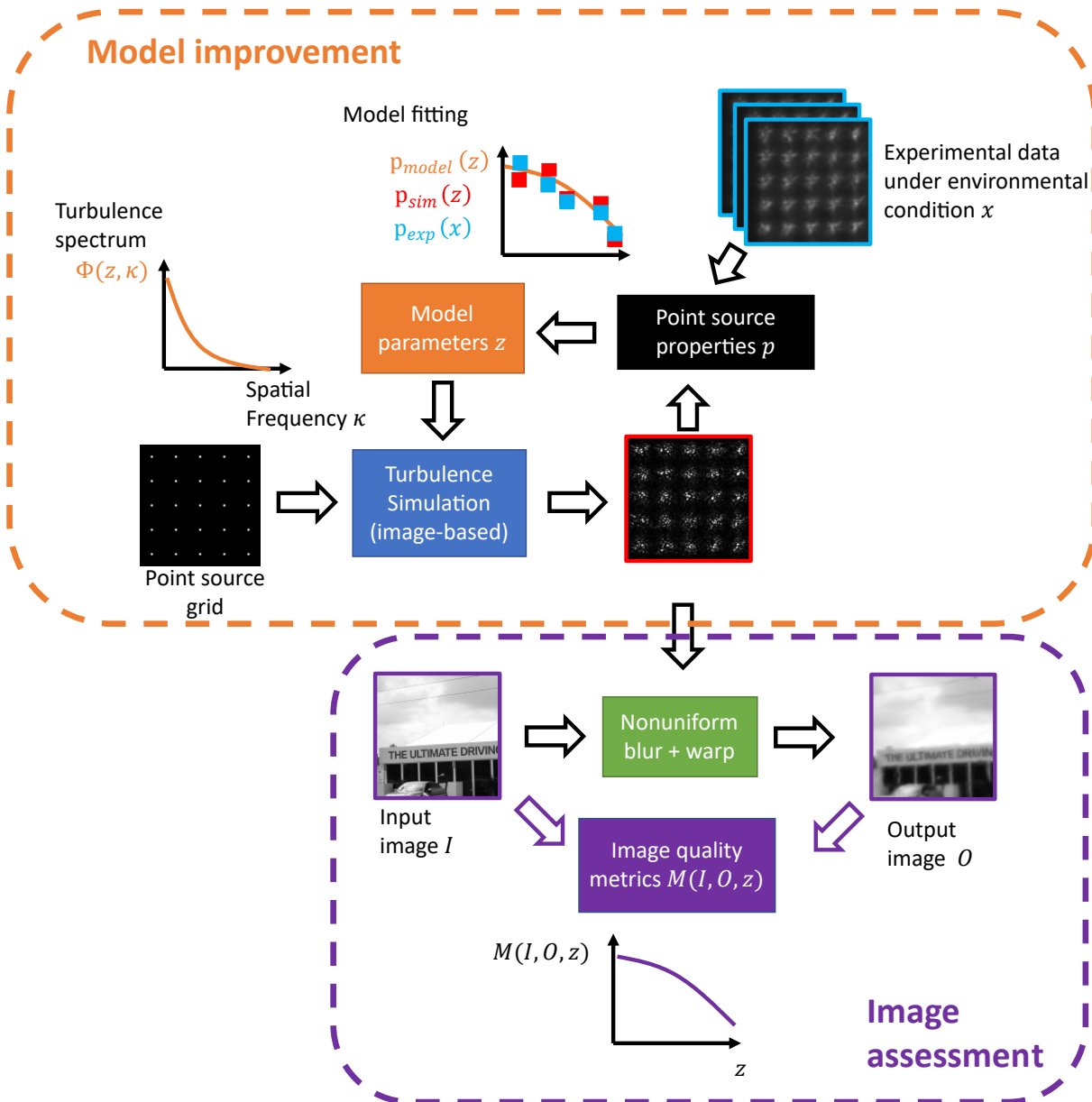
---

generated in accordance with experimentally measured noise spectra from a field trial. Sparse representations of realistic short-exposure point spread functions are calculated. The source image is then filtered by convolution with these representational point spread functions. As this step has to be applied only once for a specific input image the algorithm is faster than filtering frame-by-frame with space- and time-variant filter kernels. The final image is then formed as spatially and temporally varying superposition of these prefiltered images. Temporal variations of blur and displacements are calculated by random walk simulations leading to power law noise spectra and require a support of a single frame.

In this thesis a more general approach for image-based turbulence simulation is presented. 2D phase screens representing refractive index fluctuations are generated based on current turbulence models. Wave propagation of spherical waves through this refractive index fluctuations is applied to calculate wavefront aberrations occurring at the circular aperture of an imaging system. Then Fourier optics on these wavefront aberrations integrated over the aperture gives the point spread function representing the combined degradation due to turbulence and optical diffraction, i. e. the intensity profile in the focal plane related to a point light source at a specific distance to the imager. This image is formed by Fourier optics of the aperture-masked field transmission. Spatial shifting of the phase screens enables the calculation of point spread functions at different viewing angles. To determine which phase screen methods are best suited in terms of accuracy and speed, two methods, the FFT method with subharmonics and the sparse spectrum (SS) method are compared. Current simulation approaches use turbulence model parameters as input, which cannot trivially be derived from meteorological, location and time data. In this thesis an existing approach is used to retrieve distributions of turbulence model parameters based on current turbulence models from experimental data recorded on several days at the same location. However, if simulations with the retrieved turbulence model parameters can approximate the corresponding experimental data, has to be checked.

An image based simulation of turbulence can be helpful for several purposes. On the one hand, it can be used to improve modelling of the optical properties of air turbulence in an iterative way. On the other hand, various image quality metrics can be evaluated on simulated images with turbulence degradation. These image quality metrics can be used to develop or assess methods for digital turbulence mitigation (Kamenetsky et al. [2016]). In recent decades a vast variety of image quality metrics have been proposed and used to assess image degradations due to blur, noise, lossy compression, etc (Bosse et al. [2018]). Another application of these metrics is the assessment of imagers for remote sensing based on lab measurements (Koerber et al. [2018]). Then the turbulence simulation may serve as a building block in a chain of other degradations related to sensor sampling, digital processing, etc. This dual use scheme is depicted in figure 1.1. Depending on specific turbulence model parameters  $z$  turbulence-degraded images can be simulated based on images of point source grids. Based on the simulated images properties of the degraded point source profiles can be calculated such as width, centroid shifts or spatial correlation. The very same can be done on captured video sequences of point sources. Then the most likely turbulence parameters  $z$  for the environmental condition  $x$  can be derived by fitting an analytical model  $p_{model}(z)$

Figure 1.1.: Dual use scheme: 1. An image based simulation can be used for turbulence model improvements. 2. Simulated image sequences with turbulence degradation can be used for applications that rely on image assessment (digital turbulence mitigation, lab-based imager assessment)



---

to the point source properties in the experimental data  $p_{exp}(x)$ . Optical turbulence effects are caused by refractive index fluctuations in the air. Since the refractive index depends on pressure, temperature and humidity and convective air flows near ground are induced by solar radiation, the environmental condition  $x$  varies during a day. The simulation can be validated by comparing point source properties derived from simulated frames  $p_{sim}(z)$  with the corresponding analytical properties  $p_{model}(z)$ . A great benefit of the image based simulation compared to theoretical models is the ability to represent multi-speckle patterns resulting from single point sources at high turbulence strengths. A precise theoretical description of these multimodal distributions would require to take many high order moments into account. Moreover, an image-based simulation can be used to search for measurable quantities which are very sensitive to single model parameters. This may help for more accurate estimations of these parameters from experimental data.

Retrieval of these model parameters  $\mathbf{z}$  and its distributions may also be helpful for comparison with microscale turbulence simulations in meteorology, i.e. processes in the range of few mm to several hundred m, which are building blocks in multiscale models used in numerical weather prediction models (?). These methods are very computationally expensive. Hence, for suitable grid spacings in numerical simulations, knowledge is required about realistic inertial subranges of turbulence described by the model parameters  $\mathbf{z}$ .

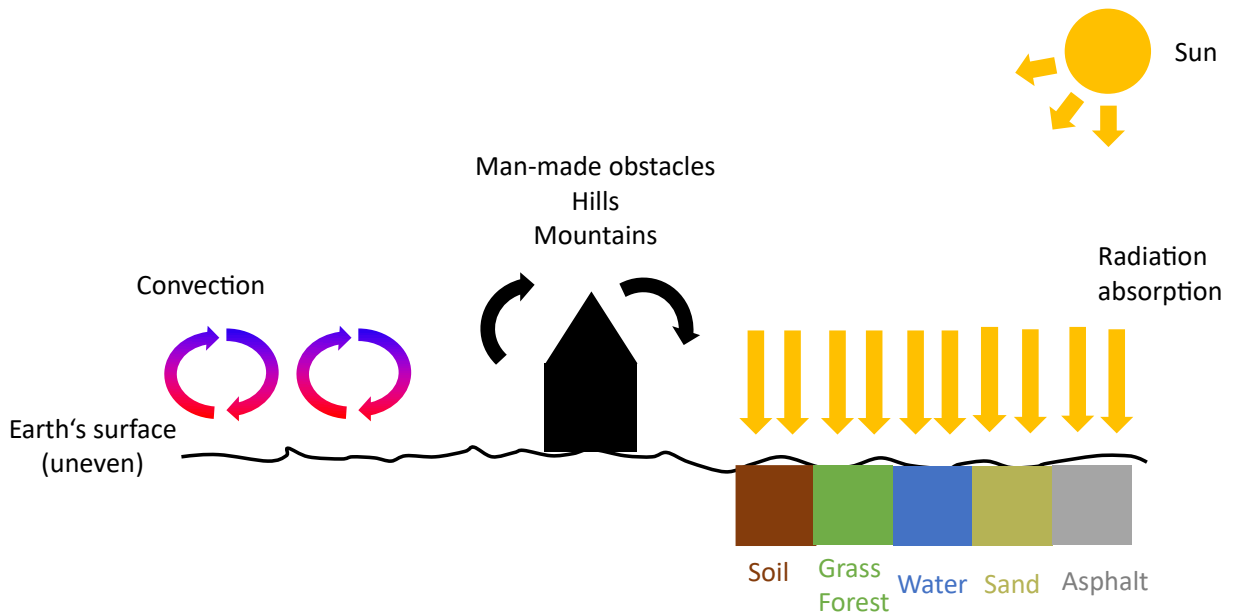
The structure of this thesis is as follows: In chapter 2 the general background and the development of turbulence models for optical propagation are explained. In chapter 3 the classical imaging process of cameras within a chain of subsequent degradational effects is described, e.g. motion, detector sampling and footprint, optical diffraction and atmospheric turbulence, whose implementation is complex due to its nonlinear nature. Also various validation metrics for the image-based turbulence simulation are introduced. As many of these metrics are only available as integral representations, which cannot be solved analytically, convergence tests of numerical integrations are made. Chapter 4 describes the phase screen method of turbulence simulation, which consists of the generation of correlated and uncorrelated 2D phase screens based on selected turbulence models and an imaging turbulence simulation via non-uniform filtering of pristine imagery of input scenes. In this chapter also statistical properties of simulated 2D phase screens are validated. Then in chapter 5 simulated projections of single point sources and grids of equidistant point sources are validated. Turbulence-degraded grids of point sources serve as filter kernels for non-uniform filtering that can be used for anisoplanatic imaging of arbitrary input scenes. For realistic image-based turbulence simulations also taking model parameter uncertainties into account, prior knowledge about real model parameter distributions is required. For this purpose, field trials at the same location conducted on several days are described in chapter 6. In these field trials projections of an LED matrix representing an equidistant grid of point sources are recorded at varying distances of about 100 m - 150 m. Acquired image data can be used for the estimation of most likely turbulence model parameters, which can be used in respective turbulence simulations. Also diversity of the retrieved turbulence model parameters over all recording dates is shown. These findings provide

realistic data distributions of model parameters, which can be used as input for the described approach and future turbulence simulations. Compared to single-shot simulations with fixed model parameters, these distributions enable the assessment of uncertainties in the simulation results due to varying environmental conditions. Finally in chapter 7 conclusions are drawn and the scope of application for an image-based turbulence simulation discussed, as well as further approaches for future improvement.

## 2. Turbulence models

Solar radiation causes turbulent air flows in the atmosphere of the earth and near the surface. Mechanical turbulence is caused by friction between air flows and the ground due to roughness of earth's surface, man-made obstacles, hills, mountains, etc (USA National Weather Service [2021]). Different types of terrain or irregularities in the terrain lead to varying absorption of sun radiation, e.g. soil and sand heat up much more rapidly than grass, and this in turn heats up much more rapidly than water. Inhomogeneous heating of the uneven ground leads to convective air flows, i.e. warm air rises and cools down, while cold air descends and warms up. These procedures are illustrated in figure 2.1. Further mechanisms for

Figure 2.1.: Illustration of turbulence near ground: 1. Solar heating of the earth's surface forms convection cells: Warm air rises and cools down, while cold air descends and warms up. 2. Obstacles and the uneven surface of the earth cause friction between air currents and the ground. 3. Different types of terrain absorb sun radiation to different degrees, which leads to temperature inhomogeneities.



the generation of turbulent air currents in the atmosphere exist, e.g. wind shear, temperature inversion or friction between opposing cold and warm air fronts (USA National Weather Service [2021]).

These turbulent air flows induced by sun radiation lead to local fluctuations of pressure  $p(\mathbf{R})$  and temperature  $T(\mathbf{R})$ . The refractive index of air is dependent on pressure and temperature (Owens [1967]) by

$$n(\mathbf{R}) = 1 + 77.6 \cdot 10^{-6} (1 + 7.52 \cdot 10^{-3} \lambda^{-2}) \frac{p(\mathbf{R})}{T(\mathbf{R})}, \quad (2.1)$$

with wavelength  $\lambda$  and position  $\mathbf{R}$ . In practice pressure fluctuations are small compared to temperature variations and can be neglected. This leads to refractive index fluctuations responsible for several degradational effects in light and laser propagation through air. Also dependencies of the refractive index on air humidity were found by measurements (Tunick and Rachele [1992], Chang et al. [2007]), since water has a refractive index  $n \geq 1.3$  for visible and longer wavelengths  $\lambda$  (Hale and Querry [1973]). This is significantly larger than that of the air  $n \approx 1$ . Also humidity influences buoyancy forces near ground. Statistically homogeneous 3D random fields of refractive index  $n(\mathbf{R})$  can be expressed by a Riemann-Stieltjes representation

$$n(\mathbf{R}) = \int \int \int_0^\infty \exp(i\mathbf{K}\mathbf{R}) d\nu(\mathbf{K}) \quad (2.2)$$

with a random amplitude  $d\nu(\mathbf{K})$  with covariance

$$\langle d\nu(\mathbf{K}) d\nu^*(\mathbf{K}') \rangle = \delta(\mathbf{K} - \mathbf{K}') \Phi_n(\mathbf{K}) d^3\kappa d^3\kappa' \quad (2.3)$$

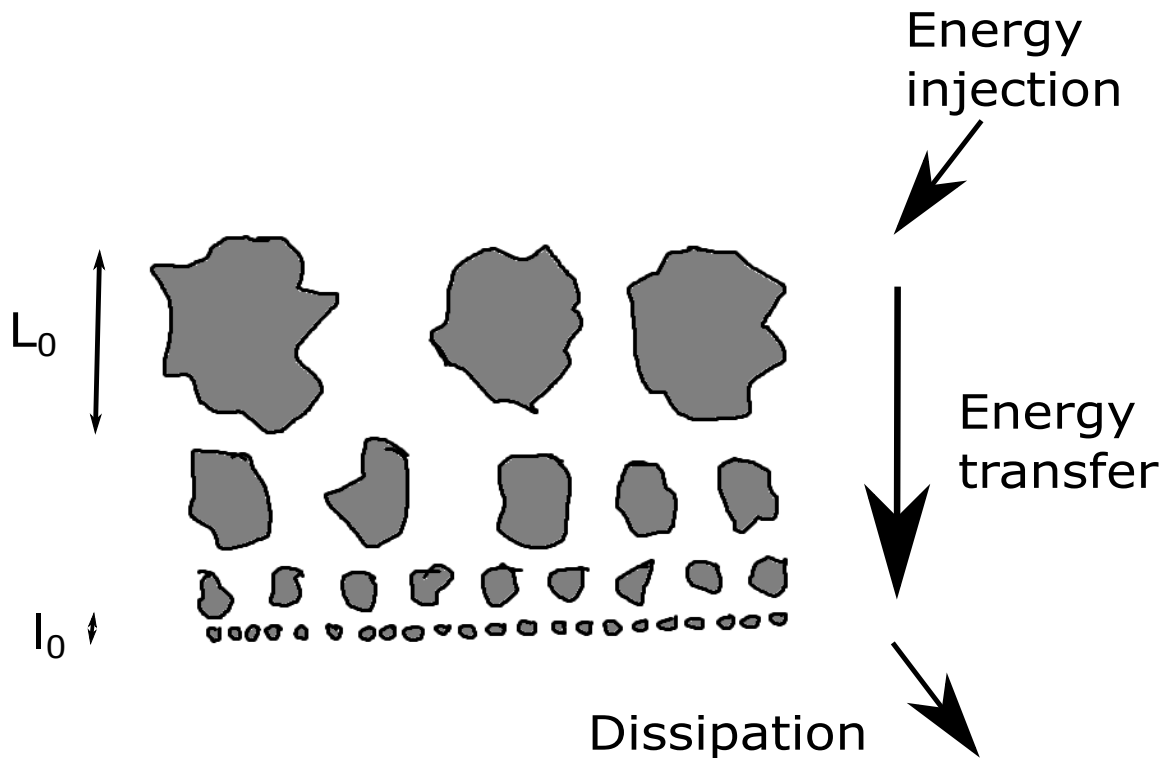
The refractive index fluctuations are then modeled by the spatial power spectrum  $\Phi_n(\mathbf{K})$ . In many cases also isotropy is assumed:

$$\Phi_n(\mathbf{K}) = \Phi_n(\kappa) \quad (2.4)$$

with  $\kappa = |\mathbf{K}|$ . Spatial temperature gradients are induced by heat diffusion and convection due to a non-vanishing velocity field of air. The atmosphere can be considered as a viscous fluid, which may be in two distinctive states, laminar flow and turbulent flow (Andrews and Phillips [2005]). While for laminar flow the velocity characteristics are uniform or regular in some fashion, for turbulent flow the velocity field loses its uniform characteristics due to dynamic mixing and acquires random subflows called turbulence eddies. The classical theory of turbulence was developed by Kolmogorov in the early 1940s (Andrews and Phillips [2005]). It concerns random fluctuations in both the magnitude and direction of the velocity field of a fluid. His theory is driven by a set of hypotheses based on physical insights. The turbulence behaviour of geometrically similar objects in a flowing fluid can be characterized by the Reynolds number

$$Re = \frac{vd}{\nu} \quad (2.5)$$

Figure 2.2.: Kolmogorov cascade theory of turbulence.  $L_0$  denotes the outer scale and  $l_0$  the inner scale. Eddies between scale sizes  $l_0$  and  $L_0$  form the inertial subrange (Adaptation of a figure in Andrews and Phillips [2005]).



$v$  is the flow velocity of the fluid,  $d$  is the characteristic scale size and  $\nu$  is the kinematic viscosity of the fluid. If the Reynolds number  $Re$  exceeds a problem-dependent critical value  $Re_{krit}$ , a laminar flow gets susceptible to smallest perturbations in the velocity field of the fluid. Hence there is a transition to turbulent flow for  $Re > Re_{krit}$ . Close to the ground the characteristic scale size is  $d \sim 2$  m, characteristic wind speed is 1 to 5 m/s and  $\nu \sim 0.15 \cdot 10^{-4} \text{ m}^2/\text{s}$ . Hence Reynolds numbers are of the order  $Re \sim 10^5$ . In such cases the motion is considered highly turbulent. Now for sufficiently large Reynolds numbers it was hypothesized that the small-scale structure of turbulence is statistically homogeneous, isotropic and independent of the large-scale structure. It was also assumed that the motion associated with the small scale is uniquely determined by the kinematic viscosity  $\nu$  and the average rate of dissipation  $\epsilon$  of the turbulent energy per unit mass of the fluid. The energy cascade theory of Richardson (Richardson [2007]) shown in figure 2.2 is a useful model to understand the structure of the atmospheric turbulence. The source of energy at large scales is wind shear or convection. In the cascade theory wind velocity increases until it reaches a point where the critical Reynolds number is exceeded. This leads to the generation of unstable air masses ("eddies") with characteristic sizes slightly smaller than the parent flow. Due to inertial forces larger eddies break up into smaller eddies to form a continuum of eddy size for the the transfer of enery from a macroscale  $L_0$  denoted as outer scale to a microscale  $l_0$  denoted as

inner scale. The family of eddies with sizes between  $l_0$  and  $L_0$  form the inertial subrange. For scale sizes smaller than  $l_0$  turbulence eddies disappear and the remaining energy is dissipated as heat.

Various methods for measurements of atmospheric turbulence have been used within the last decades. Many of these experiments are focused on the properties of the atmosphere from a meteorologic point of view, while others are concerned with the optical properties of atmosphere for applications such as laser radar (lidar) systems (Halmos and Wang [1992]), laser satellite communication (Khalighi and Uysal [2014]), laser airborne communication (Moll et al. [2015]), ground-based astronomy (McKechnie [1992]) and remote sensing. Traditional means to measure fluctuations of wind speed and temperature as parameters of atmospheric turbulence are ultrasonic anemometers and thermometers (Nosov et al. [2019]). Acoustic locators (sodars) have been used for measuring vertical profiles of mean wind speed and direction in atmosphere (Ito [1997], Rapoport et al. [2002], Engelbart et al. [2007]). Radar methods can be used to estimate the eddy dissipation rate  $\eta$  or turbulence strength  $C_n^2$  at different altitudes in the troposphere. Heterodyne Doppler lidars (HDLs) (Drobinski et al. [2000]) have been used to measure the atmospheric wind field and wind turbulence at some remote distance. However, HDL measurements only represent spatial averages of the true wind velocity along the line of sight. Additionally, signal quality is limited due to speckle fluctuations. Combinations of staring wind lidars (Mann et al. [2008]) can be used to measure temporal spectra of wind speeds in good agreement with those measured by a sonic anemometer. A comparative study (Yatcheva et al. [2015]) shows a large variety of devices and computational methods for measuring optical turbulence, such as widely used Laser and large-aperture scintillometers and Shack-Hartmann sensors. The presented methods showed good agreement in terms of turbulence strength  $C_n^2$ . Absolute and differential image motion measurements with an LED array can be used to derive turbulence model parameters.

The behaviour of the energy cascade shown in figure 2.2 is typically characterized by the Kolmogorov power-law spectrum :

$$\Phi_{n,Kolmogorov}(\kappa) = 0.033C_n^2\kappa^{-11/3} \quad 1/L_0 \ll \kappa \ll 1/l_0 \quad (2.6)$$

However, this spectrum is appropriate only for wave numbers  $\kappa$  within the inertial subrange  $[1/L_0, 1/l_0]$ . In order to account also for wave numbers outside the inertial range various models (Andrews and Phillips [2005]) have been proposed. These models include the Tatarskii spectrum:

$$\Phi_n(\kappa) = 0.033C_n^2\kappa^{-11/3}\kappa \exp\left(-\frac{\kappa^2}{\kappa_m^2}\right) \quad \kappa \gg 1/L_0 \quad \kappa_m = 5.92/l_0 \quad (2.7)$$

the modified von Karman spectrum:

$$\Phi_n(\kappa) = 0.033C_n^2 \frac{\exp(-\kappa^2/\kappa_m^2)}{(\kappa^2 + \kappa_0^2)^{11/6}} \quad 0 \leq \kappa < \infty \quad \kappa_m = 5.92/l_0 \quad (2.8)$$

and the modified atmospheric spectrum:

$$\begin{aligned} \Phi_n(\kappa) &= 0.033C_n^2[1 + 1.802(\kappa/\kappa_l) - 0.254(\kappa/\kappa_l)^{7/6}] \\ &\times \frac{\exp(-\kappa^2/\kappa_m^2)}{(\kappa^2 + \kappa_0^2)^{11/6}} \quad 0 \leq \kappa < \infty \quad \kappa_l = 3.3/l_0 \end{aligned} \quad (2.9)$$

Turbulence measurements close to ground (Gladysz et al. [2013]) have shown that the power slope  $\alpha$  can deviate from the Kolmogorov power slope  $\alpha_{Kolmogorov} = 11/3$ . In the following two isotropic state of the art turbulence models with general exponent  $\alpha$  are presented, the generalized modified von Kármán spectrum (GMVKS) and the generalized modified atmospheric spectrum (GMAS). These spectra are used for the generation of phase screens required for image-based turbulence simulation. Then they are also used for validation with experimental data.

Anisotropic turbulence models have been proposed within recent years (Toselli et al. [2011]). However, most of proposed measurable quantities are integral representations of these models. Hence, numerical evaluations of these integrals are more complex and expensive due to an additional spatial dimension compared to isotropic models. Therefore, anisotropic models are not taken into account in this thesis. Some of these measurable quantities are presented in the next chapter and used for evaluations on isotropic models described in the next sections.

## 2.1. Generalized modified atmospheric spectrum

The generalized modified atmospheric spectrum (GMAS)(Xue et al. [2011]) is given by

$$\begin{aligned} \Phi_{n,GMAS}(\kappa) &= A(\alpha)C_n^2\kappa^\alpha \left( 1 + a \left( \frac{\kappa}{\kappa_l} \right) - b \left( \frac{\kappa}{\kappa_l} \right)^\beta \right) \\ &\times \exp \left( -\frac{\kappa^2}{\kappa_l^2} \right) \left( 1 - \exp \left( -\frac{\kappa^2}{\kappa_0^2} \right) \right), \end{aligned} \quad (2.10)$$

where

$$A(\alpha) = \frac{\Gamma(\alpha-1)}{4\pi^2} \sin \left( \frac{\pi(\alpha-3)}{2} \right), \quad (2.11)$$

$$\kappa_0 = \frac{4\pi}{L_0}, \quad (2.12)$$

$$\kappa_l = \frac{(\pi A(\alpha)C_n^2)^{1/(\alpha-5)}}{l_0}, \quad (2.13)$$

$$C_\alpha = \frac{3-\alpha}{3} \Gamma \left( \frac{3-\alpha}{2} \right) + a \frac{4-\alpha}{3} - \Gamma \left( \frac{4-\alpha}{2} \right) - b \frac{3+\beta-\alpha}{3} \Gamma \left( \frac{3+\beta-\alpha}{2} \right) \quad (2.14)$$

The relevant parameters are the turbulence strength  $C_n^2$ , the exponent  $\alpha$ , the inner scale  $l_0$  and the outer scale  $L_0$ .  $a$ ,  $b$  and  $\beta$  are further parameters modifying the high frequency contributions related to inner scale  $l_0$ .

## 2.2. Generalized modified von Kármán spectrum

The generalized modified von Kármán spectrum (GMVKS) (Toselli and Larry C. Andrews [2007]) is given by

$$\Phi_{n.GMVKS}(\kappa) = A(\alpha) \cdot C_n^2 \frac{\exp\left(-\frac{\kappa^2}{\kappa_l^2}\right)}{(\kappa^2 + \kappa_0^2)^{\frac{\alpha}{2}}}, \quad (2.15)$$

where

$$A(\alpha) = \frac{\Gamma(\alpha - 1)}{4\pi^2} \cdot \cos\left(\frac{\alpha\pi}{2}\right), \quad (2.16)$$

$$\kappa_0 = \frac{2\pi}{L_0} \quad (2.17)$$

$$\kappa_l = \frac{c(\alpha)}{l_0}, \quad (2.18)$$

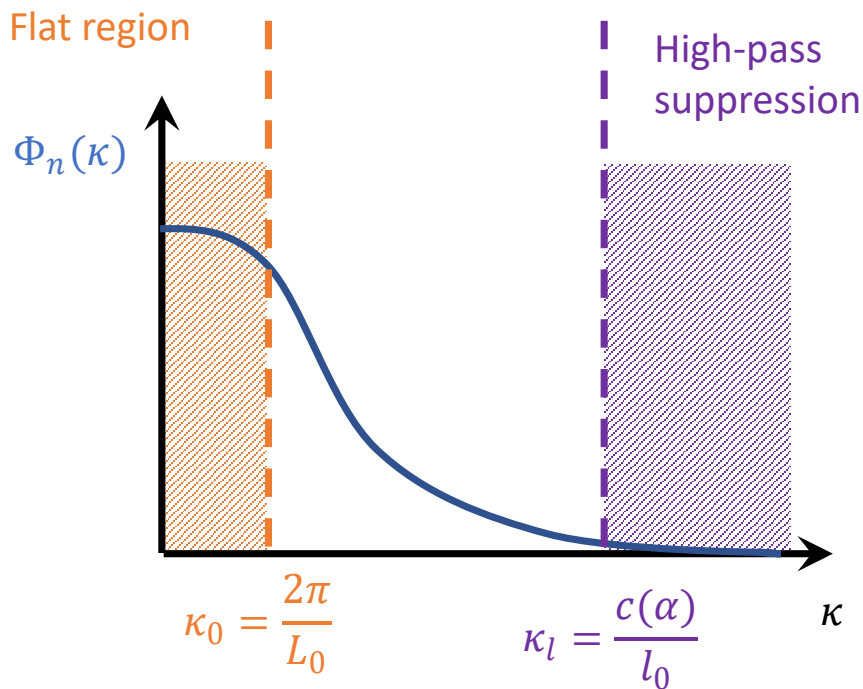
and

$$c(\alpha) = \left[ \Gamma\left(\frac{5-\alpha}{2} A(\alpha) \frac{2\pi}{3}\right) \right]^{\frac{1}{\alpha-5}} \quad (2.19)$$

Only the turbulence strength  $C_n^2$ , the outer scale  $L_0$ , the inner scale  $l_0$  and the exponent  $\alpha$  are common with the spectrum GMAS and have similar functionality. Vividly the outer scale  $L_0$  reduces the spectrum to lower frequencies  $\kappa$  and the inner scale  $l_0$  reduces the spectrum to higher values of spatial frequency  $\kappa$ . This is depicted in figure 2.3. For lengths  $L \gg L_0$  or frequencies  $\kappa \ll \kappa_0$  the spectrum gets flat. A flat spectrum is related to a spatial covariance  $Cov(R)$  (equation 3.10):

$$Cov(R) = \delta(R) = \begin{cases} R=0 & 1 \\ else & 0 \end{cases} \quad (2.20)$$

This means that there is no significant covariance  $Cov(R)$  for  $R = L \gg L_0$ .

Figure 2.3.: Effects of outer scale  $L_0$  and inner scale  $l_0$  on spectrum:

### 2.3. Height dependency of atmospheric turbulence

Atmospheric turbulence is highly dependent on altitude above ground over several meters to kilometers. Hence, for the simulation of optical turbulence effects over slant, top-bottom or bottom-top paths, e.g. from airplane to ground or vice versa it would be crucial to take this dependency into account. However, measurements on high altitudes require legal authorization and are cumbersome and expensive. Therefore this thesis is focused and limited on simulations and measurements on horizontal paths near ground with a fixed assumed turbulence strength  $C_n^2$  along the line of sight. Nevertheless, proposed height models for single turbulence model parameters can be easily integrated, if these parameters are approximated to be constant for the transversal extent of the propagated light field at any point of the line of sight. Therefore, for reasons of completeness, known height dependencies of some model parameters are just mentioned in the following. Not all required data is readily available for all model parameters of current turbulence models, e.g. realistic data distributions for a (non-)Kolmogorov power slope  $\alpha$ . The most naive approach would be to use relations similar to known height models of single model parameters. Based on measurements with balloon-borne radiosondes at several locations (Abahamid et al. [2004]), height models for some turbulence model parameters have been evaluated for the atmospheric boundary layer and the free atmosphere. The atmospheric boundary layer is the part of atmosphere whose behaviour is directly influenced by the earth surface (Hayden and Pielke [2021]). Its height can vary between 200 m (forest areas) and 5000 m (deserts). The overlying part of the atmosphere is denoted as

free atmosphere. In the atmospheric boundary layer the height dependency of turbulence strength  $C_n^2$  and outer scale  $L_0$  can be modeled by an exponential law

$$Y(h/\text{km}) = Y_0 \cdot (h/\text{km})^{-p}, \quad (2.21)$$

where  $p \sim 0.1 - 0.3$  for the outer scale  $L_0$  and  $p \sim 1.3 - 1.6$  for the turbulence strength  $C_n^2$ . Further models for the free atmosphere were also proposed. The Hufnagel model describes the turbulence strength  $C_n^2$  for altitudes  $3 \text{ km} < h < 24 \text{ km}$ :

$$C_n^2 = \left[ 2.2 \times 10^{-53} h^{10} (W/27)^2 \exp\left(-\frac{h/\text{m}}{1000}\right) + 10^{-16} \exp\left(-\frac{h/\text{m}}{1500}\right) \right] \exp[r(h, t)] \quad (2.22)$$

$W$  is a correlation factor related to scintillation and depending on wind speed  $v(h)$ :

$$W = \frac{1}{15 \text{ km}} \int_5^{20 \text{ km}} V(h)^2 dh \quad (2.23)$$

Abahamid et al. [2004] measured a mean correlation factor of  $W = 18.6 \text{ ms}^{-2}$ .  $r$  is a Gaussian random variable with  $\langle \exp r \rangle = e$ .

The Beland-Brown model describes the outer scale  $L_0$  for altitudes  $17 \text{ km} \leq h < 30 \text{ km}$ :

$$L_0(h/\text{km}) = 0.307 - 0.0324d + 0.00167d^2 + 0.000476d^3, \quad (2.24)$$

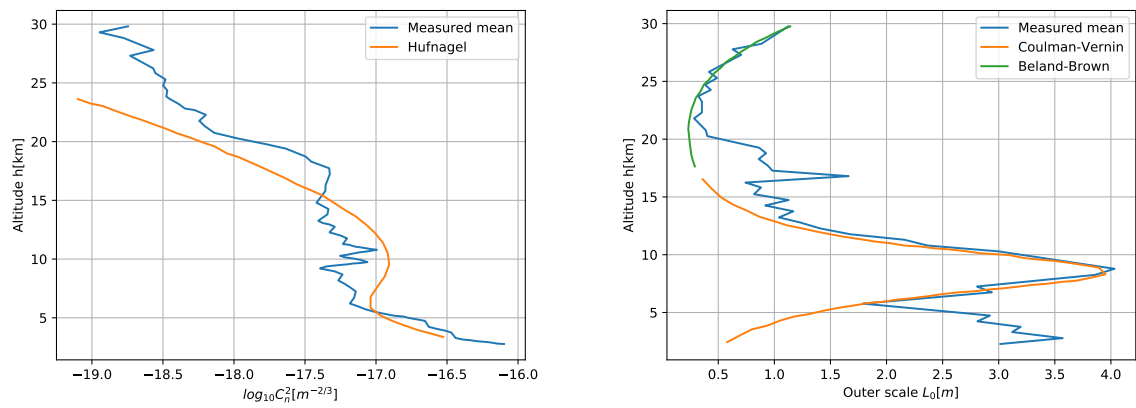
where  $d = h/\text{km} - 17$ .

The Coulman-Vernin model applies for altitudes  $2 \text{ km} < h < 17 \text{ km}$ :

$$L_0(h/\text{m}) = \frac{4}{1 + \left(\frac{h/\text{m} - 8500}{2500}\right)^2} \quad (2.25)$$

Corresponding models and measured mean values of the outer scale  $L_0$  and turbulence strength  $C_n^2$  are shown in figure 2.4. Further height models for the turbulence strength  $C_n^2$  were proposed (Lei and Tiziani [1993]).

Figure 2.4.: Measured mean values and models of outer scale  $L_0$  and turbulence strength  $C_n^2$  depending on altitude  $h$  (data extracted from Abahamid et al. [2004])





### 3. Theory

The typical image forming process of camera systems is determined by a sequence of optical and technical components. While most of these components behave like a linear shift-invariant system (LSI system), atmospheric turbulence reveals nonlinear temporal and spatial fluctuations that require special treatment. A comprehension of the linear part of the image forming process is useful to recognize the contrast to the more difficult and challenging turbulence part.

#### 3.1. Point spread function (PSF) and optical transfer function (OTF)

The point spread function describes the response of an imaging system to a point source. If a point source, e.g. in good approximation a star, is projected onto a camera sensor, the spatial intensity profile is degraded by a chain of optical and technical components as well as environmental effects. In remote sensing applications air turbulence can have a significant impact. Wind effects, camera movements or vibrating electronical components can cause stabilization errors. Optical diffraction through apertures extends the optical intensity profile. The finite size of detector elements leads to further blur of the intensity profile. Most of these degradational effects behave like a linear scale-invariant system, where each component's response to a single point source can be described by a point spread function (PSF). The 2D intensity profile  $O(x,y)$  resulting from all effects can then be described by a concatenation of convolutions on the point source profile  $I(x,y) = \delta(x)\delta(y)$ :

$$\begin{aligned} O(x,y) = & PSF_{detector}(x,y) * PSF_{aperture}(x,y) * PSF_{stabilization} \\ & * PSF_{atm}(x,y) * \dots * I(x,y), \end{aligned} \quad (3.1)$$

where a single convolution is given by

$$PSF(x,y) * I(x,y) = \int \int_{-\infty}^{\infty} dx' dy' PSF(x',y') \cdot I(x-x',y-y') \quad (3.2)$$

For a finite image with  $N_x \times N_y$  pixels, the discrete convolution is given by

$$(PSF * I)(i,j) = \sum_{i'=0}^{N_x} \sum_{j'=0}^{N_y} PSF(i',j') \cdot I(i-i',i-j'), \quad (3.3)$$

with the column indices  $i$  and  $i'$ , the row indices  $j$  and  $j'$  and the finite image with centered point source

$$I(i', j') = \begin{cases} i' = \frac{N_x}{2}, j' = \frac{N_y}{2} & 1 \\ else & 0 \end{cases} \quad (3.4)$$

Now from the computational point of view, direct numerical evaluations of convolutions for a finite image with  $N_x \cdot N_y$  pixels are expensive, as the calculation of  $N_x^2 \cdot N_y^2$  summands are required. A more efficient way is the use of optical transfer functions, which are the Fourier transforms of the point spread functions

$$OTF(v_x, v_y) = \mathcal{F}PSF(x, y) \quad (3.5)$$

The optical transfer function  $OTF(v_x, v_y)$  describes the response of the component in the spatial frequency domain. Then the Fourier transform of the output intensity profile can be calculated by subsequent multiplications on the input profile  $I(x, y)$ :

$$\begin{aligned} \mathcal{F}O(x, y) &= OTF_{detector} \times OTF_{aperture}(v_x, v_y) \times OTF_{stabilization}(v_x, v_y) \\ &\times OTF_{atm}(v_x, v_y) \times \dots \times \mathcal{F}I(x, y) \end{aligned} \quad (3.6)$$

The complex optical transfer function can be splitted into magnitude and argument. Then the magnitude is given by the modulation transfer function (MTF) and the argument is given by the phase transfer function (PhTF):

$$OTF = MTF \cdot e^{iPhTF} \quad (3.7)$$

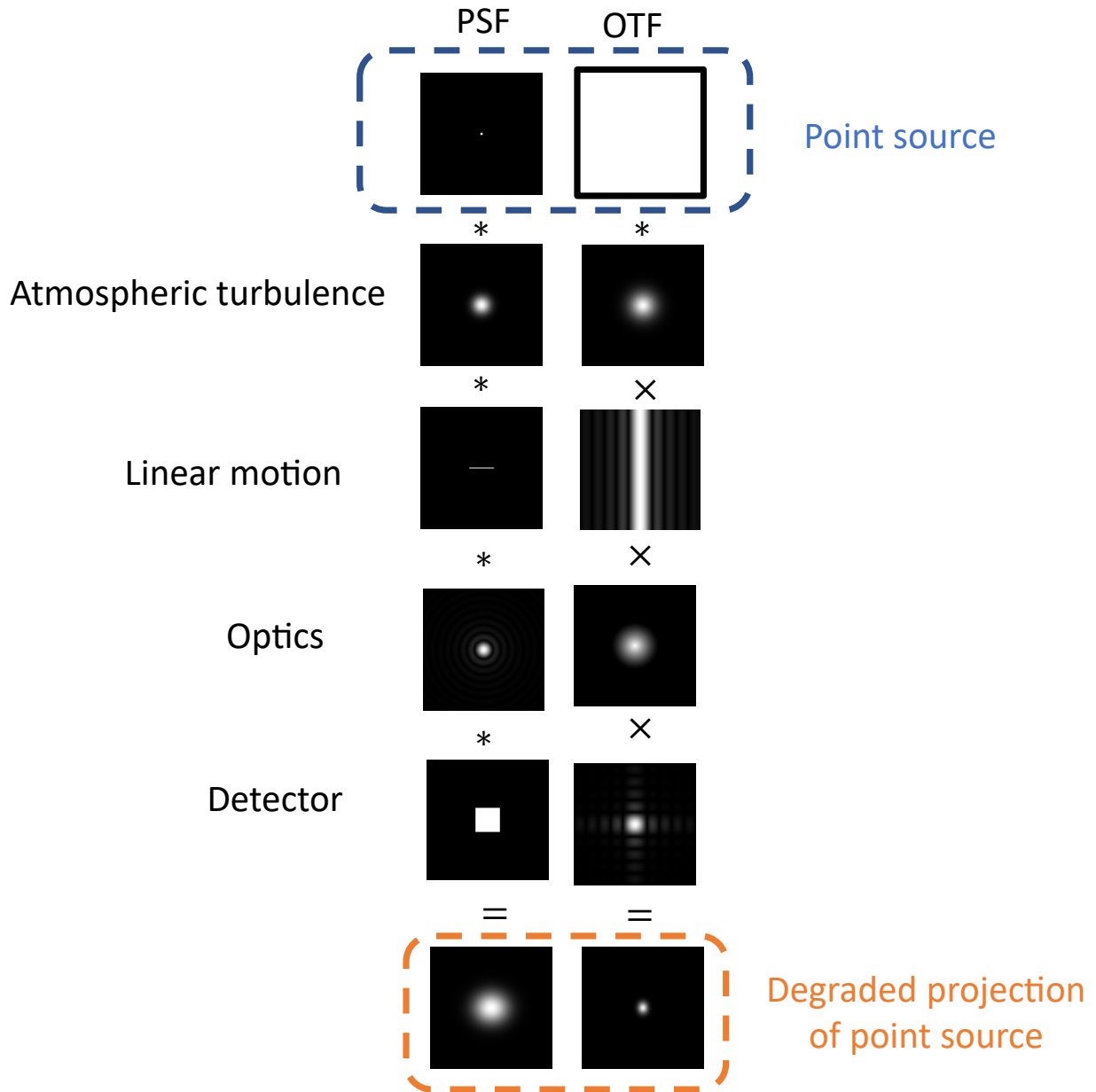
Many degradational effects have real OTFs, and so they are identical to their MTFs.

In the discrete case, the optical transfer functions can be multiplied pixelwise, so for each  $OTF$  only  $N_x \cdot N_y$  products have to be calculated. Unfortunately this multiplication of discrete OTFs  $OTF(v_i, v_j)$  corresponds to the cyclic convolution of the inverse Fourier transforms,  $PSF(i, j)$  and  $I(i, j)$ . In the evaluation of equation 3.3,  $I(i, j)$  behaves  $N_x$ -periodic in horizontal direction and  $N_y$ -periodic in vertical direction, i. e.  $I(i, j) = I(i + kN_x, j + lN_y)$  for all  $k, l \in \mathbb{Z}$ . For an intermediate image

$$I_n(x, y) = PSF_n(x, y) * PSF_{n-1}(x, y) * \dots * I(x, y) \quad (3.8)$$

with significant signal at the image borders, this leads to overlapping between opposing sides of the image in the convolution sum (equation 3.3). This is a computational artifact and physically not plausible. However, this problem can be easily eliminated by adding  $N_x$  border columns and  $N_y$  border rows with zero values. A typical workflow is depicted in figure 3.1.

Figure 3.1.: Image degradation process: Final PSF results from subsequent convolution with PSFs related to single degradation effects. Final OTF results from subsequent pixelwise multiplication of OTFs related to same single degradation effects. Gray scale images encode values in  $[0, 1]$ , with black = 0, and white = 1



As any arbitrary input scene can be thought of as superposition of multiple point sources, and all operations in the chain are linear, the procedure can be applied on input images to give the final camera images. Now for air turbulence, the long-exposure PSF is independent of viewing angle through the aperture. This is the optical intensity profile of a projected point source obtained from time integration with integration times  $t \gg t_{turb}$ , where  $t_{turb} \approx 10 - 100$  ms are typical correlation times. However for short integration times, there are instantaneous phase aberrations at the aperture which lead to temporally and spatially varying intensity profiles on the camera sensor depending on the viewing angle. Then the image

formation cannot be described by convolution but filtering with a position-dependent instantaneous PSF  $PSF(i, j, i', j')$ :

$$O(i, j) = \sum_0^{N_x} \sum_0^{N_y} PSF(i, j, i', j') I(i - i', j - j') \quad (3.9)$$

### 3.2. Figures of merit

Optical perturbation effects of atmospheric turbulence are governed by the spatially varying refractive index  $n(\mathbf{r})$ . As explained in chapter 2 the refractive index  $n(\mathbf{r})$  of air depends on pressure  $p(\mathbf{r})$  and temperature  $T(\mathbf{r})$ . Computational fluid dynamics (CFD) simulations to calculate these fields of pressure  $p(\mathbf{r})$  and temperature  $T(\mathbf{r})$  can often be computationally expensive and very time-consuming ((Jeong and Seong [2014])). A much simpler approach used for applications relying on light propagation through atmosphere is the modeling of the refractive index  $n(\mathbf{r})$  as 3D random fields. Then figures of merit are required to define and characterize these random fields. Also derived and possibly measurable quantities depending on the turbulence model  $\Phi_n(k, \mathbf{z})$  as power spectral density are necessary to validate image-based turbulence simulations and to estimate model parameters  $\mathbf{z}$  from experimental data required to feed in the simulation.

#### 3.2.1. Spatial covariance

The spatial covariance of a 3D random field  $n(\mathbf{r})$  is such a figure of merit. It is given as the Fourier transform of the corresponding 3D noise power spectral density  $\Phi_n(\boldsymbol{\kappa})$ :

$$Cov(\mathbf{R}) = \langle n(\mathbf{r}_1)n(\mathbf{r}_2) \rangle = \int_{-\infty}^{\infty} d\mathbf{K} \Phi_n(\mathbf{K}) \exp(i\mathbf{K}\mathbf{R}) \quad (3.10)$$

with  $\mathbf{R} = \mathbf{r}_1 - \mathbf{r}_2$ . As a power spectral density is an even function ( $\Phi_n(\boldsymbol{\kappa}) = \Phi_n(-\boldsymbol{\kappa})$ ), the imaginary part is eliminated:

$$Cov(\mathbf{R}) = 2 \int_0^{\infty} d\boldsymbol{\kappa} \Phi_n(\boldsymbol{\kappa}) \cos(\boldsymbol{\kappa} \cdot \mathbf{R}) \quad (3.11)$$

The covariance for a spherically symmetric noise power spectral density is given by

$$Cov(R) = \langle n(\mathbf{r}_1)n(\mathbf{r}_2) \rangle = \frac{4\pi}{R} \int_0^{\infty} d\boldsymbol{\kappa} \Phi_n(\boldsymbol{\kappa}) \sin(\boldsymbol{\kappa}R) \boldsymbol{\kappa} \quad (3.12)$$

with  $R = |\mathbf{r}_1 - \mathbf{r}_2|$ .

### 3.2.2. Structure function

The structure function of a 3D random field  $n(\mathbf{r})$  is defined as

$$D(\mathbf{R}) = \langle (n(\mathbf{r}) - n(\mathbf{r} - \mathbf{R}))^2 \rangle \quad (3.13)$$

It is related to the covariance  $Cov(\mathbf{r})$  via

$$\begin{aligned} D(\mathbf{R}) &= \langle n(\mathbf{r})^2 - 2n(\mathbf{r}) \cdot n(\mathbf{r} - \mathbf{R}) + n(\mathbf{r} - \mathbf{R})^2 \rangle \\ &= \langle n(\mathbf{r})^2 \rangle - 2 \langle n(\mathbf{r}) \cdot n(\mathbf{r} - \mathbf{R}) \rangle + \langle n(\mathbf{r} - \mathbf{R})^2 \rangle \\ &= 2(Cov(0) - Cov(\mathbf{R})) \end{aligned} \quad (3.14)$$

### 3.2.3. Wave structure function $D(\rho)$

For weak, isotropic and homogeneous turbulence, the method of small perturbations can be used to solve the wave propagation problem. The statistical properties of the resulting complex field  $U(\mathbf{r})$  can be described by the mutual coherence function (MCF) (Andrews and Phillips [2005])

$$\Gamma_2(\mathbf{r}_1, \mathbf{r}_2, L) = \langle U(\mathbf{r}_1)U^*(\mathbf{r}_2) \rangle, \quad (3.15)$$

which is an ensemble average over field  $U(\mathbf{r})$ .  $\mathbf{r}_1$  and  $\mathbf{r}_2$  are 2D coordinates in the same plane and  $L$  is the propagation distance. This can be normalized to give the modulus of the complex degree of coherence (DOC)

$$\begin{aligned} DOC(\mathbf{r}_1, \mathbf{r}_2, L) &= \frac{\Gamma_2(\mathbf{r}_1, \mathbf{r}_2, L)}{\sqrt{\Gamma_2(\mathbf{r}_1, \mathbf{r}_1, L)\Gamma_2(\mathbf{r}_2, \mathbf{r}_2, L)}} \\ &= \exp \left[ -\frac{1}{2}D(\mathbf{r}_1, \mathbf{r}_2, L) \right] \end{aligned} \quad (3.16)$$

$D(\mathbf{r}_1, \mathbf{r}_2)$  is the wave structure function. It is isotropic for plane and spherical waves and isotropic turbulence spectra  $\Phi_n(\kappa)$ . With  $\rho = |\mathbf{r}_1 - \mathbf{r}_2|$ , the spherical wave structure function  $D_{sp}(\rho)$  and the plane wave structure function  $D_{pl}(\rho)$  can be derived from the refractive power spectral density  $\Phi_n(\kappa)$  by

$$D_{sp}(\rho, L) = 8\pi^2 k^2 L \int_0^1 d\xi \int_0^\infty d\kappa \kappa \Phi_n(\kappa) [1 - J_0(\kappa\rho\xi)] \quad (3.17)$$

$$D_{pl}(\rho, L) = 8\pi^2 k^2 L \int_0^1 d\xi \int_0^\infty d\kappa \kappa \Phi_n(\kappa) [1 - J_0(\kappa\rho)] \quad (3.18)$$

### 3. Theory

$J_0(x)$  is the Bessel function of first kind and zero order.  $k = 2\pi/\lambda$  is the wavenumber with wavelength  $\lambda$ . The wave structure function  $D(\rho, L)$  can be split into the log-amplitude structure function  $D_\chi(\rho, L)$  and the phase structure function  $D_S(\rho, L)$

$$D(\rho, L) = D_\chi(\rho, L) + D_S(\rho, L), \quad (3.19)$$

where

$$D_{\chi,S}(\rho, L) = 4\pi^2 k^2 L \int_0^1 d\xi \int_0^\infty d\kappa \kappa \Phi_n(\kappa) [1 - J_0(\kappa\rho)] \left[ 1 \mp \cos\left(\frac{L\kappa^2\xi}{k}\right) \right] \quad (3.20)$$

in the case of plane wave. For separation distances  $\rho$  much greater than the first Fresnel zone and much smaller than the outer scale  $L_0$  the phase structure function  $D_S(\rho, L)$  is the same as WSF  $D(\rho, L)$ , as  $L\kappa^2/k \ll 1$ ,  $\cos(L\kappa^2\xi/k) \approx 1$  and hence  $D_\chi(\rho, L) \approx 0$ . For spherical wave the structure functions are given by

$$D_{\chi,S}(\rho, L) = 4\pi^2 k^2 L \int_0^1 d\xi \int_0^\infty d\kappa \kappa \Phi_n(\kappa) [1 - J_0(\kappa\xi\rho)] \times \left\{ 1 \mp \cos\left[\frac{L\kappa^2}{k}\xi(1-\xi)\right] \right\} \quad (3.21)$$

With the same argumentation the log-amplitude structure function  $D_\chi(\rho, L)$  can be neglected and the WSF  $D(\rho, L)$  reduces to the phase structure function  $D_S(\rho, L)$ .

Later on the phase structure function  $D_S(\rho, L)$  can be used for validation of statistical properties of generated phase screens. For some special cases ( $l_0 = 0$ ) the computer algebra software Wolfram Mathematica provides solutions in terms of special functions, which seem not yet reported in former literature. For the generalized modified von Kármán spectrum (GMVK) with inner scale  $l_0 = 0$ , it can be calculated for plane wave as

$$D_{S,GMVKs}(\rho, L) = 8\pi^2 k^2 L \cdot A(\alpha) C_n^2(\kappa_0^2)^{1-\frac{\alpha}{2}} \times \left( \frac{1}{\alpha-2} - \frac{2^{-\alpha/2} \alpha \left(\frac{1}{\kappa_0^2}\right)^{\frac{1}{2}-\frac{\alpha}{4}} \rho^{\frac{\alpha}{2}-1} K_{1-\frac{\alpha}{2}}(\rho\kappa_0)}{\Gamma\left(\frac{\alpha}{2}+1\right)} \right) \quad (3.22)$$

Here  $K_\nu(x)$  is the modified Bessel function of second kind. For the generalized modified atmospheric spectrum (GMAS) with inner scale  $l_0 = 0$  it can be calculated as

$$D_{S,GMAS}(\rho, L) = 4\pi^2 k^2 L \cdot A(\alpha) C_n^2 \Gamma\left(1 - \frac{\alpha}{2}\right) \times \left( \left(\frac{1}{\kappa_0^2}\right)^{\frac{\alpha}{2}-1} \left( L^{\frac{\alpha}{2}-1} \left(-\frac{1}{4} r^2 \kappa_0^2\right) - 1 \right) - \frac{2^{2-\alpha} \rho^{\alpha-2}}{\Gamma\left(\frac{\alpha}{2}\right)} \right) \quad (3.23)$$

Here  $L_v(x)$  is a Laguerre polynomial. If  $L_0 > 0$ , phase structure functions are limited by

$$\begin{aligned} D_{S,max,GMVKS} &= \lim_{\rho \rightarrow \infty} D_{S,GMVKS}(\rho, L) \\ &= 8\pi^2 k^2 L \cdot A(\alpha) C_n^2 \frac{\kappa_0^{2-\alpha}}{\alpha - 2} \end{aligned} \quad (3.24)$$

$$\begin{aligned} D_{S,max,GMAS} &= \lim_{\rho \rightarrow \infty} D_{S,GMAS}(\rho, L) \\ &= -4\pi^2 k^2 L \cdot A(\alpha) C_n^2 \kappa_0^{2-\alpha} \Gamma\left(1 - \frac{\alpha}{2}\right) \end{aligned} \quad (3.25)$$

### 3.2.4. Fried parameter $r_0$

The phase structure function for the Kolmogorov spectrum (equation 2.6) is given by

$$D_\varphi(\mathbf{r}) = 6.88 \left(\frac{r}{r_0}\right)^{5/3} \quad (3.26)$$

Here  $r_0$  is the atmospheric coherence radius or Fried parameter (Fried [1966]). For plane waves (Andrews and Phillips [2005]) it is related to the turbulence strength  $C_n^2$  via

$$r_0 = \left[0.42k^2 \int_0^L dz C_n^2(z)\right]^{-3/5} \quad (3.27)$$

Here  $k = 2\pi/\lambda$  is the wave number  $L$  is the path length and  $C_n^2(z)$  can be a path-dependent turbulence strength. For spherical waves (Hardie et al. [2017]) it is given by

$$r_0 = \left[0.42k^2 \int_0^L dz C_n^2(z) \left(\frac{z}{L}\right)^{5/3}\right]^{-3/5} \quad (3.28)$$

$r_0$  decreases as the turbulence strength  $C_n^2$  increases. It typically ranges at few to tens of centimeters at ground level (?).

### 3.2.5. Strehl ratio

The Strehl ratio (Andrews and Phillips [2005]) is the ratio at centers  $x = y = 0$  of the turbulence  $PSF_{turb}$  and the  $PSF_0$  unperturbed by turbulence:

$$SR = \frac{PSF_{turb}(0)}{PSF_0(0)} \quad (3.29)$$

It is related to the Fried parameter  $r_0$  (Andrews and Phillips [2005]) via

$$SR = \frac{1}{\left[1 + \left(\frac{D}{r_0}\right)^{5/3}\right]^{6/5}} \quad (3.30)$$

with the aperture diameter  $D$ .

### 3.2.6. Isoplanatic angle

The isoplanatic angle  $\theta_0$  is the viewing angle within turbulence degradation behaves approximately uniformly, i.e.

$$PSF(x, y, x', y') \approx PSF(x, y) \quad (3.31)$$

In astronomy, within an angle  $\theta \lesssim \theta_0$  between a guide star and an object of interest, Adaptive Optics (AO) systems can be used for wavefront correction. The isoplanatic angle can be calculated via

$$\theta_0 = \left[2.91k^2 \int_0^L C_n^2 z^{5/3} dz\right]^{-3/5} \quad (3.32)$$

### 3.2.7. Rytov variance $\sigma_R^2$

The Rytov variance  $\sigma_R^2$  (Andrews and Phillips [2005], L. C. Andrews [2014]) is a measure of turbulence strength, which allows for classification to either weak or strong fluctuation theories, i.e.

$$\sigma_R^2 < 1 \Rightarrow \text{Weak fluctuation regime} \quad (3.33)$$

$$\sigma_R^2 \sim 1 \Rightarrow \text{Moderate fluctuation regime} \quad (3.34)$$

$$\sigma_R^2 > 1 \Rightarrow \text{Strong fluctuation regime} \quad (3.35)$$

In the general form for a radial symmetric power spectrum it is given by

$$\sigma_R^2(L) = 8\pi^2 k^2 L \int_0^1 \int_0^\infty \kappa \Phi_n(\kappa) \left[1 - \cos\left(\frac{L\kappa^2 \xi}{k}\right)\right] d\kappa d\xi \quad (3.36)$$

For the Kolmogorov spectrum (equation 2.6) under weak fluctuation conditions ( $\sigma_R^2 \ll 1$ ) it is given by

$$\sigma_R^2 = 1.23 C_n^2 k^{7/6} L^{11/6}, \quad (3.37)$$

with the turbulence strength  $C_n^2$ , the wavenumber  $k$  and the propagation length  $L$ .

### 3.2.8. Scintillation index

The scintillation index (Andrews and Phillips [2005]) measures fluctuations of a received irradiance

$$I(x, y) = |U(x, y)|^2 \quad (3.38)$$

It is defined as the variance of irradiance variance scaled by the square of mean irradiance:

$$\sigma_I^2(x, y) = \frac{\langle I^2(x, y) \rangle}{\langle I(x, y) \rangle^2} - 1 \quad (3.39)$$

Under weak turbulence conditions  $\sigma_R^2 \ll 1$  for the Kolmogorov spectrum it is given by

$$\sigma_{I,pl}(L) = \sigma_R^2 = 1.23C_n^2 k^{7/6} L^{11/6} \text{ (plane wave)} \quad (3.40)$$

$$\sigma_{I,sp}(L) = \beta_0^2 = 0.4\sigma_R^2 = 0.5C_n^2 k^{7/6} L^{11/6} \text{ (spherical wave)} \quad (3.41)$$

$\beta_0^2$  is known as the spherical wave Rytov variance. It is a commonly used symbol for the scintillation index of a spherical wave. The scintillation index refers to irradiance fluctuations a point receiver with infinitesimal aperture size would measure. However, real camera optics have finite aperture sizes. This leads to an averaging effect of spatially varying irradiance fluctuations in the aperture plane. With the total transmitted power  $P$  the aperture-averaged scintillation index over a circular aperture with diameter  $D$  is given by

$$\sigma_I^2(D) = \frac{\langle P^2 \rangle}{\langle P \rangle^2} - 1 \quad (3.42)$$

If attenuation effects between aperture and camera sensor are neglected, the total transmitted power  $P$  arrives at the sensor plane. Hence, the aperture-averaged scintillation index can be measured by fluctuations of camera pixel counts  $C$ , if a linear response  $C \propto P$  is assumed for small power fluctuations. For weak fluctuations the aperture-averaged scintillation index can be calculated from the homogeneous and isotropic turbulence spectrum  $\Phi_n(\kappa)$

$$\sigma_I^2(D) = 8\pi^2 k^2 L \int_0^1 d\xi \int_0^\infty d\kappa \kappa \Phi_n(\kappa) \times \exp\left(-\frac{D^2 \kappa^2 \xi^2}{16}\right) \left(1 - \cos\left(\frac{L\kappa^2}{k} \xi(1-\xi)\right)\right) \text{ (spherical wave)} \quad (3.43)$$

$$\sigma_I^2(D) = 8\pi^2 k^2 L \int_0^1 d\xi \int_0^\infty d\kappa \kappa \Phi_n(\kappa) \times \exp\left(-\frac{D^2 \kappa^2}{16}\right) \left(1 - \cos\left(\frac{L\kappa^2 \xi}{k}\right)\right) \text{ (plane wave)} \quad (3.44)$$

For a Kolmogorov spectrum ( $l_0 = 0, L_0 \rightarrow \infty, \alpha = 11/3$ ) (Andrews and Phillips [2005]) the aperture averaged scintillation index  $\sigma_I^2(D)$  can be written as

$$\sigma_I^2(D) = \exp \left[ \frac{0.49\beta_0^2}{\left(1 + 0.18d^2 + 0.56\beta_0^{12/5}\right)^{7/6}} + \frac{0.51\beta_0^2(1 + 0.69\beta_0^{12/5})^{-5/6}}{1 + 0.9d^2 + 0.62d^2\beta_0^{12/5}} \right] - 1, \quad (3.45)$$

where  $\beta_0$  is the spherical wave Rytov variance (equation 3.41) and

$$d = \sqrt{\frac{kD^2}{4L}}. \quad (3.46)$$

### 3.2.9. Differential tilt variance

In a former work (Gladysz [2017]) the differential tilt variance was used to validate turbulence degraded images of multiple point sources based on a (non-)Kolmogorov spectrum. In this thesis the same method is extended and used for the spectra GMVKS and GMAS. The differential tilt variance is the ensemble average of angle of arrival differences of two point sources

$$\langle (\theta_{x/y}(\mathbf{r}) - \theta_{x/y}(\mathbf{r} + \mathbf{d}))^2 \rangle \quad (3.47)$$

for horizontal angle of arrivals  $\theta_x$  (tip) and vertical angle of arrivals  $\theta_y$  (tilt).  $\mathbf{r}$  is the physical position of a point source in the object plane.  $\mathbf{d}$  is the physical separation between this point source and a second point source. An illustration is shown in figure 3.2. A remarkable benefit of this figure of merit is the invariance to global motion, since uniform shifts cancel out in the differences of angles  $\theta_{x/y}(\mathbf{r})$  and  $\theta_{x/y}(\mathbf{r} + \mathbf{d})$ . This is crucial, since camera vibrations may further degrade projections of point sources and impede the estimation of model parameters from point source projections.

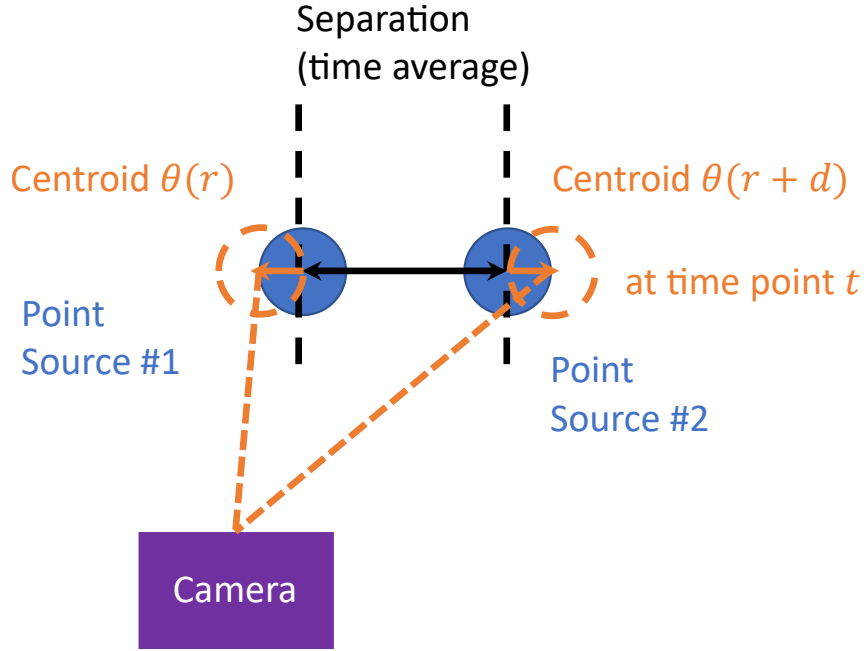
Analytical expressions for differential tilt variances in direction parallel ( $\sigma_{\parallel}^2$ ) and perpendicular ( $\sigma_{\perp}^2$ ) to the sources' separation for the Kolmogorov spectrum have been proposed (Gladysz [2017]) as

$$\begin{aligned} \begin{bmatrix} \sigma_{\parallel}^2 \\ \sigma_{\perp}^2 \end{bmatrix} &= 0.2073 \int_0^L dz C_n^2(z) \int d\kappa \begin{bmatrix} \cos^2(\varphi) \\ \sin^2(\varphi) \end{bmatrix} \kappa^{-11/3} \\ &\times \left(\frac{4}{D}\right)^2 J_1^2\left(\frac{z\kappa D}{2L}\right) 2\{1 - \cos[\kappa d \cos(\varphi)]\} \end{aligned} \quad (3.48)$$

However, the integral kernel can be enhanced for any other turbulence spectrum by

$$\begin{aligned} \begin{bmatrix} \sigma_{\parallel}^2 \\ \sigma_{\perp}^2 \end{bmatrix} &= 0.2073 \int_0^L dz C_n^2(z) \int d\kappa \begin{bmatrix} \cos^2(\varphi) \\ \sin^2(\varphi) \end{bmatrix} \kappa^{-11/3} \frac{\Phi_n(\kappa)}{\Phi_{n,Kolmogorov}(\kappa)} \\ &\times \left(\frac{4}{D}\right)^2 J_1^2\left(\frac{z\kappa D}{2L}\right) 2\{1 - \cos[\kappa d \cos(\varphi)]\} \end{aligned} \quad (3.49)$$

Figure 3.2.: Illustration of two point sources projected onto a camera. The angle of arrivals  $\sigma_x(\mathbf{r})$  and  $\theta_x(\mathbf{r} + \mathbf{d})$  fluctuate around time-averaged center positions.



For faster numerical evaluation this can be simplified to

$$\begin{bmatrix} \sigma_{\parallel}^2 \\ \sigma_{\perp}^2 \end{bmatrix} = \frac{41.7}{D^2} C_n^2 \int_0^L dz \begin{bmatrix} I_T(z) - I_1(z) \\ I_1(z) \end{bmatrix}, \quad (3.50)$$

where

$$I_1(z) = \int_0^{\infty} d\kappa \kappa^{-8/3} \frac{\Phi_n(\kappa)}{\Phi_{n,Kolmogorov}(\kappa)} J_1^2\left(\frac{z\kappa D}{2L}\right) \left(\frac{1}{2} - \frac{J_1(\kappa d(L-z)/L)}{\kappa d(L-z)/L}\right) \quad (3.51)$$

$$I_T(z) = \int_0^{\infty} d\kappa \kappa^{-8/3} \frac{\Phi_n(\kappa)}{\Phi_{n,Kolmogorov}(\kappa)} J_1^2\left(\frac{z\kappa D}{2L}\right) (1 - J_0(\kappa d(L-z)/L)) \quad (3.52)$$

These analytical expressions do not have any dependency on wavelength. This makes the differential tilt variance suitable for monochromatic or spectrally extended light sources.

Now angle of arrivals  $\theta_{x,y}$  can be easily calculated from displacements  $s_{x,y}$  on camera images in units of sensor pixels by using the instantaneous field of views

$$IFOV_{x,y} = \frac{p_{x,y}}{fl}, \quad (3.53)$$

where the focal length of an objective  $fl \in [650 \text{ mm}, 1300 \text{ mm}]$  and the pixel pitch  $p_{x,y} = 2.9 \mu\text{m}$ , i.e. the distance between adjacent pixels. These values are adopted from a camera and objective used in field trials described in a following chapter. In good approximation the pixel pitch can be assumed to be the pixel size, since from the datasheet in table 6.1 a maximum relative error of 0.2% can be deducted.

### 3.2.10. Long-exposure and short-exposure optical transfer function

Another method for validation of generated point spread functions and turbulence strength estimation is based on Fourier optics. A theoretical model for uncorrected ("long-exposure") and tip-tilt-corrected ("short-exposure") optical transfer functions (OTFs) has been derived (Fried [1966], Yatcheva et al. [2015]) as

$$OTF_{L,total}(\mathbf{v}) = OTF_0(\mathbf{v}) \times OTF_{LE}(\mathbf{v}), \quad (3.54)$$

$$OTF_{S,total}(\mathbf{v}) = OTF_0(\mathbf{v}) \times OTF_{SE}(\mathbf{v}), \quad (3.55)$$

where  $OTF_0(\mathbf{v})$  describes all remaining components in the process of degradation not related to air turbulence such as optical diffraction and finite detector footprint, etc. Fried (Fried [1966], Yatcheva et al. [2015]) developed expressions for

$$OTF_{LE}(\mathbf{v}) = \exp \left[ -3.44 \left( \frac{\bar{\lambda} fl \mathbf{v}}{r_0} \right)^{5/3} \right] \quad (3.56)$$

$$OTF_{SE}(\mathbf{v}) = \exp \left\{ -3.44 \left( \frac{\bar{\lambda} fl \mathbf{v}}{r_0} \right)^{5/3} \left[ 1 - \alpha \left( \frac{\bar{\lambda} fl \mathbf{v}}{r_0} \right)^{1/3} \right] \right\} \quad (3.57)$$

Here  $\alpha$  is a factor that varies between 1/2 when there are both intensity and phase variations across the collecting aperture and 1 when only phase distortions are present. In the following  $\alpha = 1$  is assumed. The Fried parameter  $r_0$  is given by

$$r_0 = \left( \frac{3^{5/3}}{Lk^2 C_n^2} \right)^{3/5} \quad (3.58)$$

and describes the coherence length of a wavefront propagated through turbulence with propagation length  $L$ .  $\mathbf{v}$  is the spatial frequency in the image plane,  $fl$  is the focal length and  $k = \frac{2\pi}{\lambda}$  is the wavenumber with the average wavelength  $\bar{\lambda}$ .

In the following simulation approach, diffractive effects can not really be separated from turbulence degradation. Simulated point spread functions will always be afflicted with the diffraction OTF, which is given for a circular aperture as (Yatcheva et al. [2015])

$$OTF_{diff}(\mathbf{v}) = \frac{2}{\pi} \left[ \arccos \left( \frac{\bar{\lambda} fl \mathbf{v}}{D} \right) - \frac{\bar{\lambda} fl \mathbf{v}}{D} \sqrt{1 - \left( \frac{\bar{\lambda} fl \mathbf{v}}{D} \right)^2} \right], \quad (3.59)$$

with the aperture diameter  $D$ .

From an experimental point of view artificial point sources such as LED elements always have an intensity profile with some spatial extent and hence an extended point spread function. Then the final intensity profiles can be calculated by

$$\mathcal{F}PSF_{L/S,final}(x,y) = OTF_0(\mathbf{v}_x, \mathbf{v}_y) OTF_{LE/SE}(\mathbf{v}_x, \mathbf{v}_y) \cdot \mathcal{F}PSF_{LED}(x,y) \quad (3.60)$$

However, if a ratio  $R$  between both PSFs is formed, the OTFs of all components  $OTF_0(\mathbf{v}_x, \mathbf{v}_y)$  and the spatial LED profile  $PSF_{LED}(x,y)$  cancel out:

$$R(\mathbf{v}_x, \mathbf{v}_y) = \frac{\mathcal{F}PSF_L(\mathbf{v}_x, \mathbf{v}_y)}{\mathcal{F}PSF_S(\mathbf{v}_x, \mathbf{v}_y)} = \frac{OTF_{LE}(\mathbf{v}_x, \mathbf{v}_y)}{OTF_{SE}(\mathbf{v}_x, \mathbf{v}_y)} \quad (3.61)$$

In the following only the horizontal and vertical axes are taken into account  $\mathbf{v} = \mathbf{v}_{x/y}$ . The exponentials in the OTFs can be eliminated by taking the logarithm of  $R(\mathbf{v}_{x/y})$ :

$$\begin{aligned} R(\mathbf{v}_{x/y}) &= \ln \left( \frac{OTF_{LE}(\mathbf{v}_{x/y})}{OTF_{SE}(\mathbf{v}_{x/y})} \right) \\ &= \ln OTF_{LE}(\mathbf{v}_{x/y}) - \ln OTF_{SE}(\mathbf{v}_{x/y}) \\ &= -3.44 \left( \frac{\bar{\lambda} fl \mathbf{v}}{r_0} \right)^{5/3} \left[ 1 - \left( 1 - \alpha \left( \frac{\bar{\lambda} z \mathbf{v}_{x/y}}{r_0} \right)^{1/3} \right) \right] \\ &= -3.44 \alpha \left( \frac{\bar{\lambda} z \mathbf{v}_{x/y}}{r_0} \right)^2 \\ \underbrace{R(\mathbf{v}_{x/y})}_{y(\mathbf{v}_{x/y})} &= a \mathbf{v}_{x/y}^2 \quad a = -3.44 \alpha \left( \frac{\bar{\lambda} z}{r_0} \right)^2 \end{aligned} \quad (3.62)$$

Now from sets of measured and simulated images of turbulence-degraded single point source projections, spatial frequencies  $\mathbf{v}_{x/y,i}$  and abscissa values

$$y(\mathbf{v}_{x/y,i}) = \ln \left( \frac{\mathcal{F}PSF_{L,final}(x,y)}{\mathcal{F}PSF_{S,final}(x,y)} \right) \quad (3.63)$$

can be calculated. The prefactor  $a$  can then be found by linear regression of  $v_{x/y,i}^2$  and  $y(v_{x/y,i})$ . Then it can be used to determine the Fried parameter  $r_0$  and from equation 3.58 the turbulence strength  $C_n^2$  can be calculated. The long-exposure  $PSF_{L,final}(x,y)$  can be calculated from ensemble averages  $\langle \cdot \rangle_S$  of image sequences simulated by multiple sampling of independent phase screens. For measured image sequences a time average can be calculated: For the short-exposure OTF, which describes the degradation of point source signal due to air turbulence for short integration times, tip/tilt variations are compensated. Based on images  $I_n(x,y)$  these tips/tilts can be measured by centroids

$$c_{x,n} = \frac{\sum_{x,y} x I_n(x,y)}{\sum_{x,y} I_n(x,y)}, \quad (3.64)$$

$$c_{y,n} = \frac{\sum_{x,y} y I_n(x,y)}{\sum_{x,y} I_n(x,y)}, \quad (3.65)$$

if the background signal in the images  $I_n(x,y)$  can be neglected. In the most optimal case tips/tilts are corrected by shifting the short-exposure images to have unique centroids  $(\tilde{c}_x, \tilde{c}_y)$ . This can be achieved by a phase modulation in the frequency domain:

$$\begin{aligned} I_{n,shifted}(x,y) &= \mathcal{F}^{-1} \left[ \exp \left( \frac{2\pi\mu i}{N_x} (\tilde{c}_x - c_{x,n}) + \frac{2\pi\eta i}{N_y} (\tilde{c}_y - c_{y,n}) \right) \mathcal{F} I_n(x,y) \right] \\ &= \frac{1}{N_x N_y} \sum_{\mu=0}^{N_x-1} \sum_{\eta=0}^{N_y-1} \sum_{x'=0}^{N_x-1} \sum_{y'=0}^{N_y-1} I_n(x',y') \times \\ &\quad \exp \left( \frac{2\pi\mu i}{N_x} (\tilde{c}_x - c_{x,n}) + \frac{2\pi\eta i}{N_y} (\tilde{c}_y - c_{y,n}) \right) \times \\ &\quad \exp \left( \frac{2\pi\mu x' i}{N_x} + \frac{2\pi\eta y' i}{N_y} \right) \times \\ &\quad \exp \left( \frac{2\pi\mu x i}{N_x} + \frac{2\pi\eta y i}{N_y} \right) \end{aligned} \quad (3.66)$$

The corresponding PSF can be calculated by averaging a stack of multiple instantaneous PSFs:

$$PSF_{L,final}(x,y) = \langle I_n(x,y) \rangle_n, \quad (3.67)$$

$$PSF_{S,final}(x,y) = \langle I_{n,shifted}(x,y) \rangle_n. \quad (3.68)$$

For the MTFs this gives

$$MTF_{L/S,final}(v_x, v_y) = \mathcal{F} PSF_{L/S,final}(x,y). \quad (3.69)$$

Toy experiments with multivariate 2D Gaussian profiles of varying widths and centroid positions show, that simulations for  $MTF_{S,final}(v_x, v_y)$  can be approximated by averaging magnitudes of Fourier transforms of single frames over the entire image sequence. This is equivalent to a disposal of any phase

information introduced by shifts of the image contents. If the discrete Fourier transform  $DFT_{xy}$  and the pixel-wise average over the image sequence  $Average_z$  are used the MTFs can be written as

$$MTF_{S,final}(v_x, v_y) = Average_z |DFT_{xy}I(x, y)| \quad (3.70)$$

$$MTF_{L,final}(v_x, v_y) = |DFT_{xy}Average_zI(x, y)| \quad (3.71)$$

The long-exposure MTF for a circular aperture can be calculated from the spherical wave or plane wave structure function  $D_{sp/pl}(uD)$  (Cui et al. [2010]):

$$MTF_{LE,sp/pl}(u) = \exp \left[ -\frac{1}{2}D_{sp/pl}(uD) \right] \quad (3.72)$$

Here  $u = \lambda \cdot fl \cdot v/D \in [0, 1]$  is a normalized spatial frequency with the wavelength  $\lambda$ , focal length  $fl$ , diameter  $D$  and spatial frequency  $v[1/m]$  in the sensor plane. More general integral representations of long-exposure and short-exposure MTFs for arbitrary aperture forms are described in (Charnotskii [2012]).

### 3.3. Convergence of numerical integration

The described figures of merit based on integral representations of the turbulence model  $\Phi_n(\kappa, \mathbf{z})$  are analytically solvable only for simple spectra or special cases of model parameters  $\mathbf{z}$ . Often these solutions involve special functions such as the incomplete Gamma function  $\Gamma(a, z)$ , or hypergeometric functions  ${}_pF_q(a, b, z)$ . The availability of these functions in software libraries is limited. Moreover, case distinctions depending on ranges of input parameters for specific turbulence spectra  $\Phi_n(\kappa)$  are very tedious and cumbersome. Hence, numerical integration based on the Riemann rule is applied in all cases where these integral representations have to be solved, i. e. integrals are approximated by

$$q(N) = \Delta x \sum_{k=0}^{N-1} k(x_k) \text{ (1D integral)} \quad (3.73)$$

$$q(N) = \Delta x \Delta y \sum_{k=0}^{N-1} \sum_{l=0}^{N-1} k(x_k, y_l) \text{ (2D integral)}, \quad (3.74)$$

$$q(N) = \Delta x \Delta y \Delta z \sum_{k=0}^{N-1} \sum_{l=0}^{N-1} \sum_{m=0}^{N-1} k(x_k, y_l, z_m) \text{ (3D integral)}, \quad (3.75)$$

and

$$x_k = x_{min} + k \cdot \Delta x, \quad (3.76)$$

$$y_l = y_{min} + l \cdot \Delta y, \quad (3.77)$$

$$z_m = z_{min} + m \cdot \Delta z, \quad (3.78)$$

with

$$\Delta x = \frac{x_{max} - x_{min}}{N - 1}, \quad (3.79)$$

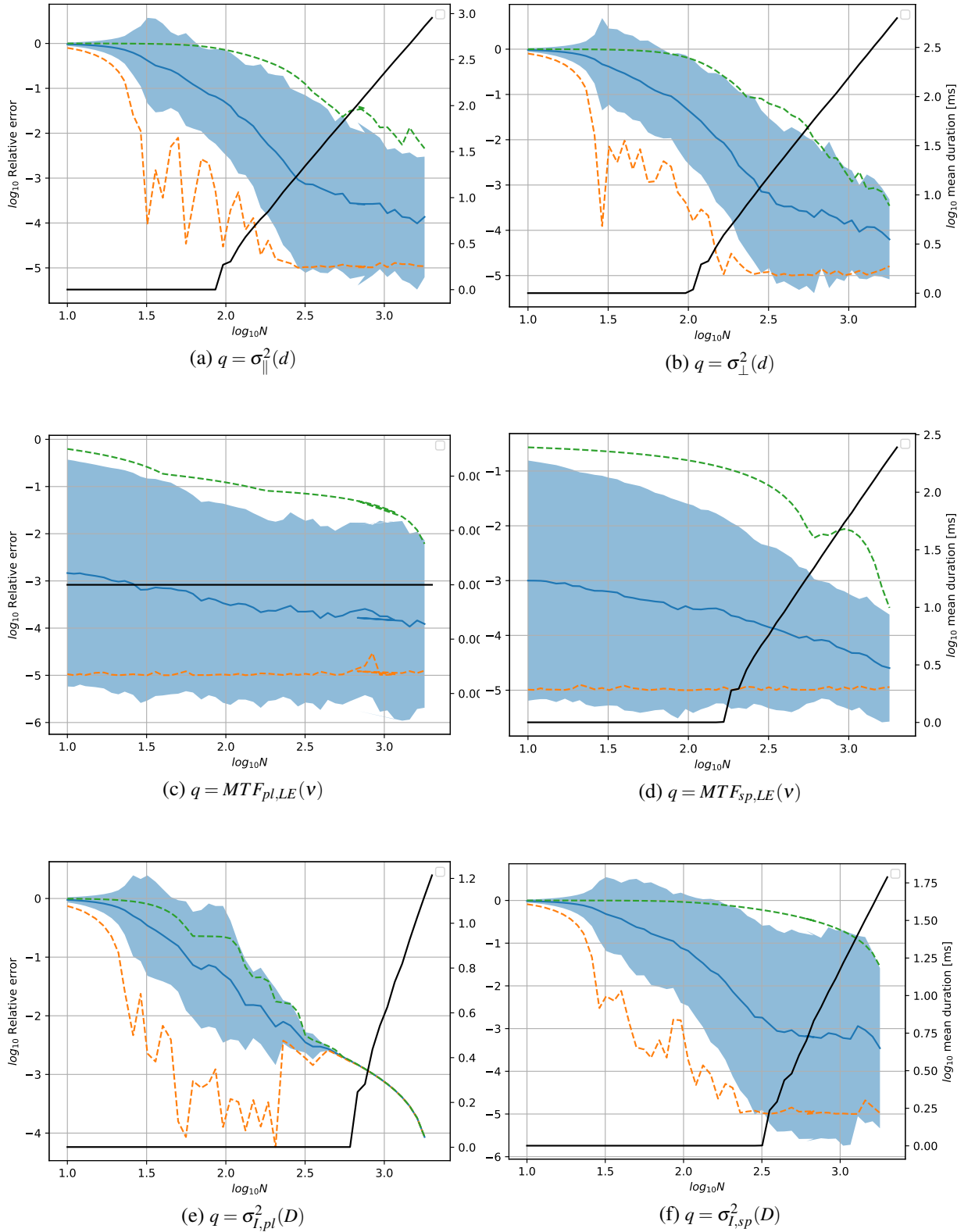
$$\Delta y = \frac{y_{max} - y_{min}}{N - 1}, \quad (3.80)$$

$$\Delta z = \frac{z_{max} - z_{min}}{N - 1}, \quad (3.81)$$

where  $k(x), k(x, y)$  and  $k(x, y, z)$  are integrand functions of the respective quantities  $q$ . Then the question arises which grid size  $N$  should be used. For this purpose convergence tests are done for different quantities with integral representations for plane waves and spherical waves, the aperture-averaged scintillation index  $\sigma_{I,pl/sp}^2(D)$  (equations 3.44 and 3.43), the long exposure  $MTF_{LE,pl/sp}(v)$  (equation 3.72) and the differential tilt variances  $\sigma_{\parallel}^2(d)$  and  $\sigma_{\perp}^2(d)$  (equation 3.49). In figure 3.3 relative errors  $\Delta q = (q(N) - q(5000))/q(5000)$  related to the largest handable grid size  $N = 5000$  and mean durations for single evaluations are shown. For each quantity  $q$ , 200 samples are generated based on uniformly distributed model parameters of the spectrum GMVKS. Due to the logarithmic nature of turbulence strength  $C_n^2$ ,  $\log_{10} C_n^2$  is chosen uniformly distributed. The parameter ranges are estimated from distributions acquired from experimental data in chapter 6. Random values for the turbulence strength  $\log_{10}[C_n^2/(m^{-2/3})] \in [-16, -12]$ , the inner scale  $l_0 \in [0.0001, 0.3]$  m, outer scale  $L_0 \in [0.01, 100.0]$  m and exponents  $\alpha \in [3.1, 3.9]$  are used. Modulation transfer functions  $MTF_{sp/pl,LE}$  additionally depend on spatial frequencies  $v \in [0, 10000]$  m<sup>-1</sup>. and differential tilt variances  $\sigma_{\parallel}^2$  and  $\sigma_{\perp}^2$  depend on separations  $d \in [0, 0.015]$  m. There is a typical tradeoff between accuracy and computation time. Hence, for all simulations a grid size  $N = 1000$  is chosen, in order to provide relative errors  $\Delta q < 10^{-2}$  for most cases. Adaptive integration schemes such as Romberg-Integration (Owren [2011]) are not used because of poor parallelizability due to unpredictable durations for different input parameters.

Additionally,  $\sigma_{\parallel}^2$  and  $\sigma_{\perp}^2$  need to be differentiable with respect to model parameters for applications in chapter 6. Some software libraries e.g. Google's tensorflow offers automatic differentiation (Neidinger [2010]), i.e. it computes numerical derivatives efficiently which renders paper-and-pencil computations of analytical derivatives obsolete. However, tensorflow needs a fixed numerical scheme to use this automatic differentiation.

Figure 3.3.:  $\log_{10}(\Delta q)$  for relative errors  $\Delta q = (q(N) - q(5000))/q(5000)$  of different quantities  $q$  depending on number of integral subdivisions  $N$ . 95%-confidence bands are shown. Min and max values are shown as dashed lines.  $\log_{10}(\text{Mean computation time in ms})$  for single calls are shown on the right vertical axis (black line).





## 4. Methods

### 4.1. Wave propagation by split-step beam propagation

A method suitable to analyze the propagation of optical waves through atmospheric turbulence is the split-step beam propagation method (Belmonte [2000]).

In classical electrodynamics, the electromagnetic field propagating in media is governed by the macroscopic Maxwell's equations:

$$\nabla \cdot \mathbf{D} = \rho \quad (4.1)$$

$$\nabla \cdot \mathbf{B} = 0 \quad (4.2)$$

$$\nabla \times \mathbf{E} = -\frac{\partial \mathbf{B}}{\partial t} \quad (4.3)$$

$$\nabla \times \mathbf{H} = \mathbf{j}_{free} + \frac{\partial \mathbf{D}}{\partial t} \quad (4.4)$$

The electrical fields  $\mathbf{E}, \mathbf{D}$  and magnetical fields  $\mathbf{H}, \mathbf{B}$  are related by

$$\mathbf{D} = \epsilon_0 \mathbf{E} + \mathbf{P} = \epsilon_0(1 + \chi_e) \mathbf{E} = \epsilon \mathbf{E} \quad (4.5)$$

$$\mathbf{B} = \mu_0 \mathbf{H} + \mathbf{M} = \mu_0(1 + \chi_m) \mathbf{H} = \mu \mathbf{H} \quad (4.6)$$

with material-dependent polarization  $\mathbf{P}$  and magnetization  $\mathbf{M}$ . In general the electrical susceptibility  $\chi_e$  and  $\chi_m$  are (3,3)-matrices, e.g. for birefringent materials polarization and magnetization can be dependent on the orientation between fields  $\mathbf{E}, \mathbf{H}$  and the crystal axes of the material. However most materials, e.g air, are isotropic and susceptibilities  $\chi_e, \chi_m$  can be treated as scalars and hence the permittivity  $\epsilon$  and the permeability  $\mu$ . Now atmospheric air can be assumed to be free of charges and currents, i.e.  $\rho = \mathbf{j}_{free} = 0$ . Combining equations 4.3 and 4.4 gives

$$\nabla \times \nabla \times \mathbf{E} = -\epsilon \mu \frac{\partial^2 \mathbf{E}}{\partial t^2} \quad (4.7)$$

This can be simplified to

$$\nabla(\nabla \cdot \mathbf{E}) - \Delta \mathbf{E} = -\epsilon \mu \frac{\partial^2 \mathbf{E}}{\partial t^2} \quad (4.8)$$

Now equation 4.1 can be simplified to

$$\nabla \cdot \mathbf{D} = \nabla \varepsilon \cdot \mathbf{E} + \varepsilon \nabla \cdot \mathbf{E} = 0 \quad (4.9)$$

If we assume that spatial changes of permeability  $\varepsilon$  can be neglected, i.e.  $\nabla \varepsilon = 0$ , we have

$$\nabla \cdot \mathbf{E} = 0 \quad (4.10)$$

Now equation 4.8 can be simplified to the wave equation:

$$\Delta \mathbf{E} + \varepsilon \mu \frac{\partial^2 \mathbf{E}}{\partial t^2} = \Delta \mathbf{E} + \frac{n^2}{c_0^2} \frac{\partial^2 \mathbf{E}}{\partial t^2} = 0 \quad (4.11)$$

Here we set  $\varepsilon \mu = n^2/c_0^2$ , where  $n$  is the refractive index and  $c_0 = \sqrt{\frac{1}{\varepsilon_0 \mu_0}}$  is the vacuum speed of light. With an approach of a monochromatic field

$$\mathbf{E} = E(x, y, z) e^{i\omega t} \quad (4.12)$$

and temporal frequency  $\omega = k/c_0$ , the wave equation yields

$$\Delta \mathbf{E} + k^2 n^2 \mathbf{E} = 0 \quad (4.13)$$

Here  $k = \frac{2\pi}{\lambda}$  is the free-space wave number. In air the refractive index is approximately 1 and has small variations  $n_1$  caused by temperature and pressure variations. So we rewrite the refractive index as

$$n = 1 + n_1 \quad (4.14)$$

Then the wave equation gives

$$\Delta \mathbf{E} + k^2 (1 + n_1)^2 \mathbf{E} = 0 \quad (4.15)$$

#### 4.1.1. Paraxial wave equation

In order to further simplify the wave equation for faster numerical evaluation, another ansatz can be made for the electrical field:

$$E(x, y, z) = U(x, y, z) \exp(ikz) \quad (4.16)$$

with an envelope  $U(x, y, z)$  slowly varying in propagation direction  $z$ . Then we can assume

$$\left| \frac{\partial^2 \mathbf{U}}{\partial z^2} \right| \ll \left| \frac{\partial \mathbf{U}}{\partial z} 2ik \right| \quad (4.17)$$

and for small perturbations  $n_1$

$$(1 + n_1)^2 = 1 + 2n_1 + n_1^2 \approx 1 + 2n_1 \quad (4.18)$$

With these assumptions, the wave equation for the envelope  $\mathbf{U}$  gives

$$2ik \frac{\partial \mathbf{U}}{\partial z} + \Delta_{xy} \mathbf{U} + 2k^2 n_1 \mathbf{U} = 0 \quad (4.19)$$

$\Delta_{xy} = \frac{\partial^2}{\partial x^2} + \frac{\partial^2}{\partial y^2}$  is the transversal Laplace operator. The free space operator can be expressed in spatial frequencies  $\kappa_x$  and  $\kappa_y$ :

$$S_F = \exp \left( -i \frac{\Delta z}{4k} (\kappa_x^2 + \kappa_y^2) \right) \quad (4.20)$$

#### 4.1.2. Split-step beam propagation method

Now the wave equation can be discretized in propagation direction  $z$ . If  $U_n$  is the solution at  $z = z_n$  then the solution  $z_{n+1} = z_n + \Delta z$  can be written exactly as

$$U_{n+1} = \exp \left[ -\frac{i}{2k} \left( \Delta z \Delta_{xy} + 2k^2 \int_{z_n}^{z_{n+1}} dz n_1(x, y, z) \right) \right] U_n + \mathcal{O}(\Delta z^3) \quad (4.21)$$

The so-called Markov assumption can be used, that the wave fluctuations are independent from the refractive index fluctuations  $n_1$ . This is equivalent to  $n_1$  being delta-correlated in propagation direction  $z$ . Then terms which refer to field derivatives and refractive index are additively separable. The solution can be approximated with third order accuracy in the step size  $\Delta z$ :

$$U_{n+1} = S_F S_{P,n} S_F U_n + \mathcal{O}(\Delta z^3) \quad (4.22)$$

with the free space operator

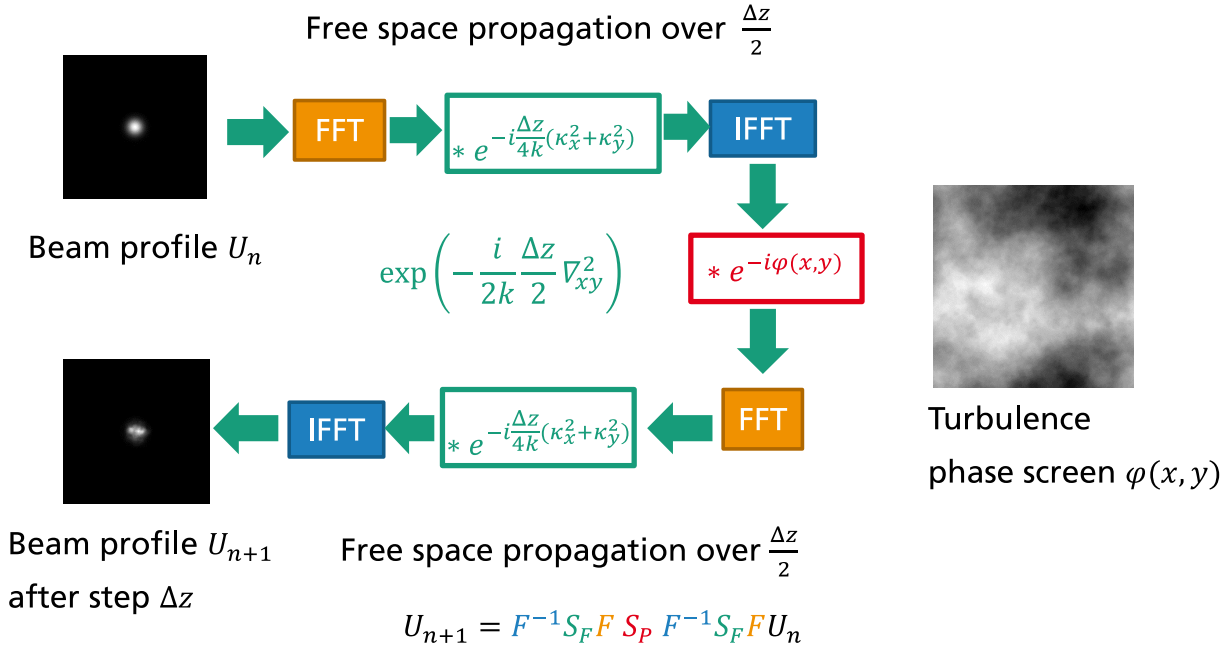
$$S_F = \exp \left( -\frac{i}{2k} \frac{\Delta z}{2} \Delta_{xy} \right) \quad (4.23)$$

and phase screen operators

$$S_{P,n} = \exp \left[ -ik \int_{z_n}^{z_{n+1}} dz n_1(x, y, z) \right] \exp[-\varphi_n(x, y)] \quad (4.24)$$

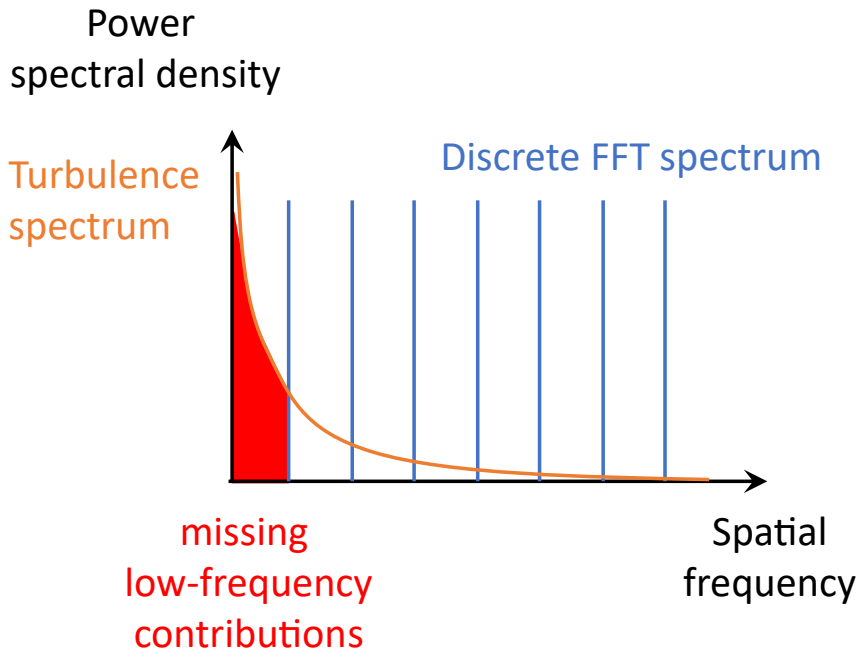
For numerical simulation 2D Fast Fourier Transform (FFT) is convenient to switch between space and frequency domain. The workflow of a single split step is illustrated in figure 4.1

Figure 4.1.: Single split step: Input beam profile  $U_n$  at  $z = z_n$  is converted to output profile  $U_{n+1}$  at  $z = z_n + \Delta z$ . Images show corresponding intensity profiles  $I = |U|^2$  of complex fields  $U$ .



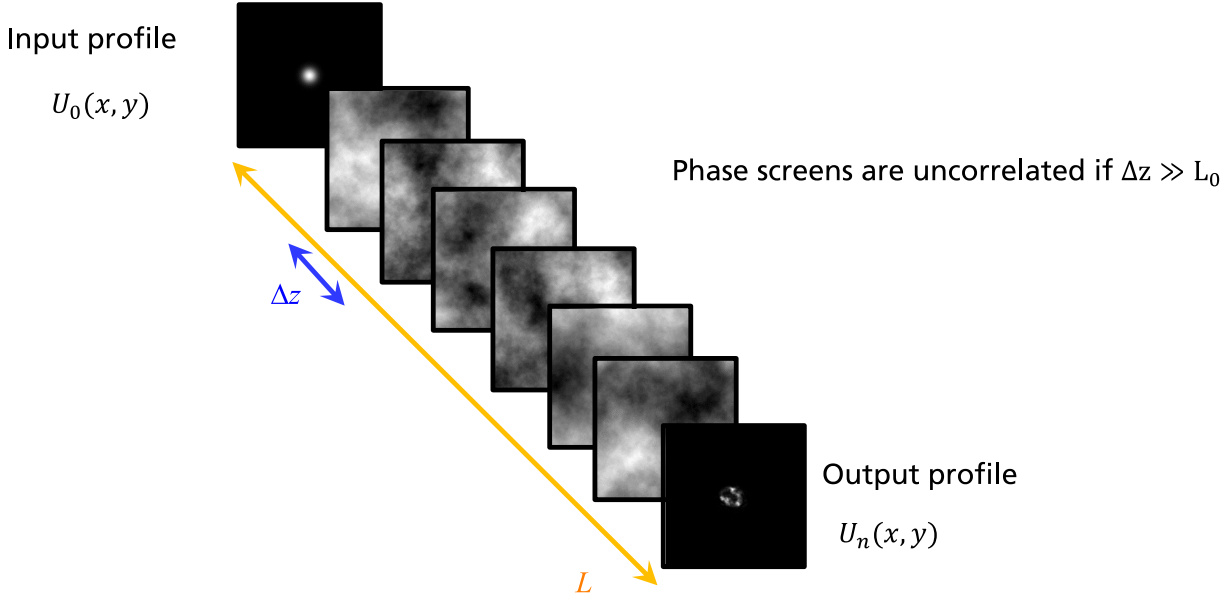
An input beam profile  $U_0$  can be propagated along a path  $L$  to give the output profile  $U_n$  by multiple successive split-steps. Uncorrelated 2D phase screens can be generated by inverse Fast Fourier transform (IFFT) of filtered 2D complex Gaussian random fields (Fleck et al. [1976]). However, such phase screens are periodic and cannot properly represent low-frequency contributions below the lowest frequency in the discrete IFFT spectrum, while most turbulence spectra have significant low-frequency contributions. This condition is illustrated in figure 4.2.

Figure 4.2.: A discrete (I)FFT spectrum can only represent a turbulence spectrum at a limited number of equidistant spatial frequencies. Most models for turbulence spectra have high contributions at low frequencies, which cannot be represented by the (I)FFT spectrum



This fact leads to an underestimation of total noise variance in the generated phase screens and hence a reduced effect of turbulence on the beam profile. A method to alleviate this problem, is the addition of subharmonics (Lane et al. [1992]), which are sinusoids based on integer fractions of the lowest frequency in the discrete spectrum. For investigation of wind effects, phase screen extension techniques have been introduced (Assémat et al. [2006], Vorontsov et al. [2008]). For low discretization error in the split-step method (equation 4.21) a low separation  $\Delta z$  is desirable. However, phase screens can only approximately be treated uncorrelated if the separation is much larger than the outer turbulence scale  $\Delta z \gg L_0$  (Markov-Assumption). This is illustrated in figure 4.3

Figure 4.3.: Beam propagation along a distance  $L$ : A final complex field  $U_n(x, y)$  is calculated by multiple iterations of the single step (4.22). For the phase screen operators  $\{S_{P,i}\}_{i=1..n}$  a sequence of varying phase screens  $\{\varphi_i(x, y)\}_{i=1..n}$  is used.



Fortunately, there are methods that can calculate correlated 2D phase screens and combine many advantages of the mentioned techniques. In the next section two methods for phase screen generation are presented. In cases where the Markov assumption ( $\Delta z \gg L_0$ ) holds, the inverse discrete Fourier transform of Gaussian noise with addition of subharmonics Lane et al. [1992] can be used for the generation of uncorrelated 2D phase screens. If the Markov assumption fails, the sparse spectrum (SS) method can be used to calculate correlated 2D phase screens by analytical integration of 3D refractive index random fields. With this method noise patterns of the refractive index can be easily rotated or shifted in arbitrary 3D directions.

## 4.2. Generation of uncorrelated 2D phase screens

2D phase screens can be generated by using inverse discrete Fourier transforms (DFT). If the phase is calculated via integration over the refractive index along the axis of propagation as in the phase screen operators (equation 4.24), i.e.

$$\varphi = k \int_{z_n}^{z_{n+1}} n(x, y, z) dz, \quad (4.25)$$

then its equivalent power spectrum  $\Phi_\varphi(\boldsymbol{\kappa})$  (Belmonte [2000]) can be calculated as

$$\Phi_\varphi(\boldsymbol{\kappa}_x, \boldsymbol{\kappa}_y) = 2\pi k^2 \Delta z \Phi_n(\boldsymbol{\kappa}_x, \boldsymbol{\kappa}_y) \quad (4.26)$$



#### 4. Methods

---

With the phase field from the inverse discrete Fourier transform  $\varphi(x, y)$  and the subharmonics  $\theta_{SH}(x, y)$ , the total phase is given by

$$\varphi_{SH}(x, y) = \varphi(x, y) + \theta_{SH}(x, y) \quad (4.29)$$

These subharmonics can be refined by multiple levels of recursion.

$$\theta_{SH}(x, y) = \sum_{p=1}^{N_p} \theta_{SH}^{(p)}(x, y) \quad (4.30)$$

The subharmonics are calculated as

$$\begin{aligned} \theta_{SH}^{(p)} &= \sum_{m=-1}^1 \sum_{n=-1}^1 [a(m, n, p) + ib(m, n, p)] \\ &\times \exp\left(\frac{1}{3^p} \left[ \frac{2\pi i}{N_x} m \cdot x + \frac{2\pi i}{N_y} n \cdot y \right]\right) \end{aligned} \quad (4.31)$$

The coefficients  $a(m, n, p)$  and  $b(m, n, p)$  are sampled from a Gaussian distribution such that variances are given by the corresponding

$$\begin{aligned} \langle a^2(m, n, p) \rangle &= \langle b^2(m, n, p) \rangle = \int_{\kappa_{x,min}(m,p)}^{\kappa_{x,max}(m,p)} d\kappa_x \int_{\kappa_{y,min}(n,p)}^{\kappa_{y,max}(n,p)} d\kappa_y \Phi_\varphi(\kappa_x, \kappa_y) \\ &\approx \left(\frac{\Delta\kappa_x}{3^p}\right) \left(\frac{\Delta\kappa_y}{3^p}\right) \Phi_\varphi(\bar{\kappa}_x(m, p), \bar{\kappa}_y(n, p)) \end{aligned} \quad (4.32)$$

with means

$$\bar{\kappa}_x^{(p)} = \frac{\kappa_{x,max}(m, p) + \kappa_{x,min}(m, p)}{2} \quad (4.33)$$

$$\bar{\kappa}_y^{(p)} = \frac{\kappa_{y,max}(n, p) + \kappa_{y,min}(n, p)}{2} \quad (4.34)$$

and boundaries

$$\kappa_{x,max}(m, p) = \left(\frac{1}{3}\right)^{p-1-\frac{m-1}{2}} \frac{\Delta\kappa_x}{2} \quad (4.35)$$

$$\kappa_{x,min}(m, p) = \left(\frac{1}{3}\right)^{p-1+\frac{m+1}{2}} \frac{\Delta\kappa_x}{2} \quad (4.36)$$

$$\kappa_{y,max}(n, p) = \left(\frac{1}{3}\right)^{p-1-\frac{n-1}{2}} \frac{\Delta\kappa_y}{2} \quad (4.37)$$

$$\kappa_{y,min}(n, p) = \left(\frac{1}{3}\right)^{p-1+\frac{n+1}{2}} \frac{\Delta\kappa_y}{2} \quad (4.38)$$

The center component  $m = n = 0$  is excluded on each subharmonic level  $p$ , i. e.

$$a(0,0,p) = b(0,0,p) = 0 \quad (4.39)$$

#### 4.2.2. Phase structure function of uncorrelated 2D phase screens

The Markov phase structure function of uncorrelated 2D phase screens (Charnotskii [2016]) is given by

$$D_{\varphi}^{(MA)}(r) = 8\pi^2 k^2 \Delta z \int_0^{\infty} \kappa \Phi_n(\kappa) [1 - J_0(\kappa r)] \quad (4.40)$$

It is identical to the plane wave structure function  $D_{pl}(r, L)$  (equation 3.18).

#### 4.2.3. Validation of phase screens

Derived and measurable quantities on propagated fields degraded by turbulence highly depend on correct features of the generated phase screens such as variance or spatial correlation within phase screens and over subsequent phase screens. A priori, this is not self-evident since generated phase screens are discrete and finite. They may also suffer from deficiencies of the generation process, e.g. periodicity of the DFT or sparsity.

In order to validate generated phase screens a default configuration of simulation parameters shown in table 4.1 is used. Device specifications are adopted from a real camera and objective used for validation later on.

Based on this default simulation parameters, phase screens with varying inner scale  $l_0$ , outer scale  $L_0$  and exponent  $\alpha$  are generated based on two models, the generalized modified von Kármán Spectrum (GMVKS) and the generalized modified atmospheric spectrum (GMAS). In figures 4.5, 4.6 and 4.7 phase screens for varying outer scale  $L_0$ , inner scale  $l_0$  and exponent  $\alpha$  are shown. It can be seen that for increasing outer scale  $L_0$  turbulence eddies get larger, as less low-frequency contributions are filtered. A similar effect has the inner scale  $l_0$ . Turbulence eddies get larger as  $l_0$  increases. A high exponent  $\alpha$  leads to stronger filtering of high spatial frequencies, which makes turbulence eddies also larger.

Table 4.1.: Default simulation parameters for single wave propagation

Parameter	Value
Wavelength $\lambda$ in nm	550
Field width/height $w_{x/y}$ in m	0.4
Field size horizontal/vertical $N_x \times N_y$ in pixel	512x512
Phase screen size horizontal/vertical	2048x2048
Phase screen width $\Delta z$ in m	15
Propagation length $L$ in m	150
# phase screens for single propagation $N_z$	10
Turbulence spectra	GMAS and GMVKS
Turbulence strength $C_n^2/(m^{-2/3})$	$10^{-13}$
Exponent $\alpha$	11/3
Inner scale $l_0$ in m	0
Outer scale $L_0$ in m	100
Subharmonic pattern	3x3
# Subharmonic recursions	10
# simulated frames $N_{ps}$	200
Focal length in m	0.8
Aperture form	Circular
Aperture diameter in m	0.086
Pixel pitch $p_{x,y}$ in $\mu\text{m}$	2.9
Physical separation of point sources horizontal/vertical $\Delta q_{x/y}$ in cm	1.5

Figure 4.5.: Phase screens for varying outer scale  $L_0$  and GMVKS: (a)  $L_0 = 0.1$  m, (b)  $L_0 = 1$  m, (c)  $L_0 = 10$  m, (d)  $L_0 = 100$  m. The outer scale  $L_0$  limits low frequency contributions. A decreasing outer scale  $L_0$  is related to decreased low frequency contributions.

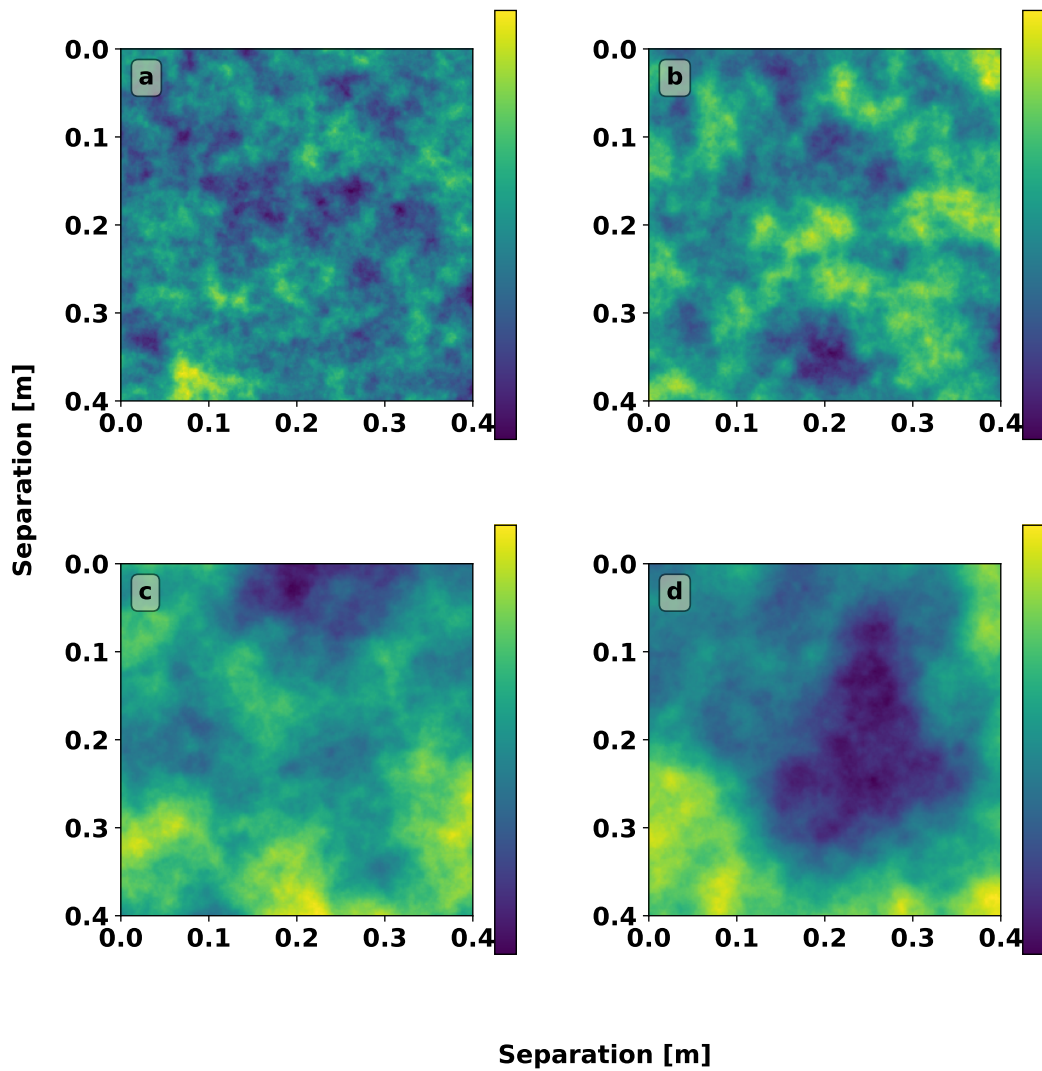


Figure 4.6.: Phase screens for varying inner scale  $l_0$  and GMVKS: (a)  $l_0 = 0.001$  m, (b)  $l_0 = 0.01$  m, (c)  $l_0 = 0.02$  m, (d)  $l_0 = 0.1$  m.

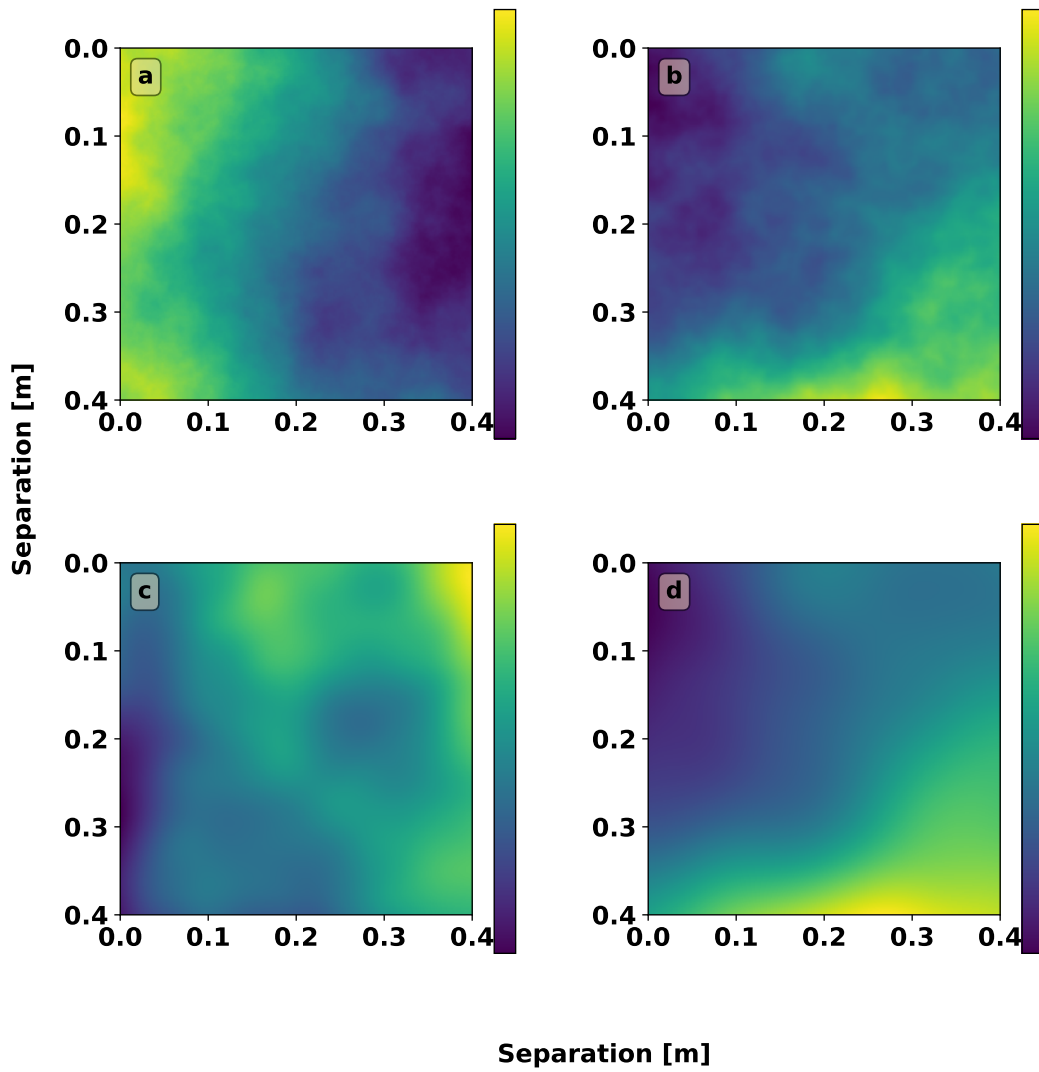
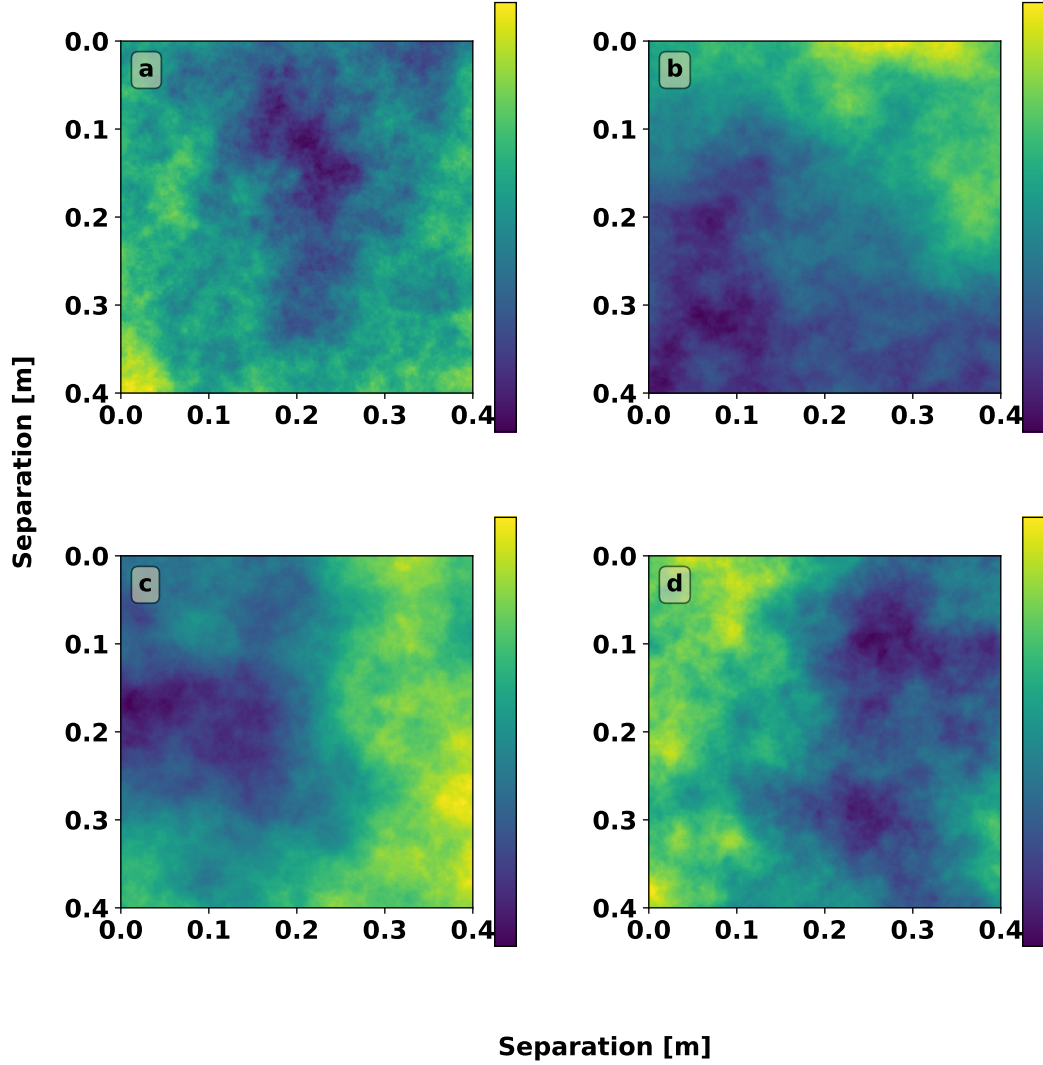


Figure 4.7.: Phase screens for varying exponent  $\alpha$  and GMVKS: (a)  $\alpha = 3.1$ , (b)  $\alpha = 3.4$ , (c)  $\alpha = 11/3$ , (d)  $\alpha = 3.9$ .



In figure 4.8 analytical plane wave structure functions from equation 3.18 are compared with numerical structure functions calculated from  $N_z = L/\Delta z = 10$  phase screens for a single beam propagation (sample  $k$ ) by

$$D_{hor,k}(x_j) = \frac{\sum_n^{N_z} \sum_k (\varphi_{kn}(x_i, 0) - \varphi_{kn}(x_j, 0))^2}{N_{total}} \quad (4.41)$$

$$D_{vert,k}(y_j) = \frac{\sum_n^{N_z} \sum_k (\varphi_{kn}(0, y_i) - \varphi_{kn}(0, y_j))^2}{N_{total}} \quad (4.42)$$

#### 4. Methods

---

with  $x_j = j\Delta x$ ,  $y_j = j\Delta y$  and the grid spacings  $\Delta x$  and  $\Delta y$ . The total size of summands is given by

$$N_{total} = N_z(N_{grid} - j) \quad (4.43)$$

with the extended phase screen grid size  $N_{grid} = 2048$ . The standard errors of the numerical structure functions are estimated as

$$\sigma_{D_{hor/vert}} \approx \sqrt{D_{hor/vert}^2 - \overline{D_{hor/vert}}^2}, \quad (4.44)$$

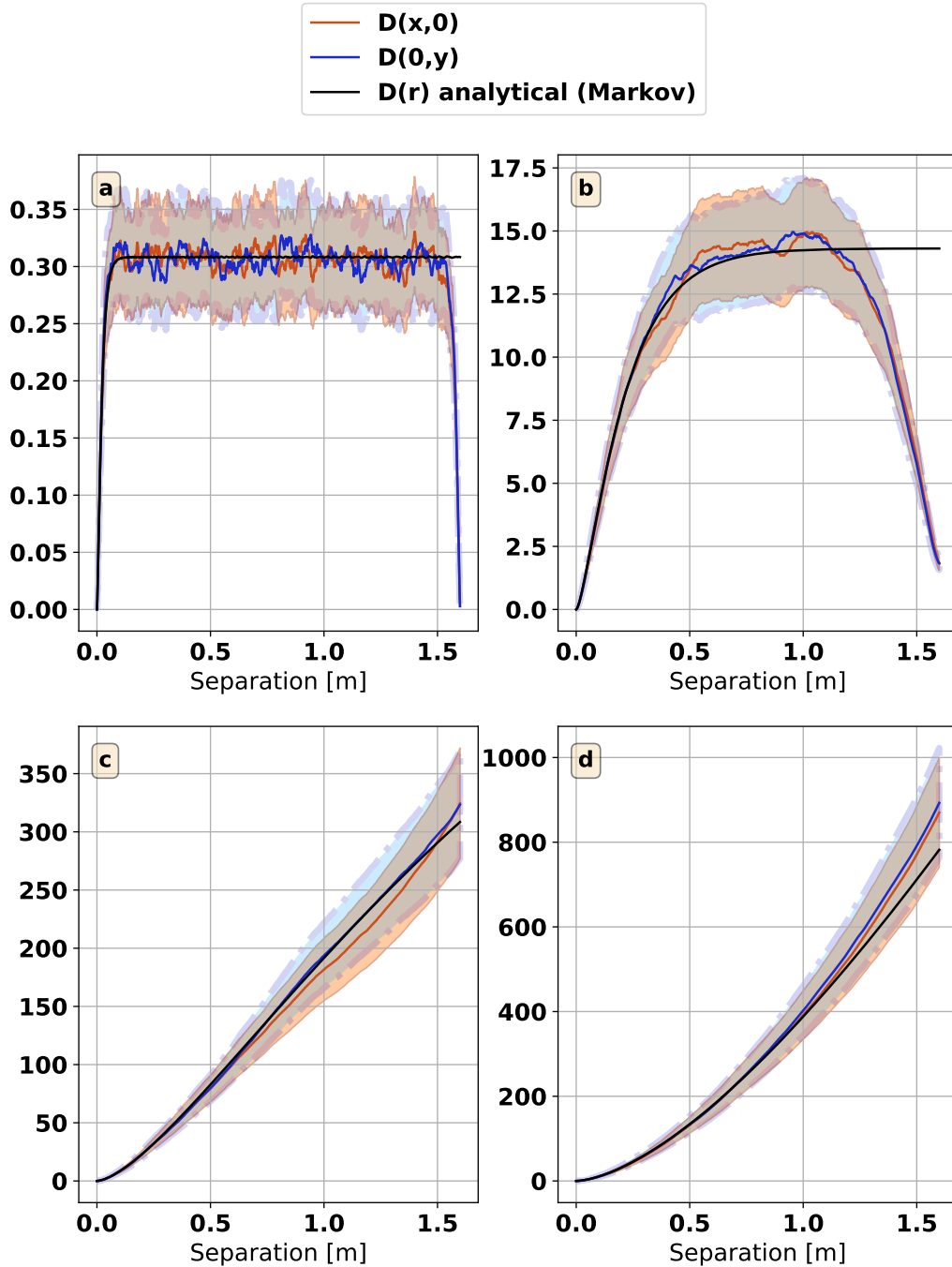
where the averages are applied over  $N_{ps} = 200$  statistically independent samples of phase screen stacks. The standard error of the mean structure function is then given as

$$\sigma_{\overline{D_{hor/vert}}} = \frac{\sigma_{D_{hor/vert}}}{\sqrt{N_{ps}}} \quad (4.45)$$

In figure 4.8 the numerical structure functions  $D_{hor/vert}$  are compared with the analytical structure function from equation 3.18 for different outer scales  $L_0$ . Also shown are 95% confidence bands ( $\pm 1.96\sigma_{\overline{D_{hor/vert}}}$ ) numerical structure functions as colored regions. The sample structure functions are in good accordance with the analytical structure function from equation. For low outer scale  $L_0$  (figure 4.8) there are drops of the numerical structure functions. The reason for this is the lack of low-frequency subharmonic contributions and the periodicity of phase screens based on pure discrete Fourier transform of filtered Gaussian noise random fields. Since the used phase screens for beam propagation are smaller image crops (512x512) of the extended phase screens (2048x2048), correlations between adjacent borders are not critical for single beam propagations and PSF calculations. Depending on the available memory larger phase screens could be calculated to alleviate correlation effects to any degree.

In figure 4.9 comparisons of the analytical structure functions for different parameters  $L_0, l_0$  and  $\alpha$  for the spectrum GMVKS are shown. The structure functions are expressed in units of the common factor  $16\pi^2 k^2 C_n^2$ . While there is only a slight shift of the structure functions for different inner scales  $l_0$ , increasing outer scales  $L_0$  and exponents  $\alpha$  let the structure function become larger. From the slight influence on inner scale  $l_0 < 1$  cm on the asymptotic value  $\lim_{r \rightarrow \infty} D_\varphi(r) = 2\sigma_\phi^2$  with the total phase variance  $\sigma_\phi^2$  it can be expected, that also measurable quantities resulting from beam propagations through these phase screens will have a slight dependency on inner scale  $l_0$ .

Figure 4.8.: Comparison of analytical phase structure functions  $D_\phi(r,0)$  and sample structure function  $D(x,0)$  and  $D(0,y)$  based on horizontal/vertical separations for varying outer scale  $L_0$  and GMVKS: (a)  $L_0 = 0.1$  m, (b)  $L_0 = 1$  m, (c)  $L_0 = 10$  m, (d)  $L_0 = 100$  m. Colored regions are 95%-confidence bands of the sample structure functions  $D_{hor/vert}$ . The analytical Markov structure function (black line) is mainly in the confidence bands of the numerical structure functions (red and blue line).



#### 4. Methods

Figure 4.9.: Analytical Markov phase structure function  $D_\phi^{(MA)}(r; 0)$  for varying turbulence parameters  $l_0$  (a),  $L_0$  (b), and  $\alpha$  (c) based on the model GMVKS. Default values are  $C_n^2/m^{3-\alpha} = 10^{-13}$ ,  $l_0 = 0.01$  m,  $L_0 = 1.0$  m,  $\alpha = 11/3$  and  $L = 150$  m.

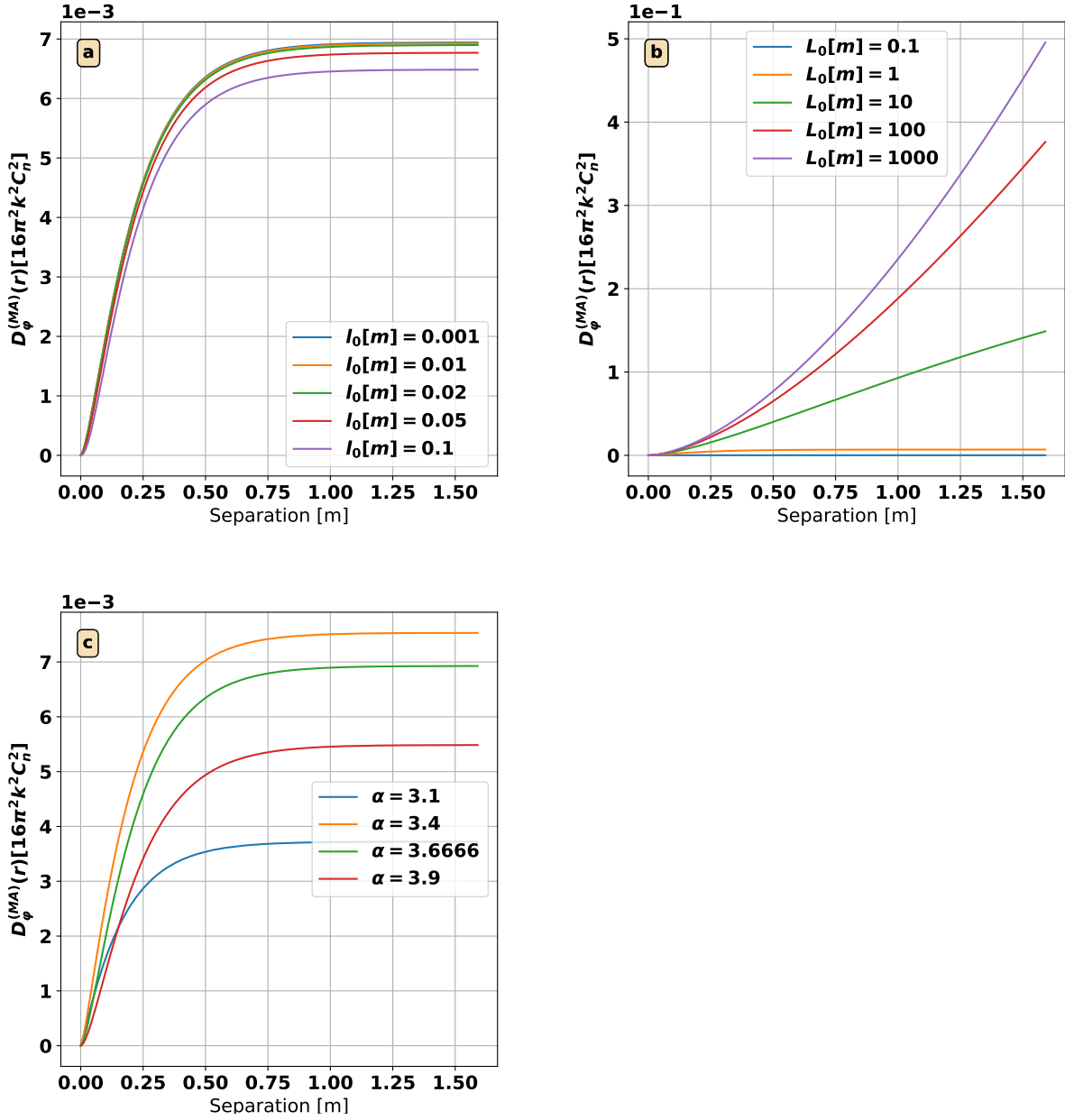


Figure 4.10.: Phase structure function for varying inner scale  $l_0$  and GMVKS: (a)  $l_0 = 0.001$  m, (b)  $l_0 = 0.005$  m, (c)  $l_0 = 0.01$  m, (d)  $l_0 = 0.1$  m.

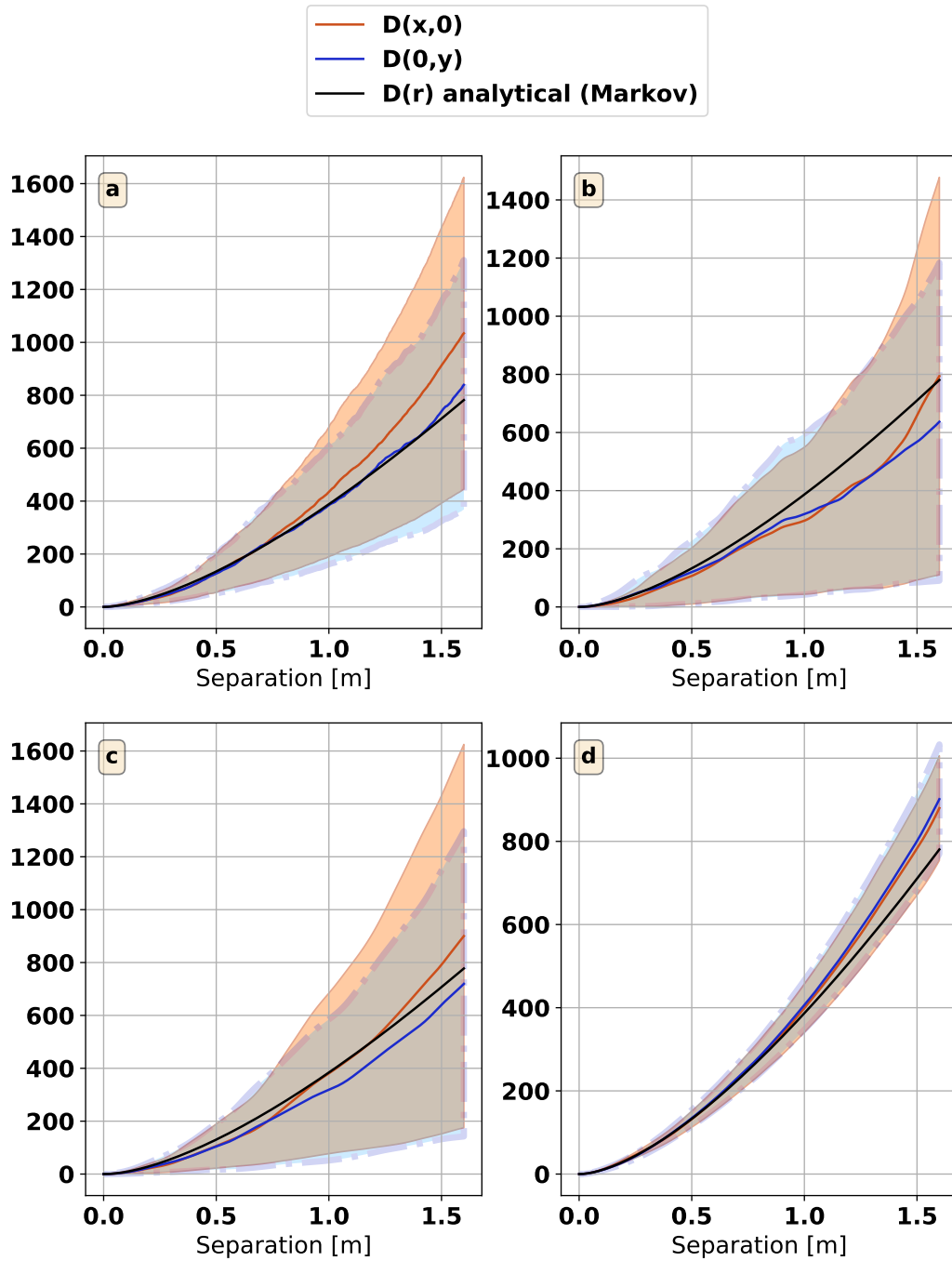
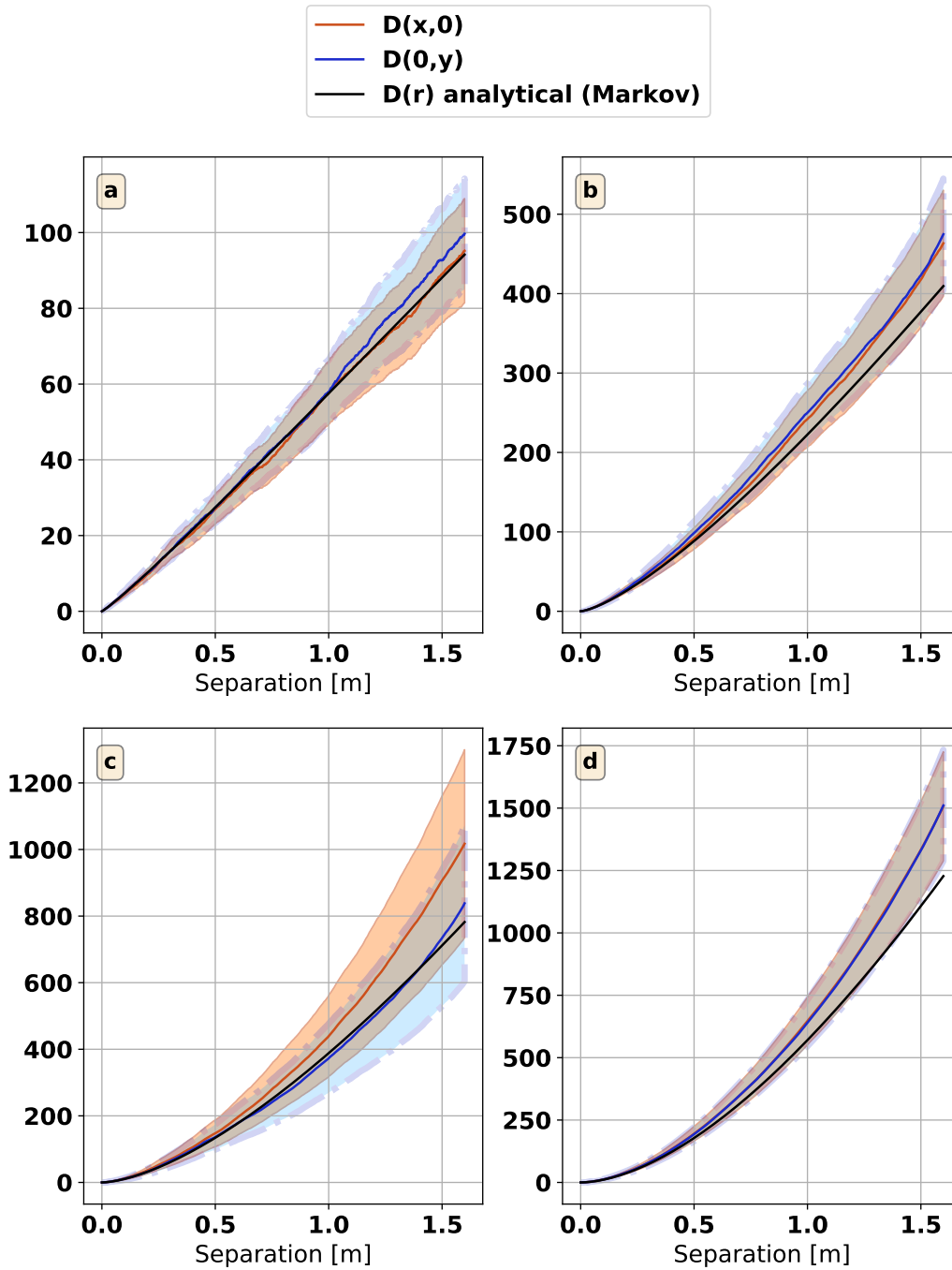


Figure 4.11.: Phase structure function for varying exponent  $\alpha$  and GMVKS: (a)  $\alpha = 3.1$ , (b)  $\alpha = 3.4$ , (c)  $\alpha = 11/3$ , (d)  $\alpha = 3.9$ .



Figures 4.10 and 4.11 show that good accordance can also be achieved for different inner scales  $l_0$  and exponents  $\alpha$ . Therefore, the number of subharmonics recursions  $N_{recursion} = 10$  used for the phase

screen generation is sufficient for deviations between simulated and analytical structure functions within statistical uncertainty.

### 4.3. Generation of correlated 2D phase screens

#### 4.3.1. 3D random fields

The use of uncorrelated phase screens as described in the previous section can be inappropriate if the Markov assumption is not met, i.e. that the outer scale  $L_0 \gg \Delta z$ . Fortunately, the outer scale  $L_0$  typically ranges about few meters up to an altitude of  $h = 30$  km as shown in chapter 2, making this restriction obsolete when propagation light signals over several 100 meters to kilometers. However for short paths under strong turbulence the neglect of correlation of adjacent phase screens can lead to an overestimation of integrated phase variance. For these cases, methods are required, which take the correlation of phase screens in the direction of propagation into account.

Correlated 3D random fields and correlated 2D phase screens can be generated by using the sparse spectrum (SS) method (Charnotskii [2011, 2016, 2020]) This method calculates a 3D random field, e.g. one representing the refractive index of turbulent air by a composition of plane waves:

$$n(x, y, z) = \text{Re} \sum_{n=1}^{N_{\text{waves}}} a_n \exp(ip_n x + iq_n y + is_n z) \quad (4.46)$$

with random complex amplitudes  $a_n$  and random wave vectors  $\mathbf{k}_n = (p_n, q_n, s_n)$  The complex amplitudes  $a_n$  are zero-average statistically independent random variables with second moments

$$\langle a_n a_m^* \rangle = w_n \delta_{nm} \quad (4.47)$$

$$\langle a_n a_m \rangle = 0 \quad (4.48)$$

If  $P_n(p, q, s)$  is the probability density for the  $n$ -th wave vector, the covariance function for  $n(x, y, z)$  is given as

$$B_n(x, y, z) = \langle n(x_0, y_0, z_0) n(x_0 + x, y_0 + y, z_0 + z) \rangle \quad (4.49)$$

$$= \frac{1}{2} \int \int \int dp dq ds \sum_{n=1}^N w_n P_n(p, q, s) \cos(px + qy + sz) \quad (4.50)$$

The general covariance function for a specific refractive index power spectral density  $\Phi_n(p, q, s)$  is given by

$$B_n(x, y, z) = \int \int \int dp dq ds \Phi_n(p, q, s) \cos(px + qy + sz) \quad (4.51)$$

So the field  $n(x, y, z)$  will have the desired covariance function if

$$\frac{1}{2} w_n P_n(p, q, s) = \Phi_n(p, q, s) \quad (4.52)$$

This is the principal equation of the SS technique. For isotropic power spectral densities  $\Phi_n(p, q, s) = \Phi_n(K)$ , the random wave vectors  $\kappa_n = (p_n, q_n, s_n)$  can be sampled from a uniform distribution in direction. The integrand in equation 4.50 can be transformed to spherical coordinates

$$P_n(p, q, s) dp dq ds = P_n(K, \varphi, \theta) K^2 dK \cos \theta d\theta d\varphi \quad (4.53)$$

Then the principal equation gives

$$\frac{1}{2} \sum_{n=1}^N w_n P_n(K) = 4\pi K^2 \Phi_n(K) \quad (4.54)$$

A desired spectral interval  $K_{MIN} \leq K \leq K_{MAX}$  can be covered by an N subinterval partition

$$K_{MIN} = K_0 \leq K_1 \leq \dots \leq K_{N-1} \leq K_N = K_{MAX} \quad (4.55)$$

Then the weights and probabilities based on the principal equation are given by

$$w_n = 8\pi \int_{K_{n-1}}^{K_n} K^2 dK \Phi_n(K) \quad (4.56)$$

$$P_n(K) = \frac{K^2 \Phi_n(K)}{\int_{K_{n-1}}^{K_n} K^2 dK \Phi_n(K)} \quad (4.57)$$

### 4.3.2. Correlated 2D phase screens

Correlated 2D phase screens can be calculated by integration of the 3D random field  $n(x, y, z)$  over a slab  $\Delta z$  in propagation direction  $z$ :

$$\varphi_j(x, y) = k \int_{(j-1)\Delta z}^{j\Delta z} dz n(x, y, z), \quad j = 1, 2, \dots, N_s \quad (4.58)$$

where  $N_s$  is the number of phase screens to be calculated. Inserting equation 4.46 and analytic integration gives

$$\varphi_j(x, y) = \text{Re} \sum_{n=1}^{N_{\text{waves}}} b_{j,n} \exp(ip_n x + iq_n y) \quad (4.59)$$

$$b_{j,n} = \frac{2ka_n}{s_n} \sin\left(s_n \frac{\Delta z}{2}\right) \exp\left(is_n \left(j - \frac{1}{2}\right) \Delta z\right) \quad (4.60)$$

For small components  $s_n$  in z-direction, equation (4.60) gets numerically unstable. To remedy this problem for small  $s_n$ , a Taylor series expansion can be used:

$$b_{j,n} = 2ka_n\Delta z s_n^2 + O(s_n^3) \quad (4.61)$$

The Sparse Uniform (SU) method (Charnotskii [2020]) is an extension which uses the approach in equation 4.59, but uses uncorrelated coefficients  $b_{j,n}$  for the generation of uncorrelated 2D phase screens. The spectral weighting of these coefficients is then determined via integration over 2D spectra.

### 4.3.3. Phase structure function of correlated 2D phase screens

The radial-symmetric Non-Markov structure function for a separation  $r = |\vec{r}_1 - \vec{r}_2|$  in a single 2D phase screen  $\varphi_j(x, y)$  (Charnotskii [2016]) is given by

$$D_\varphi^{(NM)}(r, 0) = 16\pi^2 k^2 \int_0^\infty dK \Phi_n(K) \int_0^1 \frac{dt}{t} [1 - \cos(K\Delta z t)] \left[ 1 - J_0(Kr\sqrt{1-t^2}) \right] \quad (4.62)$$

The covariance between two correlated 2D phase screens  $\varphi_j(x, y)$  and  $\varphi_k(x, y)$  with index distance  $m = |j - k|$  is given by

$$B_\varphi^{(NM)}(0, m\Delta z) = 8\pi k^2 \int_0^\infty dK \Phi_n(K) \int_0^1 \frac{dy}{y^2} [1 - \cos(Ky\Delta z)] \cos(Kym\Delta z) \quad (4.63)$$

Then the corresponding longitudinal phase structure function gives

$$D_\varphi^{(NM)}(0, m\Delta z) = 16\pi k^2 \int_0^\infty dK \varphi_n(K) \int_0^1 \frac{dy}{y^2} (1 - \cos(Ky\Delta z)) (1 - \cos(Kym\Delta z)) \quad (4.64)$$

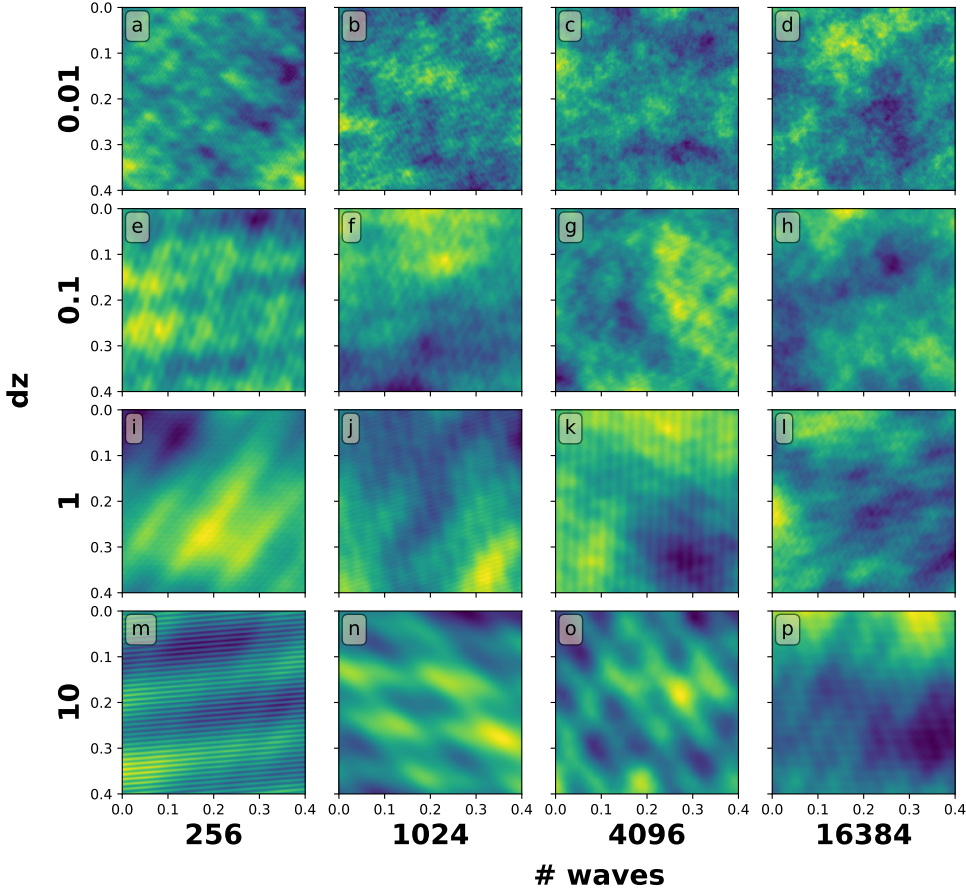
For the Kolmogorov spectrum this integral diverges at the low-number limit and only the structure function can be calculated as

$$D_\varphi(0, m\Delta z) = c_L C_n^2(\Delta z)^{8/3} \times \left[ \frac{1}{2} (m+1)^{8/3} + \frac{1}{2} (m-1)^{8/3} - \frac{1}{2} m^{8/3} - 1 \right], \quad (4.65)$$

where

$$c_L = 16\pi \cdot 0.033 \cdot \left(\frac{3}{5}\right)^2 \cdot \frac{3}{8} \cdot \frac{3}{2} \cdot \Gamma\left(\frac{1}{8}\right) \sin\frac{\pi}{6} \approx 0.225 \quad (4.66)$$

A comparison of different phase screens based on the Kolmogorov spectrum for varying phase screen thicknesses  $\Delta z$  and number of plane waves  $N_{waves}$  is shown in figure 4.12

Figure 4.12.: Comparison of phase screens for varying phase screen thickness  $\Delta z$  and number of plane waves  $N_{waves}$ 

It can be seen that high frequency contributions are decreasing for increasing thickness  $\Delta z$ . This can be explained by low pass filtering of plane waves with high longitudinal components  $s_n$  due to integration in the longitudinal direction  $z$ . Equation 4.60 shows that each plane wave is decreased by a factor

$$\frac{\sin\left(s_n \frac{\Delta z}{2}\right)}{s_n} \quad (4.67)$$

This means that integration of the 3D random field in longitudinal direction  $z$  as done in equation 4.58 leads to high degradation of plane waves with close orientation to the integration direction  $z$  (high  $s_n$ ). Therefore, phase screens with high slab sizes, e.g.  $\Delta z = 10$  reveal lower high-frequency contributions compared to lower slab sizes. There are also visible artifacts of single plane waves for low number of waves and also when slab size increases.

#### 4.3.4. Validation of phase screens

Similar to the comparisons of uncorrelated phase screens in section 4.2.3, uncorrelated phase screens generated by the sparse spectrum method are compared for varying turbulence parameters based on the simpler spectrum *GMVKS*. In figure 4.13 phase screens generated by  $N = 1024$  plane waves and  $dz = 15$  m in a field of  $0.4\text{ m} \times 0.4\text{ m}$  are shown for varying outer scale  $L_0$ . Again it can be observed that high outer scales  $L_0$  filter out low spatial frequencies.

In figure 4.14 the phase screens for varying exponent  $\alpha$  are shown. For both variations single plane wave artifacts are visible which may be alleviated with a very high number of plane waves  $N > 16384$ . However, computation would take much longer than using uncorrelated phase screens with subharmonics and render the benefits of correlated phase screens questionable.

Figure 4.13: Phase screens for varying outer scale  $L_0$  and GMVKS: (a)  $L_0 = 0.1$  m, (b)  $L_0 = 1$  m, (c)  $L_0 = 10$  m, (d)  $L_0 = 100$  m. The outer scale  $L_0$  limits low frequency contributions. A decreasing outer scale  $L_0$  is related to decreased low frequency contributions.

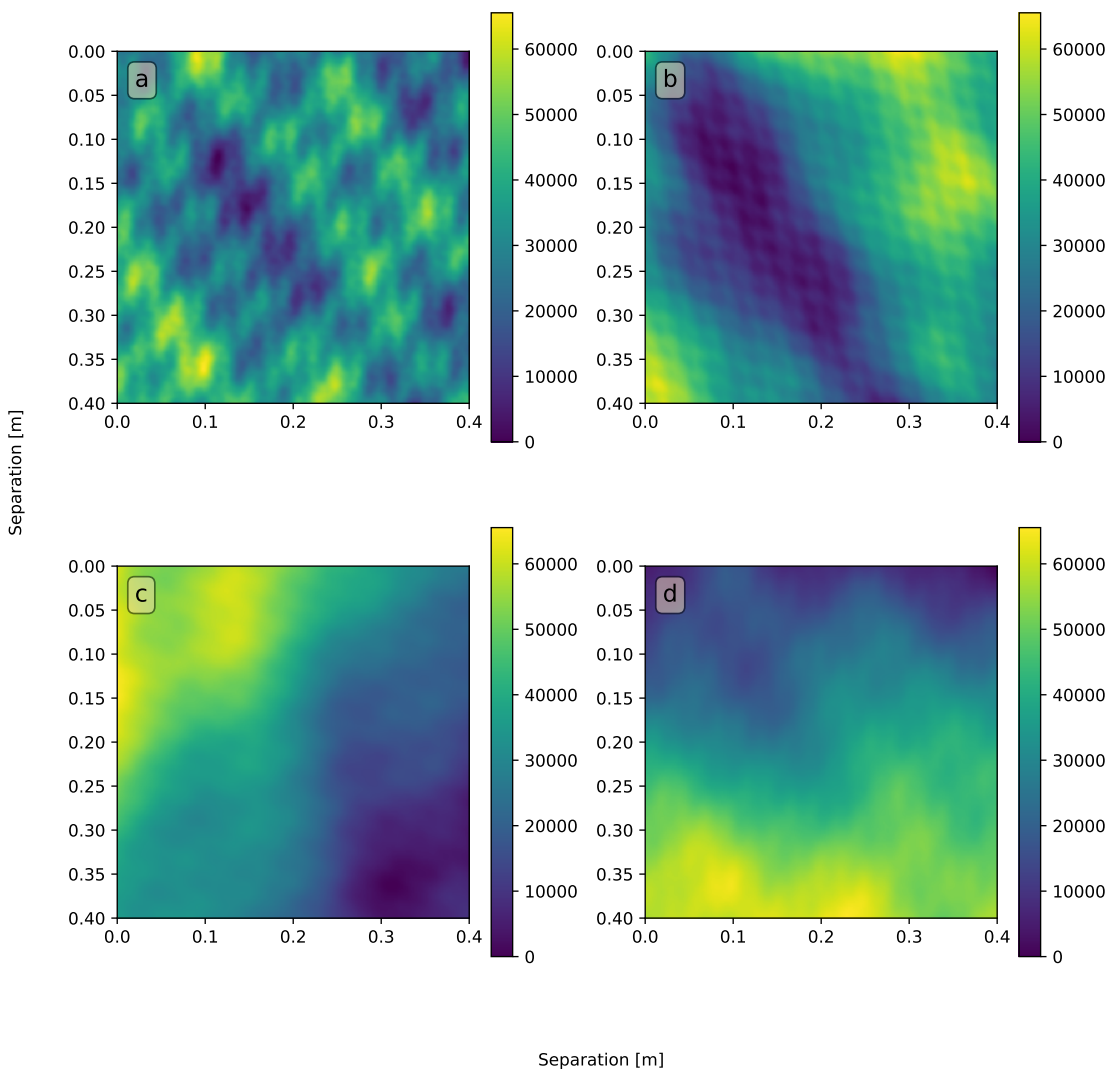
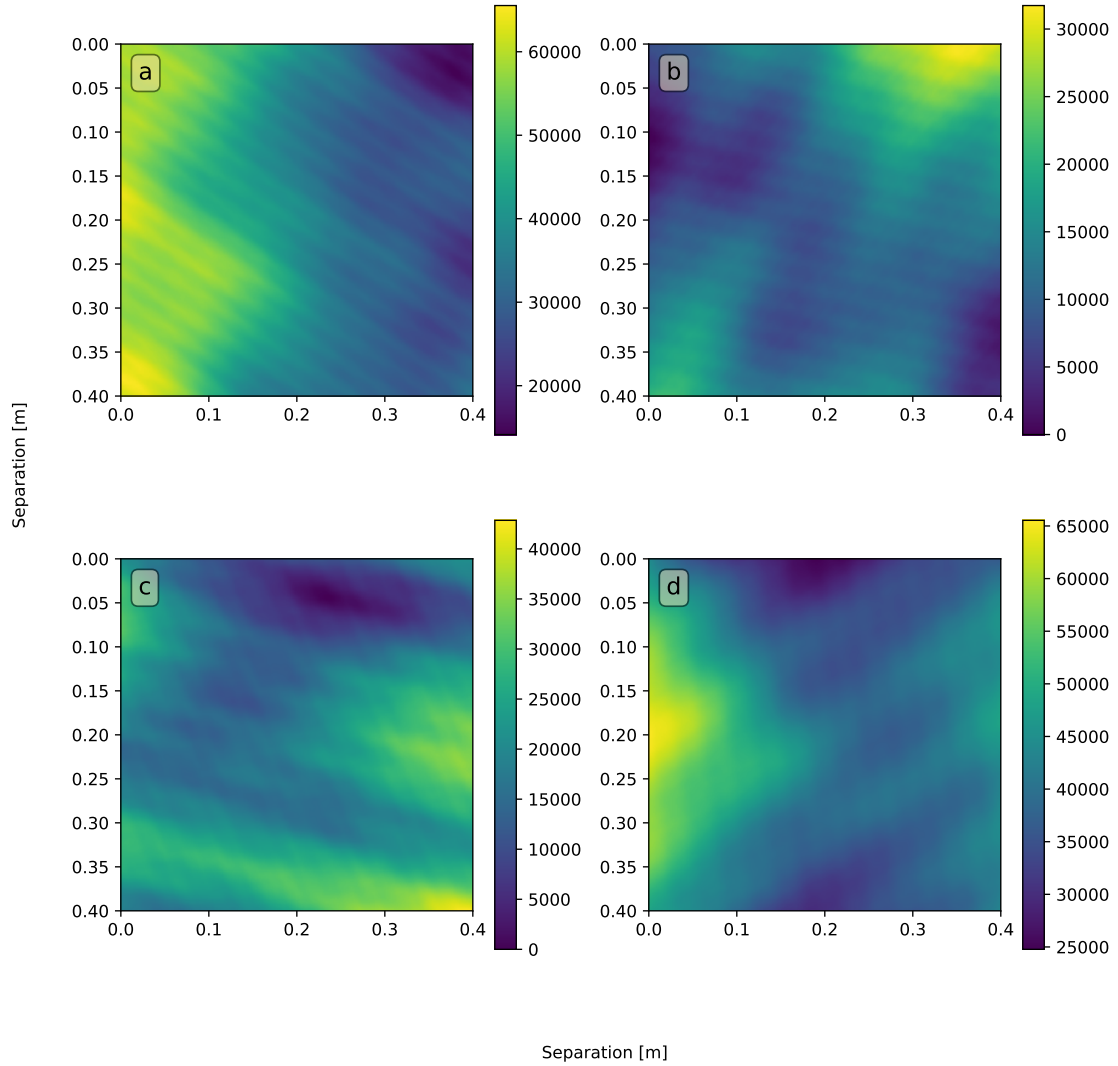


Figure 4.14.: Phase screens for varying exponent  $\alpha$  and GMVKS: (a)  $\alpha = 3.1$ , (b)  $\alpha = 3.4$ , (c)  $\alpha = 11/3$ , (d)  $\alpha = 3.9$ .



Then again a comparison of sample structure functions (equations 4.41 and 4.42) to analytical expressions (equations 4.62 and 4.64) is done.  $N_{ps} = 200$  statistically independent stacks of phase screens are generated using the default configuration (table 4.1). In figure 4.15 the transversal phase structure function  $D_\varphi(r, 0)$  for varying outer scale  $L_0$  is shown for horizontal direction  $D(x, 0)$  and vertical direction  $D(0, y)$ , while figure 4.16 shows the corresponding longitudinal phase structure function  $D_\varphi(0, m\Delta z)$  representing correlation between phase screens in a stack. A good agreement between sample structure functions and analytical structure functions can be observed. Compared to the structure functions for uncorrelated phase screens (figure 4.8), there are no dips of structure function for the lowest outer scale

#### 4. *Methods*

---

$L_0 = 0.1$  m at maximum separations of 1.6 m in figure 4.15. These separations correspond to opposing borders of the generated phase screens. Hence there is no periodicity of phase screens even for little low-frequency noise.

Figure 4.15.: Comparison of analytical transversal Non-Markov phase structure function  $D^{(NM)}(r,0)$  and sample phase structure function  $D_\phi(r,0)$  for varying outer scale  $L_0$  and GMVKS: (a)  $L_0 = 0.1$  m, (b)  $L_0 = 1$  m, (c)  $L_0 = 10$  m, (d)  $L_0 = 100$  m. Colored regions are 95%-confidence bands of the sample structure functions  $D_{hor/vert}$ . The analytical Non-Markov structure function (black line) is mainly in the confidence bands of the numerical structure functions (red and blue line).

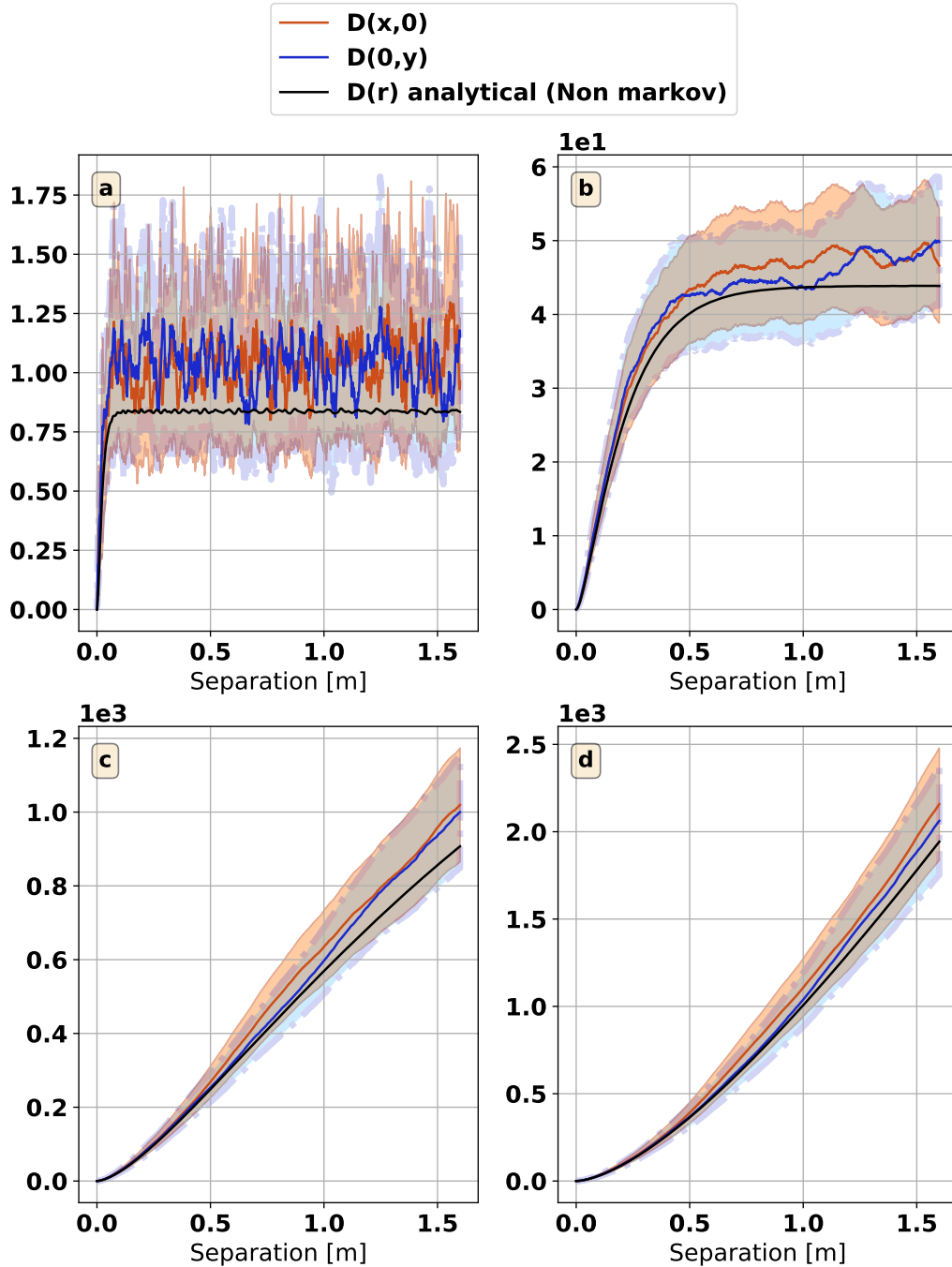
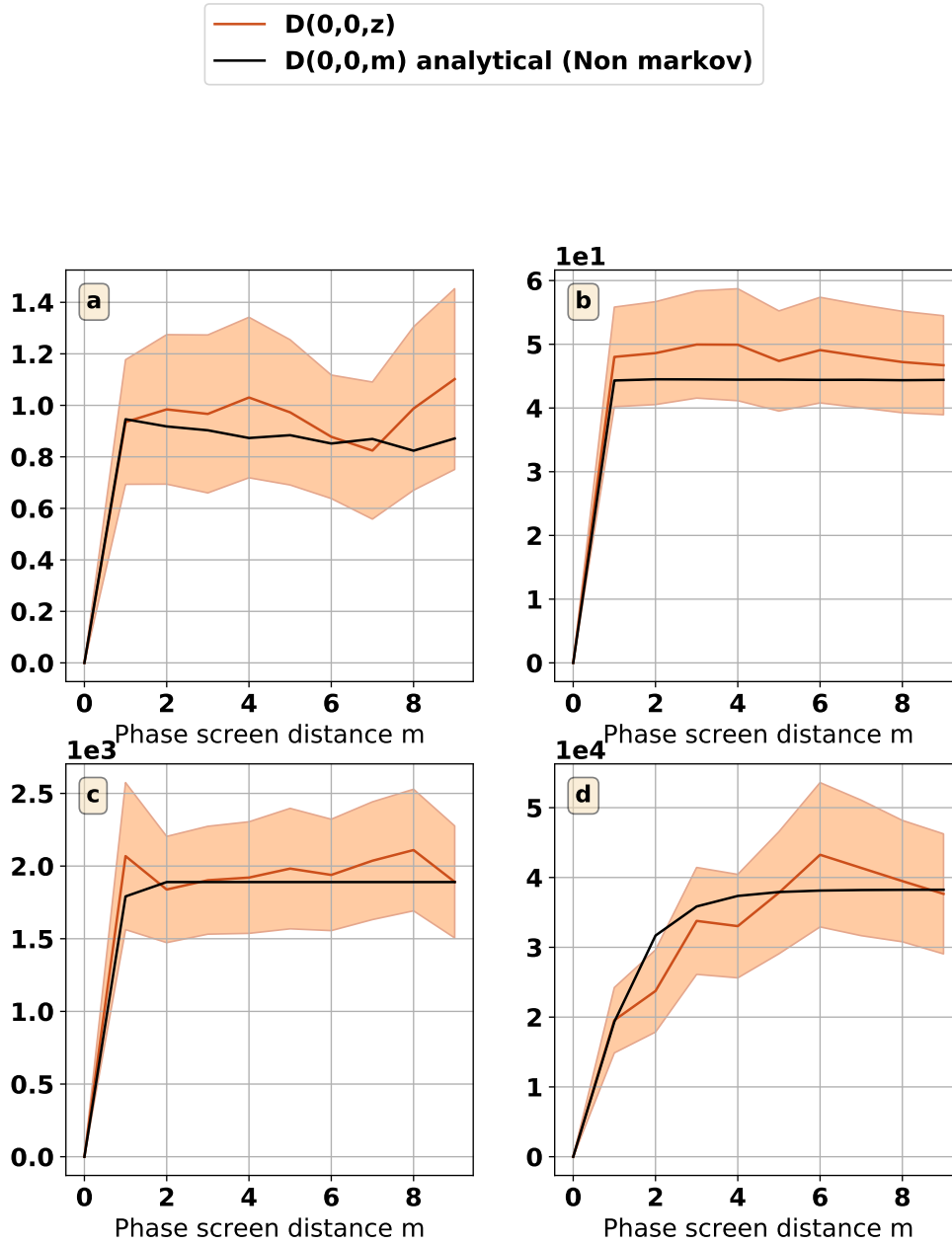


Figure 4.16.: Longitudinal phase structure function  $D_\varphi(0, m\Delta z)$  for varying outer scale  $L_0$  and GMVKS: (a)  $L_0 = 0.1$  m, (b)  $L_0 = 1$  m, (c)  $L_0 = 10$  m, (d)  $L_0 = 100$  m.



Obviously, for outer scales  $L_0$  smaller than the phase screen thickness  $\Delta z = 15$  m the longitudinal phase structure function  $D_\varphi(0, m\Delta z)$  achieves saturation for very low screen separations  $m \geq 1$ , while only for  $L_0 = 100$  m there is significant correlation for  $m \leq 3$ , since  $D(0, m\Delta z) = 2(\text{Cov}(0) - \text{Cov}(m\Delta z))$  (see equation 3.14).

In figure 4.17 the analytical radial Non-Markov phase structure function  $D_\phi^{(NM)}(r,0)$  is compared for different inner scales  $l_0$ , outer scales  $L_0$  and exponents  $\alpha$  based on the spectrum GMVKS. Default values are  $C_n^2 = 10^{-13} \text{ m}^{3-\alpha}$ ,  $l_0 = 0.01 \text{ m}$ ,  $L_0 = 1.0 \text{ m}$ ,  $\alpha = 11/3$  and  $L = 150 \text{ m}$ . It is normalized to a common prefactor  $16\pi^2 k^2 C_n^2$  with the wave number  $k$ , the phase screen thickness  $\Delta z$ , the exponent factor  $A(\alpha)$  of the spectrum GMVKS (equation 2.16). The relevant turbulence parameter ranges are chosen from data fits based on experimental data and shown in a later chapter. The influence of turbulence model parameters on the Non-Markov phase structure function  $D_\phi^{(NM)}(r,0)$  is very similar to that on the Markov phase structure function (figure 4.9). It can be observed that inner scale  $l_0$  has slight influence on the Non-Markov phase structure function  $D\phi^{(NM)}(x,y)$  for inner scales  $l_0 < 0.01 \text{ m}$ . An increasing inner scale  $l_0$  also increases the *GMVKS* spectrum cutoff and hence the upper bound of the phase structure function  $D_\phi^{(NM)}(r,0)$  is reduced. As the outer scales  $L_0$  limits the low-frequency contributions of the spectrum GMVKS, it has the opposite effect on the phase structure function compared to the inner scale  $l_0$ . An increasing outer scale  $L_0$  decreases the low-frequency cutoff and therefore increases the upper bound of Non-Markov phase structure function  $D_\phi^{(NM)}$  but also saturation sets in at higher separations. For varying exponents the upper bound of phase structure function has a local maximum at  $\alpha \approx 3.45$  for the specified default values. In figure 4.18 the same comparison is shown for the longitudinal Non-Markov phase structure function  $\Delta_\phi^{(NM)}(0,m\Delta z)$ . As the default outer scale  $L_0 = 1 \text{ m}$  is much lower than the phase screen thickness  $\Delta z$ , the Markov assumption ( $L_0 \ll \Delta z$ ) holds, phase screens are almost uncorrelated and the longitudinal phase structure function  $D_\phi^{(NM)}(0,m \cdot \Delta z)$  is saturated for separations  $m \geq 1$  in the variations of  $l_0$  and  $\alpha$ . Similar to the radial component, for increasing outer scale  $L_0$  the longitudinal phase structure function  $D_\phi^{(NM)}(0,m \cdot \Delta z)$  increases as well as separations  $m$  where saturation sets in.

Figure 4.17.: Analytical radial Non-Markov phase structure function  $D_\phi^{(NM)}(r, 0)$  for varying turbulence parameters  $l_0$  (a),  $L_0$  (b), and  $\alpha$  (c) based on the model GMVKS. Default values are  $C_n^2 = 10^{-13} \text{ m}^{3-\alpha}$ ,  $l_0 = 0.01 \text{ m}$ ,  $L_0 = 1.0 \text{ m}$ ,  $\alpha = 11/3$  and  $L = 150 \text{ m}$

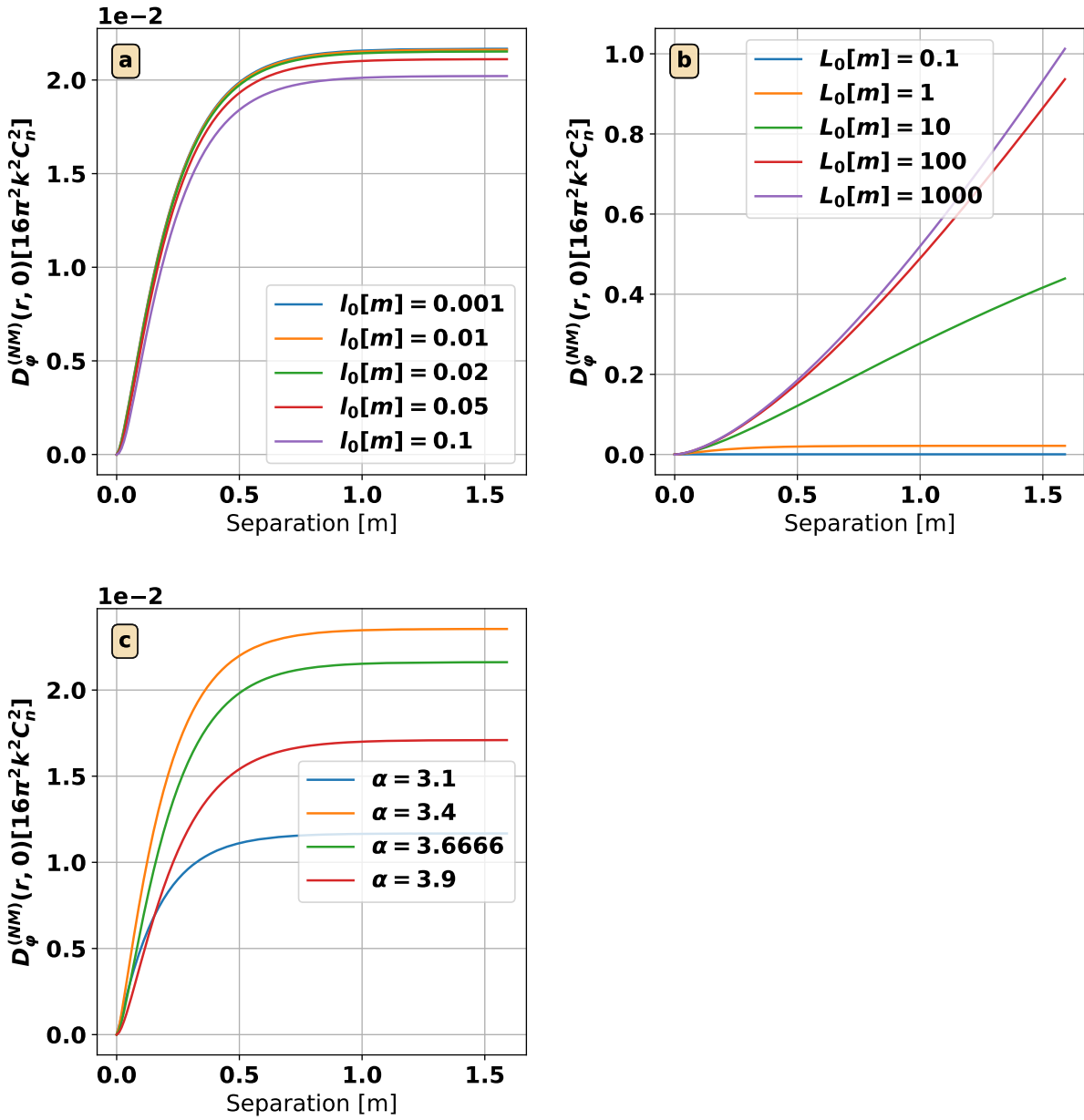


Figure 4.18.: Analytical longitudinal Non-Markov phase structure function  $D_\phi^{(NM)}(0, m \cdot \Delta z)$  for varying turbulence parameters  $l_0$  (a),  $L_0$  (b), and  $\alpha$  (c) based on the model GMVKS. Default values are  $C_n^2 = 10^{-13} \text{ m}^{3-\alpha}$ ,  $l_0 = 0.01 \text{ m}$ ,  $L_0 = 1.0 \text{ m}$ ,  $\alpha = 11/3$ ,  $L = 150 \text{ m}$  and  $\Delta z = 15 \text{ m}$ .

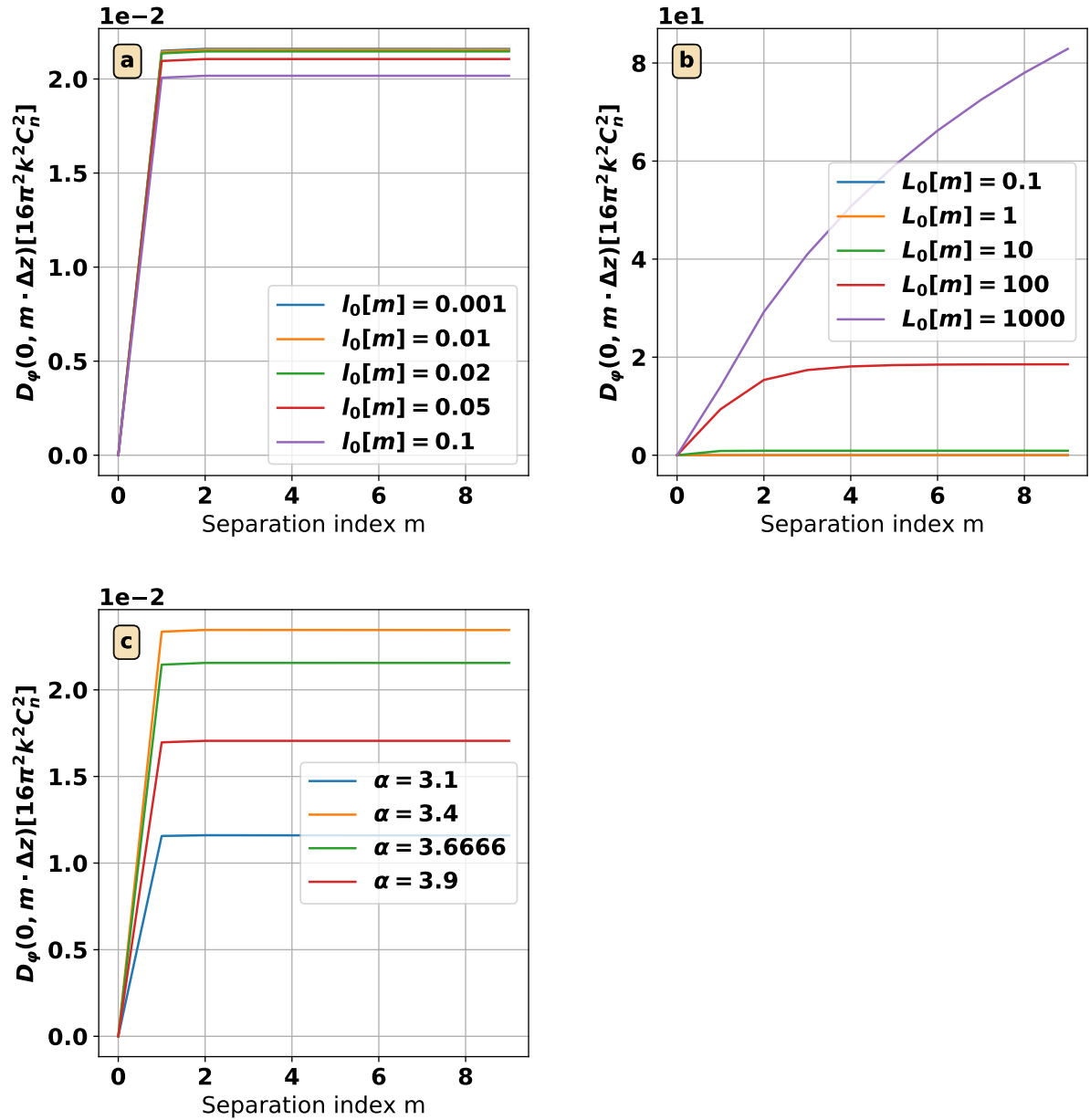
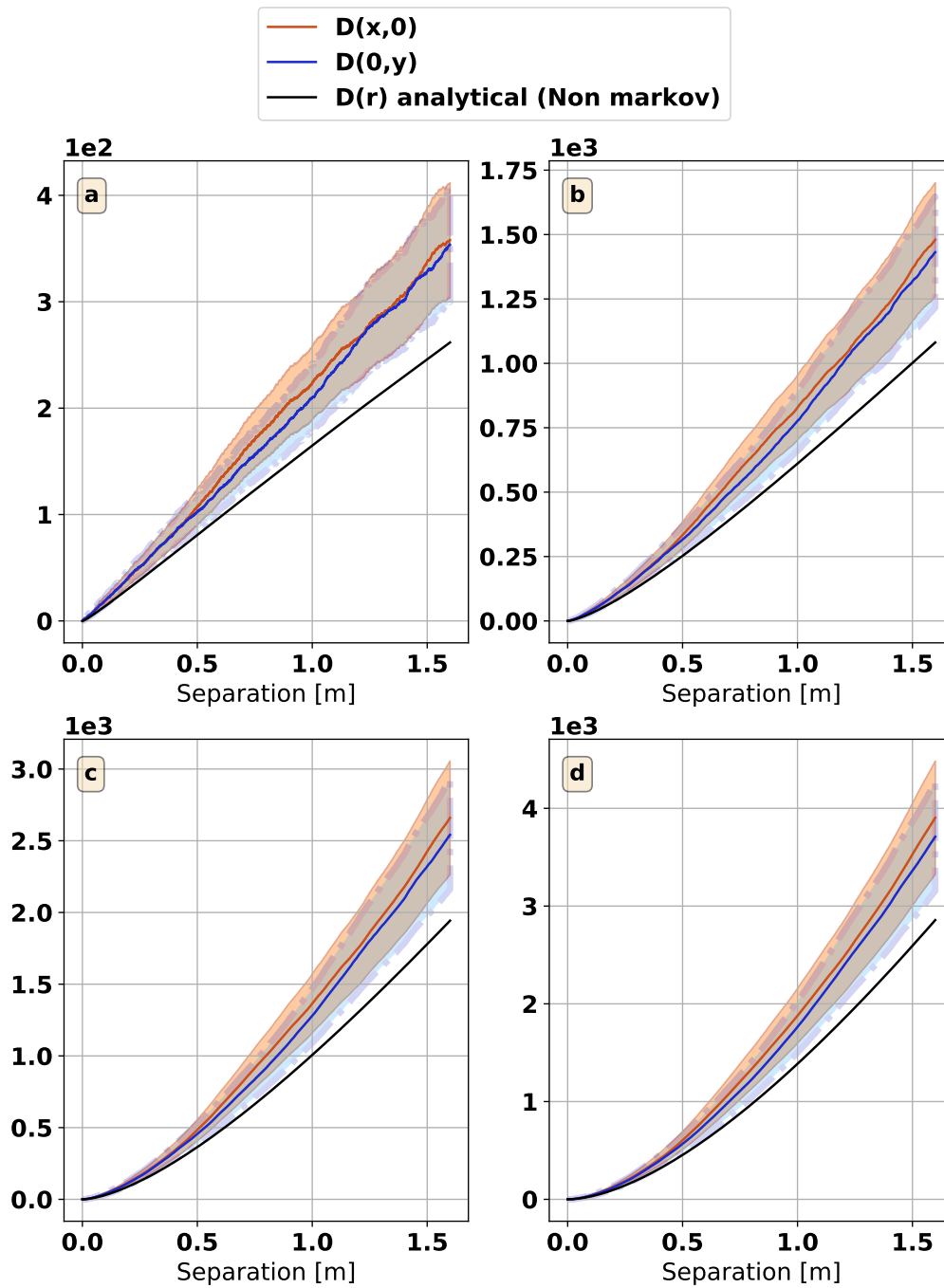


Figure 4.19.: Phase structure function for varying exponent  $\alpha$  and GMVKS: (a)  $\alpha = 3.1$ , (b)  $\alpha = 3.4$ , (c)  $\alpha = 11/3$ , (d)  $\alpha = 3.9$ .



#### 4.4. Calculation of point spread function

So how can the wave propagation involving random phase modulations by generated phase screens be used to obtain the point spread function corresponding to a point source, i.e. the profile of optical intensity in the sensor plane? In order to calculate point spread functions resulting from turbulence degradation, the wave propagation approach can be used on point sources. A point source can be modeled as a 2D Gaussian windowed sinc function with quadratic phase (Schmidt [2010]):

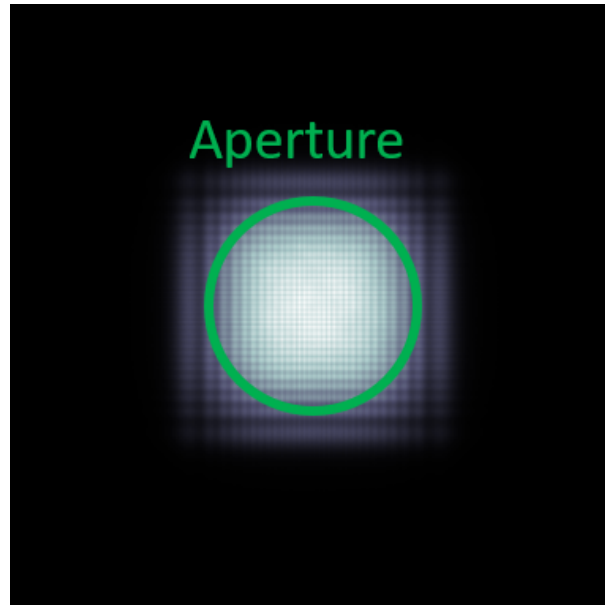
$$U_0(x, y) = \lambda L \beta^2 \exp\left(-\frac{jk}{2L}(x^2 + y^2)\right) \text{sinc}(\beta x, \beta y) \exp\left(\frac{\beta^2}{16}(x^2 + y^2)\right) \quad (4.68)$$

Here  $\beta = \bar{D}/(\lambda L)$  and  $\bar{D}$  is the width of amplitude field at the pupil plane where a uniform amplitude is desired. It should be greater than the aperture  $D$  but smaller than the phase screen width  $W_x$  or height  $W_y$ . One possibility to get a best-focus  $PSF(x, y)$  in the focal plane, is filtering the resulting profile  $U_n(x, y)$  by an aperture mask  $a(x, y)$  and a collimation-type phase compensation to allow the lens operation to focus the image on the focal length (Hardie et al. [2017]):

$$p(x, y) = a(x, y) U_n(x, y) \exp\left(-\frac{j\pi(x^2 + y^2)}{\lambda L}\right) \quad (4.69)$$

However, when input beam profiles  $U_0(x, y)$  narrow compared to the grid size are used, rippling effects can occur as shown in figure 4.20. This intensity profile is then filtered by a circular aperture.

Figure 4.20.: Example of rippling effects in beam profile  $I_n(x, y) = |U_n(x, y)|^2$  for a propagated point source. Aperture masking filters only pixels in the aperture area.



The best-focus PSF is achieved when there is a flat profile at the aperture in the case of no turbulence. A new approach for field correction can achieve this. A filter  $A_0(x, y)$  has to be found so that

$$\begin{aligned} \tilde{U}_{n,0}^{(\text{no turb})}(x, y) &= A_0(x, y)U_{n,0}^{(\text{no turb})}(x, y) \\ &= \begin{cases} (x, y) \in \text{Aperture} & \text{const} \\ \text{else} & 0 \end{cases} \end{aligned} \quad (4.70)$$

A filter  $A_0(x, y)$  with this property can be chosen as

$$A_0(x, y) = \begin{cases} U_{n,0} > cU_{max} & \frac{U_{max}}{U_{n,0}(x, y)} \\ \text{else} & 1 \end{cases} \quad (4.71)$$

where

$$U_{max} = \max_{xy}(U_{n,0}^{(\text{no turb})}(x, y)) \quad (4.72)$$

and  $c = 0.01$  is a small factor to exclude pixels not corresponding to the aperture. A flat profile at the aperture in the case of zero turbulence is associated with the absence of high-order aberrations, often described by Zernike modes (Noll [1976]). Then for a simulation with non-zero turbulence the same filter can be used to give a corrected field

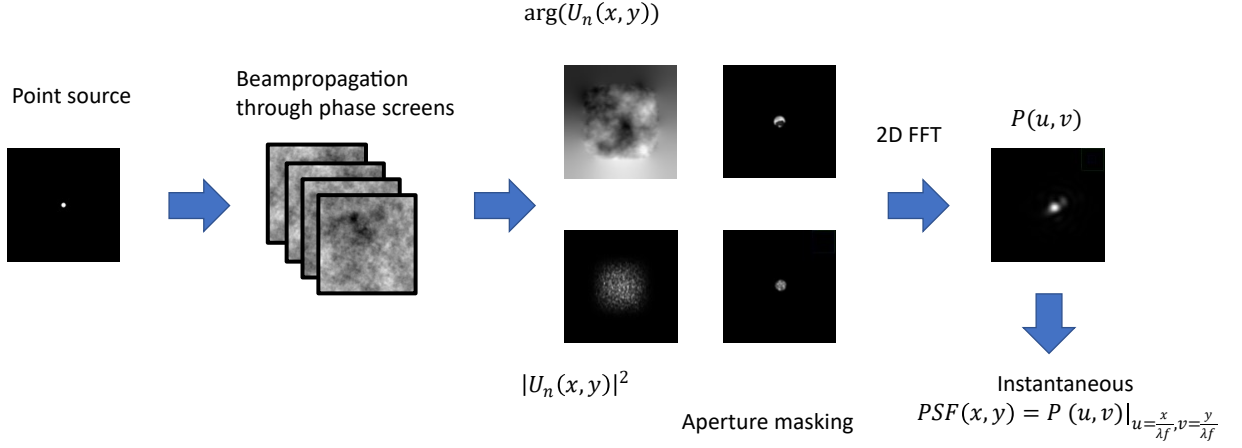
$$\tilde{U}_{n,0}^{\text{turb}}(x, y) = A_0(x, y)U_{n,0}^{\text{turb}} \quad (4.73)$$

It is an advantage, that the filter  $A_0(x, y)$  has to be calculated only once and can be cached for a specific setting of aperture and computational field. The incoherent PSF (Goodman [2005]) can then be found by Fourier optics as

$$PSF(x, y) = \left( |P(u, v)|^2 \right) \Big|_{u=\frac{x}{\lambda L}, v=\frac{y}{\lambda L}}, \quad (4.74)$$

where  $P(u, v) = \mathcal{F}\tilde{U}_{n,0}^{\text{turb}}(x, y)$ . This procedure is shown in figure 4.21

Figure 4.21.: Workflow of PSF calculation: 1. A beam profile emulating a point source is propagated through a sequence of phase screens. 2. The resulting profile  $U_n(x, y)$  is masked by a circular aperture. 3. Fourier optics gives the point spread function  $P(u, v)$ . 4. A rescaling of frequencies  $x = u/(\lambda f)$  and  $y = v/(\lambda f)$  gives the point spread function  $P(x, y)$  in the sensor plane



This procedure can then be repeated for different lines of sight to give the point spread function  $PSF(\alpha_x, \alpha_y, x, y)$  for a point source at horizontal and vertical viewing angles  $(\alpha_x, \alpha_y)$ . Similar approaches were used in former anisoplanatic turbulence simulations (Bos and Roggemann [2012], Hardie et al. [2017]). For small viewing angles the planes of turbulence phase screens for different point sources can be assumed to be parallel to each other. Then the phase screens for single point sources can be cropped from larger phase screens at different positions  $s(x, y)$  relative to its centers, i. e.

$$s_{x/y,i} = \Delta s_{x/y,0} + \Delta s_{x/y}(N - i) \quad (4.75)$$

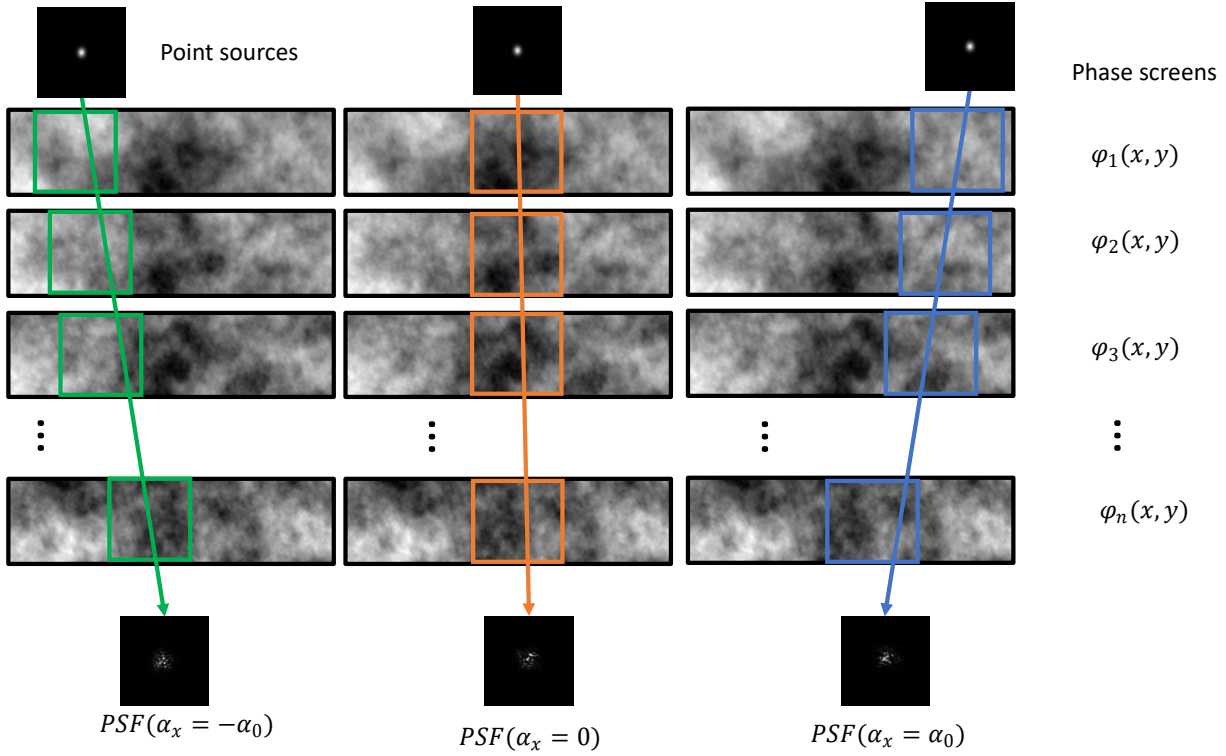
for the  $i$ -th phase screen of  $N$  total phase screens. The physical shift per phase screen is given by

$$\Delta s_{x/y} = \alpha_{x/y} \Delta z \quad (4.76)$$

$$\Delta s_{x/y,0} = \frac{\Delta s_{x/y}}{2} \quad (4.77)$$

with the phase screen thickness or wave propagation step size  $\Delta z$ . For the horizontal direction this is shown in figure 4.22.

Figure 4.22.: Spatial subsampling of phase screens: PSFs for different viewing angles are calculated by subsampling of different regions of interest (colored boxes) of same phase screens  $\varphi_n(x, y)$  via bilinear interpolation



Also additional transversal wind effects can be included by adding physical shifts

$$\Delta s_{wind,x/y} = \frac{v_{cross}}{f} i, \quad (4.78)$$

depending on the cross-sectional wind speed  $v_{cross}$ , the camera frame rate  $f$  and the image sequence ID  $i$ . Caching of larger phase screens and subsampling of these screens for different point targets can be comparably much faster than calculating new phase screens for each point target, e.g the sparse spectrum (SS) method. However, this approach is strongly memory-limited depending on the field of view to be simulated.

#### 4.5. Turbulence simulation via non-uniform filtering

The generated point spread functions (PSFs) are the impulse responses of single point sources. If one is interested in the degradation of arbitrary input scenes, filtering of pristine input images by these point spread functions is required. Uniform filtering with single point spread functions is sufficient when field of views  $\theta < \theta_0$  with the isoplanatic angle  $\theta_0$  (equation 3.32) are used (isoplanatic imaging). Otherwise, a non-uniform filtering procedure with spatially varying PSFs is required. Fast shift-variant blur (FSV) (Miller et al. [2019]) was proposed, which uses spatially varying interpolations of multiple versions of

the pristine image filtered by different PSFs. However, this approach requires caching of these filtered versions. In the following a more general memory-efficient approach is presented.

#### 4.5.1. Generation of local point spread functions

If a set of PSFs  $PSF(x', y', x - x', y - y')$  has been calculated for a specified field of view and matching the spatial sampling frequency of a camera sensor, an arbitrary input scene  $I(x, y)$  can be non-uniformly filtered to give a turbulence-degraded image  $O(x, y)$ :

$$O(x, y) = \sum_{x'} \sum_{y'} PSF(x', y', x - x', y - y') I(x', y') \quad (4.79)$$

However, computation of point spread functions for each pixel of the input image  $I(x, y)$  can be computationally very expensive. Computational effort can be drastically reduced by calculation of PSFs on an equidistant grid overlaying the image and interpolation between adjacent grid PSFs for each image pixel. If the image has dimensions  $(N_x, N_y)$  and the equidistant grid has dimensions  $(M_x, M_y)$ , where  $M_x = (N_x - 1)/k_x$  and  $M_y = (N_y - 1)/k_y$  then a pixelwise PSF can be calculated by linear interpolation

$$PSF(x', y', \Delta x, \Delta y) = (1 - f_y) [(1 - f_x) PSF_{i,j}(\Delta x, \Delta y) + f_x PSF_{i+1,j}(\Delta x, \Delta y)] \\ + f_y [(1 - f_x) PSF_{i,j+1}(\Delta x, \Delta y) + f_x PSF_{i+1,j+1}(\Delta x, \Delta y)], \quad (4.80)$$

with

$$\Delta x = x - x' \quad \Delta y = y - y', \quad (4.81)$$

and the indices

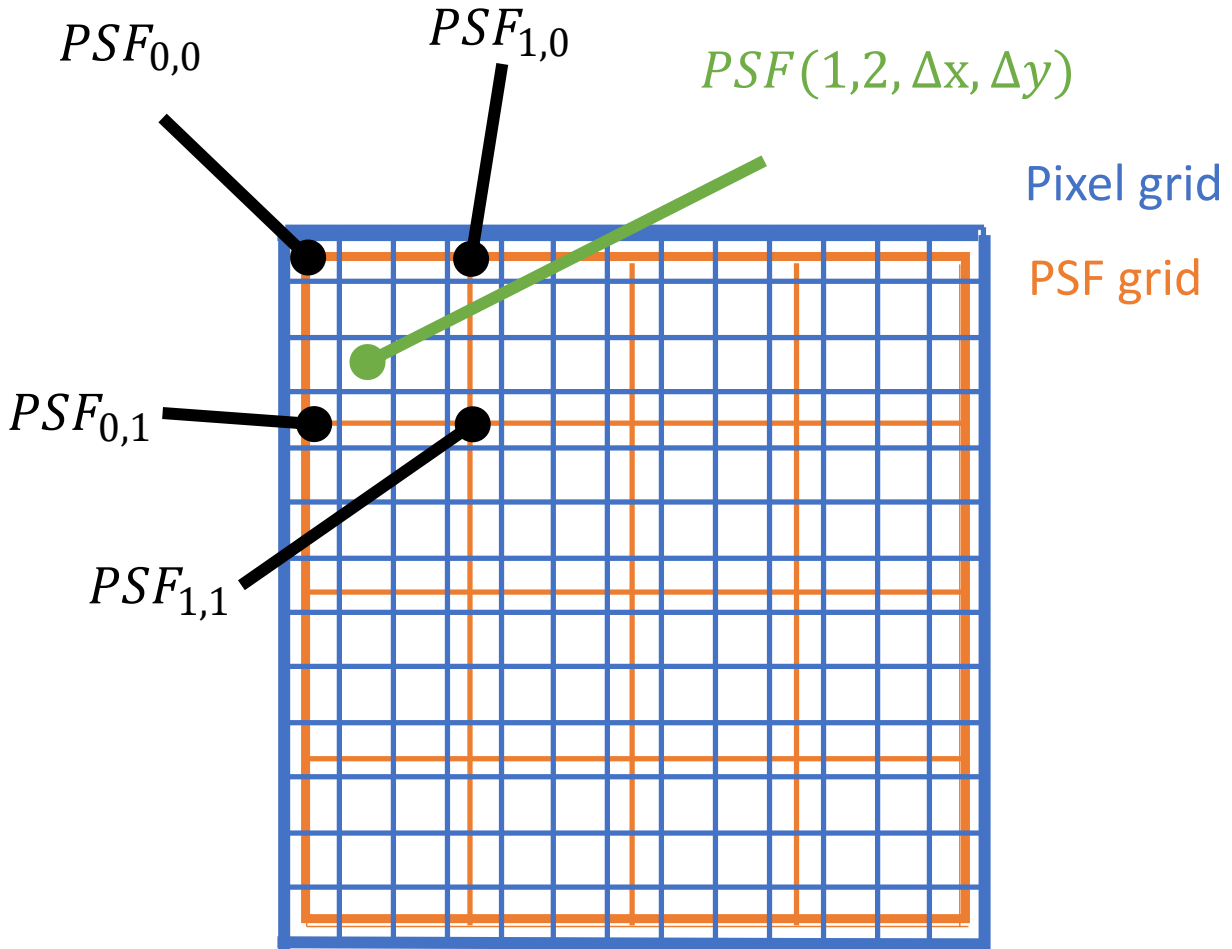
$$i = \left\lfloor \frac{x'}{k_x} \right\rfloor \quad j = \left\lfloor \frac{y'}{k_y} \right\rfloor \quad (4.82)$$

and the factors

$$f_x = \frac{x'}{k_x} - \left\lfloor \frac{x'}{k_x} \right\rfloor \quad f_y = \frac{y'}{k_y} - \left\lfloor \frac{y'}{k_y} \right\rfloor, \quad (4.83)$$

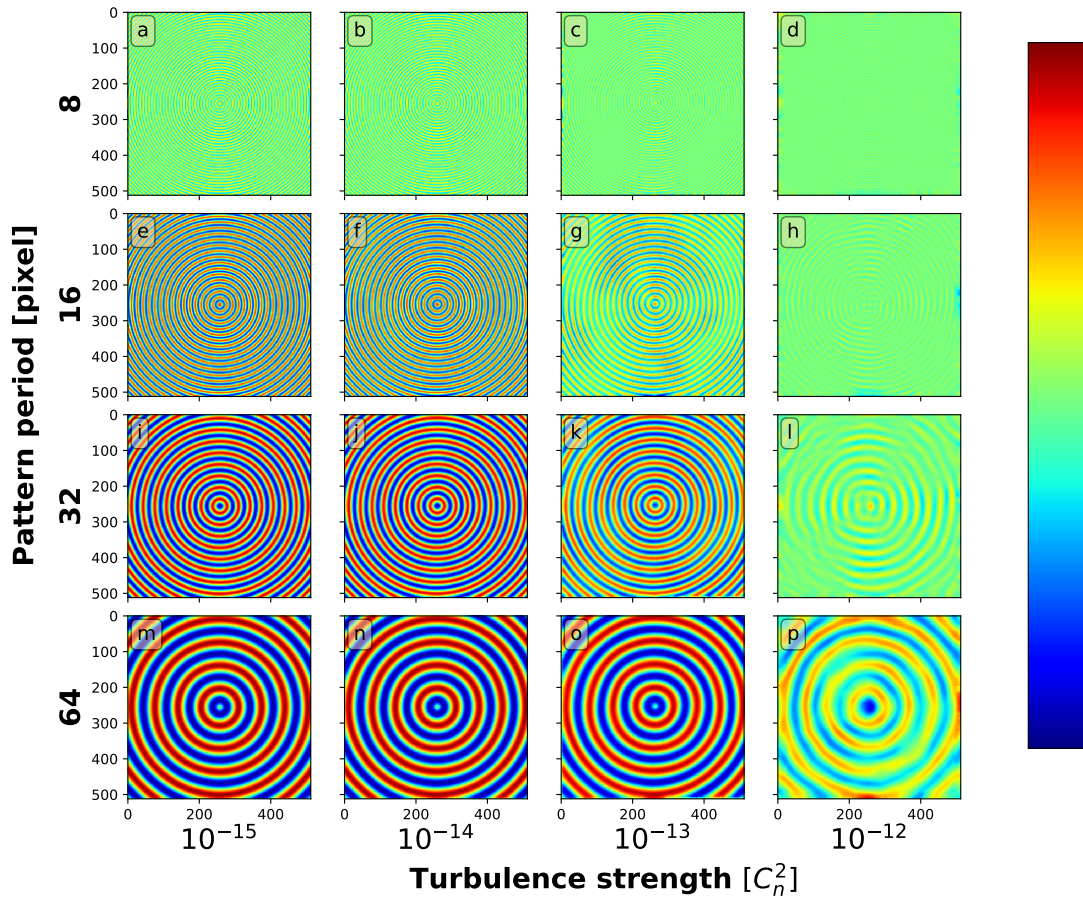
where  $\lfloor \cdot \rfloor$  is the floor-function, rounding the argument to the closest smaller integer. An example for a 13x13 image with skip factors  $k_x = k_y = 3$  is depicted in figure 4.23.

Figure 4.23.: Example of PSF interpolation for 13x13 image.  $PSF(1,2,\Delta x,\Delta y)$  is calculated based on four adjacent point spread functions  $PSF_{0,0}, PSF_{0,1}, PSF_{1,0}$  and  $PSF_{1,1}$  according to equation 4.80



Methods for fast shift-variant blur (Miller et al. [2019]) can be used to accelerate imaging simulation for long time sequences by Eigenvalue decomposition of the generated point spread functions and using a limited number of components with the highest magnitudes. Then the degraded image can be formed by spatially nonuniform superposition of uniformly filtered versions of the pristine image with the Eigenvectors as filter kernels. However, this requires modeling the spatial correlation of the spatially varying weights of the filtered versions depending on the turbulence model. Additionally, for strong turbulence instantaneous PSFs with multimodal intensity profiles can occur, which is shown in the next chapter. There is no guarantee, that a fixed limited number of Eigenvalue components can represent these PSFs without significant loss of accuracy. In figure 4.24 turbulence simulations for a radial sinusoidal pattern with varying period and turbulence strengths based on the default configuration (table 4.1) is shown. 15x15 PSF grids are calculated and equidistantly mapped on the 512x512 16bit input image. Therefore the input image represents a target of physical width and height of  $l = (14 \cdot 1.5) \text{ cm} = 21 \text{ cm}$  at a range of  $L = 150 \text{ m}$ . The dynamic range is uniquely set to  $[0,65535]$ . It can be observed that the modulation

Figure 4.24.: Turbulence-degraded frames of radial sinusoidal pattern with varying pattern period in pixel and varying turbulence strengths  $C_n^2/(m^{-2/3})$ . Color range is set uniquely to  $[0,65535]$ .



at higher spatial frequencies are more affected by turbulence strength  $C_n^2$  than lower spatial frequencies. There are visible spatial variations of degradation only in transitions between low and high turbulence strengths  $C_n^2$ . Based on precalculated PSF grids, arbitrary input images can be processed. A CUDA implementation of the presented non-uniform image filtering enables the generation of video sequences of 512x512 images with about 20 frames per second on a RTX 2080 Ti.

#### 4.5.2. Rescaling of point spread functions to sensor units

The PSF images calculated by Fourier transform of the transmission field at the aperture as shown in figure 4.21 are given in units of

$$\delta_{x,y} = \lambda f \delta_{u,v} \quad (4.84)$$

$$\delta_{u,v} = \frac{n_{x/y}}{W_{x,y}}, \quad (4.85)$$

where  $n_{x,y}$  are the grid sizes for computational field used for wave propagation.  $W_{x,y}$  are the physical dimensions of the computational field. Point spread functions  $PSF_{sensor}(\Delta x, \Delta y)$  in units of sensor pixels can be calculated by downsampling or area interpolation on the simulated point spread functions  $PSF_{opt}(\Delta x, \Delta y)$

$$PSF_{sensor}(\Delta x, \Delta y) = \int_{t_x \Delta x}^{t_x(\Delta x+1)} \int_{t_y \Delta y}^{t_y(\Delta y+1)} P_{opt}(x, y) dx dy, \quad (4.86)$$

with the scaling factors

$$t_{x,y} = \frac{p_{x,y}}{\delta_{x,y}} \quad (4.87)$$

and the pixel pitches  $p_{x,y}$ .

## 5. Evaluation of simulated images

### 5.1. Uncorrelated 2D phase screens

For reliable simulations of PSFs that can be used for image-based turbulence simulation it is important to validate properties of the PSFs for which analytical expressions exist. Unfortunately many figures of merit are only given as integral representations involving the turbulence power spectral density  $\Phi_n(\kappa)$  and cannot be solved analytically for advanced spectra such as GMVKS and GMAS. If this is the case, the corresponding integrals are solved numerically by trapez integration in the following. Long-exposure MTFs and short-exposure MTFs, the Strehl ratio  $S$  and the aperture-averaged scintillation index  $\sigma_I^2(D)$  represent shape properties of single PSFs, while the differential tilt variance  $DTV(\Delta x, \Delta y)$  represents spatial correlation between spatially separated PSFs in a grid of PSFs.

#### 5.1.1. Validation of modulation transfer function

Based on the default configuration (4.1) multiple simulations of beam propagation with subsequent PSF calculation are made based on statistically independent stacks of phase screens. A long-exposure PSF is calculated by pixelwise averaging of single PSFs, whose centroids are slightly shifted against each other depending on turbulence strength  $C_n^2$ . A short-exposure PSF is calculated by pixelwise averaging of a set of corrected PSFs, where centroids are shifted to be unique as described in section 3.2.10. These shifts of centroids are related to tip/tilt correction. Then 2D fast Fourier transforms (FFTs) are applied on long-exposure and short-exposure PSFs. This gives the corresponding optical transfer functions (OTFs). Taking the moduli of the complex OTFs gives the modulation transfer functions (MTFs). Then corresponding spatial frequencies in the image plane can be found by the frequency step per pixel

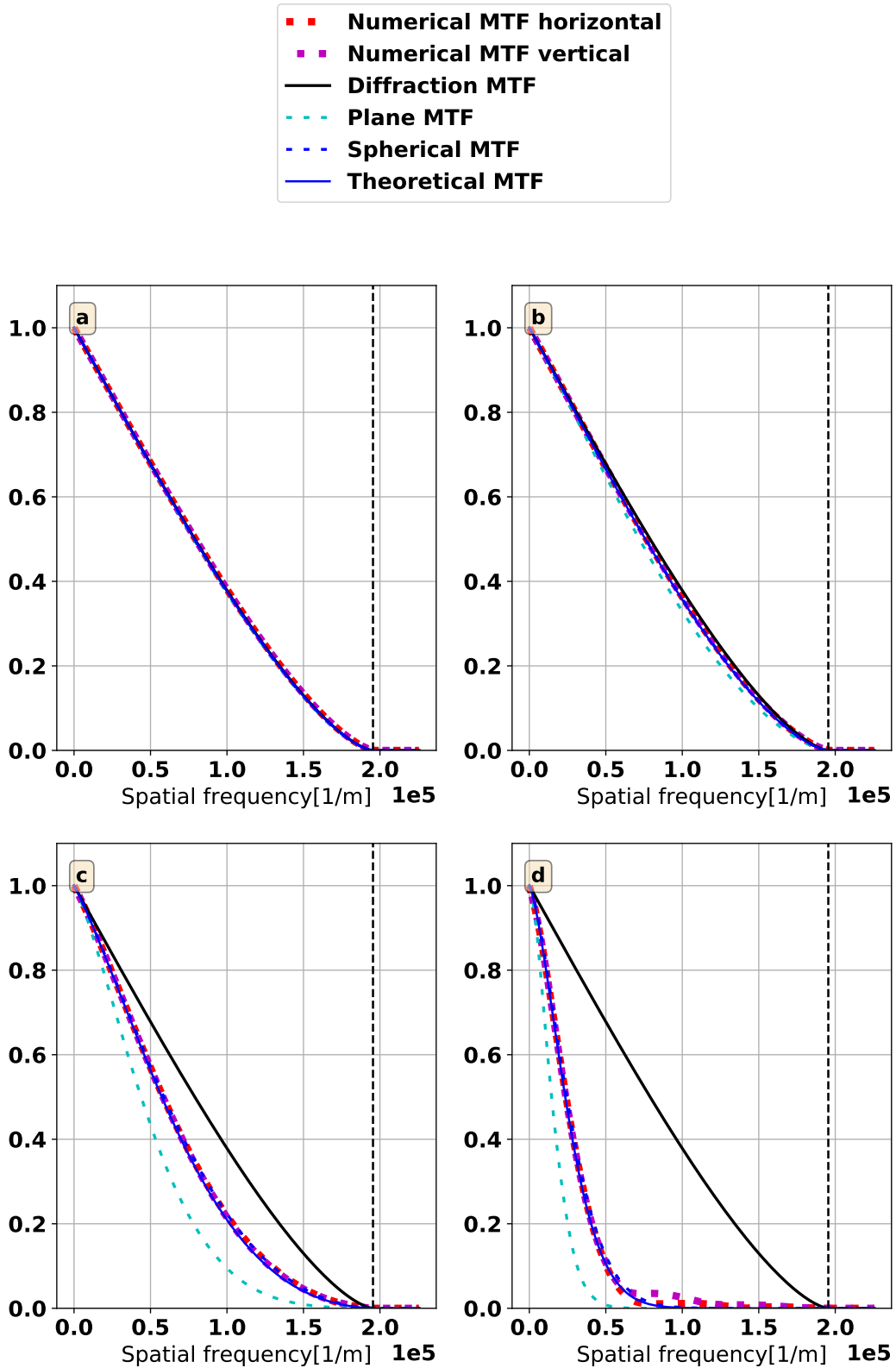
$$\Delta v_{x/y} = \frac{f_{max,x/y}}{N_{x/y}} = \frac{1}{N_{x/y} p_{x/y}} v_{x/y} = \Delta v_{x/y} \cdot (x/y) \quad (5.1)$$

with pixel pitches  $p_{x/y}$ , column  $x$  and row  $y$  of the MTF images. In figure 5.1 horizontal and vertical profiles  $MTF_{L,total}(v_x, 0)$  and  $MTF_{L,total}(0, v_y)$  of the 2D long-exposure MTFs  $MTF_{L,total}(v_x, v_y)$  for varying turbulence strength  $C_n^2$  based on the model GMVKS are shown. The optical cutoff frequency shown as dashed vertical line is given by

$$v_{cutoff} = \frac{D}{\lambda fl} \quad (5.2)$$

with the diameter  $D$ , wavelength  $\lambda$  and focal length  $fl$ . Also shown are the theoretical Fried MTFs (equation 3.54) based on the Kolmogorov spectrum (GMVKS with  $\alpha = 11/3$ ,  $l_0 = 0$  and  $L_0 \rightarrow \infty$ ) and the spherical wave and plane wave MTF (3.72). Joint MTFs including diffraction are shown, since a comparison in the vicinity of the cutoff frequency  $\nu_{cutoff}$  and above is pointless due to an arbitrarily bad signal-to-noise ratio of the numerical sample MTFs for high frequency  $\nu$ .

Figure 5.1.: Long-exposure MTF for varying turbulence strengths  $C_n^2$  and GMVKS: (a)  $C_n^2 = 10^{-16} \text{ m}^{-2/3}$ , (b)  $C_n^2 = 10^{-15} \text{ m}^{-2/3}$ , (c)  $C_n^2 = 10^{-14} \text{ m}^{-2/3}$ , (d)  $C_n^2 = 10^{-13} \text{ m}^{-2/3}$ . The cutoff frequency  $\nu_{cutoff}$  is shown as vertical line.

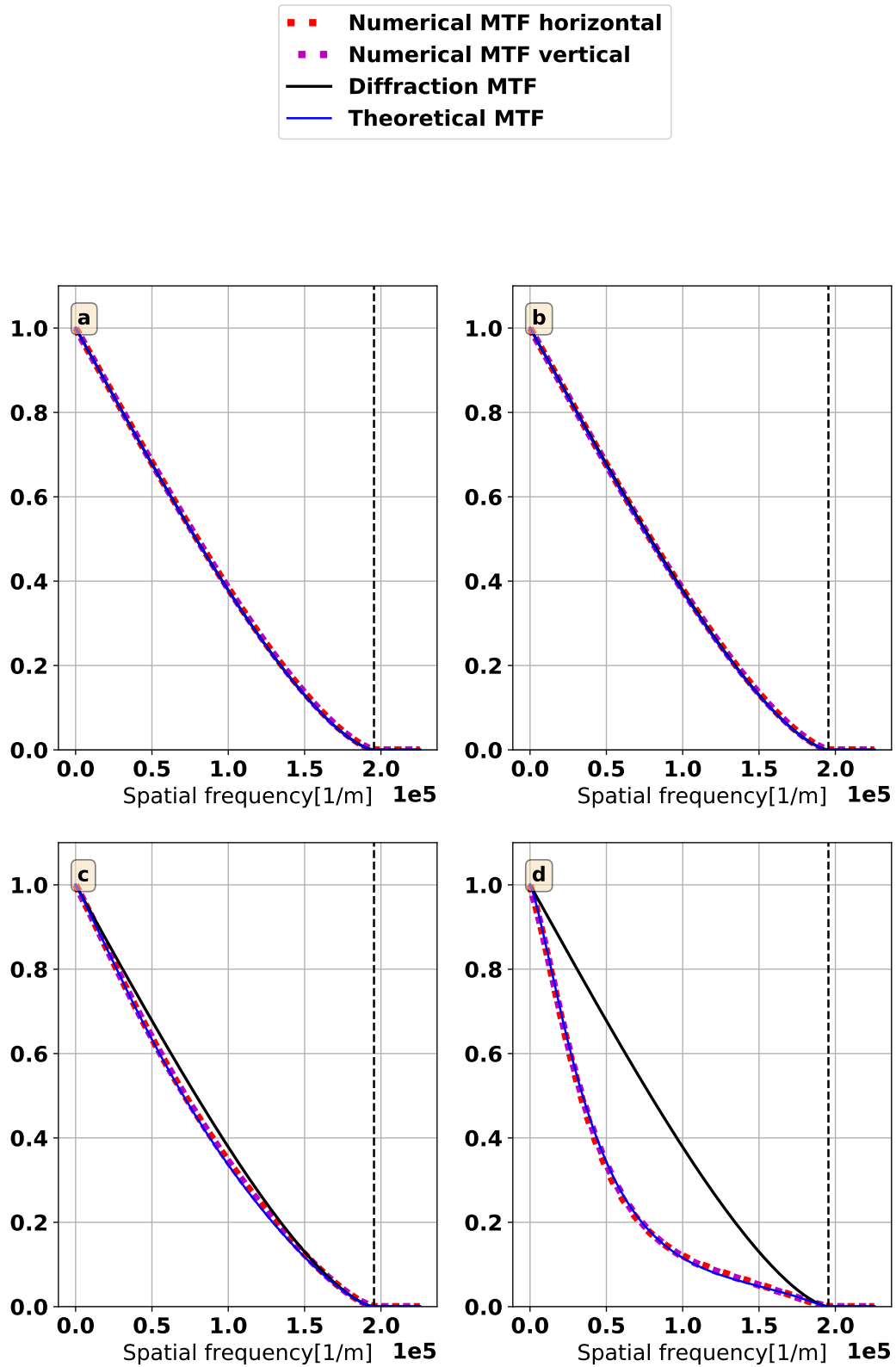


The spherical MTF and (theoretical) Fried MTF are almost identical, minor differences can only be attributed to outer scale effects ( $L_0 = 100\text{m}$ ), which are not considered in the Fried MTF. The diffraction MTF representing the turbulence-free case is shown as upper bound. Obviously, for this configuration turbulence has no significant impact for turbulence strengths  $C_n^2 \leq 10^{-15} \text{m}^{-2/3}$ . It can also be observed that plane wave MTFs tend to drop faster than spherical wave MTFs. This can be explained by the fact, that phase noise accumulated through beam propagation and received by the aperture is weighted by optical intensity. However, for spherical waves the intensity profile is very narrow in the vicinity of the emitting point source, while for plane waves all accumulated phase noise is uniformly weighted, if accumulated power fluctuations are neglected.

In figure 5.2 the corresponding numerical short-exposure MTFs and analytical Fried MTFs (equation 3.55) are shown. There is also very good agreement between numerical and analytical MTFs. The good accordance of both, i.e. long-exposure and short-exposure MTFs, implies also a good match of their ratios

$$R(\mathbf{v}_x, \mathbf{v}_y) = \frac{MTF_{LE}(\mathbf{v}_x, \mathbf{v}_y)}{MTF_{SE}(\mathbf{v}_x, \mathbf{v}_y)} \quad (5.3)$$

Figure 5.2.: Short-exposure MTF for varying turbulence strengths  $C_n^2$  and GMVKS: (a)  $C_n^2 = 10^{-16} \text{m}^{-2/3}$ , (b)  $C_n^2 = 10^{-15} \text{m}^{-2/3}$ , (c)  $C_n^2 = 10^{-14} \text{m}^{-2/3}$ , (d)  $C_n^2 = 10^{-13} \text{m}^{-2/3}$ .



### 5.1.2. Validation of differential tilt variance

Besides the correct features of the single PSFs, e.g. long-exposure and short-exposure MTFs, for anisoplanatic imaging it is also crucial for PSFs representing separated point sources to have proper spatial correlation. For this purpose a grid of 15x15 PSFs representing an equally sized grid of point sources is simulated based on the default configuration (table 4.1). Depending on the physical separation of point sources simulations are done on shifted crops (512x512) from the extended phase screens (2048x2048) as described in section 4.4.  $N_{ps} = 200$  frames with statistically independent stacks of phase screens are simulated. In figure 5.3 smaller image subareas with 10x10 grids of PSFs for two high turbulence strengths  $C_n^2 = 10^{-13} \text{ m}^{-2/3}$  and  $C_n^2 = 10^{-12} \text{ m}^{-2/3}$  are depicted. Subareas are shown for better visibility of single PSFs. For realistic spacings between adjacent PSFs the 512x512 images of PSFs have to be cropped. The angular subtense  $AS$  between two adjacent point sources as seen from a camera is given by

$$AS_{x/y} = \frac{\Delta q_{x/y}}{L}, \quad (5.4)$$

with the physical separation of point sources  $\Delta q_{x/y}$  and the propagation length  $L$ . So the relevant subarea of the PSF image has dimensions

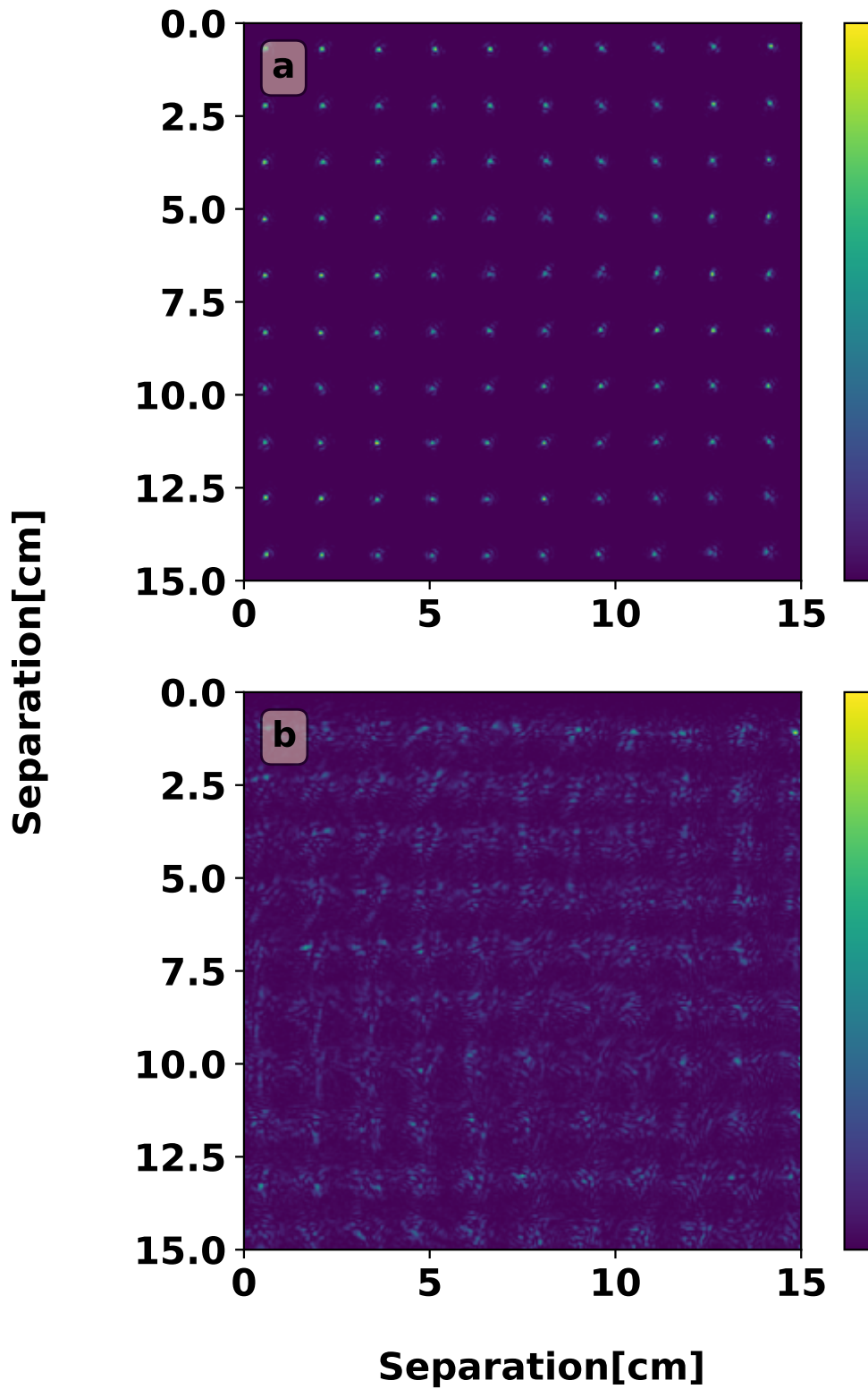
$$w_{x/y} = \frac{AS_{x/y}}{IFOV_{x/y}} \quad (5.5)$$

with the instantaneous field of views

$$IFOV_{x/y} = \frac{p_{x/y}}{fl} \quad (5.6)$$

with the pixel pitches  $p_{x/y}$  and focal length  $fl$ .

Figure 5.3.: Image section with 10x10 PSFs for two turbulence strengths: (a)  $C_n^2 = 10^{-13} \text{ m}^{-2/3}$ , (b)  $C_n^2 = 10^{-12} \text{ m}^{-2/3}$ . Shapes of PSFs vary spatially. PSFs are correlated between different positions depending on distance.



For analysis of single PSFs in the grid, this image cropping is not convenient as there may be overlapping effects for high turbulence strengths  $C_n^2$ .

For the original PSF images centroids can be estimated by

$$c_x = \frac{\sum_{xy} xPSF(x,y)}{\sum_{xy} PSF(x,y)} \quad (5.7)$$

$$c_y = \frac{\sum_{xy} yPSF(x,y)}{\sum_{xy} PSF(x,y)} \quad (5.8)$$

These centroid shifts can be easily converted in units of viewing angle:

$$c_{x/y}/\text{rad} = IFOV_{x/y}c_{x/y}/\text{sensor pixel} \quad (5.9)$$

Then they can be identified as tips/tilts and used to calculate differential tilt variances as described in section 3.2.9. The numerical differential tilt variance based on the centroid shifts can be estimated by

$$DTV_{x/y}(\Delta i_x, \Delta i_y) = \frac{\sum_{i_x, i_y, i_z} (c_{x/y}(i_x, i_y, i_z) - c_{x/y}(i_x + \Delta i_x, i_y + \Delta i_y, i_z))^2}{N} \quad (5.10)$$

$i_x$  and  $i_y$  are horizontal and vertical grid indices,  $\Delta i_x$  and  $\Delta i_y$  horizontal and vertical separations.  $i_z \in [0, N_z - 1]$  is the frame index.  $N = (N_x - |\Delta i_x|)(N_y - |\Delta i_y|)N_z$  is the number of summands. Then the index differences can be converted into physical separations

$$\Delta x = \Delta i_x \Delta q_x \quad (5.11)$$

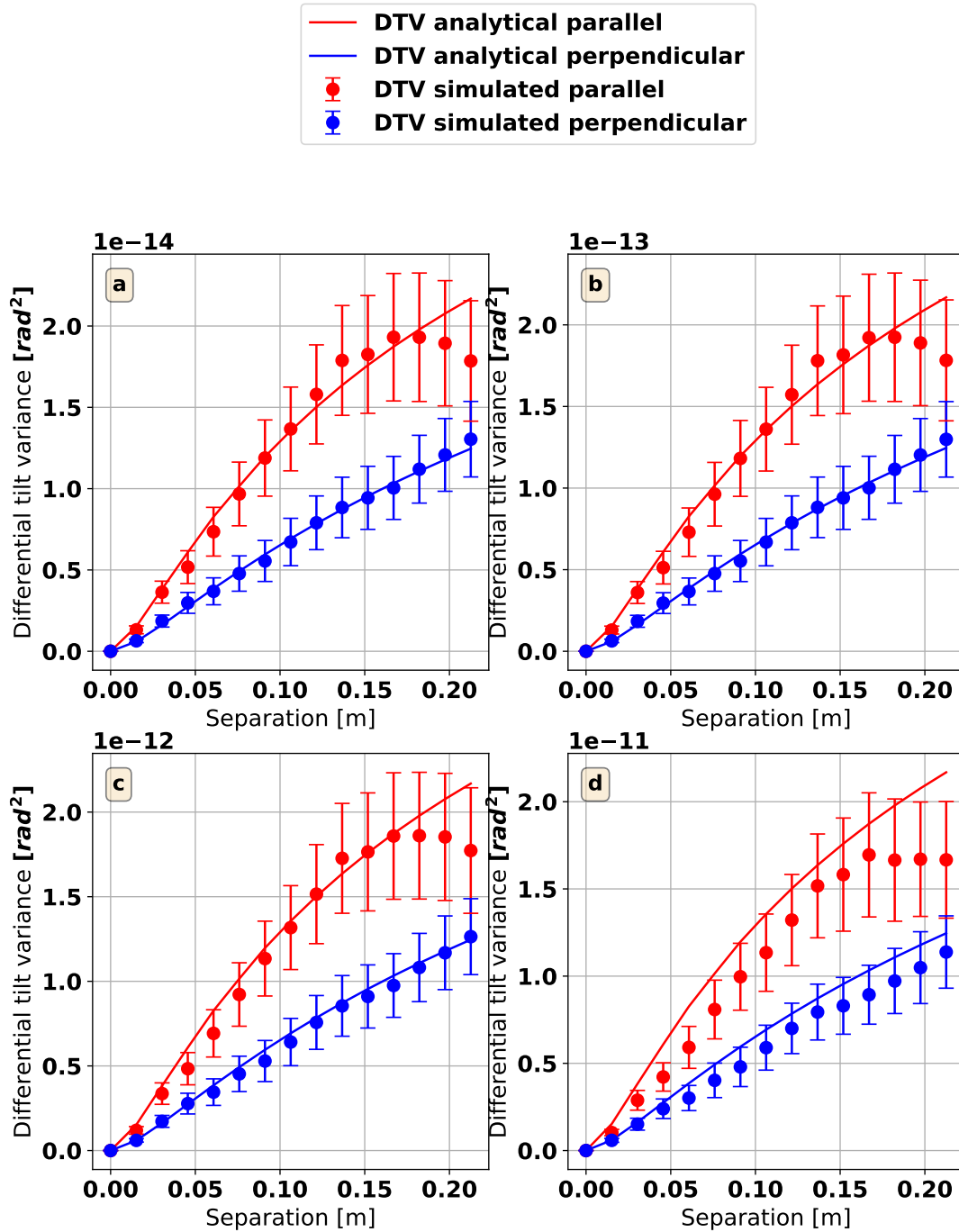
$$\Delta y = \Delta i_y \Delta q_y \quad (5.12)$$

The error on the mean DTV is estimated as

$$\sigma_{DTV_{x/y}} = \sqrt{\frac{DTV_{x/y}^2 - \overline{DTV_{x/y}}^2}{N_{ps}}}, \quad (5.13)$$

where averages are taken over  $N_{ps} = 200$  statistically independent frames. The corresponding analytical differential tilt variance is evaluated from numerical integration of equation 3.50. In figure 5.4 numerical DTVs parallel to the axis of separation  $DTV_x(\Delta x, 0)$  and vertical to the axis of separation  $DTV_y(\Delta x, 0)$  are compared with the corresponding analytical DTVs.

Figure 5.4.: Differential tilt variance (DTV) for varying turbulence strengths  $C_n^2$  and GMVKS with 95%-confidence bands: 1. Parallel:  $DTV_{V_x}(\Delta x, 0)$ , 2. Perpendicular  $DTV_{V_y}(\Delta x, 0)$ , (a)  $C_n^2 = 10^{-15} \text{ m}^{-2/3}$ , (b)  $C_n^2 = 10^{-14} \text{ m}^{-2/3}$ , (c)  $C_n^2 = 10^{-13} \text{ m}^{-2/3}$ , (d)  $C_n^2 = 10^{-12} \text{ m}^{-2/3}$ .



Obviously, numerical and analytical DTVs match well within the given uncertainty.

### 5.1.3. Validation of scintillation index

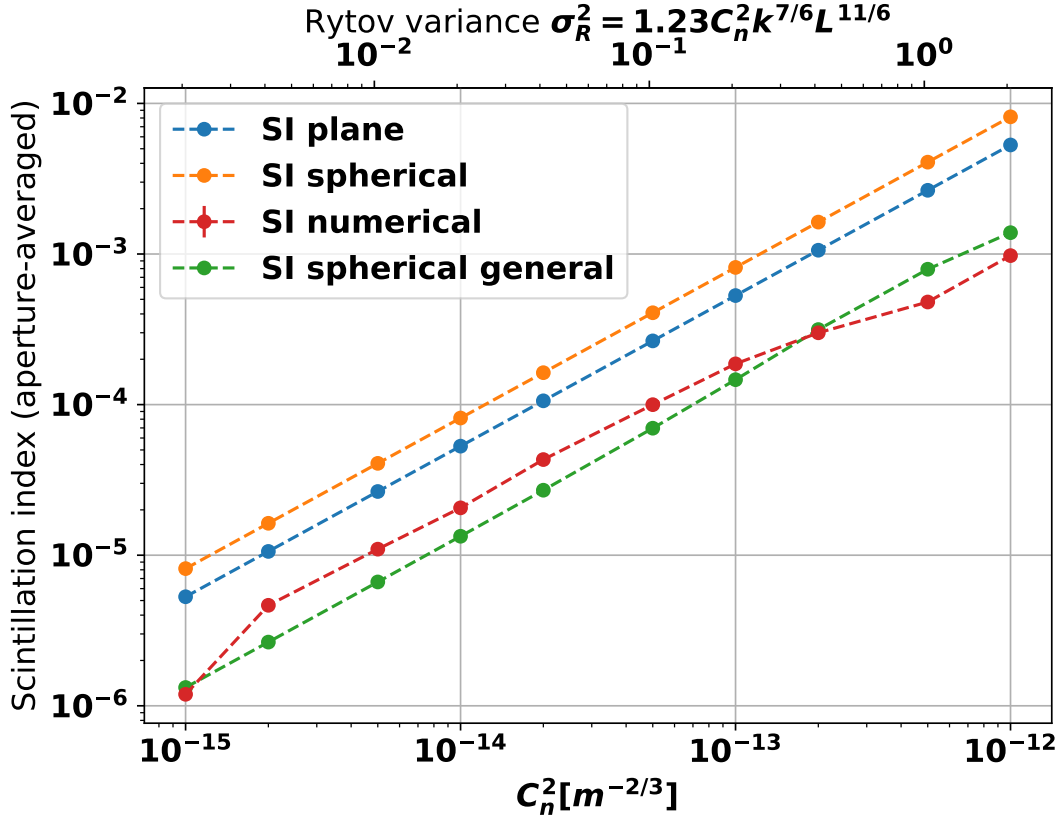
The aperture-averaged scintillation index  $\sigma_I^2(D)$  (equation 3.42) represents fluctuations of integrated irradiance. It can be numerically calculated from images of simulated PSFs based on the default configuration (table 4.1). The average power  $P_i$  for the PSF sample  $i$  can be summation over the entire PSF image:

$$P_i = \sum_{x,y} PSF_i(x,y) \quad (5.14)$$

Then the aperture-averaged scintillation index is calculated as

$$\sigma_{I,num}^2(D) = \frac{\overline{P^2}}{\overline{P}^2} - 1, \quad (5.15)$$

where averages are taken for  $N_{ps} = 200$  independent PSF samples. In figure 5.5 the sample aperture-averaged scintillation index  $\sigma_{I,num}^2(D)$  is compared to the spherical wave and plane wave aperture-averaged scintillation indices (equations 3.43 and 3.44) and the Kolmogorov aperture-averaged scintillation index (equation 3.45). Also shown is the Rytov variance  $\sigma_R^2$  indicating the corresponding fluctuation regime. The largest range of shown turbulence range lies in the weak fluctuation regime. Obviously, all aperture-averaged scintillation indices are approximately proportional to the turbulence strength  $C_n^2$  or the Rytov variance  $\sigma_R^2$  and differ only by a constant factor. This is evident, since the turbulence strength  $C_n^2$  occurs as constant factor in the integral representations of the scintillation indices. Yet this is not generally true. For strong turbulence conditions  $\sigma_R^2 \approx 2$  the aperture-averaged scintillation indices reach a maximum and even decrease for higher turbulence strengths  $C_n^2$  (Andrews and Phillips [2005]). However, for realistic levels of turbulence strength  $C_n^2 < 10^{-12} \text{ m}^{-2/3}$  (Yatcheva et al. [2015]) this domain is not reached under the specified settings.

Figure 5.5.: Aperture-averaged scintillation  $\sigma_I^2(D)$  dependent on turbulence strengths  $C_n^2$  for the turbulence spectrum GMVKS

#### 5.1.4. Validation of Strehl Ratio

Another figure of merit to validate is the Strehl ratio (equation 3.30) Here single PSFs are simulated based on the default configuration, but for different turbulence strengths  $C_n^2$ . Then the numerical Strehl ratio is calculated as

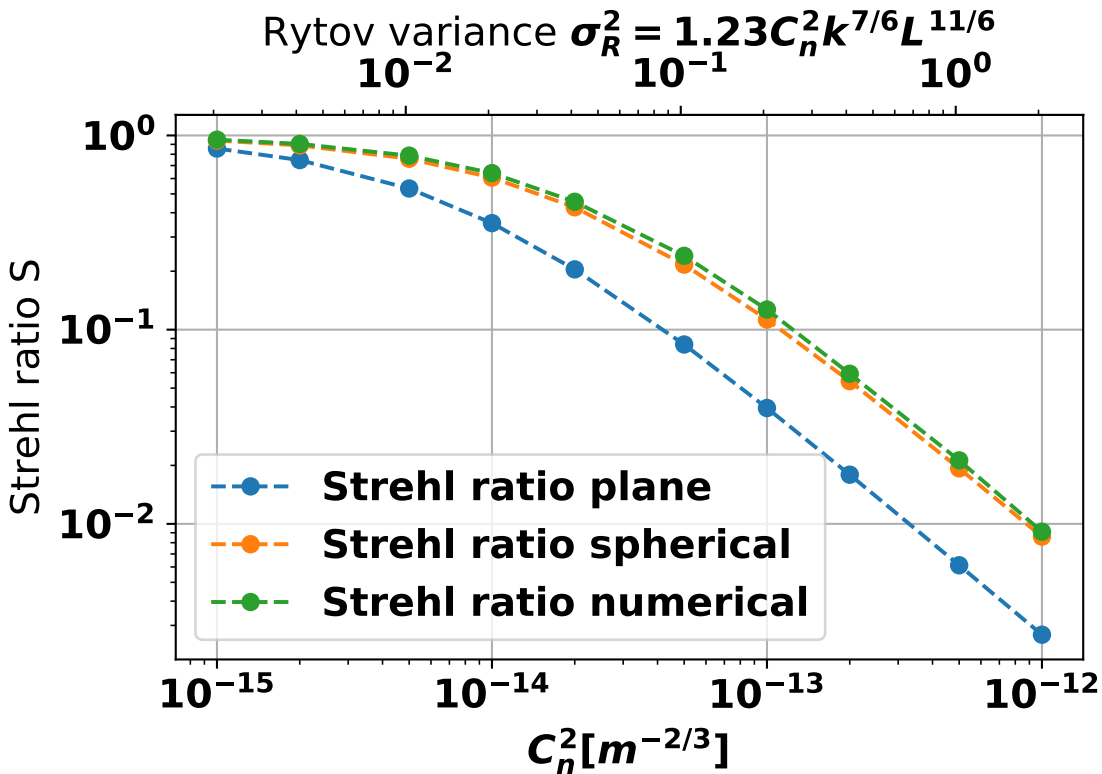
$$SR_{num} = \frac{\max_{xy}(PSF_{turb}(x,y))}{\max_{xy}(PSF_0(x,y))}, \quad (5.16)$$

with a long-exposure  $PSF_{turb}(x,y)$  for a certain turbulence strength  $C_n^2$  and  $PSF_0(x,y)$  for no turbulence. As the number of samples  $N_{ps}$  increases, maxima and center values of the numerical long-exposure PSFs converge to each other, as the theoretical long-exposure PSF is radially symmetric. Here again  $N_{ps} = 200$  is used.

In figure 5.6 the Strehl ratio is shown for different turbulence strengths  $C_n^2$ . It is compared to the analytical Strehl ratio (equation 3.30) by using the spherical wave and plane wave fried parameters  $r_0$  (equations 3.28 and 3.27). As expected the numerical Strehl ratio and the spherical wave Strehl ratio match well,

there are only slight differences for increasing turbulence strength  $C_n^2$ . The plane wave Strehl ratio is lower than the spherical wave Strehl ratio. This is related to the fact that a PSF is the Fourier transform of an MTF and a more sloping plane wave long-exposure MTF leads to a broader PSF with a lower maximum or center value. The Rytov variance  $\sigma_R^2$  (equation 3.37) indicates, that the shown range of turbulence strengths  $C_n^2$  is mainly in the regime of weak fluctuation.

Figure 5.6.: Strehl ratio  $S$  dependent on turbulence strength  $C_n^2$  for the turbulence spectrum GMVKS



## 5.2. Correlated 2D phase screens

The same validation procedures as for uncorrelated 2D phase screens were applied for PSFs based on phase screens generated by the sparse spectrum (SS) method (section 5.1). Sample figures of merit are calculated in the same manner as for uncorrelated phase screens. Again  $N_{ps} = 200$  statistically independent stacks of phase screens are calculated and simulations done on the default configuration 4.1. General analytic expressions for these figures of merit do not yet exist for 3D correlated phase noise. Hence sample results are compared with the same analytical expressions for uncorrelated 2D noise used in section 5.1.

### 5.2.1. Validation of modulation transfer function

In figures 5.7 and 5.8 long-exposure and short-exposure modulation transfer functions (MTFs) based on phase screens generated by the sparse spectrum method are shown. Sample MTFs for varying turbulence strength  $C_n^2$  are compared to the theoretical Fried MTFs (equations 3.56 and 3.57) as well as the spherical and plane MTF (equation 3.72). Sample MTFs and analytical MTFs match well except for the short-exposure MTF at highest turbulence strength  $C_n^2 = 10^{-13} \text{ m}^{-2/3}$ . This deviation could be due to undersampling of high frequencies in the SS phase screens which are not cancelled out by centroid shifting.

Figure 5.7.: Long-exposure MTF for varying turbulence strengths  $C_n^2$  and GMVKS: (a)  $C_n^2 = 10^{-16} \text{ m}^{-2/3}$ , (b)  $C_n^2 = 10^{-15} \text{ m}^{-2/3}$ , (c)  $C_n^2 = 10^{-14} \text{ m}^{-2/3}$ , (d)  $C_n^2 = 10^{-13} \text{ m}^{-2/3}$ .

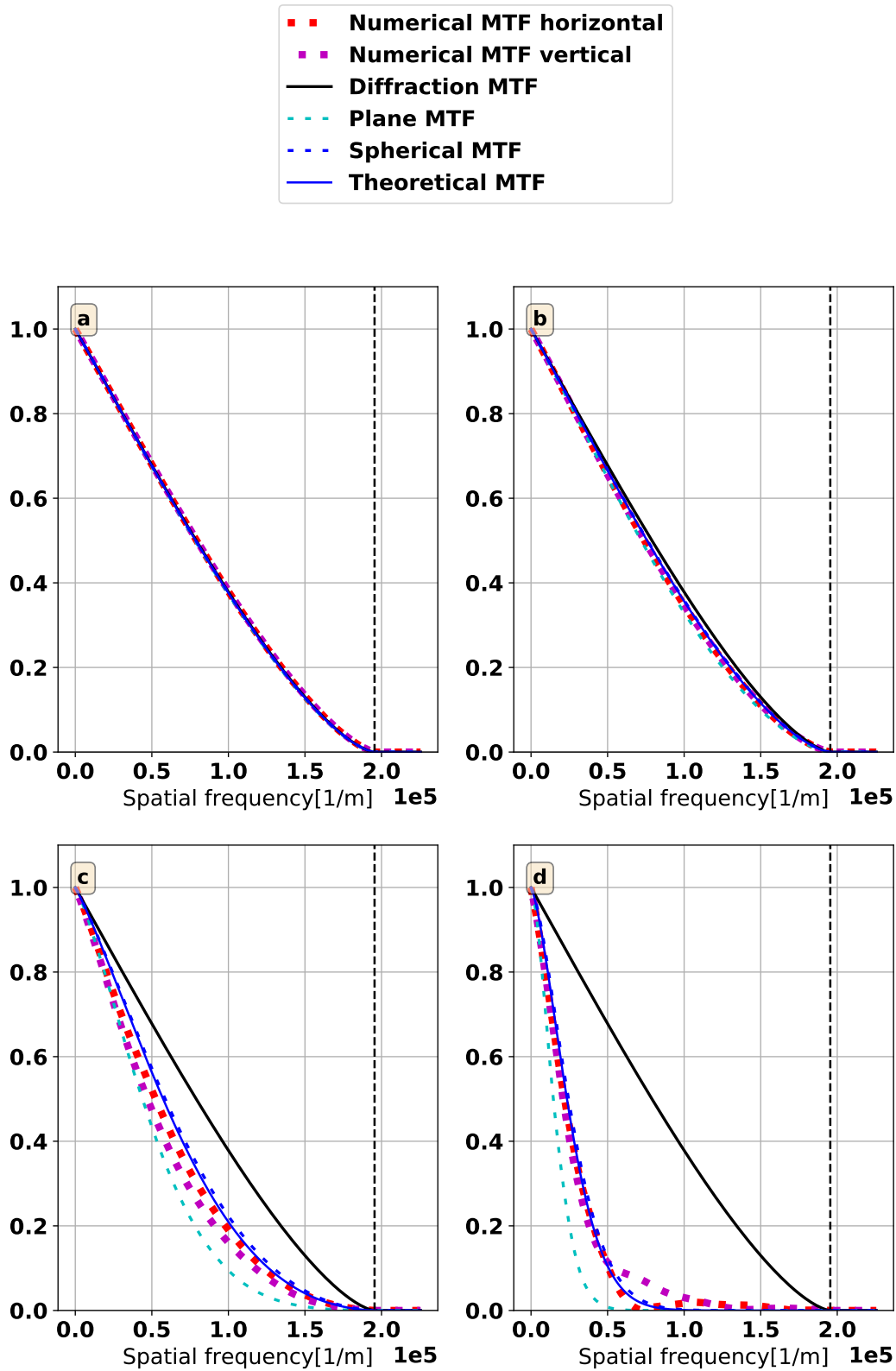
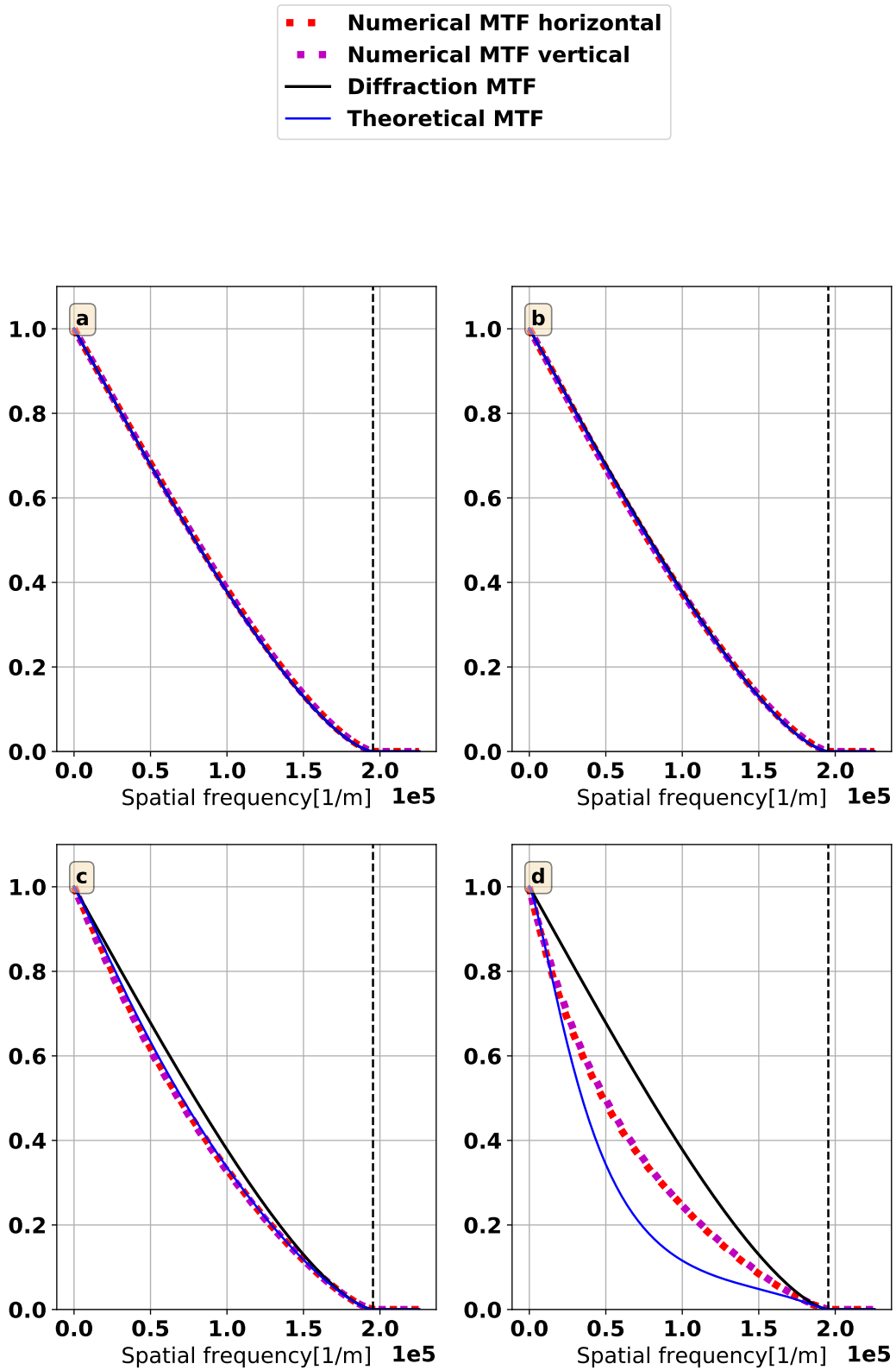


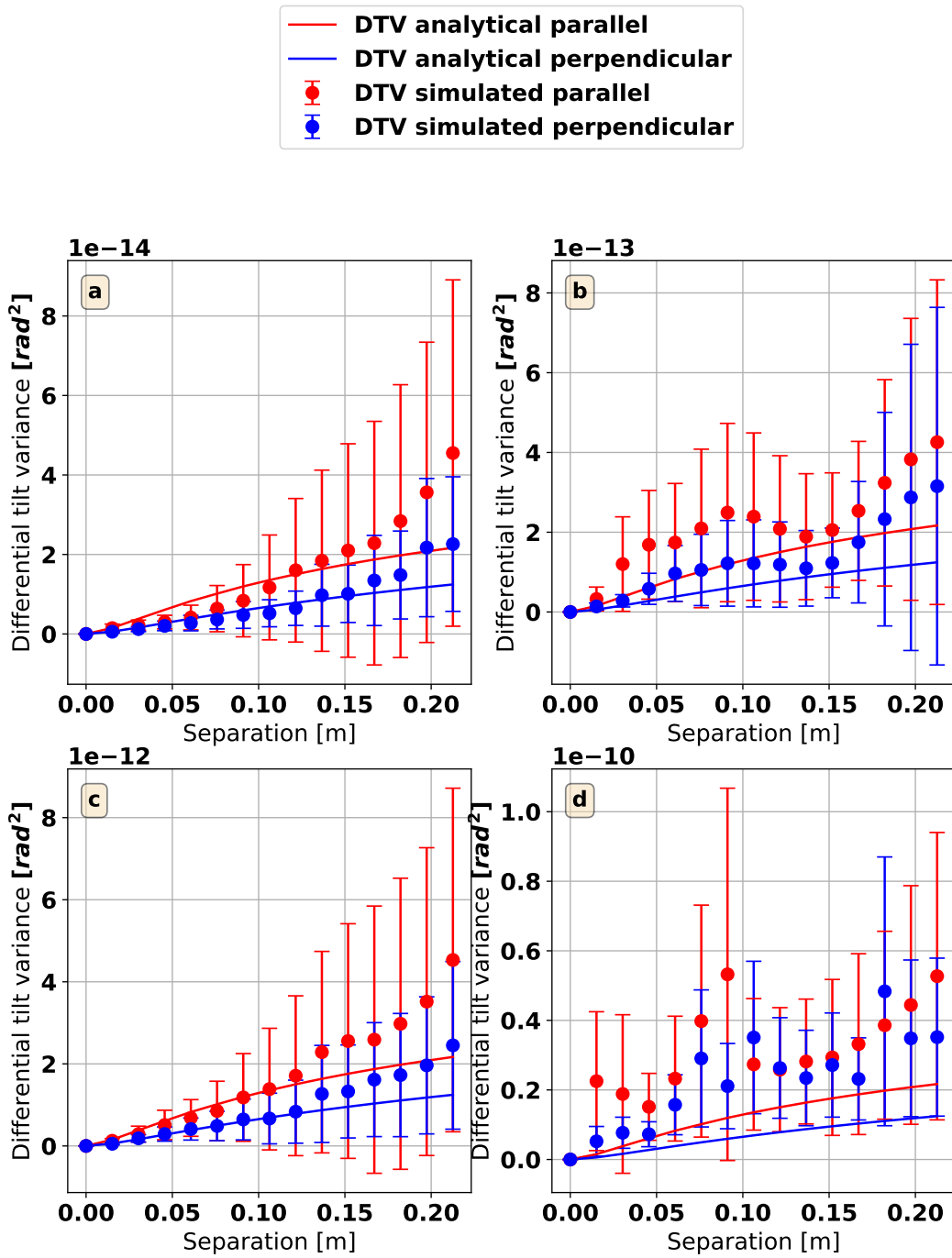
Figure 5.8.: Short-exposure MTF for varying turbulence strengths  $C_n^2$  and GMVKS: (a)  $C_n^2 = 10^{-16} \text{m}^{-2/3}$ , (b)  $C_n^2 = 10^{-15} \text{m}^{-2/3}$ , (c)  $C_n^2 = 10^{-14} \text{m}^{-2/3}$ , (d)  $C_n^2 = 10^{-13} \text{m}^{-2/3}$ .



### 5.2.2. Validation of differential tilt variance

For  $N_{ps} = 200$  samples of  $15 \times 15$  PSF grids based on SS phase screens with  $N_{waves} = 1024$  DTV (equation 5.10) can be calculated. This is shown in figure 5.9. Compared to the case of uncorrelated phase screens (figure 5.4) uncertainties of the sample DTV values are high. A reason for this could be under-sampling due to the low number of plane waves  $N_{waves} = 1024$  compared to the number of sinusoids in the FFT method with subharmonics  $N_{uncorrelated} = N_{FFT} + N_{subharmonics}$ , where  $N_{FFT} = 2048 \times 2048$  and  $N_{subharmonics} = 80$ . This hypothesis is supported by the observation of single significant plane waves in the generated SS phase screens (figure 4.12). Plane waves with strong alignment with the axis of propagation (high  $s_n$  in equation 4.67) are highly degraded and hence increase the relative sample variances of the summed remaining plane waves. Nevertheless, sample DTV values scale with increasing turbulence strength  $C_n^2$ .

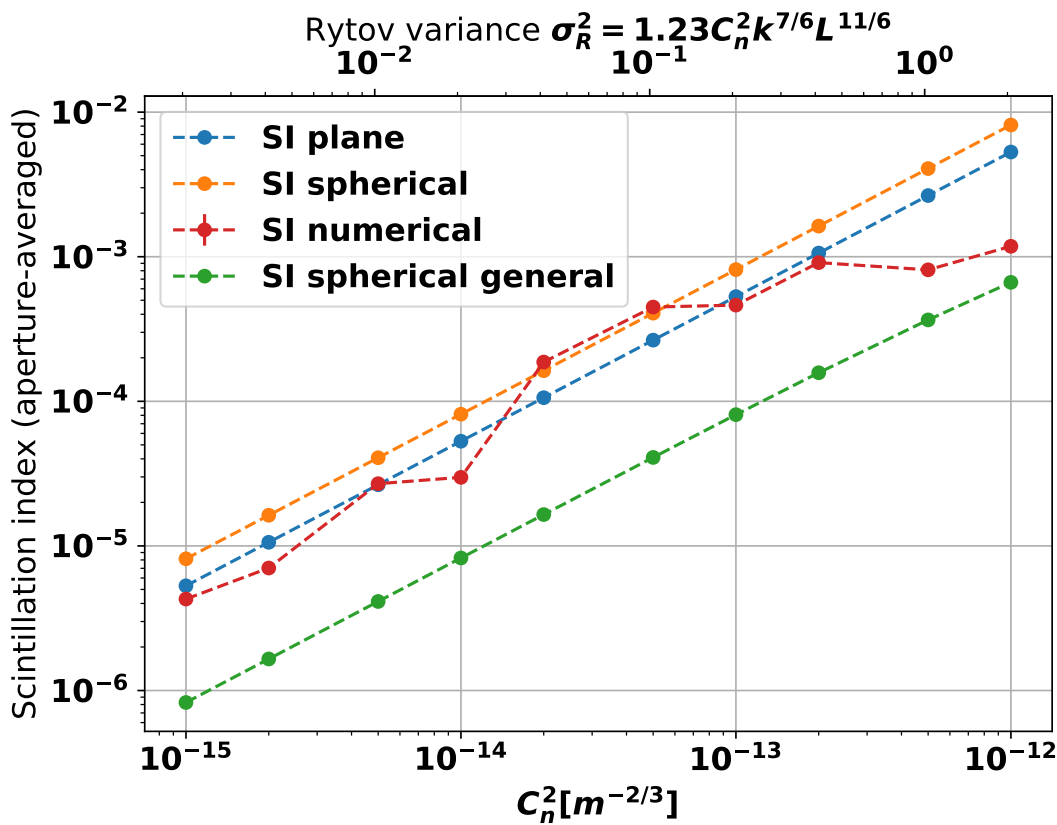
Figure 5.9.: Differential tilt variance (DTV) for varying turbulence strengths  $C_n^2$  and GMVKS: (a)  $C_n^2 = 10^{-15} \text{ m}^{-2/3}$ , (b)  $C_n^2 = 10^{-14} \text{ m}^{-2/3}$ , (c)  $C_n^2 = 10^{-13} \text{ m}^{-2/3}$ , (d)  $C_n^2 = 10^{-12} \text{ m}^{-2/3}$ .



### 5.2.3. Validation of scintillation index

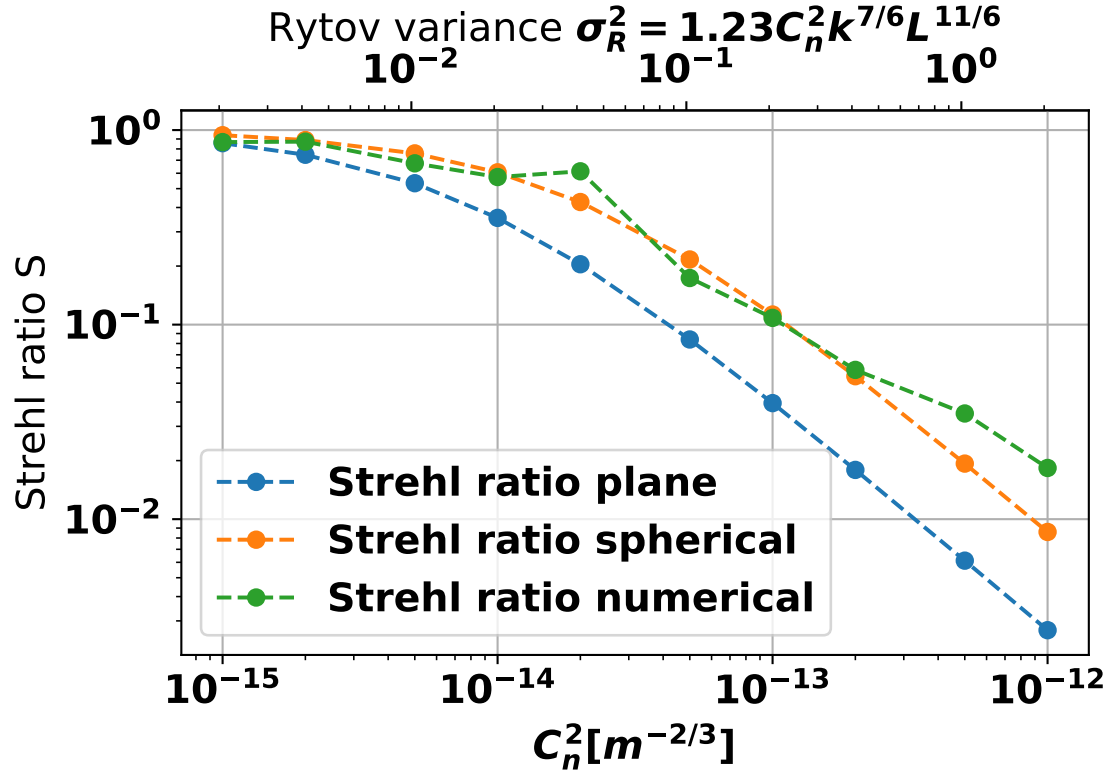
Simulations based on SS phase screens for varying turbulence strengths  $C_n^2$  show the linear relationship of aperture-averaged sample scintillation indices and corresponding analytical expressions (equations 3.45, 3.44 and 3.43). Compared to sample scintillation index (SI) values for uncorrelated 2D phase screens (figure 5.5) the sample SI values in figure 5.10 are a factor about 4 higher and reveal more fluctuations. The increased SI values may be attributed to the stronger influence of individual plane waves in the SS phase screens. similar to DTV.

Figure 5.10: Aperture-averaged scintillation index dependent on turbulence strengths  $c_n^2$  for the turbulence spectrum GMVKS



### 5.2.4. Validation of Strehl ratio

Simulations are done based on correlated SS phase screens for varying turbulence strengths  $C_n^2$  to compare sample Strehl ratios (SR) to the corresponding analytical expression (equation 3.30). Besides higher fluctuations compared to the case of uncorrelated phase screens (figure 5.11) the sample SR values fit well with the analytical spherical SR values.

Figure 5.11.: Strehl ratio dependent on turbulence strengths  $c_n^2$  for the turbulence spectrum GMVKS

### 5.3. Implementation and benchmarks

Besides accuracy of simulation, computation time is also a crucial factor for possibly large sample sizes and statistically robust simulations. The generation of phase screens using multiple FFTs or superposition of multiple plane waves used for the sparse spectrum (SS) method can highly benefit from the parallel computation capabilities of GPUs. The same applies for the entire split-step beam propagation. For this reason C++ libraries are developed, which use the CUDA framework from NVIDIA. In table 5.1 benchmark results are shown for a GTX 1080 Ti for the generation of 2048x2048 SS phase screens depending on the number of plane waves  $N_{waves}$ . Compared to the superposition of plane waves durations for weight and wave vector initialization are neglectable. In figure 5.2 durations for the split-step simulation with 2D uncorrelated phase screens are shown. Obviously the generation of SS phase screens is the bottleneck in the simulation for  $N_{waves} > 128$ , so benefits of the SS method must justify the additional costs. In the previous sections based on the chosen simulation parameters the FFT method with subharmonics shows better compliance with theoretical results than the SS method with  $N_{waves} = 1024$ . So if the Markov assumption  $\Delta z \ll L_0$  is not violated, the FFT method can be preferred. For a PSF grid

Table 5.1.: Computation times of the generation of 10 SS phase screens with 2048x2048 pixels on a GTX 1080 Ti depending on number of waves  $N_{waves}$

$N_{waves}$	Duration in ms
128	$121 \pm 130$
256	$240 \pm 40$
1024	$1039 \pm 4$
4096	$6110 \pm 30$

Table 5.2.: Other durations for 2D uncorrelated phase screens and simulation on a GTX 1080 Ti

Method	Computation time in ms
Generation of 10 phase screens (ps) (2048x2048)	$75 \pm 4$
Single Propagation with 10 ps (512x512)	$10 \pm 1$
PSF calculation (512x512)	$10 \pm 40$

the number of required single propagations and PSF calculations scale with the number of PSFs. A good speedup can be achieved by batch processing of multiple propagations and PSF calculations, although this approach is limited by GPU memory. In this thesis extended  $2048 \times 2048$  phase screens are generated for both approaches to use common modules for sub sampling on these phase screens. However, it has to be considered that the SS method can extend phase screens arbitrarily in contrast to the FFT method by sampling sinusoids at different spatial coordinates. A monolithic software design with phase screens as large as the  $512 \times 512$  computational field could perform better, if a low PSF grid size is needed.

#### 5.4. Comparison: Inverse Fourier method with subharmonics versus sparse spectrum (SS) method

Both investigated methods for phase screen generation, the Inverse fast Fourier transform (IFFT) method with addition of subharmonics described in section 5.1 and the SS method described in section 5.2 show good agreement to theoretical expressions in terms of long-exposure and short-exposure MTFs. This can be seen in figures 5.1 and 5.2 for the IFFT method and figures 5.7 and 5.8 for the SS method. Within 95%-confidence bands, the differential tilt variance (DTV) also shows good accordance to theoretical expressions for different turbulence strengths  $C_n^2$  (figure 5.4 versus figure 5.9). However, the SS method shows significantly higher statistical fluctuations compared to the IFFT method. Similarly, for the SS method, there are higher fluctuations around the theoretical values for the aperture-averaged scintillation index (figure 5.5 versus figure 5.10) and the Strehl ratio (5.6 versus 5.11). One reason for this could be the sparsity of spectrum, i.e. the much lower number of sinusoids (1024) in the SS method compared to the dense equidistant grid of sinusoids for the IFFT method (2048x2048) along with the  $N_{levels}N_{SH}$

subharmonics with the number of subharmonic recursions  $N_{levels} = 10$  and the number of subharmonics per recursion  $N_{SH} = 3 \times 3 - 1 = 8$ .

Hence, the IFFT method seems to be preferable for simulations of perturbed point grids which are suitable for validation of experimental data in terms of long-exposure and short-exposure MTFs as well as DTV. While the SS method has the intrinsic ability to extend phase screens by shifting spatial coordinates, for the IFFT method, spatial and temporal translations of phase screens, e.g. for investigation of wind effects, are possible by techniques for phase screen extension based on covariance with border values (Assémat et al. [2006]). The translation of phase screens (Taylor frozen turbulence) is a common way of modeling temporal variations of air refractive index (Andrews and Phillips [2005]), if wind effects are the dominant source of these variations. However, the investigation of wind effects by translation of phase screens are not within the scope of this work, since temporal correlation of derived figures of merit are often unknown in terms of theoretical expressions. Aggravatingly, there may be strong spatial and temporal variations of wind direction and strength along the optical path in an experiment, leading to lots of scenarios to be simulated. For all these reasons, only the IFFT method is used for the following experimental validation of the turbulence simulation. The experimental settings are chosen so that temporal correlation of measured figures of merit can approximately be neglected.



## 6. Evaluation of observed degraded images

### 6.1. Experimental acquisition of turbulence degraded imagery

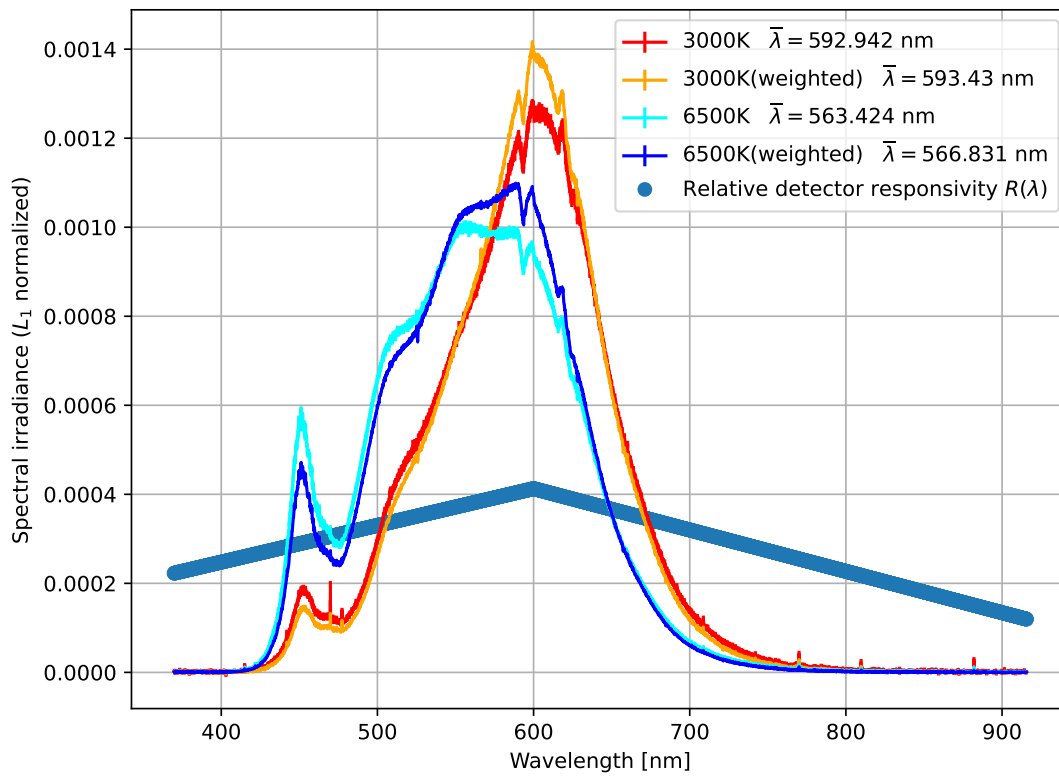
For validation of simulated point spread functions (PSFs), field measurements were done on multiple days in a nature reserve. As target two LED mini-matrices were used, each with 28x18 LEDs and dimensions of 42cm x 27cm. The lefthand LED mini-matrix was at a color temperature of  $T = 6500$  K, while the righthand LED mini-matrix was at a color temperature of  $T = 3000$  K. For simplified power supply they were soldered together at the shorter side in the vertical direction. An uninterruptible power supply (UPS) with an AC voltage  $U = 230$  V was used. Due to technical specifications of the LED matrices and to increase operating time limited by the UPS capacity, a lab power supply with current limiter was used to provide the LED matrices with a DC voltage  $U = 24$  V and a current  $I = 4$  A. The LED matrices were mounted on a tripod at a height of 2m above ground. Devices for data acquisition were mounted on a wooden plate about 10cm above ground. Each day of measurement they were placed approximately 150m from the target. These devices are a monochrome telescope camera ZWO ASI290MM Mono with a telezoom objective Wallimex Pro 650 mm-1300 mm, which is connected to a laptop via USB3. An impeller anemometer Holdpeak HP-886A is placed next to the objective in transversal direction, i.e. perpendicular to the line of sight. It is also connected to the laptop via USB and can measure temperature, relative humidity and wind speed with one readout per second. An overview of the device specifications is given in table 6.1. The experimental scene is shown in figure 6.2. The main advantage of an active LED array target over passive targets is a relatively constant bright illumination leading to very good signal-to-noise ratios in the acquired camera data. Brightness drifts due to sun and cloud movements are significantly reduced.

Two color temperatures,  $T = 6500$  K (blue) and  $T = 3000$  K (orange) are used in order to check for differences in the point profiles or corresponding MTFs for varying average wavelengths. For determining average wavelengths, spectrometer measurements were made. These measurements are shown in figure 6.1. Also shown are the  $L_1$ -normalized spectral irradiances weighted by relative responsivity of the used camera sensor.

The relative responsivity  $R(\lambda)$  of the camera sensor "ASI 290MM mono" can be approximated by

$$R(\lambda/\text{nm}) = \begin{cases} \lambda/\text{nm} < 600 & 1 - \frac{0.4}{200}(600 - \lambda/\text{nm}) \\ else & 1 - \frac{0.9}{400}(\lambda/\text{nm} - 600) \end{cases} \quad (6.1)$$

Figure 6.1.: Luminix LED spectrum measured by QWave spectrometer and weighted by ASICAM 290MM Mono spectral responsivity



For the telezoom objective an optical transmittance of unity is assumed over the shown spectral range. To clarify the differences for strong and weak turbulence conditions in terms of spatial fluctuations, two recorded example images are shown in figure 6.3, one for a summer day at 8/22/2020 and  $T = 30^{\circ}\text{C}$  and another for a winter day at 12/18/2020 and  $T = 6^{\circ}\text{C}$ .

Table 6.1.: Device specifications

Camera	ZWO ASI290MM Mono Sensor: 1/2.8" Monochrome CMOS Bit depth: 14bit Resolution: 2.13 Megapixels Diagonal: 6.46 mm Image Array: 1936x1096 Pixel Size: 2.9um Max Frame Rate at Full Resolution: 170 FPS
Objective	Wallimex Pro Focal length: 650 mm-1300 mm Aperture diameter: 8.6 cm
Target	Two Lumitronix LED mini-matrices (soldered) LED elements: 28 (horizontal) x 18 (vertical) each Dimensions: 42cm (horizontal) x 27 cm (vertical) each Color temperatures: $T = 6500\text{ K}$ (left hand), $= 3000\text{ K}$ (right hand) Average wavelengths: $\bar{\lambda}_{blue} = 567\text{ nm}$ (left hand), $\bar{\lambda}_{orange} = 593\text{ nm}$ (right hand)
Anemometer	Holdpeak HP-866A Accuracies: Wind: $\pm 2\% \pm 0.5\text{ m/s}$ Temperature: $\pm 1.5^{\circ}\text{C}$ Relative humidity: $\pm 3\%$

## 6. Evaluation of observed degraded images

---

Figure 6.2.: Experimental scene at 48°59'55"N 8°17'05"E: A telezoom objective Wallimex Pro 650 mm-1300 mm is plugged to a monochrome telescope camera ZWO ASI290MM. For data acquisition the camera is connected to a laptop via USB3. The camera is pointing to a target of 56x18 LEDs in about 150 m

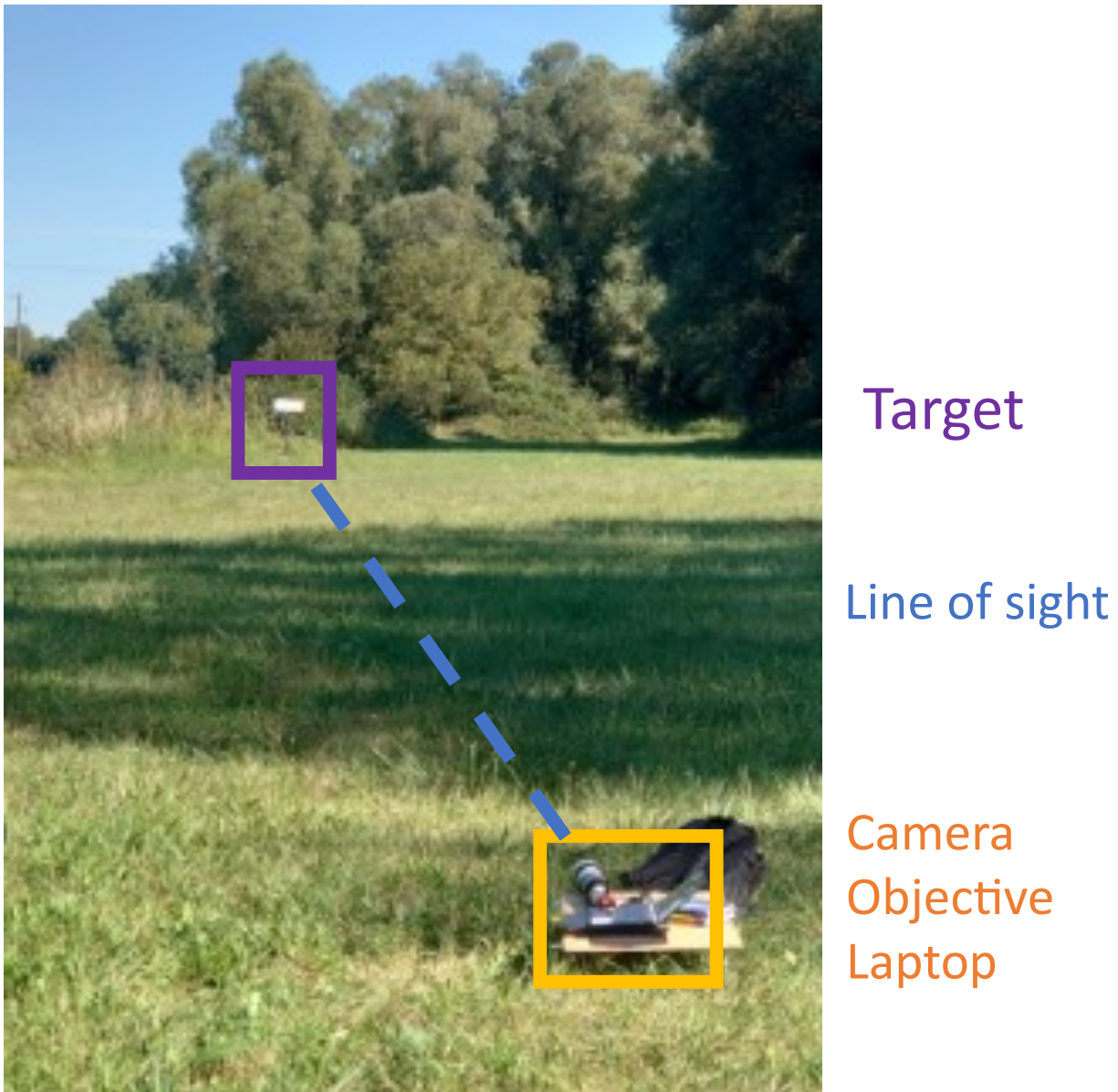
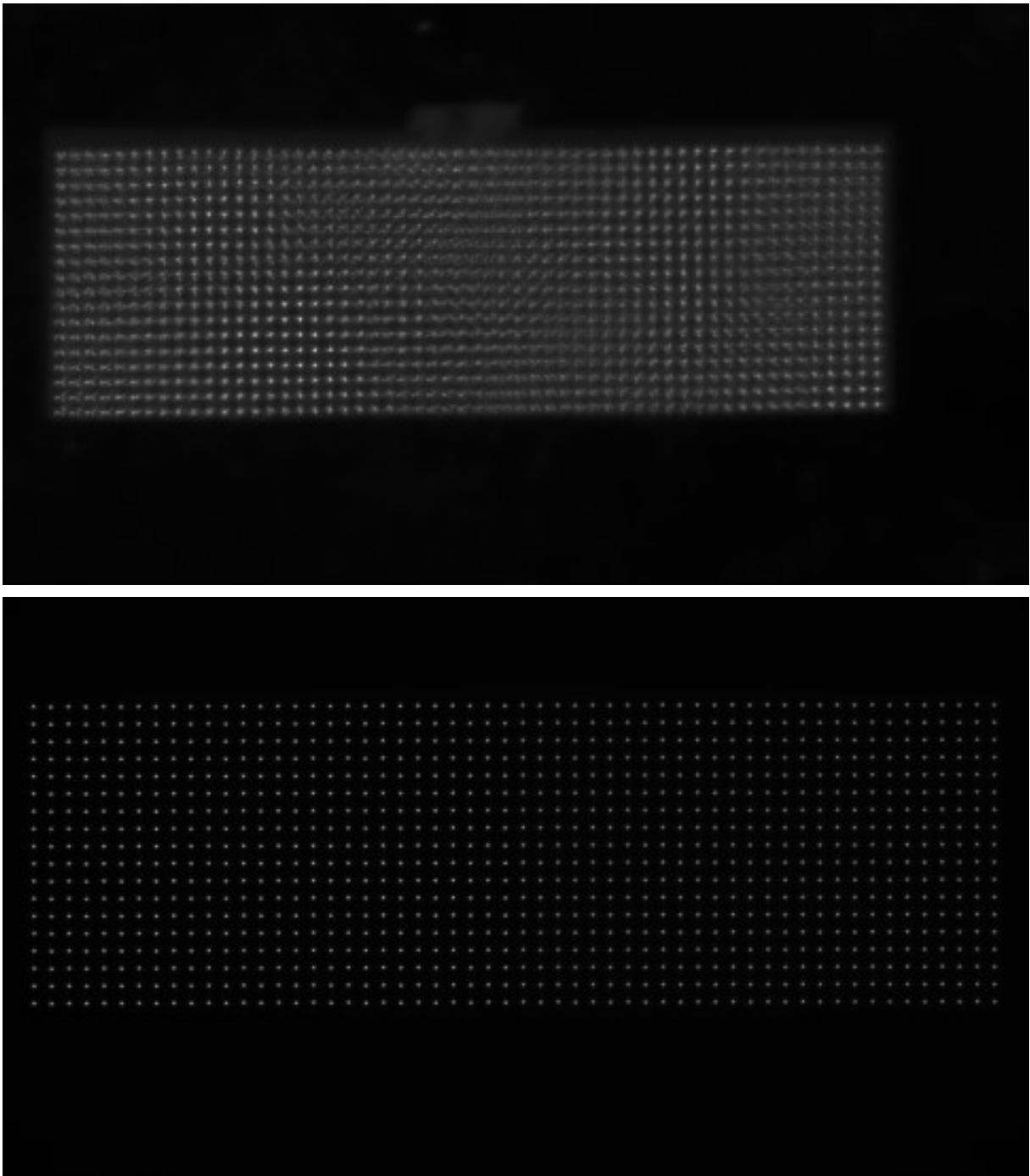


Figure 6.3.: Example images of the  $(2*28)*18$  LED target degraded by air turbulence at ground: 1. Warm summer day at 8/22/2020 (Top) at  $30^{\circ}$  C, 2. Cold winter day 12/18/2020 at  $6^{\circ}$  C(Bottom)



### 6.1.1. Experimental settings

Measurements with the LED grid are made on several days in 2020 and 2021. As no continuous power supply was available for the LED grid, recording time was limited to about 1 hour each day by use an uninterruptible power supply. The integration time was chosen such that the signals for single LEDs

are not saturated and the distribution of camera pixel values covers about half of the grayscale range. It ranges between the minimal integration time  $t_{min} = 32 \mu s$  and  $t_{max} = 100 \mu s$ . A short integration time is also important to prevent motion blur caused by temporal fluctuations caused by turbulence. 16 bit raw monochrome video sequences are captured with a nominal frame rate of 8 Hz. A fixed focal length of  $fl = 0.8m$  is used. A varying number of sequences  $N_{seq}$  was recorded for different days due to limited battery capacity for the LED matrix and different time requirements for experimental setup.

Table 6.2.: Record information about captured video sequences

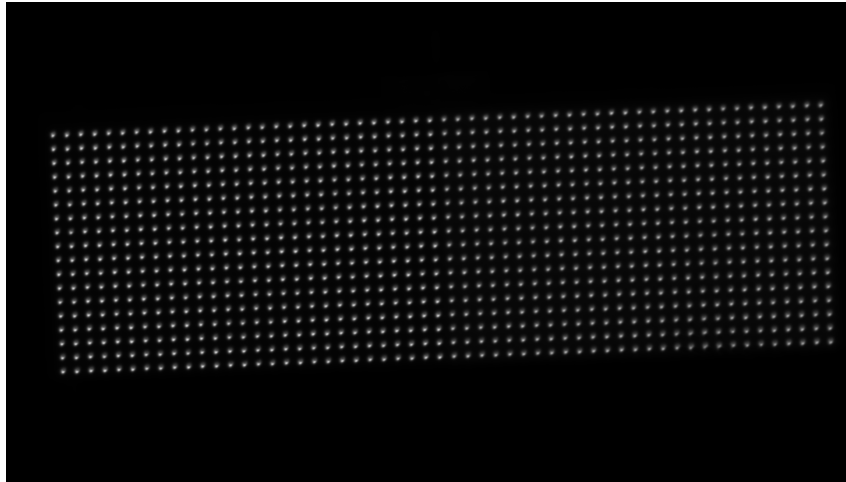
Date	Day time	Range $L$ in m	Temperature in °C	Humidity in %	$N_{seq}$
2020/08/22	16:55 - 17:47	$149.4 \pm 0.5$	24.7 - 30.3	36.8 - 62.6	129
2020/08/26	18:22 - 18:28	$115.7 \pm 0.1$	22.3 - 28.4	28.3 - 44.6	15
2020/09/08	11:35 - 12:23	$105.7 \pm 0.8$	19.4 - 23.3	42.8 - 64.3	143
2020/09/11	18:33 - 19:00	$91.3 \pm 0.3$	19.7 - 22.5	60.7 - 70.9	73
2020/09/15	17:45 - 18:11	$107.9 \pm 0.2$	23.3 - 35.7	38.5 - 64.1	89
2020/11/06	13:45 - 14:09	$109.4 \pm 0.9$	9.9 - 11.5	49.3 - 55.2	56
2020/11/07/1	09:04 - 09:57	$107.1 \pm 0.1$	2.7 - 5.3	70.7 - 79.7	102
2020/11/07/2	16:12 - 16:57	$131.6 \pm 0.2$	5.2 - 8.7	65.7 - 72.6	110
2020/11/09	16:05 - 16:40	$131.7 \pm 0.4$	8.3 - 11.4	68.4 - 76.9	106
2020/12/18	15:47 - 16:06	$127.2 \pm 0.1$	3.1 - 5.9	74.6 - 80.7	56
2020/12/26	16:37 - 16:59	$154.0 \pm 0.2$	0.9 - 3.3	71.0 - 75.1	54
2021/03/06	16:29 - 17:18	$170.2 \pm 1.3$	4.0 - 7.5	32.9 - 46.9	90
2021/03/08	09:58 - 11:07	$182.1 \pm 1.9$	0.9 - 4.9	50.7 - 64.1	201

### 6.1.2. Image evaluation on regions of interest

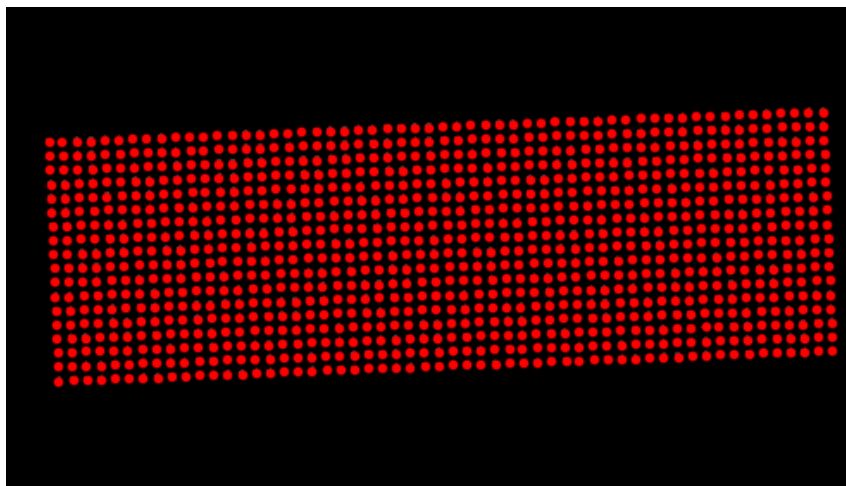
Acquired camera data of LED grid projections can be evaluated by manually setting regions of interest (ROIs) with single centered LEDs. However, this approach can be very tedious if there is a large amount of data or different positions of the grid in the field of view for different recording dates. A more convenient way is to automatically calculate a grid of ROIs based on time-averages of video sequences. Then local maxima can be determined by peak detection. Each local maxima can represent the center of a square ROI. This procedure is shown in figure 6.4. A unique ROI size of 28x28 is chosen for all recording dates, so that adjacent ROIs do not overlap. For strong centroid shifts the LED profiles might be cutoff by the finite ROI size. This leads to a bias of the estimated centroids. In order to prevent this, the ROI position is iteratively adapted per captured frame by centering on estimated centroid positions until the ROI positions do not change anymore or have converged.

Figure 6.4.: Calculation of ROIs

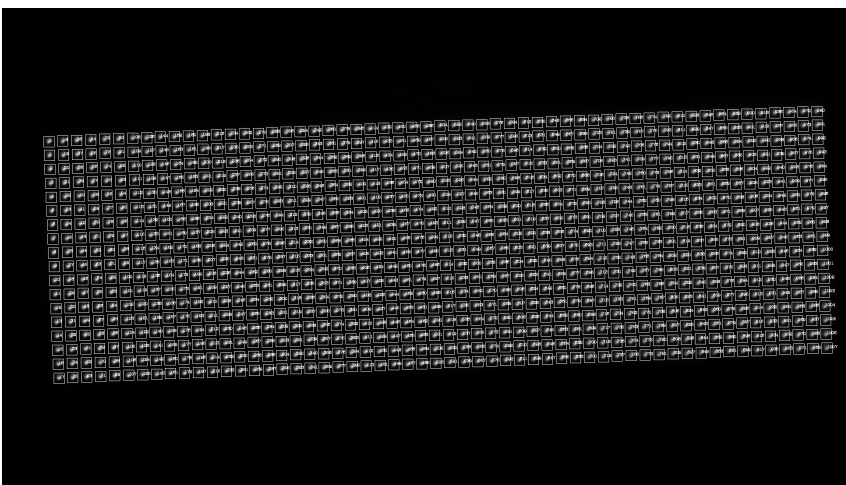
(a) A video sequence is time-averaged



(b) Local maxima are determined by peak detection.



(c) A region of interest with centered local maximum is formed for all local maxima



As the used camera objective has an adjustable focal length between  $fl = 650$  mm and  $fl = 1300$  mm, the objective tube to which the camera sensor is attached is freely rotatable. This makes it necessary to manually adjust the alignment between the axes of the LED grid and the axes of the camera sensor for each trial setup on different recording dates. However, the misalignment angle can be determined as the angle between the connecting line of two corner maxima and the horizontal axis.

### 6.1.3. Calculation of LED footprint MTF

For evaluation of deviations between experimental and simulated long-exposure and short-exposure MTFs, it is crucial to take the blur due to the extended LED footprint into account. For this purpose, close captures of some LEDs with a Tamron objective in a distance of  $R \sim 1$  m were made, where air turbulence can be neglected. The physical length per pixel  $l_{pixel}$  in the object plane can be found by calculating image centroids for adjacent LEDs  $\mathbf{c}_1$  and  $\mathbf{c}_2$  and using the physical separation  $c = 0.41/27$  m from the target specifications:

$$l_{pixel} = \frac{c}{|\mathbf{c}_1 - \mathbf{c}_2|}. \quad (6.2)$$

Then the sampling frequency in the object plane is given as

$$f_{S,object} = \frac{1}{l_{pixel}} \quad (6.3)$$

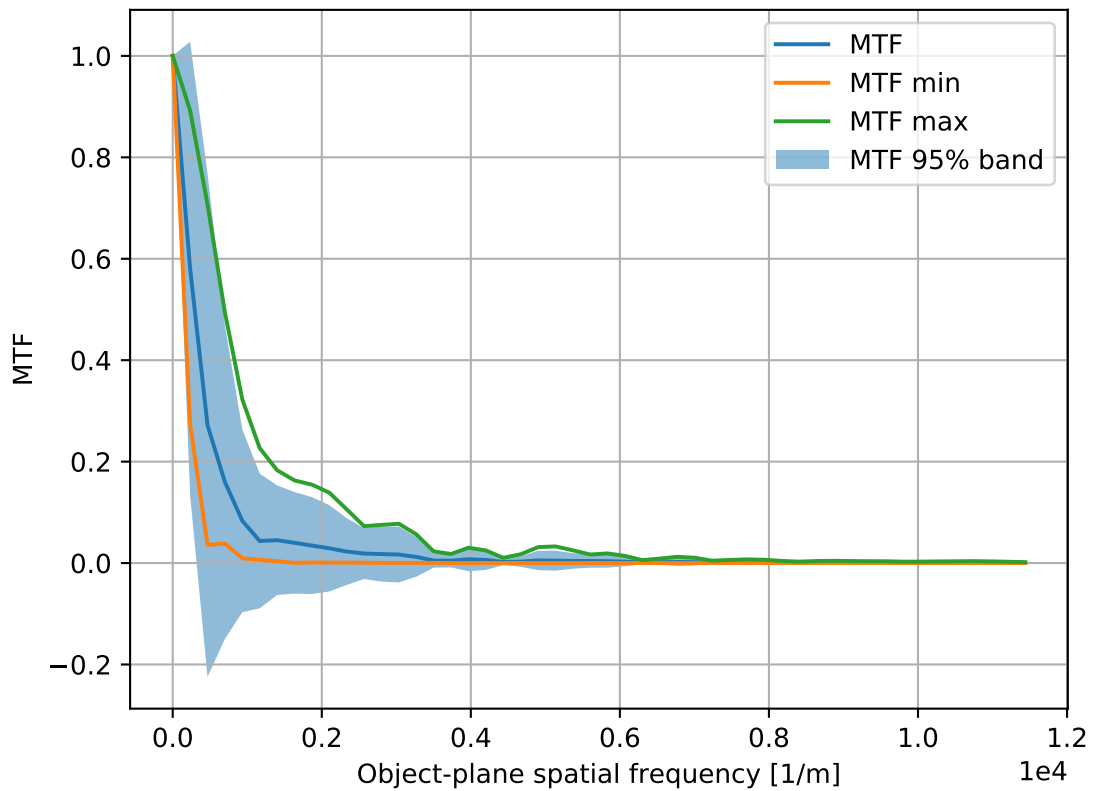
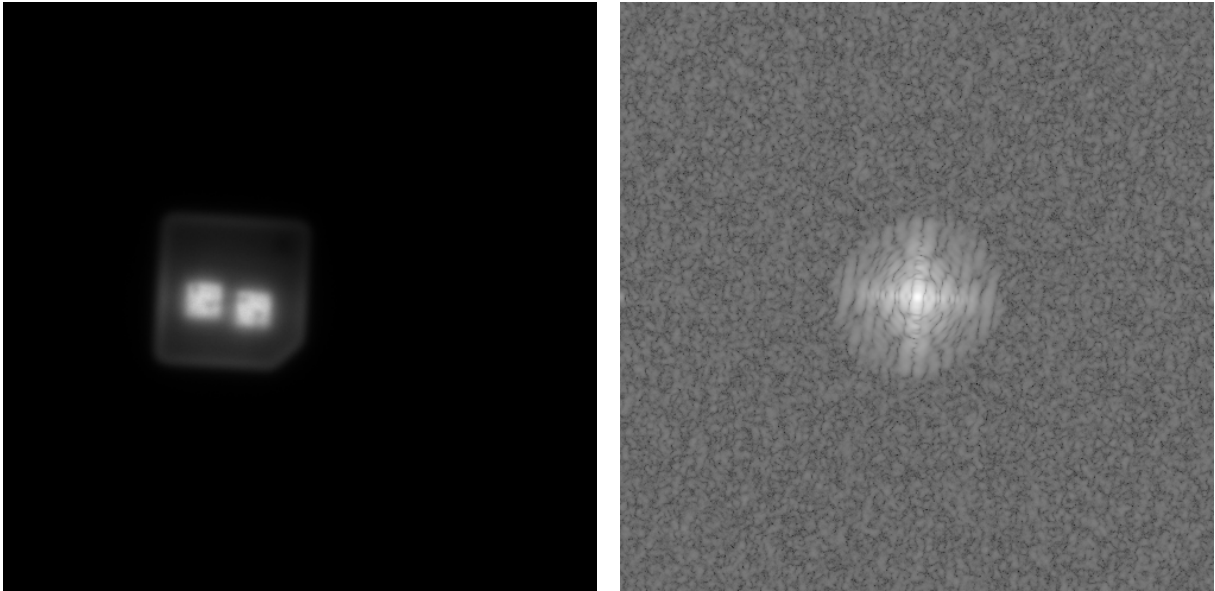
For analyzing a single LED footprint a square image section  $M \times M$  containing one LED is cropped. Then the 2D FFT is calculated of this image crop. The minimal frequency step along the horizontal and vertical axis is hence

$$\Delta f_{object} = \frac{f_{S,object}}{M}. \quad (6.4)$$

During the experiments some misalignment between the LED grid and the camera field of view is unavoidable. For estimating best-case and worst case MTFs, 1D profiles of the 2D FFT are calculated along integer step sizes  $(k, l)$ , where  $k, l \in [0, 5]$ . To avoid duplicates, only distinct fractions  $k/l$  are taken into account. In figure 6.6 the close capture image of a single LED is shown and the corresponding min, max and mean values of 1D profiles of the 2D FFT depending on object-plane spatial frequency  $f_{object}$  are shown. The measured footprint MTF depending on the object-plane spatial frequency  $f_{object}$  is unique for different recording dates since the LED signatures and separations are fixed. However, the corresponding focal-plane spatial frequencies  $f_{focal}$  vary for different recording dates, since the ranges also vary. Focal plane spatial frequencies  $f_{focal}$  can be obtained by

$$f_{focal} = \frac{R}{fl} f_{object}, \quad (6.5)$$

Figure 6.6.: Close capture of a single LED at distance  $R \sim 1$  m by using a Tamron objective and ZWO ASICAM 290 MM Mono(left). Normalized log magnitude of 2D FFT of the close capture. The DC coefficient is centered. White is associated with maximum and black with minimum (right). Min/max/mean values and 95% confidence band of 1D profiles from the 2D FFT of the image depending on object-plane spatial frequency (bottom).



with the range  $R$  between camera and target and the focal length  $fl$ . As the range  $R$  increases, the LED footprint MTF shown in figure 6.6 also becomes increasingly flat with respect to focal-plane spatial frequency  $f_{focal}$ . Therefore, the contribution of the LED footprint drops compared to other degradations. Of course, the captured frame is also afflicted with degradations by detector footprint, optical diffraction, defocussing, etc. However, due to the extended LED footprint over several sensor pixels these degradations are neglectable. The LED footprint MTF has to be taken into account when comparing simulated intensity profiles of perfect point profiles degraded by turbulence with measured intensity profiles afflicted with the LED footprint. The additional blur due to the LED footprint could also be directly included in the simulation. Though, this would aggravate the comparison of intensity profiles between simulation and theoretical expressions e. g. for long-exposure and short-exposure MTF.

#### 6.1.4. Calculation of modulation transfer function (MTF) ratios

So how strong is the dependency of measured LED profiles on the used spectral band? Is it possible to detect significant differences from experimental data between the orange and blue spectrum and between the horizontal and vertical direction?

The log ratio

$$R(\lambda, v_x, v_y) = \ln \left( \frac{MTF_{SE}(\lambda, v_x, v_y)}{MTF_{LE}(\lambda, v_x, v_y)} \right) \quad (6.6)$$

described in section 3.2.10 is a figure of merit which is robust against other types of degradation such as LED footprint, detector footprint and sampling, etc. The reason for this is the reduction of these degradations in the fraction. For all calculated regions of interest, long-exposure and short exposure MTFs for single point sources can be calculation by using the procedure described in section 3.2.10. Instead of using entire frames, only square regions of interest  $ROI_{ij}$  with  $w_{ROI} \times w_{ROI}$  pixels each and  $w_{ROI} = 28$  are used:

$$MTF_{ij,SE}(v_x, v_y) = \mathcal{F}PSF_{SE}(x, y) = \mathcal{F} \langle I_{n,shifted}(x, y) \rangle_{n,x/y \in ROI_{ij}}, \quad (6.7)$$

$$MTF_{ij,LE}(v_x, v_y) = \mathcal{F}PSF_{LE}(x, y) = \mathcal{F} \langle I_n(x, y) \rangle_{n,x/y \in ROI_{ij}}, \quad (6.8)$$

with the column index  $i \in [0, 55]$  and row index  $j \in [0, 17]$ . Spatial frequencies can be easily converted between pixel space and angular or focal plane place, by identifying the sampling frequency

$$v_{s,angular} = \frac{fl}{p_x} \quad (6.9)$$

$$v_{s,focal\ plane} = \frac{1}{p_x} \quad (6.10)$$

with the pixel pitch  $p_x = 2.9 \mu\text{m}$  and the focal length  $fl = 0.8\text{m}$ . Then the spatial frequencies can be converted as

$$v_{x/y}[\text{rad}^{-1}] = \frac{w_{ROI}}{v_{S,\text{angular}}} v_{x/y}[\text{pixel}^{-1}] \quad (6.11)$$

$$v_{x/y}[\text{m}^{-1}] = \frac{w_{ROI}}{v_{S,\text{focal plane}}} v_{x/y}[\text{pixel}^{-1}] \quad (6.12)$$

Denoting the image section for  $ROI_{ij}$  as  $I_{n,ij}(x,y) = I_n(x + x_{0,ij}, y + y_{0,ij})$ , where  $(x_{0,ij}, y_{0,ij})$  are coordinates of the left top corner of  $ROI_{ij}$ , the long-exposure and short-exposure MTFs can be written as

$$MTF_{ij,LE}(v_x, v_y) = |DFT_{xy} \text{Average}_z I_{n,ij}(x,y)|, \quad (6.13)$$

$$MTF_{ij,SE}(v_x, v_y) = \text{Average}_z |DFT_{xy} I_{n,ij}(x,y)|, \quad (6.14)$$

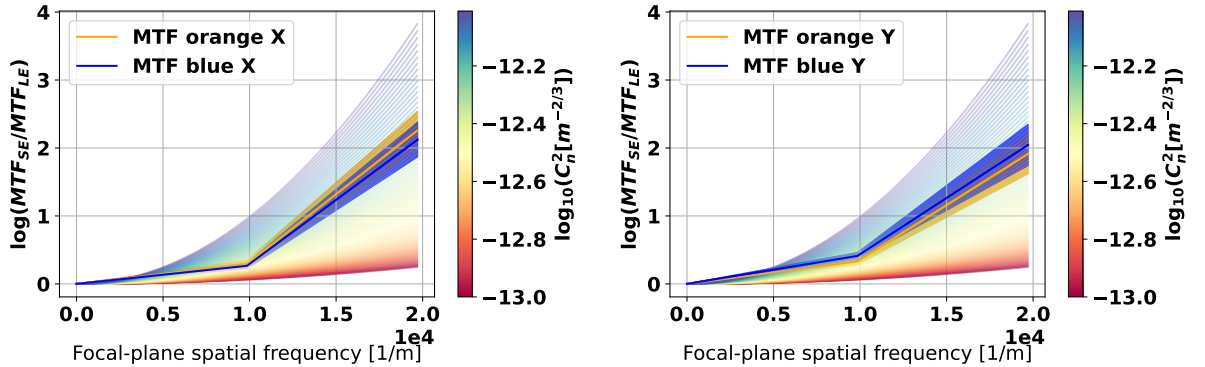
with the pixel-wise average  $\text{Average}_z$  over the image sequence and the frame-based discrete Fourier transform  $DFT_{xy}$ . For averaging by  $\text{Average}_z$ , a fixed number of  $N = 100$  frames is used. Single axis profiles  $MTF(v_x, 0)$  and  $MTF(0, v_y)$  for horizontal and vertical direction can be formed.

Then, these MTFs for single ROIs can be averaged over the respective LED minimatrix (orange or blue,  $N_{ROI} = 504$ ). In figure 6.7 the ROI-averaged log ratio  $\langle R \rangle_{ROI}$  is shown for the orange and blue spectrum with 95%-confidence bands are shown for a single video sequence at a hot summer day, 8/22/2020. Since the calculated MTFs are highly dominated by background noise for high spatial frequencies, i.e.  $v_{x/y} > 2000 \text{m}^{-1}$ , there are also large fluctuations in the log ratio  $R$ . Hence, the spatial frequency  $v_{x/y}$  is cutoff, for  $MTF_{SE}(v_{x/y}) < 0.01$  or  $MTF_{LE}(v_{x/y}) < 0.01$ .

Figure 6.7.: log ratio  $R$  for a single video sequence at 8/22/2020 based on  $N_f = 100$  frames. Mean values and its 95%-confidence bands are calculated by averaging over  $N_{ROI} = 28 \times 18 = 504$  ROIs. Expected log ratio  $R$  based on Fried MTFs at the orange average frequency  $\bar{\lambda}_{orange} = 593 \text{nm}$  are shown color-coded for varying turbulence strengths  $\log_{10} C_n^2$

(a) horizontal log ratio  $R_{hor}$

(b) vertical log ratio  $R_{vert}$



Also color-coded are the expected log ratios  $R$  based on the analytical Fried MTFs (equations 3.56 and equations 3.57) for varying turbulence strengths  $\log_{10} C_n^2$ . However, the Fried MTFs are based on the Kolmogorov spectrum not taking into account effects of inner scale  $l_0$ , outer scale  $L_0$  and non-Kolmogorov power slope  $\alpha$ . Besides different apparent turbulence strengths  $\log_{10} C_n^2$ , also for other video sequences of the same and other recording dates, the overlapping of confidence bands of the orange spectrum and the blue spectrum can be observed. The difficulty to clearly distinguish log ratios  $R$  between both spectra supports the conjecture that these two spectra with a difference of  $\Delta\lambda = \bar{\lambda}_{orange} - \bar{\lambda}_{blue} = 26$  nm cannot provide significant additional information for model parameter estimation compared to one spectrum under the given conditions.

However, if the wavelength dependency is extracted from the analytical Fried MTFs (equations 3.56 and equations 3.57) and the dependency on spatial frequencies  $\nu_x$  and  $\nu_y$  is neglected for a moment, a relation

$$R(\lambda) = c\lambda^{12/5} \quad (6.15)$$

can be identified. Hence, for both spectra with average wavelengths  $\bar{\lambda}_{orange} = 593$  nm and  $\bar{\lambda}_{blue} = 567$  nm a relative deviation of

$$\Delta R_{theo} = \frac{R(\bar{\lambda}_{orange}) - R(\bar{\lambda}_{blue})}{R(\bar{\lambda}_{blue})} = 0.11 \quad (6.16)$$

can be expected. Relative deviations of log ratio  $R$  can be calculated for the frame  $n$  comparing the spectral bands

$$\Delta R_{n,orange-blue} = \frac{R_n(\bar{\lambda}_{orange}) - R_n(\bar{\lambda}_{blue})}{R_n(\bar{\lambda}_{orange})}, \quad (6.17)$$

and comparing the direction

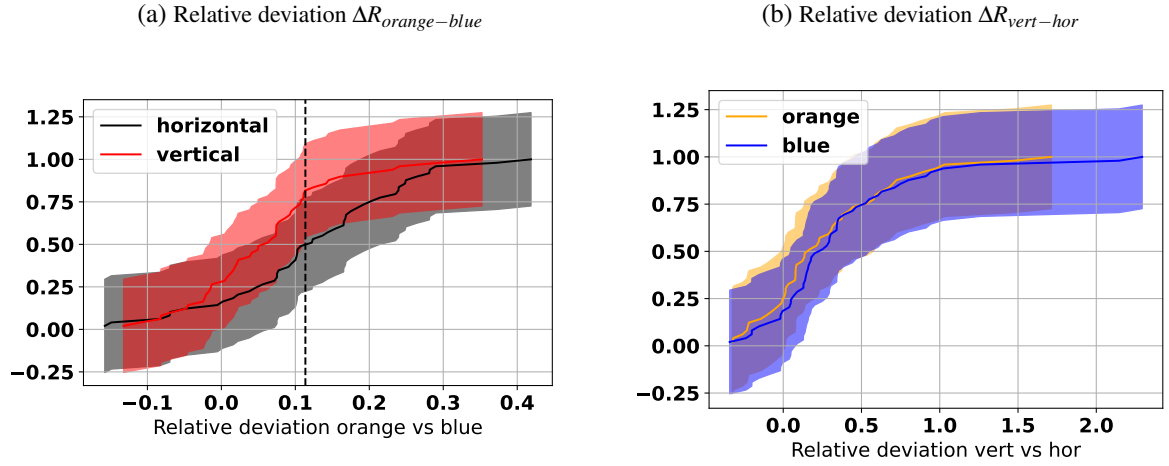
$$\Delta R_{n,vert-hor} = \frac{R_{n,vert} - R_{n,hor}}{R_{n,hor}}. \quad (6.18)$$

In figure 6.9 the cumulative distribution function (CDF) of relative deviations  $\Delta R$  for  $N = 100$  video sequences at 3/8/2020 are shown. The confidence band  $[CDF_{sample}(x) - \varepsilon, CDF_{sample}(x) + \varepsilon]$  is determined from the Dvoretzky–Kiefer–Wolfowitz inequality (Dvoretzky et al. [1956]):

$$\varepsilon = \sqrt{\frac{\ln\left(\frac{2}{\alpha}\right)}{2N}}, \quad (6.19)$$

where  $1 - \alpha$  is the confidence level with  $\alpha = 0.05$ . Indeed it can be observed that the theoretical deviation  $\Delta R_{theo}$  is close to the median of relative deviations  $\Delta R$ , i.e. the  $\Delta R$ , where the CDF is 0.5. Unfortunately, there are also large fluctuations over multiple video sequences compared to  $\Delta R_{theo}$ . These fluctuations might be reduced by increasing the number of LEDs or increasing the number of acquired frames  $N$ .

Figure 6.9.: Cummulative distribution function of relative deviation  $\Delta R$  with 95%-confidence bands for  $N = 100$  video sequences at 3/8/2021. Theoretical deviation  $\Delta R_{theo}$  is shown as vertical line.



The occurrence of these fluctuations can only be attributed to intrinsic ensemble statistics, since changing turbulence conditions are annihilated in the relative errors  $\Delta R_{n,orange-blue}$ , if  $R = cv^2$  as described in section 3.2.10. A better separability between  $R$  can be achieved by using larger wavelength separations, e.g. by using narrow-banded light sources at the lower and upper end of the visible range.

Obviously, distributions of  $\Delta R_{vert-hor}$  are very similar for both spectra and  $\Delta R_{vert-hor}$  is about 30% on average. Hence, log ratios  $R$  are larger in the vertical direction compared to the horizontal direction. This is also a general trend observed for the other recording dates.

Values for the log ratio  $R$  with low noise are only available for few discrete spatial frequencies (2 in figure 6.7). Due to the limited number of degrees of freedom, model parameter estimation for current turbulence models with 4 or 8 parameters (turbulence models GMVKS and GMAS) based on MTFs suffers from overfitting and seems not to be reasonable. For increasing the number of significant values of MTFs or the log ratio  $R$ , the frequency step  $\Delta v_{x/y}$  has to be decreased. It scales as

$$\Delta v_{x/y} = \frac{v_{s,angular}}{w_{ROI}} \quad (6.20)$$

Therefore, either the ROI size  $w_{ROI}$  has to be increased, which also requires increased physical separations of adjacent LED elements, or the sampling frequency  $v_{s,angular}$  is decreased by a smaller focal length  $fl$  or a larger pixel pitch  $p_x$ .

### 6.1.5. Calculation of centroids

Turbulence degradation also leads to spatially varying local image shifts often denoted as image dancing. The strength and spatial correlation of these shifts can be used for model parameter estimation, especially

the turbulence strength  $C_n^2$ . Centroid shifts related to single LED elements are calculated as first central moments of the respective regions of interest:

$$c_{x,ijk} = \frac{\sum_{x,y \in \text{ROI}_{ij}} x I_k(x,y)}{\sum_{x,y \in \text{ROI}_{ij}} I_k(x,y)} \quad (6.21)$$

$$c_{y,ijk} = \frac{\sum_{x,y \in \text{ROI}_{ij}} y I_k(x,y)}{\sum_{x,y \in \text{ROI}_{ij}} I_k(x,y)}. \quad (6.22)$$

$i \in [0, 27]$  is the horizontal LED grid index,  $j \in [0, 17]$  is the vertical LED grid index and  $k$  is the frame index in the video sequence.  $I_k(x, y)$  is the image for frame index  $k$ . Only the left LED grid with 28x18 elements is used for evaluation, since full data for the right LED grid is not available for all recording dates. Then the centroids  $c_{hor/vert,ijk}$  aligned with the LED grid are calculated by inverse rotation by the misalignment angle  $\alpha$ :

$$\begin{pmatrix} c_{hor,ijk} \\ c_{vert,ijk} \end{pmatrix} = \begin{pmatrix} \cos(\alpha) & \sin(\alpha) \\ -\sin(\alpha) & \cos(\alpha) \end{pmatrix} \begin{pmatrix} c_{x,ijk} \\ c_{y,ijk} \end{pmatrix} \quad (6.23)$$

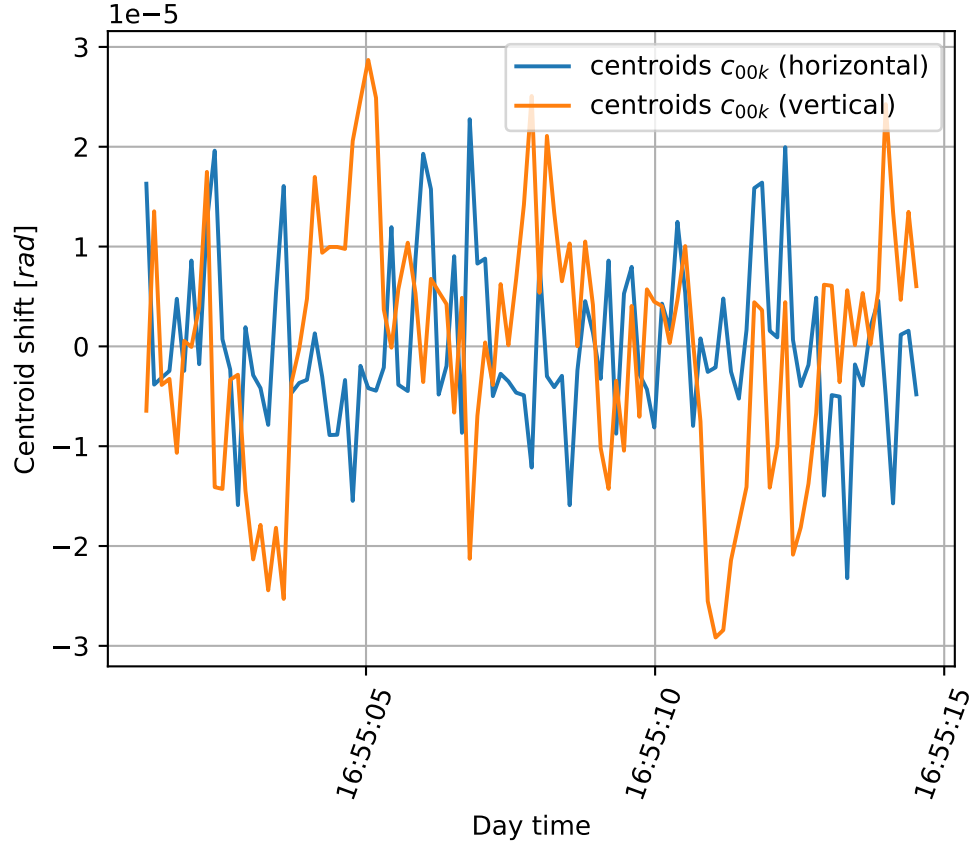
These centroid shifts are in units of sensor pixels. They can be calculated in units of viewing angle by

$$c_{hor/vert}/\text{rad} = IFOV c_{hor/vert}/\text{pixel}, \quad (6.24)$$

where  $IFOV = p_x/fl$  is the instantaneous field of view, i.e. the angular subtense of a single pixel.  $p_x = 2.9 \mu\text{m}$  is the pixel pitch.  $fl = 0.8\text{m}$  is the focal length. As centroids  $c_{ijk}$  of different region of interest have different center positions, for tip/tilt variations the time average  $\sum_k^{N_z} c_{ijk}/N_z$  is subtracted, which is approximately the ensemble average:

$$\tilde{c}_{ijk} = c_{ijk} - \sum_k \frac{c_{ijk}}{N_z} \quad (6.25)$$

A time sequence of centered centroid shifts  $\tilde{c}_{hor/vert,00k}$  for the top left region of interest of a single video sequence is shown in figure 6.11.

Figure 6.11.: Example of centroids  $\tilde{c}_{00k}$  for the top left region of interest for a single video sequence with 100 frames

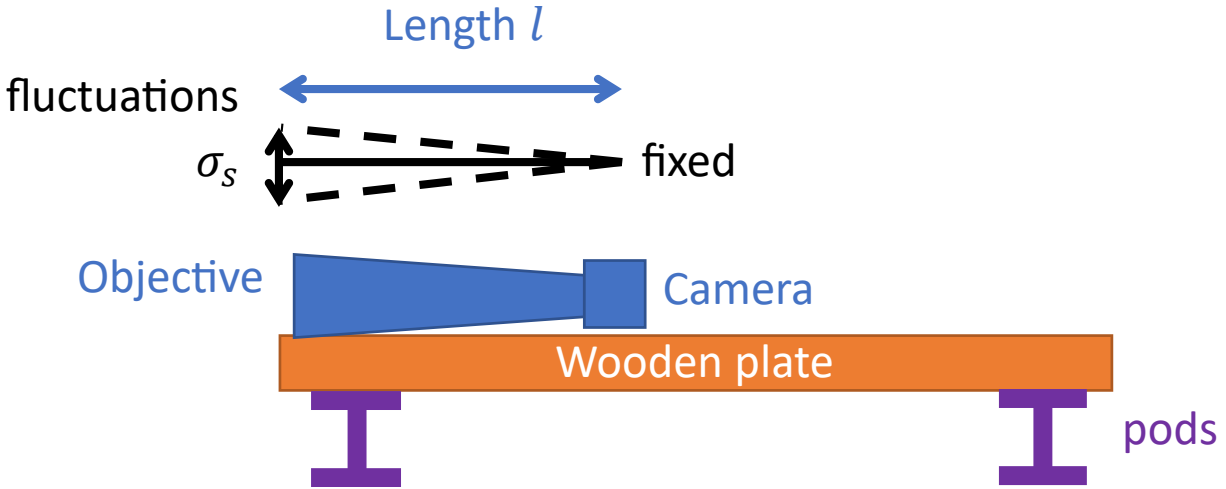
### 6.1.6. Mechanical stability of experimental setup

Foot steps in the vicinity of the experimental setup and wind effects may have caused mechanical vibrations of camera and objective placed on the wooden plate. How great is the influence of these mechanical vibrations on the centroid measurements? Over the several recording dates (table 6.2), angle of arrival fluctuations of  $\sigma_\theta = 5 - 50 \mu\text{rad}$  could be observed. This obviously represents an upper limit for mechanical vibrations. If the object and the camera is supported by the wooden plate, vibrations can be modeled so that one end of the camera-objective setup is fixed and the other end is freely movable. Then the required physical shift variation  $\sigma_s$  under small angle approximation is given as

$$\sigma_s = \sigma_\theta l, \quad (6.26)$$

where  $l$  is the length of the camera-objective setup. This vibration scenario is depicted in figure 6.12. With a length  $l = 0.5 \text{ m}$ , the angle of arrival fluctuations are associated with physical shift fluctuations of

Figure 6.12.: The camera and objective are placed on a wooden plate about 20 cm above ground. The worst case vibration in terms of angle of arrival fluctuations occurs when one end is fixed and the other is freely movable.



$\sigma_s = 10 - 100 \mu\text{m}$ . Assuming sinusoidal motion for vibrational modes

$$s(t) = s_0 \cos(\omega t) \quad (6.27)$$

$$a(t) = \ddot{s}(t) = -s_0 \omega^2 \cos(\omega t) \quad (6.28)$$

maximum accelerations  $a_{max} = \sigma_s \omega^2$  can be expected. During adjustments of the focal length and the camera orientation vibrations in terms of few oscillations per second could be observed  $f \sim 2\text{Hz}$ . A precise measurement by an accelerometer would require sensitivities lower than  $a_{max} < 0.01 \text{ m/s}^2$ . and susceptibility in the relevant frequency range.

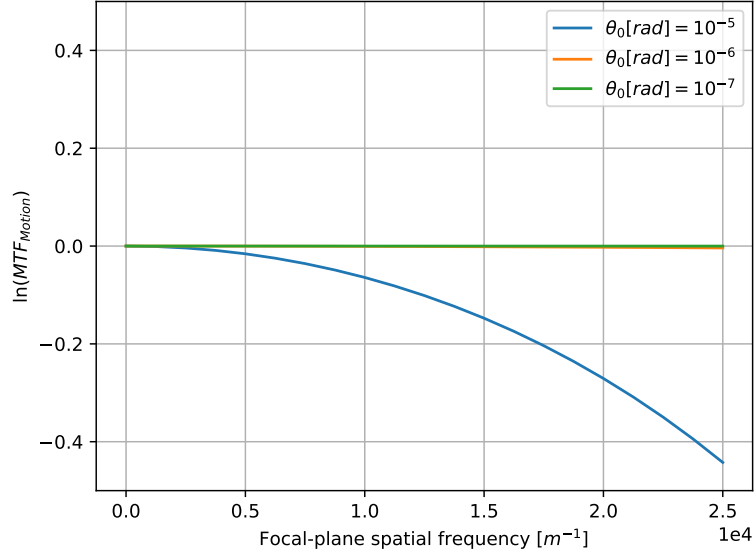
A rough estimate of the influence of single vibrational modes is possible by means of the modulation transfer function for a sinusoidal motion (Holst [2008]) given as

$$MTF_{motion}(v) = J_0(2\pi\theta_0 v), \quad (6.29)$$

where  $\theta_0 = s_0/l$  is the amplitude of angular subtense of the sinusoidal motion. In figure 6.13  $MTF_{motion}$  is shown for different amplitudes  $\theta_0$  over the relevant frequency range used for MTF calculations. It can be observed that  $MTF_{motion}$  has only significant impact for amplitudes as high as  $\theta_0 = 10^{-5}$  rad. However, in the temporal spectra of centroid shifts no significant peaks could be observed. Hence, vibrational modes seem to be neglectable.

For future experiments possible vibrations might be reduced by putting additional weights on the wooden plate to dampen vibrational modes.

Figure 6.13.:  $\log MTF_{motion}$  dependent on different subtense amplitudes  $\theta_0$ . Only strong subtense amplitudes  $\theta_0 \sim 10^{-5}$  rad lead to significant degradation in the relevant frequency range  $\nu < 2.5 \cdot 10^4 \text{ m}^{-1}$



### 6.1.7. Calculation of differential tilt variance (DTV)

Based on the calculated centered centroid values  $c_{hor/vert,ijk}$ , the differential tilt variance in horizontal and vertical direction can be calculated as

$$DTV_{hor/vert}(\Delta i, \Delta j, \Delta k) = \frac{\sum_i^{N_x - \Delta i} \sum_j^{N_y - \Delta j} \sum_k^{N_z - \Delta k} (c_{hor/vert,ijk} - c_{hor/vert,i+\Delta i, j+\Delta j, k+\Delta k})^2}{N(\Delta i, \Delta j, \Delta k)} \quad (6.30)$$

The sum over  $i$ ,  $j$ , and  $k$  is applied for all indices for which  $c_{hor/vert,ijk} c_{hor/vert,i+\Delta i, j+\Delta j, k+\Delta k}$  exists. The number of summands is hence given by

$$N(\Delta i, \Delta j, \Delta k) = (N_x - |\Delta i|)(N_y - |\Delta j|)(N_z - |\Delta k|) \quad (6.31)$$

with  $N_x = 28$ ,  $N_y = 18$  and  $N_z = 100$ . DTV can be calculated in units of the physical separation by using the LED grid specifications

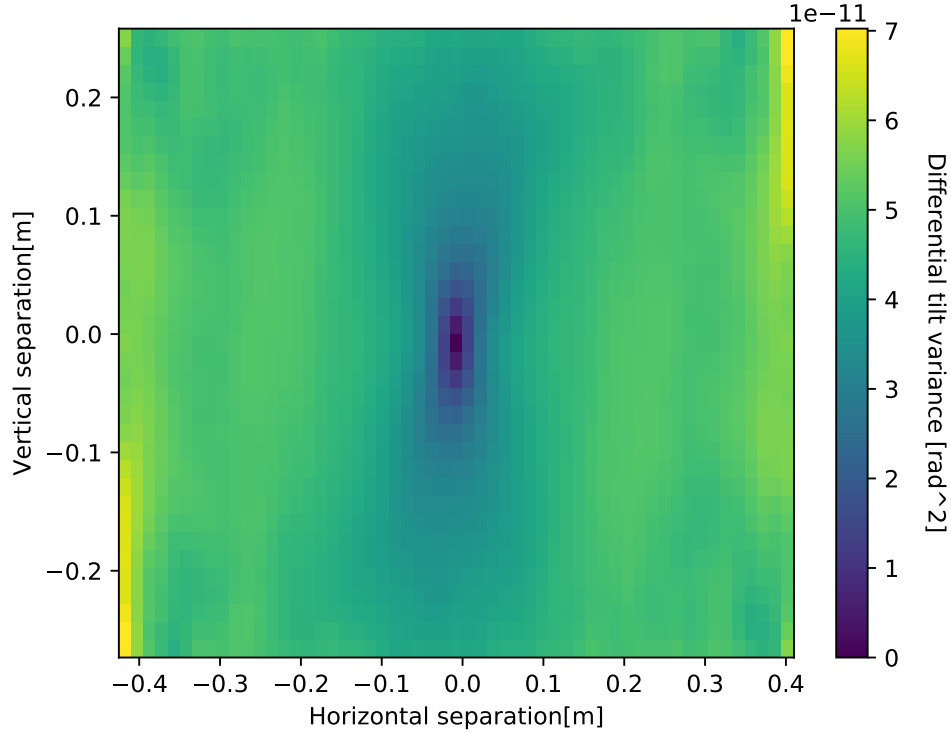
$$\Delta x = c \Delta i \quad (6.32)$$

$$\Delta y = c \Delta j \quad (6.33)$$

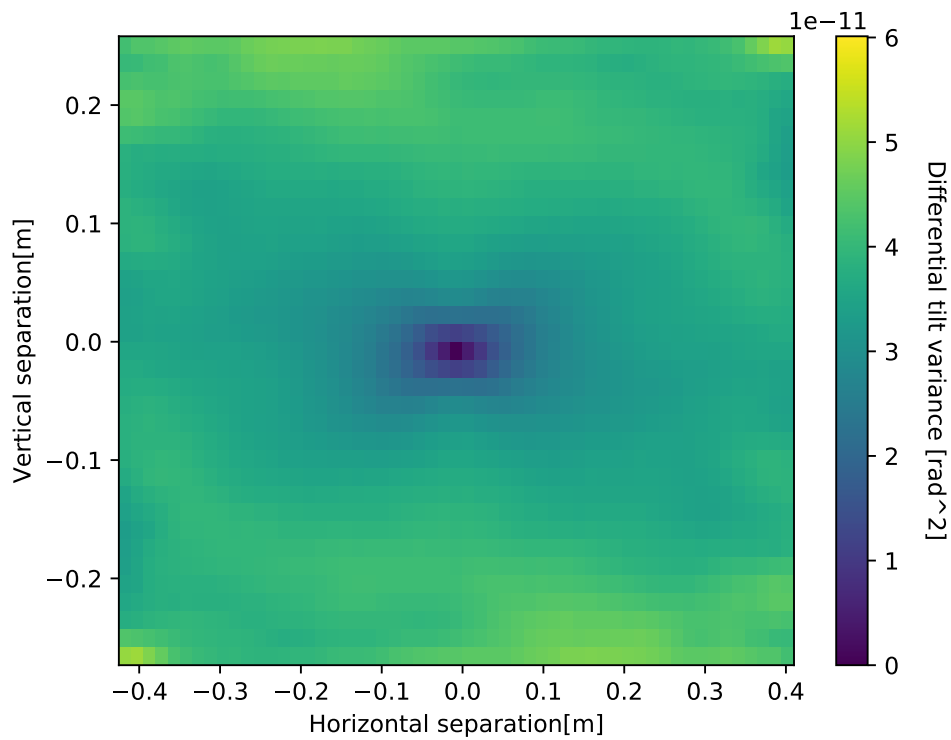
$$\Delta z = \frac{1}{f} \Delta k \quad (6.34)$$

with  $c = 0.4/27 \text{ m}$  and the average frame rate  $\bar{f} \approx 7 \text{ Hz}$  for the respective video sequence.

Figure 6.14.: Differential tilt variances  $DTV_{hor/vert}(\Delta x, \Delta y, 0)/\text{rad}^2$  depending on horizontal and vertical separations  $\Delta x/\text{m}$  and  $\Delta y/\text{m}$



(a) Horizontal differential tilt variance  $DTV_{hor}(\Delta x, \Delta y, 0)$



(b) Vertical differential tilt variance  $DTV_{vert}(\Delta x, \Delta y, 0)$

In figure 6.14 2D projections  $DTV_{hor/vert}(\Delta x, \Delta y, 0)$  depending on horizontal and vertical separation  $\Delta x$  and  $\Delta y$  are shown. Obviously both components are not radially symmetric. However, various numerical evaluations on the parallel component  $\sigma_{\parallel}^2$  by equation 3.50, i.e. the horizontal component  $DTV_{hor}(\Delta x, 0, 0)$  and the vertical component  $DTV_{vert}(0, \Delta y, 0)$ , have shown, that it is always larger than the perpendicular component  $\sigma_{\perp}^2$ , i.e. the vertical component  $DTV_{hor}(0, \Delta y)$  and the horizontal component  $DTV_{vert}(\Delta x, 0)$ . These asymmetric shapes of  $DTV_{hor/vert}(\Delta x, \Delta y, 0)$  were observed on all recording dates. In the following only the parallel components  $\sigma_{\parallel}^2$  and perpendicular components  $\sigma_{\perp}^2$  are used for the estimation of most likely turbulence model parameters, which are required for comparable turbulence simulations.

## 6.2. Estimation of the most likely turbulence model parameters

Single-axis projections of the differential tilt variances  $DTV_{hor/vert}(\Delta x, \Delta y, 0)$  can be fitted by the analytical expressions  $\sigma_{\parallel}^2[\Phi_n(\boldsymbol{\kappa})]$  and  $\sigma_{\perp}^2[\Phi_n(\boldsymbol{\kappa})]$  (equation 3.49) as functionals of the turbulence spectrum  $\Phi_n(\boldsymbol{\kappa}) \equiv \Phi_n(\boldsymbol{\kappa}, \mathbf{z})$  or functions of the turbulence parameters  $\mathbf{z}$ .

Least squares fits with the loss functions

$$\begin{aligned} f_{hor}(\mathbf{x}|\mathbf{z}_{hor}) &= \sum_i \left[ \sigma_{\parallel}^2(\Delta x_i|\mathbf{z}_{hor}) - DTV_{hor}(\Delta x_i, 0, 0) \right]^2 \\ &\quad + \sum_i \left[ \sigma_{\perp}^2(\Delta x_i|\mathbf{z}_{hor}) - DTV_{vert}(\Delta x_i, 0, 0) \right]^2 \\ f_{vert}(\mathbf{x}|\mathbf{z}_{vert}) &= \sum_i \left[ \sigma_{\parallel}^2(\Delta y_i|\mathbf{z}_{vert}) - DTV_{vert}(0, \Delta y_i, 0) \right]^2 \\ &\quad + \sum_i \left[ \sigma_{\perp}^2(\Delta y_i|\mathbf{z}_{vert}) - DTV_{hor}(0, \Delta y_i, 0) \right]^2 \end{aligned} \quad (6.35)$$

can be applied to find turbulence parameters  $\mathbf{z}_{hor}$  and  $\mathbf{z}_{vert}$  for horizontal and vertical axes based on the measurements  $\mathbf{x}$ . The separations are

$$\Delta x_i = \Delta y_i = i \cdot \Delta_0 \quad (6.36)$$

with  $\Delta_0 = 0.41/27m$ .  $\mathbf{x}$  is the set of measurements:

$$\mathbf{x} = \{DTV_{hor/vert}(\Delta x_i, 0, 0), DTV_{hor/vert}(0, \Delta y_i, 0)\}_i \quad (6.37)$$

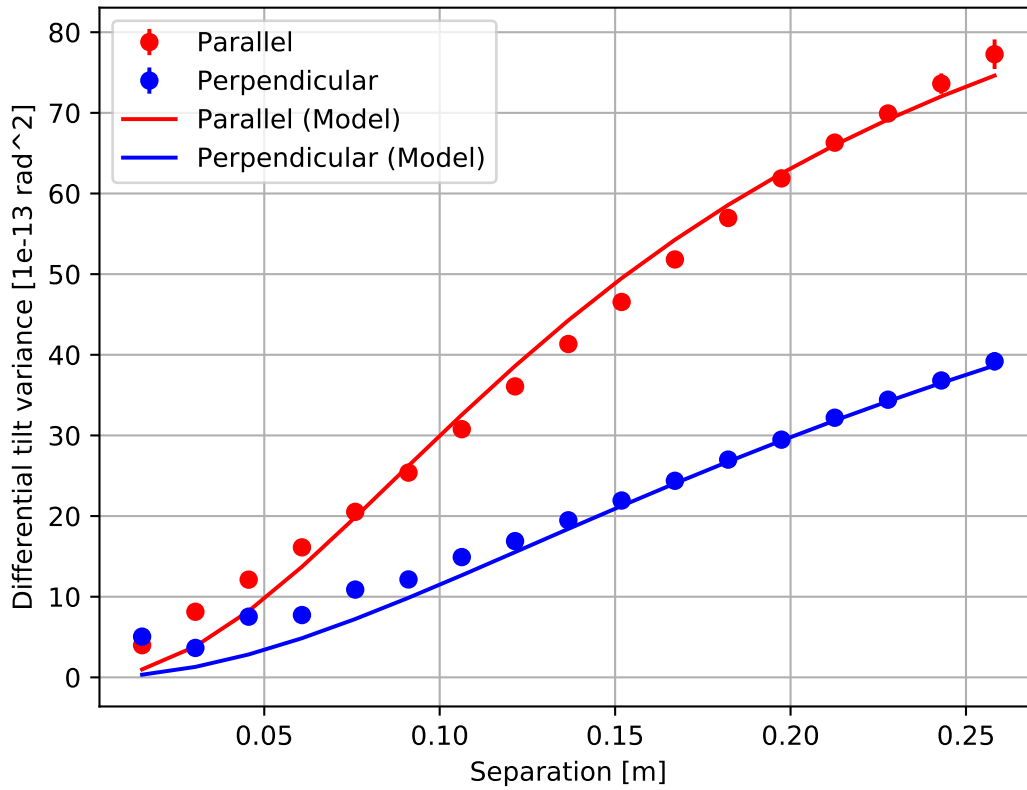
For minimization of the loss function, Google's tensorflow is used. As this framework can use CPUs/GPUs with unique code, calculations are done on GPU. Moreover, it can do automatic differentiation, which renders manual calculation of derivatives for steepest descent methods obsolete. The adaptive method Adam (Kingma and Ba [2014]) with  $N_{iteration} = 2000$  and learning rate  $\eta = 0.001$  is used, which is enough to ensure a final relative change of loss function less than 1% in most cases.

Unfortunately, the analytical expressions  $\sigma_{\parallel}^2$  and  $\sigma_{\perp}^2$  are integrals which are not analytically solvable for the turbulence spectra GMVKS and GMAS. Hence, numerical integration (trapezoid rule) is applied and an integral transformation  $\kappa = \tan(t)$  for forming a definite integral with respect to spatial frequency  $\kappa$ :

$$\int_0^{\infty} d\kappa f(\kappa) = \int_0^{\frac{\pi}{2}} dt (1 + \tan^2 t) f(\tan(t)) \quad (6.38)$$

An example fit with the spectrum GMVKS is shown in figure 6.16.

Figure 6.16.: Example of Differential tilt variance (DTV) fit to experimental data for a single video sequence with 100 frames



If normal distributed residuals between analytical and measured values are assumed, the loss functions are related to a multivariate Gaussian likelihood function  $L_{hor/vert}(\mathbf{x}|\mathbf{z})$  by

$$f_{hor/vert}(\mathbf{x}|\mathbf{z}) = -2 \ln L_{hor/vert}(\mathbf{x}|\mathbf{z}). \quad (6.39)$$

Bayes theorem states

$$L(\mathbf{z}|\mathbf{x}) = \frac{L(\mathbf{x}|\mathbf{z})f(\mathbf{z})}{g(\mathbf{x})} \quad (6.40)$$

with prior distribution  $f(\mathbf{z})$  and posterior distribution  $g(\mathbf{x})$ . If a flat prior distribution  $f(\mathbf{z}) = const$  is assumed, the propability density function  $L(\mathbf{z}|\mathbf{x})$  with respect to the true parameters  $\mathbf{z}$  is proportional to the likelihood function  $L(\mathbf{x}|\mathbf{z})$ . This distribution can be approximated to be locally Gaussian in the vicinity of the mean value  $\bar{\mathbf{z}}$

$$L(\mathbf{z}|\mathbf{x}) \approx c \times \exp\left(-\frac{1}{2}(\mathbf{z}-\bar{\mathbf{z}})^T C_{\mathbf{z}}^{-1}(\mathbf{z}-\bar{\mathbf{z}})\right) \quad (6.41)$$

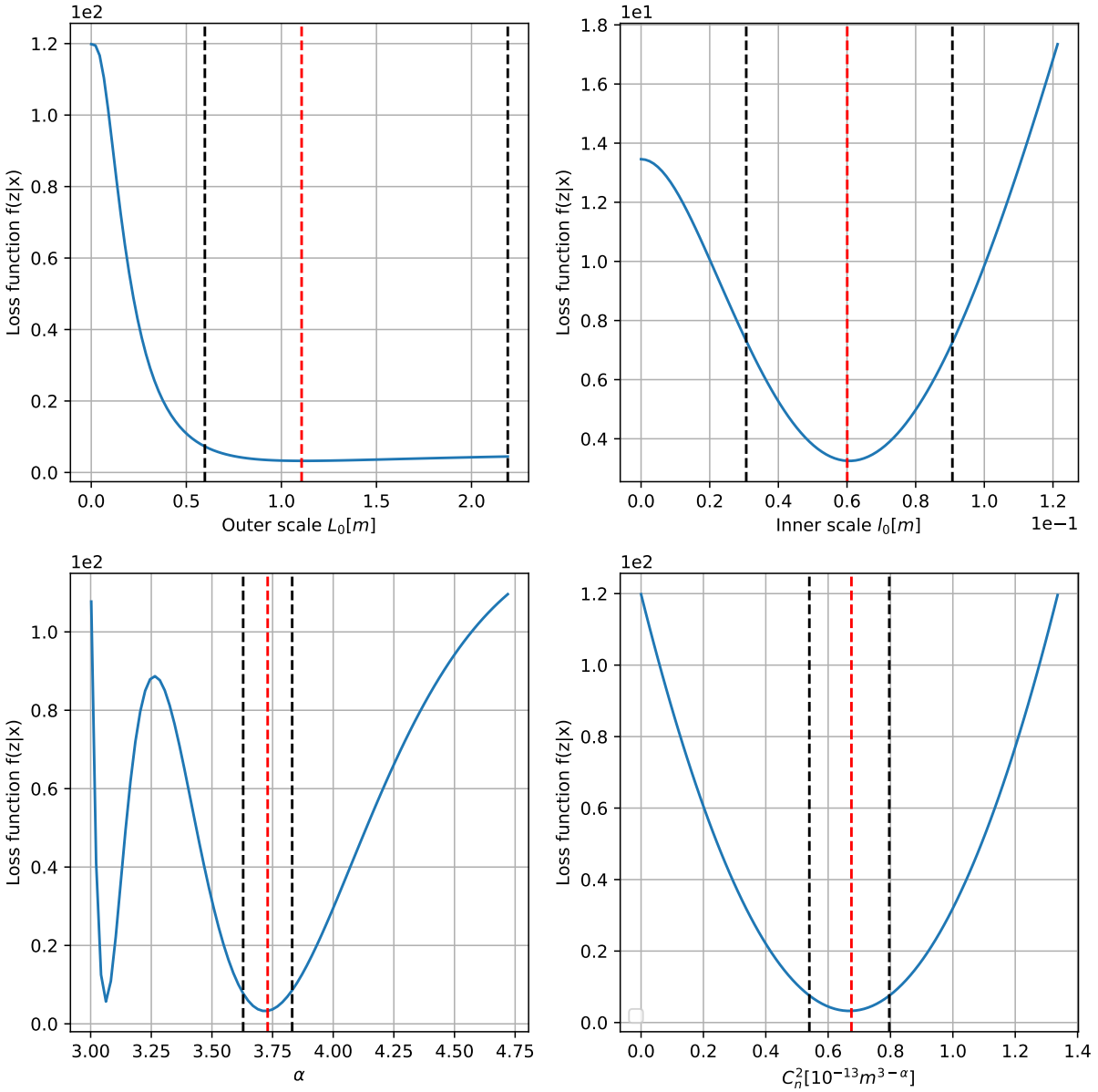
$$f(\mathbf{z}|\mathbf{x}) = -2 \ln c + (\mathbf{z}-\bar{\mathbf{z}})^T C_{\mathbf{z}}^{-1}(\mathbf{z}-\bar{\mathbf{z}}) \quad (6.42)$$

with the covariance matrix  $C_{\mathbf{z}}$  of the turbulence parameters  $\mathbf{z}$ . If non diagonal elements in the covariance matrix  $C_{\mathbf{z}}$  are neglected, confidence intervals can be found by searching single parameters  $z_i$ , where  $|z - \bar{z}| = k\sigma_i$  and  $\sigma_i^2 = C_{z,ii}$  ( $k = 1.96$  for 95% integrated propability). This is equivalent for searching bounds  $z_{i,upper}$  and  $z_{i,lower}$  for each parameter  $i$ , where

$$f(\mathbf{z}_{upper/lower}|\mathbf{x}) = f_{min} + k^2 \quad (6.43)$$

In figure 6.17 1D grid scans of the loss function  $f(z|x)$  for the single parameters  $L_0$ ,  $l_0$ ,  $\alpha$  and  $C_n^2$  for a single DTV fit based on the spectrum GMVKS are shown. The range for the outer scale  $L_0$  is cropped to higher values. As the turbulence strength  $C_n^2$  occurs as constant factor in the analytical DTV (equation), the loss function  $f(z|x)$  is strictly parabolic for  $C_n^2$ . Not surprisingly the outer scale  $L_0$  is in general larger than the inner scale  $l_0$ .

Figure 6.17.: 1D grid scans of the loss function  $f(\mathbf{z}|\mathbf{x})$  (DTV fitting function) for single turbulence parameters  $L_0, l_0, C_n^2$  and  $\alpha$  for a single video sequence based on the spectrum GMVKS. 95%-confidence intervals of parameters (vertical black lines) and modal values  $f(z_{min}|\mathbf{x}) = f_{min}$  (red dashed lines) are shown. The upper bound for outer scale  $L_0$  is cutoff for better illustration.



This fitting procedure was applied for  $N = 1112$  video sequences over 12 recording dates (table 6.2) to obtain an equal number of parameter sets for the turbulence models GMVKS and GMAS. For the spectrum GMVKS initial parameters were chosen as  $C_n^2 = 10^{-17} m^3^{-\alpha}$ ,  $L_0 = 0.1$  m,  $l_0 = 0.00001$  m,  $\alpha = 11/3$ . For the spectrum GMAS additional parameters  $a = 1.802$ ,  $b = 0.254$  and  $\beta = 7/6$  are adopted from Gao et al. [2015].

In the next sections, a subset of these retrieved model parameters is used to feed simulations, which are then compared to analytical expressions and experimental data with respect to several metrics, i.e. differential tilt variances  $DTV_{hor/vert}(\Delta x, \Delta y)$ , long-exposure and short exposure modulation transfer functions  $MTF_{LE/SE}(v_x, v_y)$  and the aperture-averaged scintillation index  $\sigma_I^2(D)$ .

### Comparison of DTV

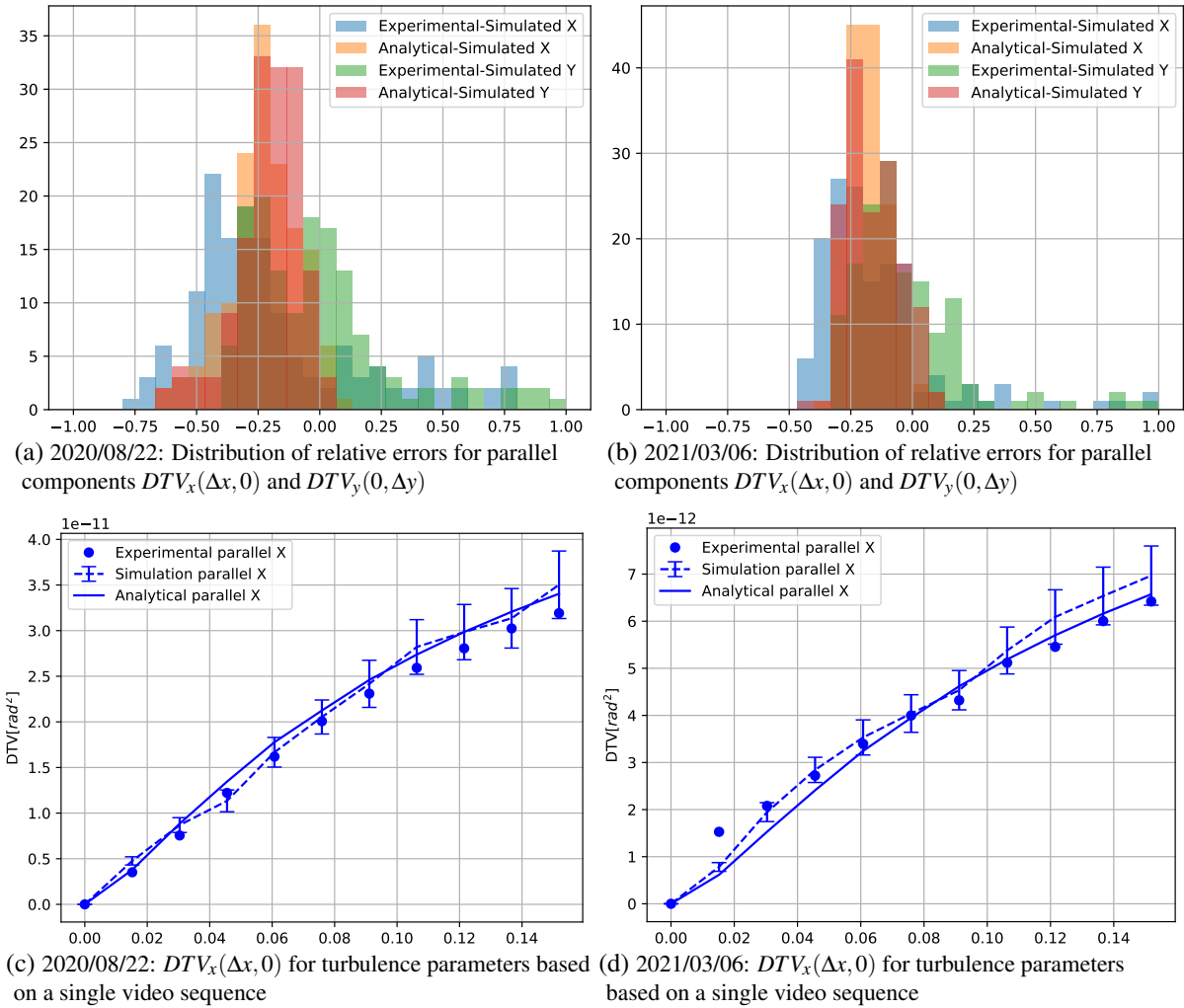
Now the simulator can be fed by these retrieved turbulence parameters. The resulting DTV values for  $N_{ps} = 200$  frames of a  $11 \times 11$  PSF grid can then be compared to corresponding experimental data. In figure 6.18 distributions of relative errors between simulation, experiment and analytical data is shown:

$$\Delta DTV_{hor/vert, Ana-Sim} = \frac{DTV_{hor/vert, Ana} - DTV_{hor/vert, Sim}}{DTV_{hor/vert, Sim}}, \quad (6.44)$$

$$\Delta DTV_{hor/vert, Exp-Sim} = \frac{DTV_{hor/vert, Exp} - DTV_{hor/vert, Sim}}{DTV_{hor/vert, Sim}}. \quad (6.45)$$

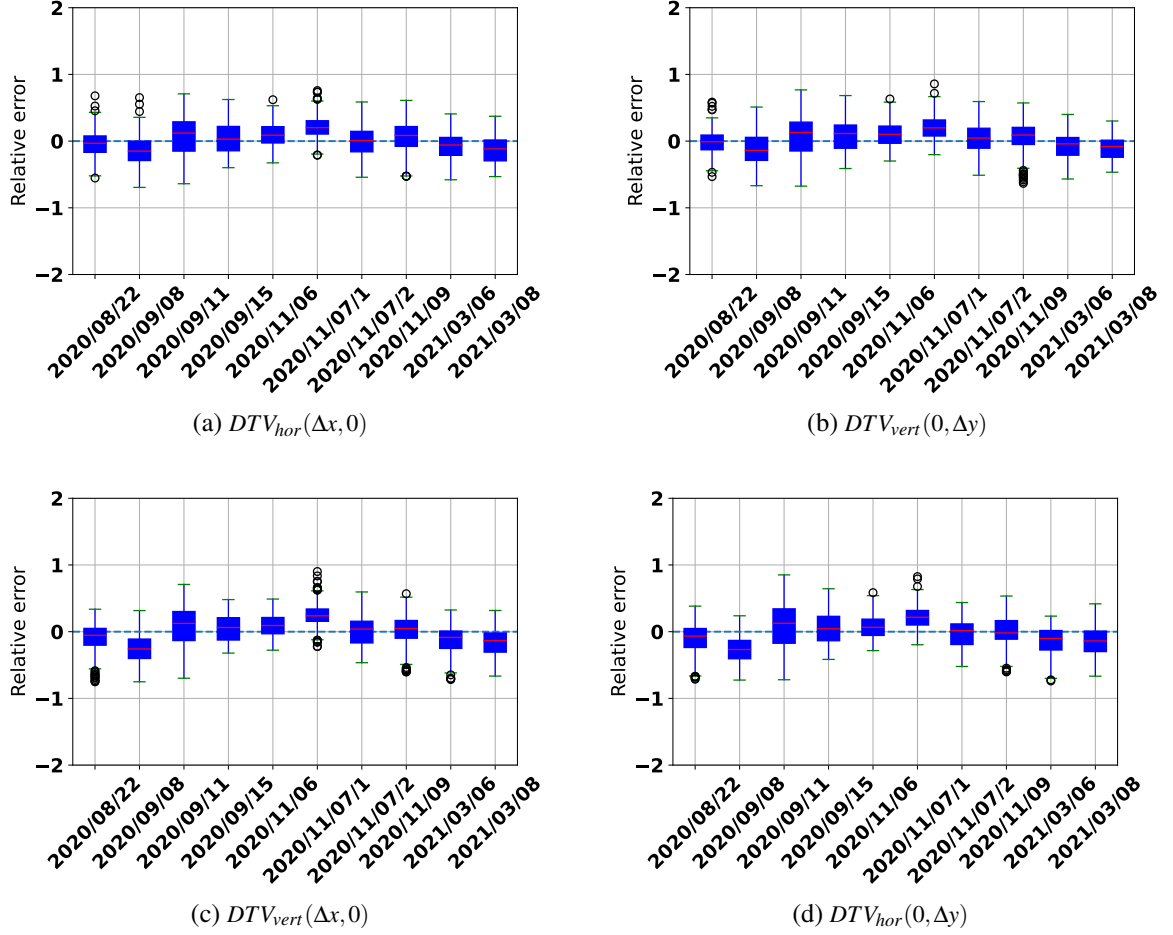
Two dates, 2020/08/22 and 2021/03/06, were chosen to obtain results for very different temperature ranges.  $DTV_{x,y}(0,0) = 0$  is excluded since their relative errors is obviously not well-defined. Since the relative errors are not centered around zero, there is bias between simulation and analytical/experimental data. On average the simulated values are slightly higher than the analytical and experimental values. However, as DTV is proportional to turbulence strength  $C_n^2$ , this bias can be reduced by scaling the turbulence strength  $C_n^2$  in the simulation by a factor  $1 + \bar{r}$ , where  $\bar{r}$  is the average relative error. Figures 6.19a and 6.19b also show that this bias is similar between both dates. Only the distribution of relative errors is more dense for 2021/03/06, which may be attributed to lower turbulence strengths on that date. This can also be seen in the order of magnitude difference in the DTV plots (figures 6.19c and 6.19d). Recording settings as equal as possible for different dates were used to ensure comparability. The integration time was varied between  $t_{int} \in [32 \mu s, 100 \mu s]$  to use about half of the sensor's dynamic range under different lighting conditions and to prevent saturation. Tests for temporal correlation of centroid shifts have shown that these integration times are much smaller than significant changes due to turbulence ( $1/e$  decay at few tens of milliseconds). This is important to prevent temporal low pass filtering of the centroid shifts. On the one hand the statistical fluctuations of the experimental DTV values could be decreased by capturing more frames. This may result in lower relative errors. On the other hand turbulence conditions can become instationary over long recording times e.g. due to changing wind conditions, cloud movements, etc.

Figure 6.18.: DTV relative errors of simulations based on turbulence model parameters of 15 video sequences and single examples for two recording dates 2020/08/22 and 2021/03/06



For a better overview of the variety of relative errors, the same simulations can be repeated for various recording dates with a smaller grid size  $9 \times 9$  for faster calculations based on the data for the orange LED matrix with  $\bar{\lambda} = 593 \text{ nm}$ . For each model parameter set corresponding to one video sequence  $N = 200$  frames of perturbed point grids are simulated. Again the spectrum GMVKS is used due to lower complexity than GMAS. In figure 6.19 box plots for relative errors between the  $DTV$  of simulated point grids and analytical  $DTV$  are shown for 1D profiles  $DTV_{hor/vert}(\Delta x, 0)$  and  $DTV_{hor/vert}(0, \Delta y)$ . The red lines show the medians, the boxes show the range between third and first quartil, in which 50% of the values in the respective dataset are. This range is often denoted as interquartile range (IQR). The whiskers, which look like error bars, extend the IQR by 1.5 IQR at maximum on the lower and upper end respectively, but are limited by the largest and smallest values in the respective dataset. Values outside the range of whiskers are shown as outliers. It can be observed that the interquartile ranges are fluctuations around zero and remain under  $\pm 50\%$ . For different profiles  $DTV_{hor/vert}(\Delta x, 0)$  and  $DTV_{hor/vert}(0, \Delta y)$ .

Figure 6.19.: Box plots of relative errors of  $DTV$  simulated versus analytical for several recording dates.  $DTV$  values are calculated for  $N = 50$  simulations based on retrieved model parameter sets from  $DTV$  fits, one per video sequence. Each simulation generates  $N_s = 200$  frames of perturbed  $9 \times 9$  point grids.

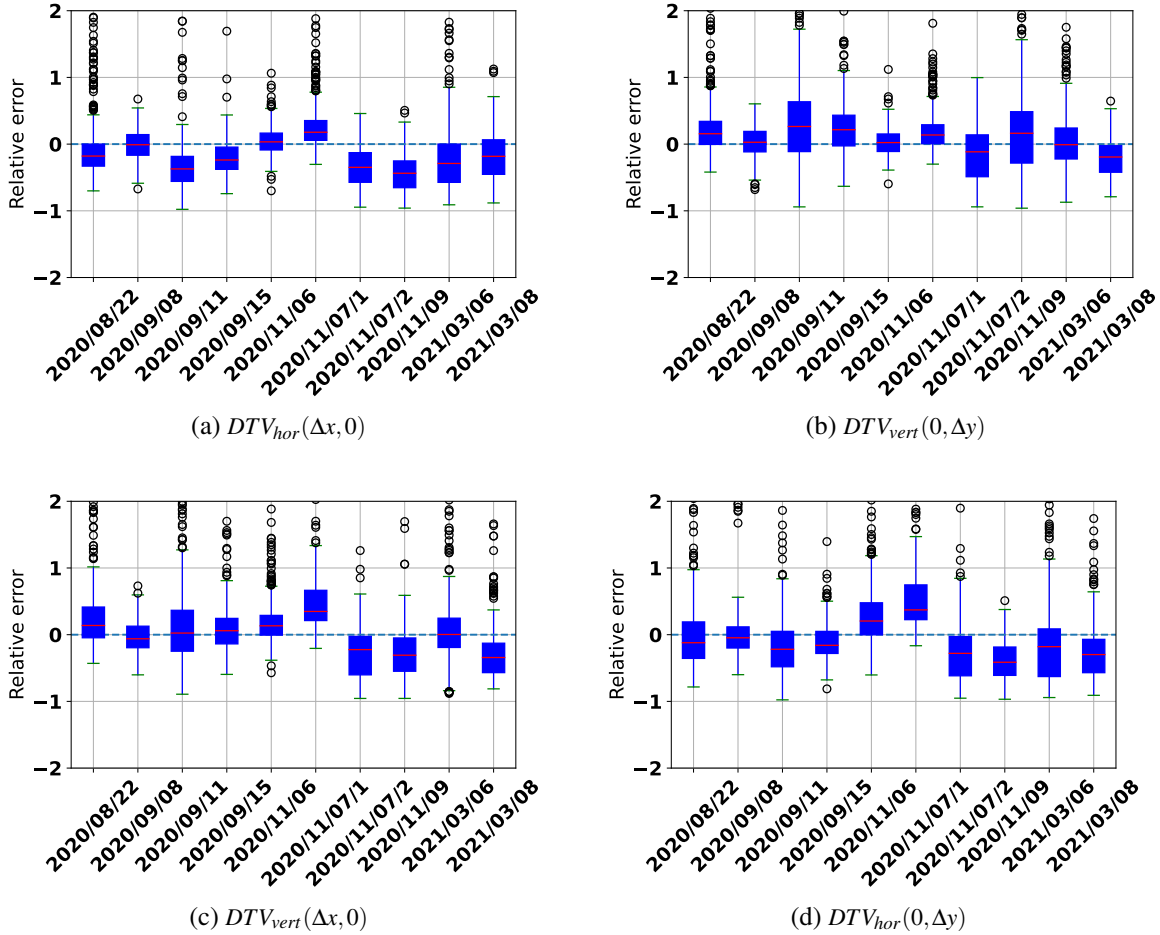


Then the relative errors between  $DTV$  values from recorded video sequences and  $DTV$  values from the simulated point grids can be compared. This comparison is depicted in figure 6.20.

Here the fluctuations are slightly higher and more outliers with positive relative errors can be observed. These values are related to higher experiment-based  $DTV$  values than simulation-based  $DTV$  values. A reason for these outliers might be temporal drifts of turbulence conditions within the recording time of one video sequences, i.e. about 12 seconds each. This can result in biased  $DTV$  values which are not well fit by the turbulence model  $\Phi_n(k, \mathbf{z})$ . Future experiments may clarify if shorter capture times lead to a lower number of outliers. Additional enhancements on the fitting procedure may also reduce the number of outliers.

In summary, turbulence model parameters can be estimated from  $DTV$  values from experimental data which can be fed to the turbulence simulation providing perturbed point grids with comparable  $DTV$  values and also in good agreement with theoretical values. For using the turbulence simulation for image degradation of arbitrary scenes as described in section 4.5, the similarity of  $DTV$  values or the

Figure 6.20.: Box plots of relative errors of  $DTV$  simulated versus experimental for several recording dates.  $DTV$  values are calculated for  $N = 50$  simulations based on retrieved model parameter sets from  $DTV$  fits, one per video sequence. Each simulation generates  $N_s = 200$  frames of perturbed  $9 \times 9$  point grids.



variance of centroid shifts is crucial for degraded frames to have proper intensity and spatial correlation of local image shifts. Under the given conditions, MTFs or MTF ratios do not provide enough degrees of freedom for model fits based on the models GMVKS and GMAS. However, they enable a coarse estimate of turbulence strength  $C_n^2$  for the Kolmogorov spectrum, which is a special case of GMVKS and GMAS, where  $l_0 = 0$ ,  $L_0 = \infty$  and  $\alpha = 11/3$ .

### Comparison of MTF

Do the very same turbulence model parameters retrieved from  $DTV$  fits also provide good accordance for long-exposure and short-exposure MTFs? To answer this question, simulations of single perturbed point sources were done on the same recording dates. 50 model parameter sets per day are used, each retrieved from a single video sequence. Low values for MTFs severely suffer from high relative statistical fluctuations e.g. due to ensemble statistics or camera noise in the recorded data. For the image forming

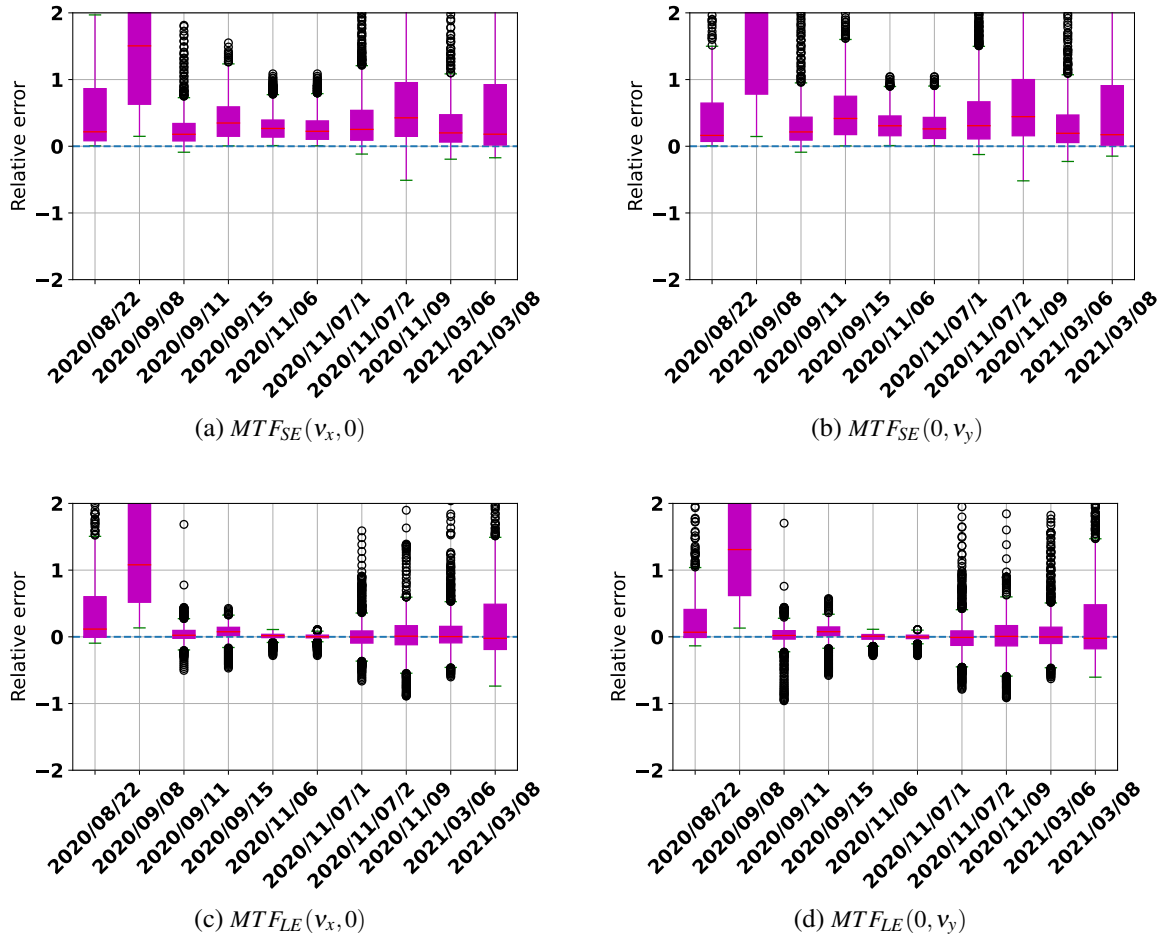
process, they have negligible impact anyway. Hence, for comparison, only values  $MTF_{SE/LE} > MTF_{thres}$  with  $MTF_{thres} > 0.01$  are taken into account. For ease of comparison and to obtain a higher spatial frequency resolution and number of relevant spatial frequencies, detector subsampling as described in section 4.5.2 is omitted in the simulations.

The relative deviations

$$\Delta MTF_{SE/LE, Ana-Sim} = \frac{MTF_{SE/LE, Ana} - MTF_{SE/LE, Sim}}{MTF_{SE/LE, Sim}} \quad (6.46)$$

over several recording dates between theoretical MTF values and the corresponding MTF values of simulated point sources is shown in figure 6.21.

Figure 6.21.: Box plots of relative errors of  $MTF$  simulated versus analytical for several recording dates.  $MTF$  values are calculated for  $N = 50$  simulations based on retrieved model parameter sets from DTV fits, one per video sequence. Each simulation generates  $N_s = 1000$  frames of single perturbed point sources.



The relative deviations of short-exposure MTFs (top row in figure 6.21) are biased about 25%. For most recording dates the median of relative deviations for long-exposure MTFs is located near 0. Positive biases are equivalent to higher theoretical MTF values compared to those for the simulated point sources.

2020/09/08 seems to form entirely an outlier with lower MTFs values for simulated point sources in general. As shown in a following section 6.5, measurements at noon on this day had very high turbulence strengths  $C_n^2 \sim 4 \cdot 10^{-13} \text{ m}^{3-\alpha}$ . This can lead to high fluctuations and an exceedance of optical power beyond the simulation field. Then the real intensity profiles are effectively clipped. This windowing effect smears the corresponding MTF and leads to lower MTF values. To mitigate these effects, higher simulation field sizes  $w_{x/y}$  or convergence-based adaptive procedures may be used if needed. In contrast, measurements at 2020/11/07/1 revealed comparably weak turbulence strengths  $C_n^2 \sim 10^{-14} \text{ m}^{3-\alpha}$  and have very low variances of deviations  $\Delta MTF_{SE/LE}$ . Also a general trend of a variance of  $\Delta MTF_{SE/LE}$  increasing with turbulence strength  $C_n^2$  can be observed. Then the relative errors between MTFs from recorded video sequences and MTFs from the simulated point sources can be compared:

$$\Delta MTF_{SE/LE,Exp-Sim} = \frac{MTF_{SE/LE,Exp} - MTF_{SE/LE,Sim}}{MTF_{SE/LE,Sim}} \quad (6.47)$$

The mean MTFs over  $504=28 \times 18$  LED elements of the orange LED grid with  $\bar{\lambda}_{orange} = 593 \text{ nm}$  are used as  $MTF_{SE/LE,Exp}$  to provide a more robust estimate compared to MTFs related to single LED elements. The mean LED footprint MTF as described in section 6.1.3 is multiplied to the long-exposure and short exposure MTFs calculated from simulated point sources. For different recording dates the object-plane spatial frequencies  $f_{object}$  are converted to the corresponding focal-plane spatial frequencies  $f_{focal}$  depending on the range  $R$  as provided in table 6.2. Then linear interpolation is used evaluate the LED footprint MTF at the focal-plane spatial frequencies of the simulation

$$f_i = i\Delta f \quad \Delta f = \frac{w_{x/y}}{N_{x/y}\bar{\lambda}_{orange}fl} \quad i \in [0, N_{x/y}/2], \quad (6.48)$$

, with the simulation field width/height  $w_{x/y} = 0.4 \text{ m}$  and the focal length  $fl = 0.8 \text{ m}$  and the simulation field size  $N_{x/y} = 512$ . This comparison is depicted in figure 6.22. Obviously, the deviation  $\Delta MTF_{Exp-Sim}$  is biased over several recording dates about  $-25\%$ . This is equivalent to experimental MTFs lower than the simulated MTFs. A reason for this may be residual effects of degradation  $MTF_{residual}$  not yet considered in the simulation. The values of

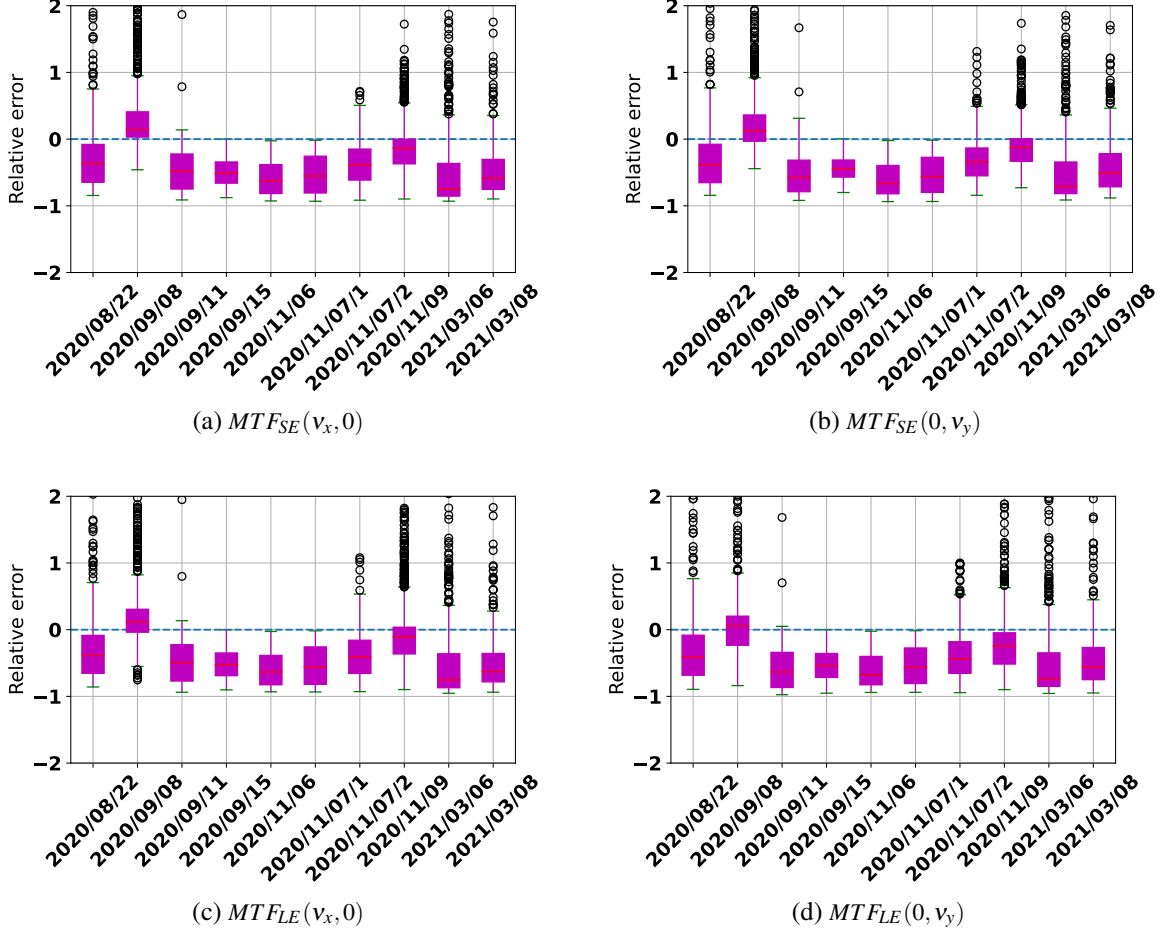
$$MTF_{residual} = \frac{MTF_{Exp}}{MTF_{Sim}} = \Delta MTF_{Exp-Sim} + 1 \quad (6.49)$$

can be ordered by spatial frequencies  $v_x$  and  $v_y$ .

In figure 6.23 interquartile ranges of  $MTF_{residual}$  are shown for the different recording dates. Also shown are the optical cutoff frequency

$$v_{cutoff} = \frac{D}{\lambda fl} \quad (6.50)$$

Figure 6.22.: Box plots of relative errors of  $MTF$  simulated versus experimental for several recording dates.  $MTF$  values are calculated for  $N = 50$  simulations based on retrieved model parameter sets from DTV fits, one per video sequence. Each simulation generates  $N_s = 200$  frames of perturbed  $9 \times 9$  point grids.

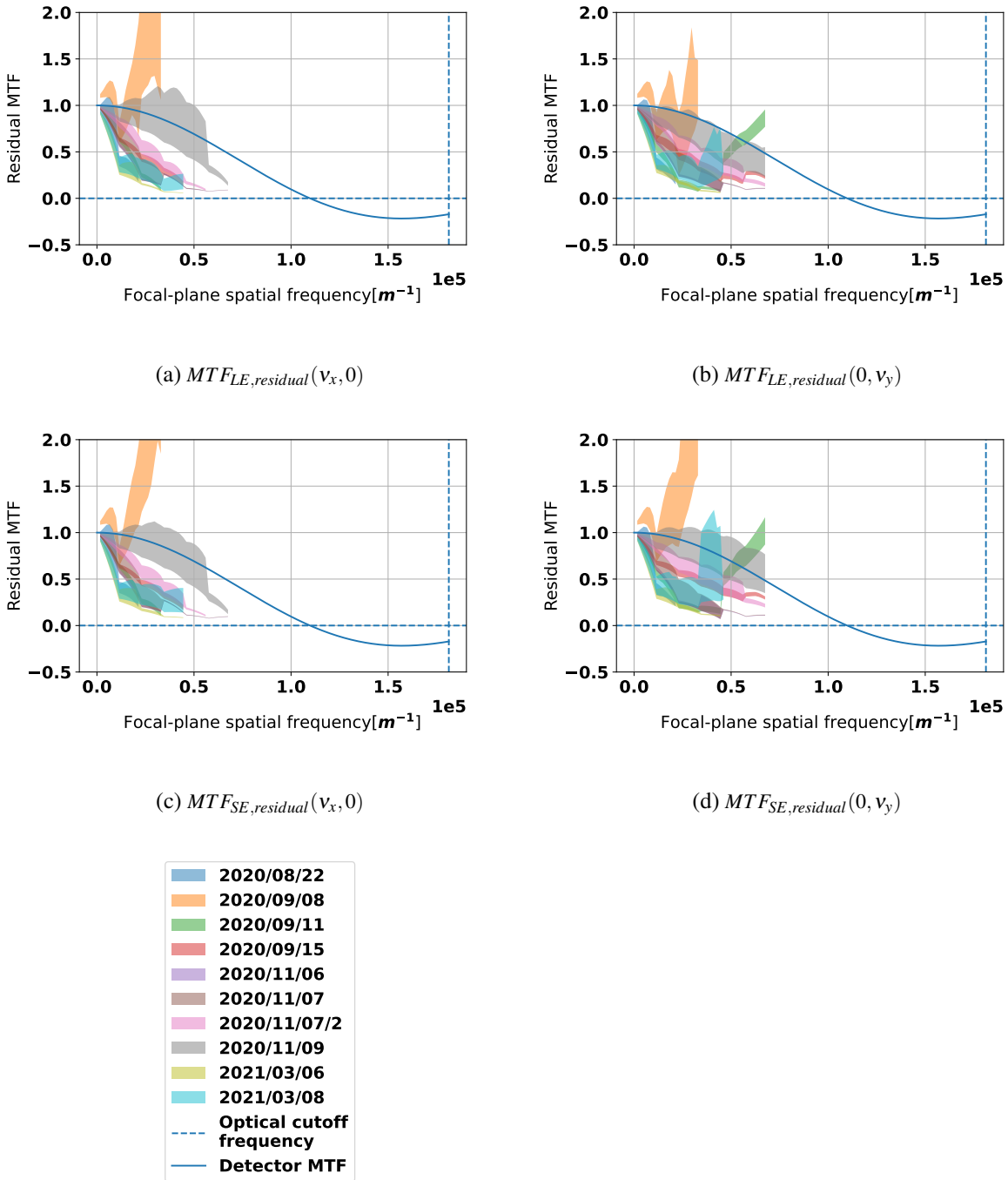


with diameter  $D = 0.086$  m and focal length  $fl = 0.8$  m as well as the detector MTF (Holst [2008])

$$MTF_{detector}(v_x) = \text{sinc}(\pi p_{x/y} v_x) \quad (6.51)$$

with the pixel pitch  $p_{x/y} [\mu m] = 2.9$ . The discrepancy due to the detector MTF is expectable, since detector subsampling was omitted in the simulation. It can be observed that  $MTF_{residual}$  are similar for long-exposure and short-exposure MTFs in horizontal and vertical direction besides some outliers, the hot summer day 2020/09/08 and 2020/11/09. The  $MTF_{SE/LE,residual}(0, v_y)$  for the vertical direction are also slightly higher than  $MTF_{SE/LE,residual}(v_x, 0)$  for the horizontal direction. The slightly worse horizontal MTFs may be attributed to horizontal air flows leading to temporal averaging of moving turbulence eddies during the detector integration time. Besides the  $MTF_{residual}$ , which is similar for several dates, there is also good agreement between analytical, simulated and experimental MTF values. Statistical fluctuations may be further reduced by increasing the number of simulated frames  $N_f$ . The trend of

Figure 6.23.: Interquartile ranges for  $MTF_{residual}$  for long-exposure and short-exposure  $MTF$  values in horizontal and vertical direction.



increasing biases for rising turbulence strengths  $C_n^2$  can be encountered by using larger simulation field sizes  $N_{x/y}$ , which also increases the spatial extent of the simulated PSFs and reduces the windowing effect for wide PSF profiles. The discrepancy between  $MTF_{SE/LE,Exp}$  values and  $MTF_{SE/LE}$  values indicates, that for matching a good characterization of the residual system components is required.

### Comparison of aperture-averaged scintillation index

In the identical manner as for the MTFs, single perturbed point sources can be simulated for the comparison of the aperture-averaged scintillation index

$$\sigma_I^2(D) = \frac{\langle P^2 \rangle}{\langle P \rangle^2} - 1 \quad (6.52)$$

The analytical value can be calculated via numerical integration (equation 3.43). As the aperture-averaged scintillation index  $\sigma_I^2(D)$  is proportional to the turbulence length  $C_n^2$ , which can vary over several orders of magnitude,  $\log \sigma_I^2(D)$  values are compared. The relative deviations are again given as

$$\Delta \ln \sigma_{I,exp-sim}^2(D) = \frac{\ln \sigma_{I,exp}^2(D) - \ln \sigma_{I,sim}^2(D)}{\ln \sigma_{I,sim}^2(D)} \quad (6.53)$$

$$\Delta \ln \sigma_{I,ana-sim}^2(D) = \frac{\ln \sigma_{I,ana}^2(D) - \ln \sigma_{I,sim}^2(D)}{\ln \sigma_{I,sim}^2(D)} \quad (6.54)$$

The simulated values can be calculated by averages  $\langle P \rangle$  and  $\langle P^2 \rangle$  over the sum of pixel counts  $P$  of the perturbed point source profile in the 512x512 simulation field. The scintillation index  $\sigma_{I,sim}^2(D)$  is then determined by averaging over all samples  $N_s = 1000$ :

$$\sigma_{I,sim}^2(D) = \frac{\langle P^2 \rangle_{N_s=1000}}{\langle P \rangle_{N_s=1000}^2} - 1 \quad (6.55)$$

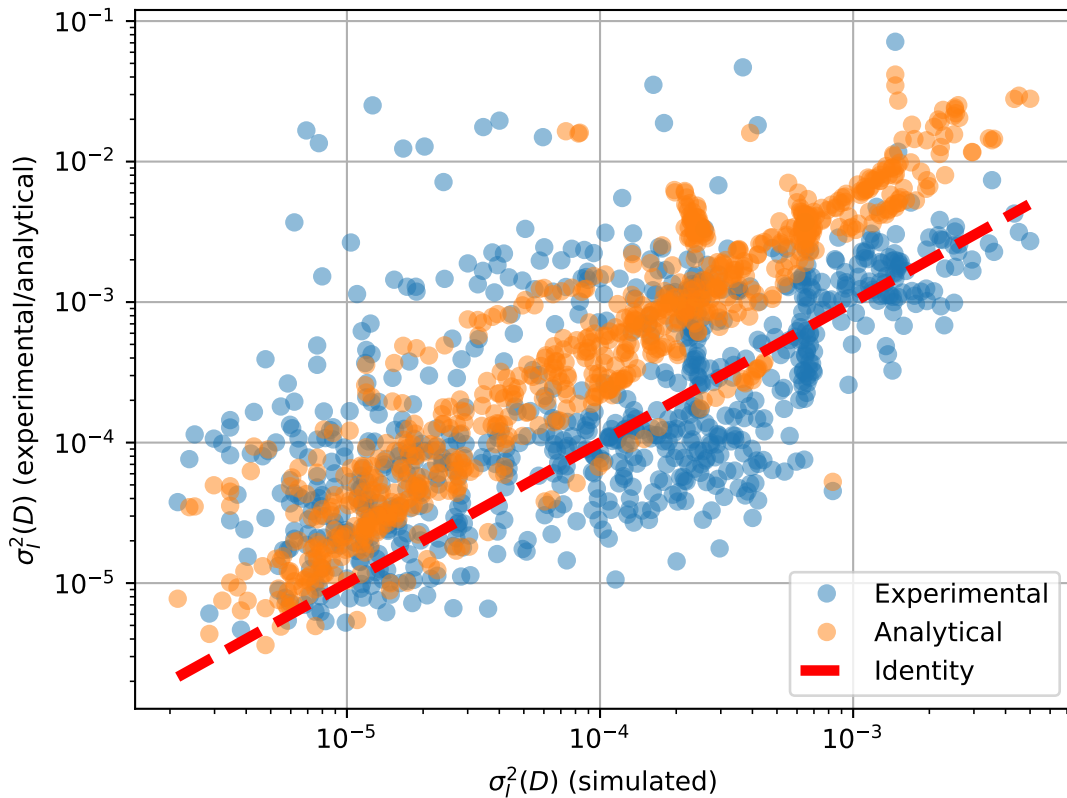
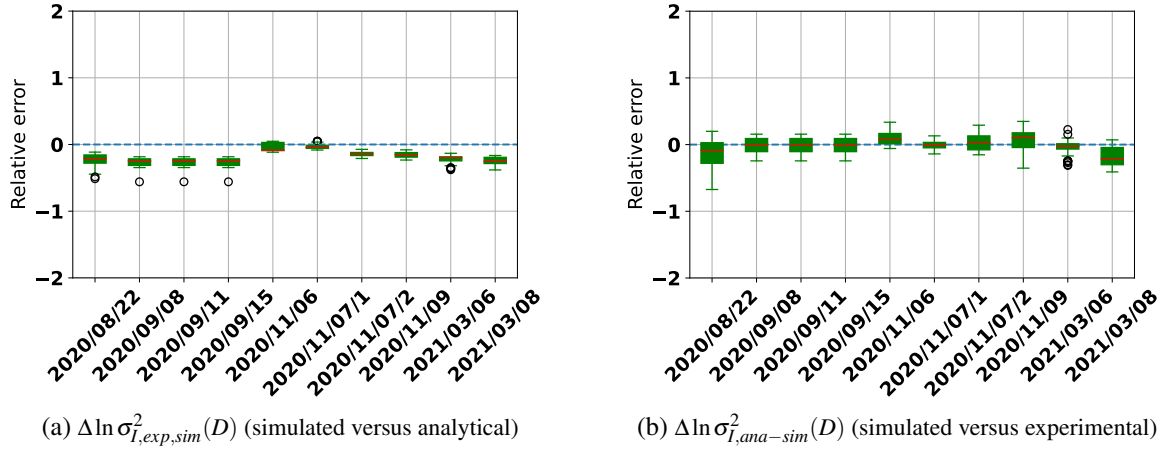
With the assumption of pixel counts approximately proportional to the received optical power per sensor pixel, for the experimental values the integrated optical power  $P$  can be calculated by averaging pixel counts over a single 28x28 region of interest (ROI). Furthermore, it is necessary to assume full coverage of aperture-averaged optical power related to a single LED element by the 28x28 ROIs. For very strong turbulence this assumption may be violated if significant irradiance contributions exceed the ROI or adjacent LED elements lead to additional irradiance fluctuations due to overlapping effects.

Then the single-ROI scintillation index can be calculated by averaging over the number of frames  $N = 100$  per video sequence:

$$\sigma_{I,ROI,exp}^2(D) = \frac{\langle P^2 \rangle_{N=100}}{\langle P \rangle_{N=100}^2} - 1 \quad (6.56)$$

Finally these values can be averaged over the entire LED matrix of  $N_{ROI_s} = 1008$  elements, i.e.  $\sigma_{I,exp}^2(D) = \left\langle \sigma_{I,ROI,exp}^2(D) \right\rangle_{N_{ROI_s}=1008}$ . In figure 6.24 box plots for the single comparisons simulated versus analytical and simulated versus experimental are shown over 10 recording dates. An average bias of about 25% for simulated vs analytical can be observed. This trend is also confirmed by the scatter plot for these recording dates in the same figure. It was already observed in the validation of simulations with uncorrelated phase screens (section 5.1.3). In contrast, the relative errors simulated versus experimental are much lower on average. This might be a hint for a multiplicative offset in the integral representation of  $\sigma_I^2(D)$  (equation 3.43). Also several outliers to high values can be observed in the experimental data.

Figure 6.24.: Box plots of relative errors of the log aperture-averaged scintillation index  $\ln \sigma_I^2(D)$  simulated versus analytical (left) and experimental (right) for several recording dates.  $\sigma_I^2(D)$  values are calculated for  $N = 50$  simulations based on retrieved model parameter sets from DTV fits, one per video sequence. Each simulation generates  $N_s = 1000$  frames of single perturbed point sources.



A higher number of acquired camera frames  $N$  or simulated frames  $N_s$  may further reduce these fluctuations. However, summations of pixel counts as integrated optical power  $P$  are also inflicted with camera

noise. So how strong is the camera noise in the experiment? And how large is its influence on the resulting effective  $\sigma_I^2(D)$  calculated from camera data? For Gaussian beam profiles a log-normal distribution of center irradiance can be assumed under weak turbulence conditions (Andrews and Phillips [2005]). With this assumption the real integrated power  $P$  can be modelled as  $\ln P$  to be normal distributed with  $\langle P \rangle = 1$  in arbitrary units. With the camera noise  $\varepsilon$  integrated over all pixels of a single ROI, the effective scintillation index can be calculated as

$$\sigma_{I,eff}^2 = \frac{\langle (P + \varepsilon)^2 \rangle}{\langle P + \varepsilon \rangle^2} - 1 \quad (6.57)$$

Detector noise can be modelled as Gaussian white noise with standard deviation  $\sigma_\varepsilon$ . If the scintillation index is assumed to be very low, i.e.  $\sigma_I^2(D) \ll 1$ , the difference between the maximum integrated power  $P$  and  $\langle P \rangle = 1$  can be neglected. Then the signal-to-noise ratio of detector noise can be expressed as

$$SNR[dB] = \log_{10} \left( \frac{1}{\sigma_\varepsilon} \right) \cdot 10 \quad (6.58)$$

In figure 6.25 effective scintillation indices  $\sigma_{I,eff}^2(D)$  are calculated by Monte Carlo simulations.  $N = 100$  values for  $P$  and  $\varepsilon$  are sampled for each  $\sigma_{I,eff}^2(D)$ . The same number  $N = 100$  values of  $\sigma_{I,eff}^2(D)$  are generated for different noise level  $\sigma_\varepsilon$ . Then a 95% confidence band is calculated for each noise level. It can be seen, that the effective  $\sigma_{I,eff}^2$  can be severely biased if the signal-to-noise ratio  $SNR[dB] < 30$  is bad. This effect will be all the more pronounced, the smaller the real scintillation index  $\sigma_I^2(D)$  is. The camera noise level  $\sigma_{\varepsilon,exp}$  in pixel counts can be estimated from camera data, by pixelwise calculation of standard deviations in dark 128x128 image sections from image corners far from the LED projections and averaging over all pixels in these image sections, i.e.

$$\sigma_{\varepsilon,exp} = \left\langle \sqrt{\left\langle (N_{ijk} - \langle N_{ijk} \rangle_i)^2 \right\rangle_i} \right\rangle_{jk} \quad (6.59)$$

with the image section data  $N_{ijk}$ , the frame index  $i$  and the row and column indices  $j$  and  $k$ . The maximal value  $P_{max}$  can be calculated from single frames containing all LED projections. Then the best case  $SNR$  is given as

$$SNR[dB] = \log_{10} \left( \frac{P_{max}}{\sigma_{\varepsilon,exp}} \right) \cdot 10 \quad (6.60)$$

The influence of different ROI sizes on the  $SNR$  can be investigated by applying pixel binning to the camera data with different binning factors before noise and peak power estimation, i.e. reducing the image dimensions by summing pixel counts within square blocks of sizes  $2^n \times 2^n$  with  $n \in [0, 6]$ . This is identical to the procedure of summing pixel values over regions of interest for the estimation of  $\sigma_I^2(D)$ . In figure 6.26 also the  $SNR$ , the peak value  $P_{max}$  and the noise level  $\sigma_{\varepsilon,exp}$  depending on the binning factors is shown for different recording dates based on a single video sequence captured on the respective date.

While cold days, e.g. 2020/11/09, tend to have a high  $SNR[dB] \approx 40$ , warm days, e.g. 2020/08/22, have a low  $SNR[dB] \approx 27$ . It can be observed that peak level  $P_{max}$  and noise level  $\sigma_{\varepsilon,exp}$  are reduced with increasing binning factor, as the image averaging leads to low pass filtering of the image content. Also the noise level  $\sigma_{\varepsilon,exp}$  strongly varies for different recordings dates, obviously with lower noise on cold days.

Therefore, camera noise can be a limitation factor for some days. The signal-to-noise ratio may be further improved by using better cameras with lower noise and a higher dynamic range. e.g. 16 bit per pixel instead of 14 bit used by the ZWO ASICAM 290MM Mono camera. Also active cooling and protection against direct sun exposure may be advisable. More powerful LEDs allow for shorter integration times to make the best use of the camera's dynamic range.

Figure 6.25.: Effective scintillation index  $\sigma_{I,eff}^2(D)$  for different real scintillation indices  $\sigma_I^2(D)$  depending on signal-to-noise ratio  $SNR[dB]$  associated with detector noise. A low  $SNR$  leads to biases of the effective scintillation index  $\sigma_{I,eff}^2(D)$  towards larger values.

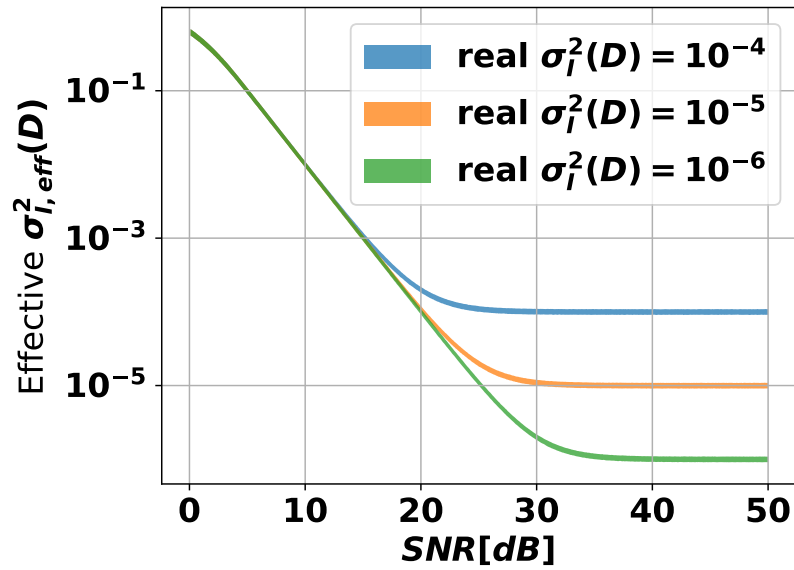
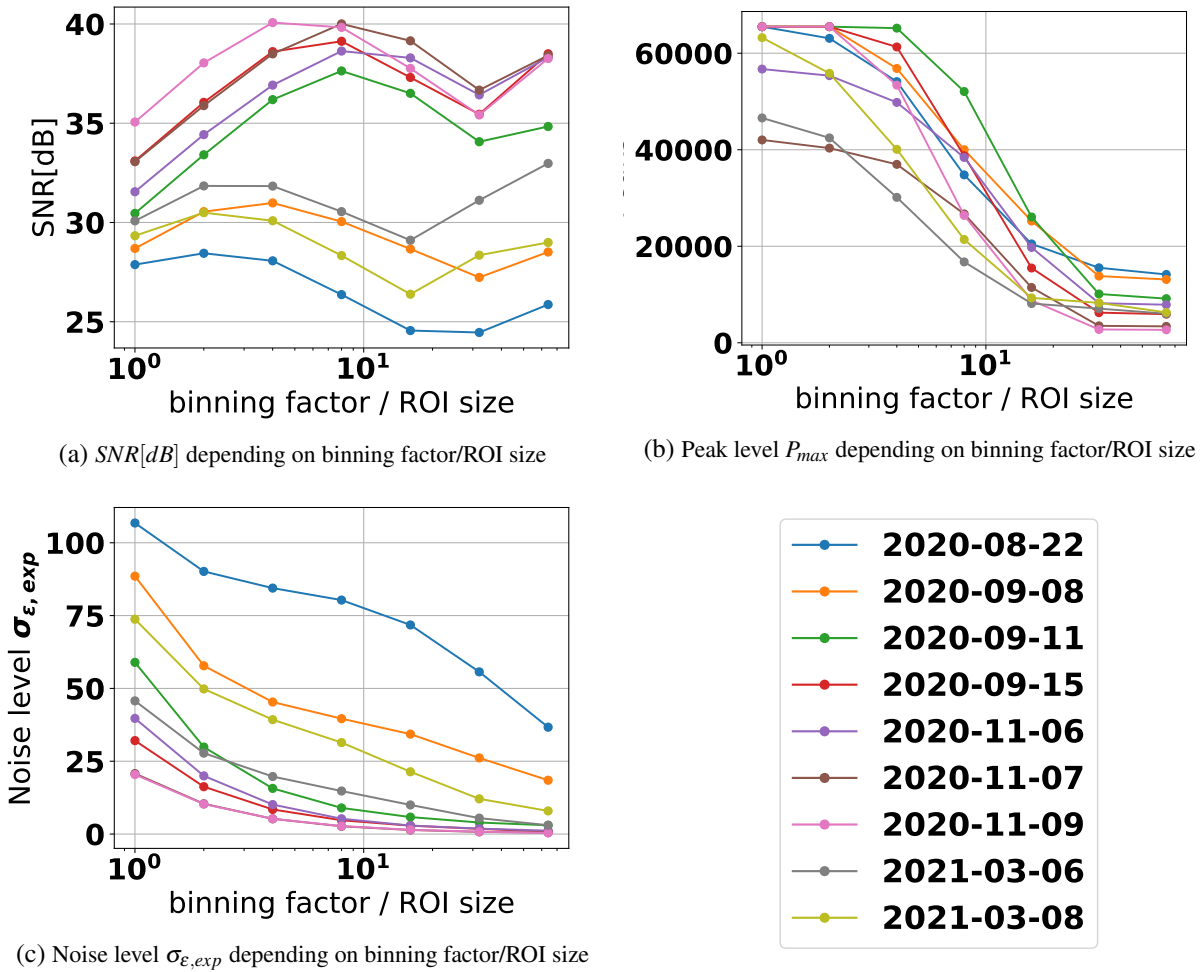


Figure 6.26.: Signal-to-noise ratio  $SNR[dB]$ , peak  $P_{max}$  and noise level  $\sigma_{\epsilon,exp}$  depending on binning factor/ROI size for different recording dates.



In summary, 500 video sequences are compared with simulations and analytical expressions based on the same turbulence parameters retrieved from DTF fits. 50 video sequences were used for 9 recording dates (2 data sets for 2020/11/7). 1D projections of the differential tilt variance  $DTV_{hor/vert}(\Delta x, \Delta y)$  and the long-exposure and short-exposure modulation transfer functions  $MTF_{LE/SE}(v_x, v_y)$  in horizontal and vertical direction were compared as well as the aperture-averaged scintillation index  $\sigma_I^2(D)$ . Within the given uncertainties these metrics showed good agreement between simulated values and experimental/analytical values. The deviations simulated versus analytical tend to be lower for DTVs and MTFs than the deviations simulated versus experimental. The deviations between simulated and experimental MTFs showed systematic biases indicating residual degradational effects represented by  $MTF_{residual}$ , which are similar on several recording dates. It is noteworthy, that these deviations could be achieved, although model parameter estimates were only based on DTV fits. It can be seen that MTF comparisons are vulnerable to residual degradational effects. On the other hand, measurements of the scintillation index  $\sigma_{I,eff}(D)$  are susceptible to camera noise. In principle, the signal-to-noise ratio can be increased

by pixel binning over larger image sections. However, this also requires larger separations of LED elements. Hence, a lower number of LEDs can be placed in the camera's field of view. Therefore, there is a tradeoff between fluctuations due to ensemble statistics and camera noise.

### 6.3. Cumulative distribution functions of turbulence parameters

For simulation and modelling of optical phenomena in the the atmosphere, scientific community often relies on turbulence models  $\Phi_n(\kappa, \mathbf{z})$  representing refractive index fluctuations in the air as power spectral densities. However, data distributions of these model parameters  $\mathbf{z}$  is quite unknown, especially their dependencies on environmental conditions such as terrain, daytime, weather, etc. Publicly available ground data is very rare. Hence, for realistic image-based turbulence simulations also considering uncertainties of model parameters  $\mathbf{z}$ , prior knowledge of the frequency distributions of these turbulence parameters is required.

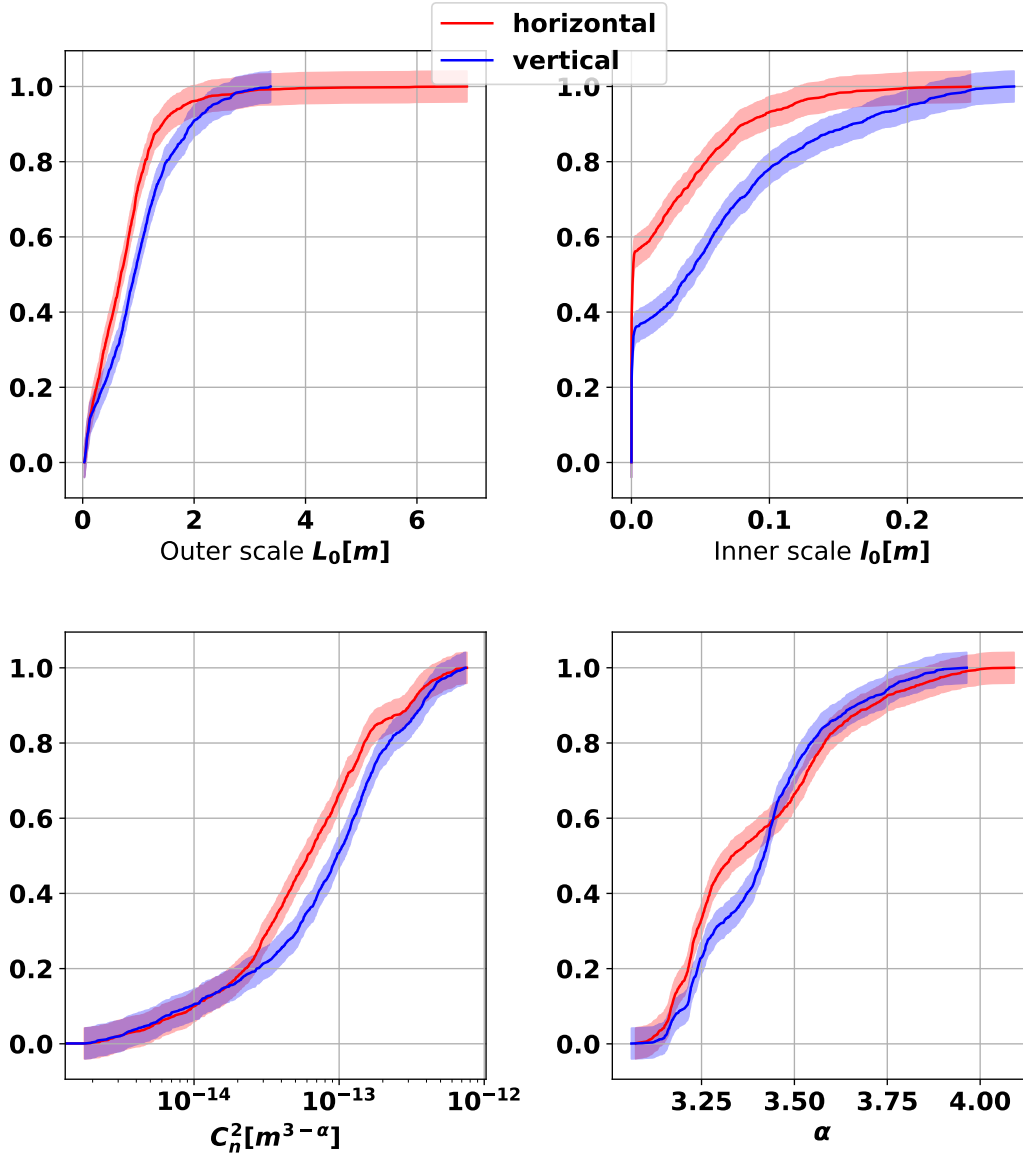
#### 6.3.1. Generalized modified von Kármán spectrum

In figure 6.27 the sample cumulative distribution functions  $CDF_{sample}(x)$  of the parameters  $L_0$ ,  $l_0$ ,  $\alpha$  and  $C_n^2$  for single turbulence parameters  $L_0$ ,  $l_0$ ,  $\alpha$  and  $C_n^2$  based on the spectrum GMVKS for the parameter sets retrieved from the  $N = 1112$  DTV fits are shown. The confidence band  $[CDF_{sample}(x) - \varepsilon, CDF_{sample}(x) + \varepsilon]$  is determined from the Dvoretzky–Kiefer–Wolfowitz inequality (Dvoretzky et al. [1956]):

$$\varepsilon = \sqrt{\frac{\ln\left(\frac{2}{\alpha}\right)}{2N}}, \quad (6.61)$$

where  $1 - \alpha$  is the confidence level with  $\alpha = 0.05$ . It can be seen that parameters in the horizontal direction have slightly lower values than in the vertical direction, especially the inner scale  $l_0$  and outer scale  $L_0$ . One possible explanation for this would be horizontal air flows contracting turbulence eddies in the horizontal direction. Interestingly this also occurs when only video sequences where no wind strength could be measured by the Anemometer are regarded. This may indicate that non-detectable small air flows can influence isotropy of turbulence significantly. For inner scale there is a cluster point at  $l_0 = 0$ . This reflects a low sensitivity of DTV on inner scale  $l_0$  compared to other turbulence parameters. As  $L_0 \ll dz$  compared to the default configuration for simulation (table 4.1), the use of 2D uncorrelated phase screens is justified under specified settings.

Figure 6.27.: Sample cummulative distribution function of turbulence parameter resulting from  $N = 1112$  DTV data fits based on the spectrum GMVKS. 95%-confidence bands based on the Dvoretzky–Kiefer–Wolfowitz inequality (Dvoretzky et al. [1956]) are shown.



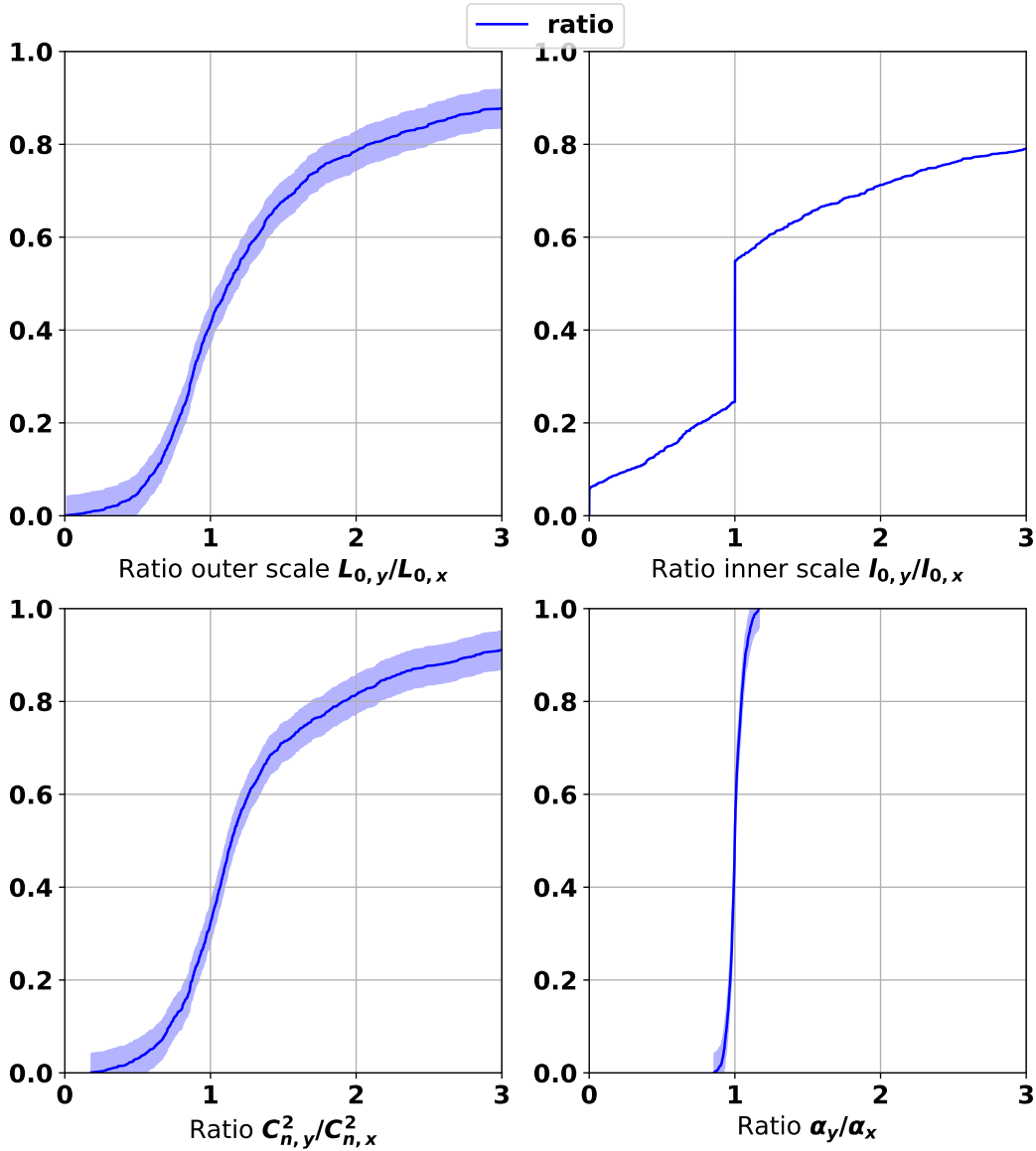
In table 6.3 sample means and standard deviations of the turbulence parameters for data fits in horizontal and vertical direction  $p_x$  and  $p_y$  are shown. The sample means for inner scale  $l_0$  and outer scale  $L_0$  are in good accordance with former experiments measuring inner scale  $l_0$  (Consortini et al. [2003]) and outer scale  $L_0$  (Gladysz [2017]). In order to assess anisotropy of turbulence parameters, also parameter ratios  $p_y/p_x$  are shown in figure 6.28. For the inner scale the ratio is set to 1 for very small  $l_0 < 10^{-10}$  m as ratios get numerically unstable. While the vertical vs horizontal ratios for turbulence strength  $C_n^2$ , the inner scale  $l_0$  and the outer scale  $L_0$  have similar empirical cummulative distribution functions, the ratio

Table 6.3.: Sample means and standard deviations of turbulence parameters based on spectrum GMVKS

Parameter	Horizontal	Vertical	Ratio Vertical/Horizontal
Outer scale $L_0$ in m	$0.8 \pm 1.3$	$1 \pm 1.4$	$1.7 \pm 1.6$
Inner scale $l_0$ in m	$0.03 \pm 0.08$	$0.06 \pm 0.13$	$1.5 \pm 1.8$
$C_n^2$ in $10^{-13} \text{m}^{3-\alpha}$	$1.1 \pm 2.5$	$1.4 \pm 2.9$	$1.6 \pm 1.3$
$\alpha$	$3.4 \pm 0.4$	$3.4 \pm 0.3$	$1.01 \pm 0.05$

for the exponent  $\alpha$  is very narrow. This may justify anisotropic models (Cui et al. [2015]) that have a fixed exponent but two-axis inner scales  $l_{0,x/y}$  and outer scales  $L_{0,x/y}$ .

Figure 6.28.: Cummulative distribution function of ratio vertical/horizontal of turbulence parameters resulting from  $N = 1112$  DTV data fits based on the spectrum GMVKS.



### 6.3.2. Generalized modified atmospheric spectrum

The same procedure as for the spectrum GMVKS can be repeated for the spectrum GMAS (equation 2.10). The empirical cumulative distribution functions for the parameters  $C_n^2$ ,  $L_0$ , and  $\alpha$  shown in figure 6.29 are similar to those for GMVKS. The additional parameters  $a, b$  and  $\alpha$  modify the spectrum for large spatial frequencies  $\kappa$ . Obviously the inner scale  $l_0$  is not stuck at very low values, in the fits. This can be explained by the fact, that the involving factor  $1 + a(\kappa/\kappa_l) + b(\kappa/\kappa_l)^\beta$  in equation 2.10 grows as the inner scale  $l_0$  increases, while for the spectrum GMVKS the corresponding factor  $\exp(-\kappa^2/\kappa_l^2)$  decays

exponentially and just as well partial derivatives of the loss function  $L(\mathbf{z}|\mathbf{x})$  with respect to the inner scale  $l_0$  required for the DTV fits. Again the horizontal components are slightly lower in distribution than the vertical components. In figure 6.30 the corresponding parameter ratios  $z_y/z_x$  are shown. While medians of  $a_y/a_x$ ,  $\alpha_y/\alpha_x$ ,  $\beta_y/\beta_x$  are centered at 1, medians of the remaining parameters are significantly larger than 1. Sample means for the GMAS parameters are shown in 6.4 Based on the losses  $f(\mathbf{z}|\mathbf{x})$  achieved in the DTV fits the additional parameters of the spectrum GMAS do not show significant improvements compared to the spectrum GMVKS. However, evaluations of GMAS were much slower compared to GMVKS due to case distinctions.

Figure 6.29.: Cummulative distribution function of turbulence parameters resulting from  $N = 1112$  DTV data fits based on the spectrum GMAS.

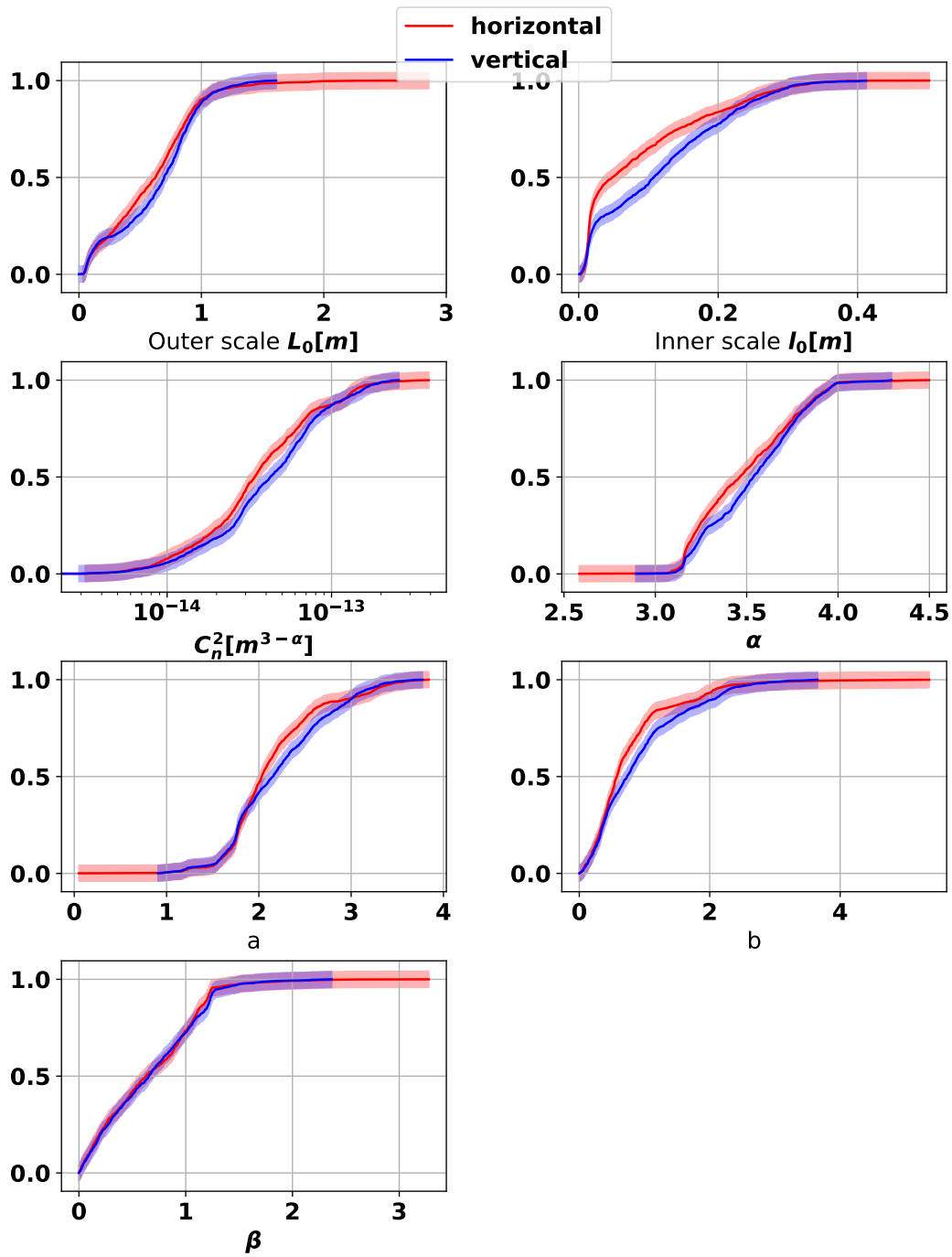


Figure 6.30.: Cumulative distribution function of ratio vertical/horizontal of turbulence parameters resulting from  $N = 1112$  DTV data fits based on the spectrum GMAS.

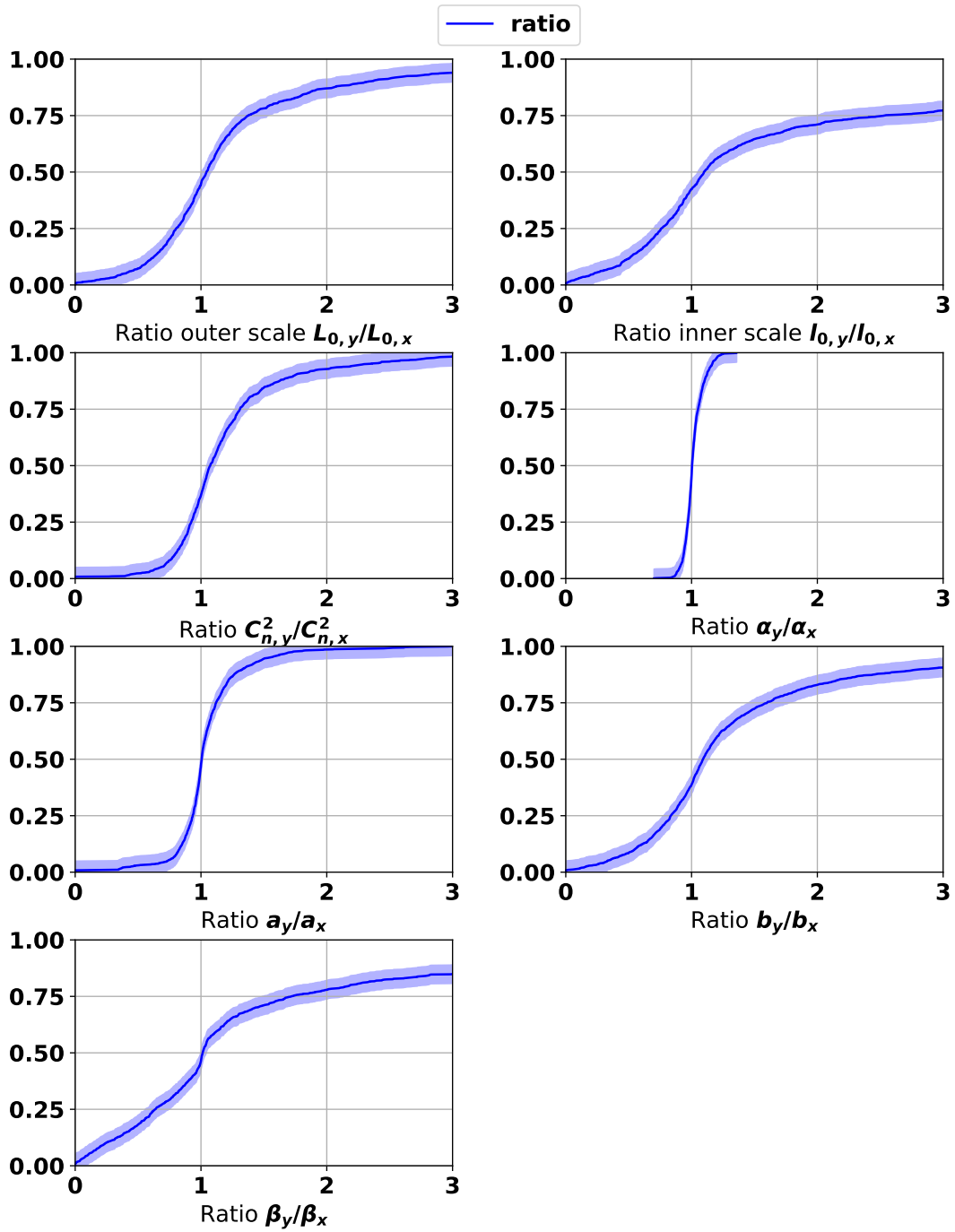


Table 6.4.: Sample means and standard deviations of turbulence parameters based on spectrum GMAS

Parameter	Horizontal	Vertical	ratio y/x
Outer scale $L_0$ in m	$0.5 \pm 0.7$	$0.6 \pm 0.7$	$1.4 \pm 1.2$
Inner scale $l_0$ in m	$0.09 \pm 0.2$	$0.1 \pm 0.2$	$3.2 \pm 4.7$
$C_n^2$ in $10^{-13} \text{m}^{3-\alpha}$	$0.4 \pm 0.9$	$0.5 \pm 1$	$1.3 \pm 0.6$
$\alpha$	$3.5 \pm 0.6$	$3.5 \pm 0.5$	$1.01 \pm 0.07$
a	$2.1 \pm 1.1$	$2.2 \pm 1.1$	$1.1 \pm 0.3$
b	$0.7 \pm 1.3$	$0.9 \pm 1.6$	$1.9 \pm 2.9$
$\beta$	$0.8 \pm 0.9$	$0.8 \pm 1$	$1.6 \pm 2.3$

Here model parameter distributions based on *DTV* fits for the two models GMVKS and GMAS were shown. For the common parameters  $C_n^2, L_0, l_0$  and  $\alpha$  both models have similar distributions.

It has to be taken into consideration, that any finite sample of recorded or simulated frames of perturbed point sources will always be inflicted with ensemble fluctuations. This inevitable also leads to fluctuations of the estimated model parameters and their degree of isotropy. While in a simulation the sample size can be arbitrarily increased for constant turbulence conditions, in experiments there is a tradeoff between stationary turbulence conditions and an increased number of recorded frames with lower ensemble fluctuations. Therefore, the simulation offers the possibility to investigate the expectable intrinsic parameter fluctuations for any sample size.

#### 6.4. Correlation between turbulence parameters

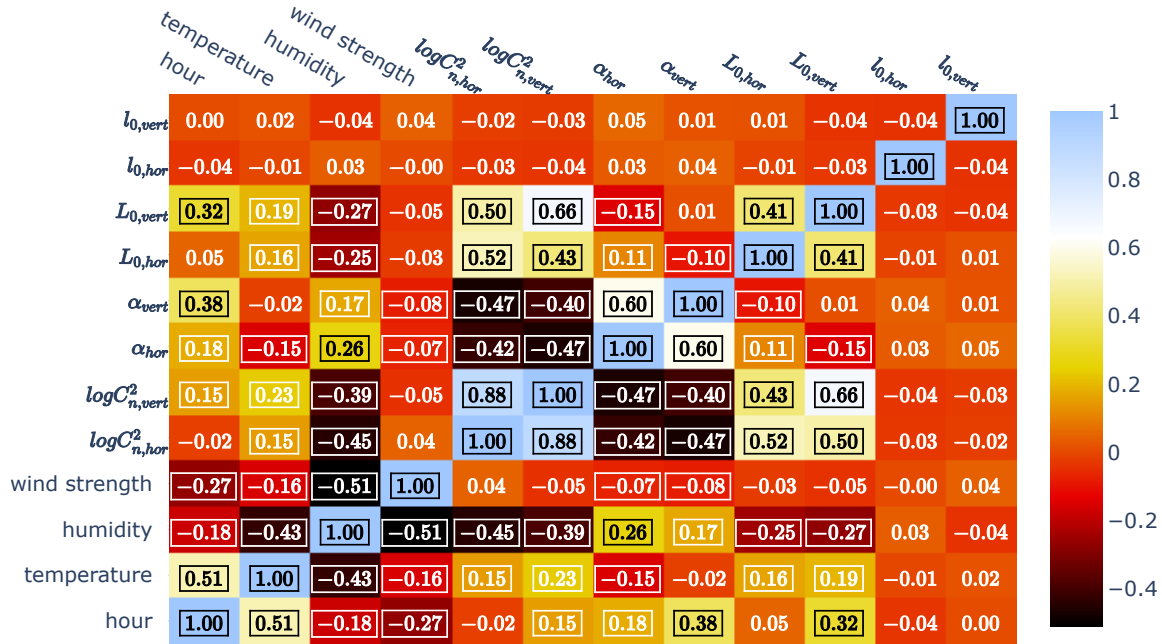
Measurements over several days have shown strong scattering of the meteorological data and the retrieved turbulence model parameters  $\mathbf{z}$ . The low amount of data makes it difficult to highlight dependencies between two quantities while fixing or binning the others. The knowledge of the interrelation of measurable meteorological quantities such as temperature, humidity, wind speed, etc. and the turbulence model parameters  $\mathbf{z}$  is useful, since data acquisition of these quantities is much faster than the image processing required for the *DTV* fitting approach. Hence, knowing these meteorological quantities would allow more precise estimations of the distributions of model parameters  $\mathbf{z}$ .

Nevertheless, a correlation matrix in figure 6.31 shows the correlation of parameters on the  $N = 1112$  *DTV* fits based on the spectrum GMVKS. For all fitted turbulence model parameters and the collected meteorological data, i.e. temperature, humidity and wind strength Pearson correlation coefficients  $r$  are calculated. These are parameter correlations over multiple video sequences and must not be confused with correlations between parameters for single *DTV* fits. Significant correlations with  $|r| > 1.96\sigma_r$ , where

$$\sigma_r = \sqrt{\frac{1-r^2}{n-2}} \quad (6.62)$$

are shown in frame boxes. Due to the logarithmic nature of the turbulence strength  $\log C_n^2$  is considered instead of  $C_n^2$ . It can be observed that for  $L_0, \alpha$  and  $C_n^2$  strong correlations exist between vertical and horizontal components. In contrast the inner scale  $l_0$  is not significantly correlated between axes as well as with outer parameters. One reason may be that for low values the influence on DTV is neglectable. There are strong correlations, positive ones between  $\log C_n^2$  and outer scale  $L_0$  and negative ones between  $\log C_n^2$  and  $\alpha$ . Significant correlations between model parameters and daytime hour, temperature, relative humidity exist. However, the acquired data may be biased due to the limited coverage of different environmental conditions, as these conditions are not intentionally controllable and measurements were done over limited time windows. Projections of retrieved model parameters on single meteorological properties from more extended field trials could provide better insight in the relevance of single turbulence model parameters. The parameter distributions in the previous section and the given correlation matrix may serve as a basis for comparison with further data acquisition experiments. Prior knowledge about turbulence model parameters and their dependency on measurable quantities, e.g. temperature, humidity and wind strength, geo location and daytime, is required for realistic simulations based on these model parameters.

Figure 6.31.: Correlation matrix of daytime hour, temperature, relative humidity, wind strength, and turbulence parameters for horizontal and vertical direction based on DTV fits on  $N = 1112$  video sequences with nominal frame number of 100 and a framerate  $f = 7$  Hz:  $C_{n,hor/vert}^2$ ,  $\alpha_{hor/vert}$ ,  $L_{0,hor/vert}$  and  $l_{0,hor/vert}$



### 6.5. Turbulence parameters versus date

In figures 6.32 and 6.33 the mean turbulence parameters resulting from the DTV fits for the GMVKS and the spectrum GMAS depending on recording date are shown. It can be observed that some days have strong anisotropic behaviour of inner and outer scales while other days, e.g. 2020/12/18 and 2020/12/26, are highly isotropic. This anisotropy is most often associated with longer vertical scales  $l_0$  and  $L_0$  compared to horizontal scales. For simulation this anisotropy can be taken into account by using anisotropic spectra for phase screen generation. For both spectra means of common turbulence model parameters  $l_0$ ,  $L_0$ ,  $\alpha$  and  $C_n^2$  are approximately in the same range. Anisotropy also seems to be lower for GMAS. However, the losses in the DTV fits were slightly lower than for GMAS. So the additional parameters  $a$ ,  $b$ ,  $\beta$  haven't improved the quality of fits.

To summarize, fitting of analytical expressions of differential tilt variances (equation 3.49) to numerical values (equation 5.10) calculated from recorded data can be used for estimation of turbulence model parameters  $\mathbf{z}$  of arbitrary 1D turbulence models  $\Phi_n(\kappa, \mathbf{z})$ . This is the first time, that a comparison of these

turbulence parameters was performed on several days at the same location under different meteorological conditions, i.e. daytime, temperature, humidity, for two current models, GMVKS and GMAS. The common parameters  $C_n^2$ ,  $\alpha$ ,  $l_0$  and  $L_0$  exhibited similar trends over several days. While some days are quite isotropic, i.e. have similar horizontal and vertical parameters, other days a highly anisotropic. On those days vertical scales  $l_0$  and  $L_0$  are generally larger compared to the horizontal ones. This fact confirms the necessity of anisotropic 2D turbulence models  $\Phi_n(\kappa_x, \kappa_y, \mathbf{z})$  (Cui et al. [2015]).

6. Evaluation of observed degraded images

Figure 6.32.: Means of turbulence parameters versus date for horizontal and vertical direction based on DTV fits for GMVKS on  $N = 1112$  video sequences with nominal frame number of 100 and a framerate  $f = 7\text{ Hz}$ :  $C_{n,hor/vert}^2$ ,  $\alpha_{hor/vert}$ ,  $L_{0,hor/vert}$  and  $l_{0,hor/vert}$

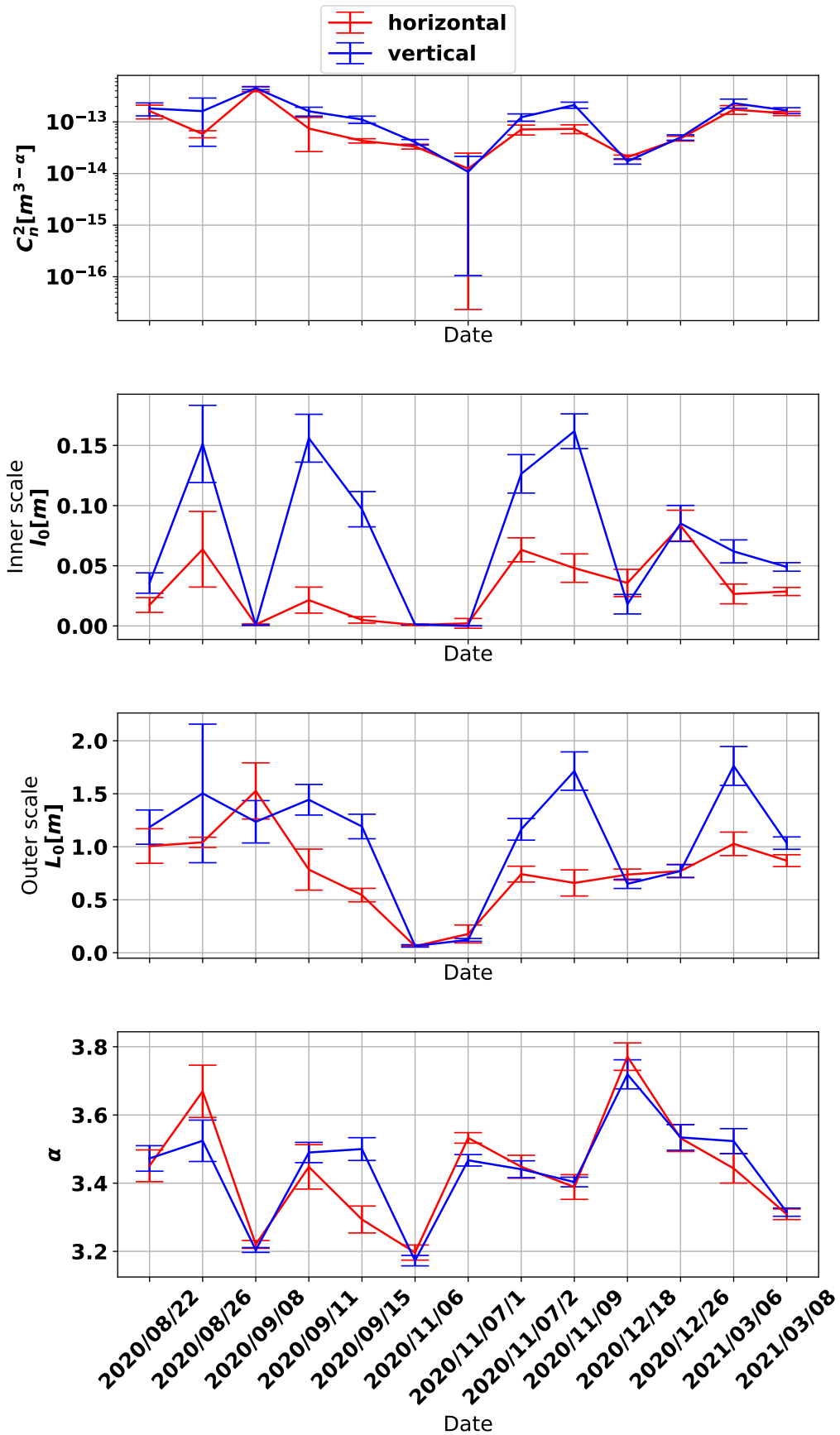
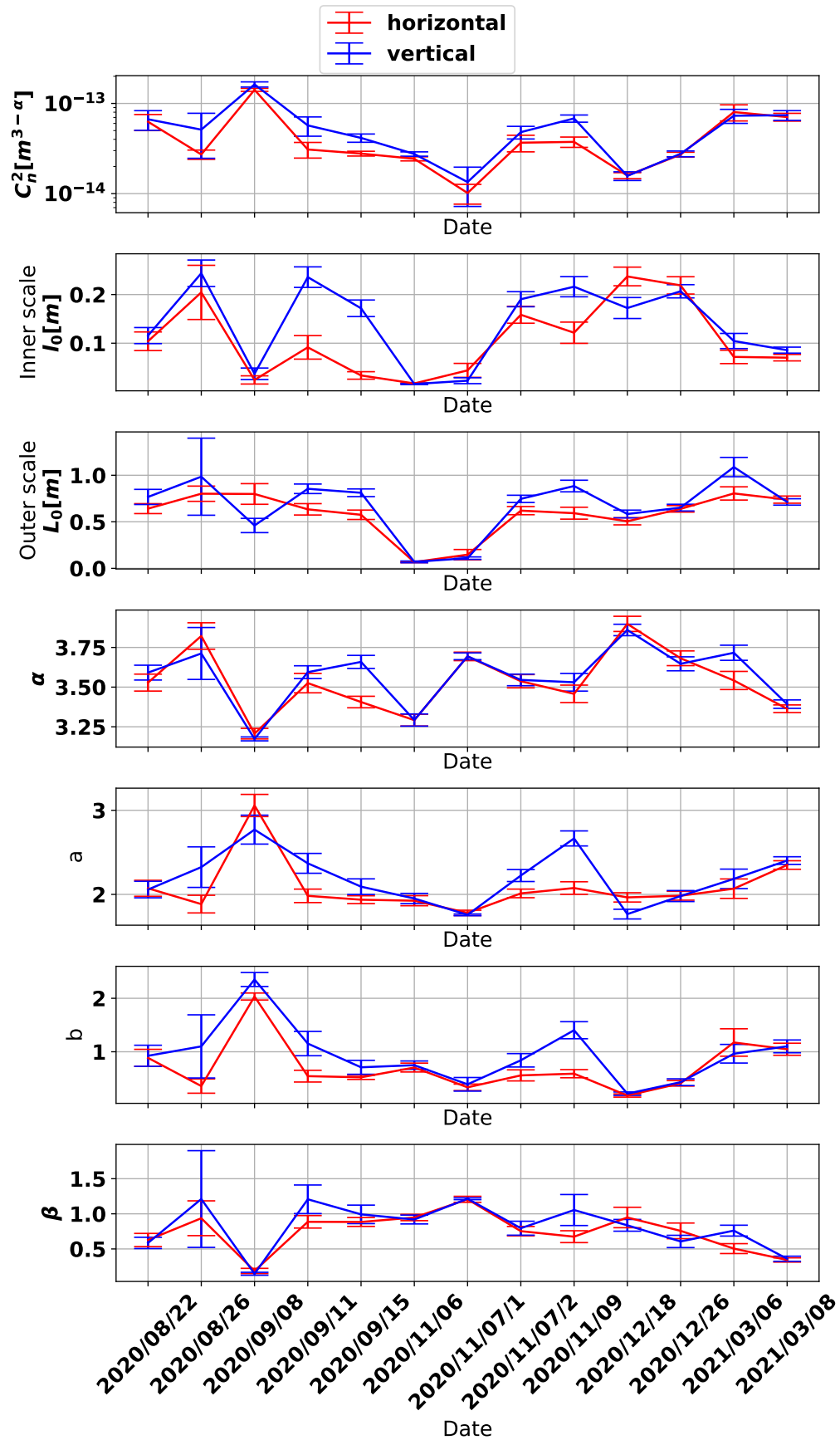


Figure 6.33.: Means of turbulence parameters versus date for horizontal and vertical direction based on DTV fits for GMAS on  $N = 1112$  video sequences with nominal frame number of 100 and a framerate  $f = 7$  Hz:  $C_{n,hor/vert}^2$ ,  $\alpha_{hor/vert}$ ,  $L_{0,hor/vert}$  and  $l_{0,hor/vert}$





## 7. Summary and outlook

In this thesis an implementation of the split-step beam propagation method based on turbulence phase screens was presented. Two methods for phase screen generation were compared, the FFT method with subharmonics for 2D uncorrelated phase screens and the sparse spectrum (SS) method for the generation of 2D correlated phase screens. Phase screens have been validated by the phase structure functions and properties of generated point spread functions have been validated for well-known figures of merit, i.e. long-exposure/short exposure modulation transfer functions (MTFs), Strehl ratio, differential tilt variance. The simulations with the FFT method showed lower statistical fluctuations around the expected analytical results than the sparse spectrum method for comparable computation times. Subsampling of shifted phase screens can be used to generate spatially correlated point spread function (PSF) grids. In general, these PSF grids can be used to simulate anisoplanatic turbulence degradation on multiple input images.

A new robust approach using ratios of long-exposure and short-exposure MTFs of measured LED profiles was able to give a rough estimate of turbulence strength  $C_n^2$  based on the Kolmogorov spectrum. In field trials projections of a LED matrix degraded by turbulence were recorded. It was shown that two spectra in the visible range,  $T = 6500$  K (blue) and  $T = 3000$  K (orange), have significant expected differences in the MTF ratios averaged over several video sequences, while statistical fluctuations were too high to distinguish between both reliably for single video sequences due to the low wavelength difference  $\Delta\lambda = \bar{\lambda}_{orange} - \bar{\lambda}_{blue} = 26$  nm.

Recorded video sequences of LED projections perturbed by air turbulence also allowed for determination of most likely turbulence model parameters by DTV data fitting based on measured centroid shifts. For each video sequence a single data set of model parameters could be calculated. For 1112 video sequences over several recording dates with an amount of about 500GB raw data these model parameters were calculated as well as their means and distributions. The calculated model parameter distributions and variety of average values over several recording dates is unprecedented. In contrast to single-shot simulations with known model parameters, these distributions also enable the assessment of uncertainties of simulation results related to varying environmental conditions represented by variations of the model parameters. The estimated model parameters were the key factor to feed turbulence simulations with the best possible match to measured data.

The two investigated turbulence models, the generalized modified von Kármán spectrum (GMVKS) and the generalized modified atmospheric spectrum (GMAS), showed similar model parameter distributions for the common parameters  $C_n^2$ ,  $\alpha$ ,  $l_0$  and  $L_0$ . Also similar are the distributions of parameter ratios vertical

versus horizontal. For both models it was shown, that the turbulence strength  $C_n^2$ , the outer scale  $L_0$  and the inner scale  $l_0$  tend to be larger in the vertical direction than in the horizontal direction, while the ratio vertical versus horizontal of the power slope  $\alpha$  is close to 1. However, projections of the model parameters on individual recording dates also show, that this anisotropy can strongly vary over several dates. More extensive field trials and projections of retrieved model parameters on meteorological data may help to identify the causes of this anisotropy and give adequate predictions of the strength of this anisotropy under certain environmental conditions. Despite the additional parameters  $a, b$  and  $\beta$  mainly modifying the high-frequency domain  $\kappa \approx 1/l_0$ , GMAS is not superior to GMVKS when comparing loss functions in the DTV fits. On the contrary, evaluations on GMAS are more complex and slower than those on GMVKS. As the refractive index of air  $n$  is dependent on temperature, pressure and humidity, the diagnosed distributions of model parameters  $\mathbf{z}$  for these two turbulence models  $\Phi_n(\kappa, \mathbf{z})$  may be used for validation of simulations or measurements of atmospheric microscale phenomena (Thunis and Bornstein [1996]). Estimated values for the outer scale  $L_0 \approx 1$  m indicated that for the specified simulation settings the assumption of uncorrelated phase screens holds and the FFT method with subharmonics can be safely used.

For two different recording dates simulations based on estimated model parameters  $\mathbf{z}$  showed good agreement between simulation, theory and experiment with respect to differential tilt variance. A mean bias of about 25% between simulation and experiment was observed which can be corrected by adapting turbulence strength  $C_n^2$  in the simulation accordingly. However, the data showed relatively low anisotropy in the model parameters for the two recording dates.

A new aspect is the comparison between differential tilt variances (DTV), long-exposure and short-exposure modulation transfer functions (MTFs) and the aperture-averaged scintillation index  $\sigma_I^2(D)$  for experimental, simulated and analytical data over several recording dates. The relative deviations between simulated and experimental or analytical data was similar for different dates and their medians below  $\pm 50\%$ .

The magnitude and variety of anisotropy observed in the distributions of retrieved model parameters shows the need and potential for further model enhancements to be used in the simulation. For more accurate modeling of strong anisotropy the differential tilt variance (DTV) fitting approach can be extended to anisotropic spectra. However, this increases the dimensionality of numerical integration and hence significantly the computational effort.

A great advantage of the split-step beam propagation method over other simulation methods, e.g. using Zernike modes (Chimitt and Chan [2020]) or data-constrained algorithms (Miller et al. [2019]), is the easy extensibility to other aperture forms such as telescope optics having obscurations. Also wind effects can be easily integrated by shifting phase screens or resampling at shifted spatial coordinates for the sparse spectrum method. A validated image-based turbulence simulation paves the path to find interrelations between model parameters  $\mathbf{z}$  and measurable quantities, for which analytical expressions

are not available. Simulated speckle patterns may help to design features sensitive to individual model parameters.

In practice, it is very difficult to adjust focus perfectly especially under strong turbulence conditions. In the simulation, additional defocussing effects can be easily investigated by adding parabolic phase modulations on the beam profiles arriving at the aperture plane.

In future experiments more metrics besides differential tilt variance could be measured and fitted to further refine estimates of most likely turbulence model parameters. One possibility are long-exposure and short-exposure MTFs. However, this requires a very good characterization of the other technical and optical components contributing to image degradation. Especially camera vibration induced by technical components or wind can lead to additional image shifts and hence deteriorate long-exposure MTF. As most current metrics are functionals of the turbulence model also depending on the aperture form, artificial aperture masking may help to increase the sensitivity to single model parameters. Random walks of shifted phase screens can be used to simulate temporally correlated frames for high acquisition frame rates where significant temporal correlation occurs. With this approach spatial correlation within the resulting frames is conserved, since the spatial statistics of the phase screens remain unchanged. Parameters controlling the random walks have to be adapted to obtain desired or measured temporal spectra of PSF centroid shifts in the simulated video sequence.



## A. Bibliography

- A. Abahamid, A. Jabiri, J. Vernin, Z. Benkhaldoun, M. Azouit, and A. Agabi. Optical turbulence modeling in the boundary layer and free atmosphere using instrumented meteorological balloons. *Astronomy & Astrophysics*, 416(3):1193–1200, Mar. 2004. ISSN 0004-6361, 1432-0746. doi: 10.1051/0004-6361:20031390. URL <https://www.aanda.org/articles/aa/abs/2004/12/aa3974/aa3974.html>.
- L. Andrews and R. Phillips. *Laser Beam Propagation Through Random Media*. SPIE Press monograph. SPIE Press, 2005. ISBN 9780819459480. URL <https://books.google.de/books?id=4NXHYg70qqIC>.
- F. Assémat, R. W. Wilson, and E. Gendron. Method for simulating infinitely long and non stationary phase screens with optimized memory storage. *Opt. Express*, 14(3):988–999, Feb 2006. doi: 10.1364/OE.14.000988. URL <http://www.opticsexpress.org/abstract.cfm?URI=oe-14-3-988>.
- A. Belmonte. Feasibility study for the simulation of beam propagation: Consideration of coherent lidar performance. *Appl. Opt.*, 39(30):5426–5445, Oct 2000. doi: 10.1364/AO.39.005426. URL <http://ao.osa.org/abstract.cfm?URI=ao-39-30-5426>.
- J. P. Bos and M. C. Roggemann. Technique for simulating anisoplanatic image formation over long horizontal paths. *Optical Engineering*, 51(10):1 – 9, 2012. doi: 10.1117/1.OE.51.10.101704. URL <https://doi.org/10.1117/1.OE.51.10.101704>.
- T. W. D. Bosq and E. Repasi. Detector integration time dependent atmospheric turbulence imaging simulation, 2015. URL <https://doi.org/10.1117/12.2176985>.
- S. Bosse, D. Maniry, K. R. Müller, T. Wiegand, and W. Samek. Deep neural networks for no-reference and full-reference image quality assessment. *IEEE Transactions on Image Processing*, 27(1):206–219, Jan 2018. ISSN 1057-7149. doi: 10.1109/TIP.2017.2760518.
- C. J. Carrano. Speckle imaging over horizontal paths. In J. D. Gonglewski, M. A. Vorontsov, M. T. Gruneisen, S. R. Restaino, and R. K. Tyson, editors, *High-Resolution Wavefront Control: Methods, Devices, and Applications IV*, volume 4825, pages 109 – 120. International Society for Optics and Photonics, SPIE, 2002. doi: 10.1117/12.453519. URL <https://doi.org/10.1117/12.453519>.

- M. P. J. L. Chang, C. O. Font, G. C. Gilbreath, and E. Oh. Humidity's influence on visible region refractive index structure parameter  $C(n)(2)$ . *Applied Optics*, 46(13):2453–2459, May 2007. ISSN 1559-128X. doi: 10.1364/ao.46.002453.
- M. Charnotskii. Sparse spectrum model of the sea surface. 01 2011. doi: 10.1115/OMAE2011-49958.
- M. Charnotskii. Intensity fluctuations of flat-topped beam in non-kolmogorov weak turbulence: comment. *J. Opt. Soc. Am. A*, 29(9):1838–1840, Sep 2012. doi: 10.1364/JOSAA.29.001838. URL <http://josaa.osa.org/abstract.cfm?URI=josaa-29-9-1838>.
- M. Charnotskii. Wave propagation modeling with non-markov phase screens. *J. Opt. Soc. Am. A*, 33(4): 561–569, Apr 2016. doi: 10.1364/JOSAA.33.000561. URL <http://josaa.osa.org/abstract.cfm?URI=josaa-33-4-561>.
- M. Charnotskii. Comparison of four techniques for turbulent phase screens simulation. *J. Opt. Soc. Am. A*, 37(5):738–747, May 2020. doi: 10.1364/JOSAA.385754. URL <http://josaa.osa.org/abstract.cfm?URI=josaa-37-5-738>.
- N. Chimitt and S. H. Chan. Simulating Anisoplanatic Turbulence by Sampling Inter-modal and Spatially Correlated Zernike Coefficients. *arXiv:2004.11210 [astro-ph, physics:physics]*, June 2020. URL <http://arxiv.org/abs/2004.11210>. arXiv: 2004.11210.
- A. Consortini, Y. Y. Sun, C. Innocenti, and Z. P. Li. Measuring inner scale of atmospheric turbulence by angle of arrival and scintillation. *Optics Communications*, 216(11&frac12;3):19 – 23, 2003. ISSN 0030-4018. doi: [http://dx.doi.org/10.1016/S0030-4018\(02\)02294-0](http://dx.doi.org/10.1016/S0030-4018(02)02294-0). URL <http://www.sciencedirect.com/science/article/pii/S0030401802022940>.
- L. Cui, B. Xue, and F. Zhou. Generalized anisotropic turbulence spectra and applications in the optical waves; propagation through anisotropic turbulence. *Optics Express*, 23(23):30088–30103, Nov. 2015. ISSN 1094-4087. doi: 10.1364/OE.23.030088. URL <https://www.osapublishing.org/oe/abstract.cfm?uri=oe-23-23-30088>.
- L.-y. Cui, X. Bin-dang, C. Xiao-guang, D. Jian-kang, and W. Jie-ning. Generalized atmospheric turbulence mtf for wave propagating through non-kolmogorov turbulence. *Opt. Express*, 18(20): 21269–21283, Sep 2010. doi: 10.1364/OE.18.021269. URL <http://www.opticsexpress.org/abstract.cfm?URI=oe-18-20-21269>.
- P. Drobinski, A. M. Dabas, and P. H. Flamant. Remote Measurement of Turbulent Wind Spectra by Heterodyne Doppler Lidar Technique. *Journal of Applied Meteorology (1988-2005)*, 39(12):2434–2451, 2000. ISSN 0894-8763. URL <https://www.jstor.org/stable/26184420>.

- A. Dvoretzky, J. Kiefer, and J. Wolfowitz. Asymptotic Minimax Character of the Sample Distribution Function and of the Classical Multinomial Estimator. *The Annals of Mathematical Statistics*, 27(3):642–669, Sept. 1956. ISSN 0003-4851, 2168-8990. doi: 10.1214/aoms/1177728174. URL <https://projecteuclid.org/journals/annals-of-mathematical-statistics/volume-27/issue-3/Asymptotic-Minimax-Character-of-the-Sample-Distribution-Function-and-of/10.1214/aoms/1177728174.full>.
- D. A. M. Engelbart, M. Kallistratova, and R. Kouznetsov. Determination of the turbulent fluxes of heat and momentum in the ABL by ground-based remote-sensing techniques (a Review). *Meteorologische Zeitschrift*, pages 325–335, Aug. 2007. ISSN ., doi: 10.1127/0941-2948/2007/0224. URL [https://www.schweizerbart.de/papers/metz/detail/16/55972/Determination\\_of\\_the\\_turbulent\\_fluxes\\_of\\_heat\\_and\\_momentum\\_in\\_the\\_ABL\\_by\\_ground\\_based\\_remote\\_sensing\\_techniques\\_a\\_Review](https://www.schweizerbart.de/papers/metz/detail/16/55972/Determination_of_the_turbulent_fluxes_of_heat_and_momentum_in_the_ABL_by_ground_based_remote_sensing_techniques_a_Review).
- J. A. Fleck, J. R. Morris, and M. D. Feit. Time-dependent propagation of high energy laser beams through the atmosphere. *Applied physics*, 10(2):129–160, June 1976. ISSN 1432-0630. doi: 10.1007/BF00896333. URL <https://doi.org/10.1007/BF00896333>.
- R. Foy and A. Labeyrie. Feasibility of adaptive telescope with laser probe. *Astronomy and Astrophysics*, 152(L29-L31), 1985.
- D. L. Fried. Optical resolution through a randomly inhomogeneous medium for very long and very short exposures. *J. Opt. Soc. Am.*, 56(10):1372–1379, Oct. 1966. URL <http://www.osapublishing.org/abstract.cfm?URI=josa-56-10-1372>.
- C. Gao, L. Su, and W. Yu. Long-term spreading of gaussian beam using generalized modified atmospheric spectrum. In *2015 IEEE International Conference on Mechatronics and Automation (ICMA)*, pages 2375–2380, Aug 2015. doi: 10.1109/ICMA.2015.7237858.
- S. Gladysz. Nearly complete characterization of optical turbulence with an led array. In *Imaging and Applied Optics 2017 (3D, AIO, COSI, IS, MATH, pcAOP)*, page PW1D.1. Optical Society of America, 2017. doi: 10.1364/PCAOP.2017.PW1D.1. URL <http://www.osapublishing.org/abstract.cfm?URI=pcAOP-2017-PW1D.1>.
- S. Gladysz, K. Stein, E. Sucher, and D. Sprung. Measuring non-kolmogorov turbulence. volume 8890, pages 8890 – 8890 – 10, 2013. doi: 10.1117/12.2031052. URL <http://dx.doi.org/10.1117/12.2031052>.
- J. W. Goodman. Introduction to fourier optics. *Introduction to Fourier optics, 3rd ed., by JW Goodman*. Englewood, CO: Roberts & Co. Publishers, 2005, 1, 2005.

- G. M. Hale and M. R. Query. Optical Constants of Water in the 200-nm to 200- $\mu$ m Wavelength Region. *Applied Optics*, 12(3):555–563, Mar. 1973. ISSN 2155-3165. doi: 10.1364/AO.12.000555. URL <https://www.osapublishing.org/ao/abstract.cfm?uri=ao-12-3-555>.
- M. J. Halmos and J. H. S. Wang. Laser radar systems and applications. In *Optical Technologies for Aerospace Sensing: A Critical Review*, volume 10269, page 102690H. International Society for Optics and Photonics, Nov. 1992. doi: 10.1117/12.161579. URL <https://www.spiedigitallibrary.org/conference-proceedings-of-spie/10269/102690H/Laser-radar-systems-and-applications/10.1117/12.161579.short>.
- R. C. Hardie, J. D. Power, D. A. LeMaster, D. R. Droege, S. Gladysz, and S. Bose-Pillai. Simulation of anisoplanatic imaging through optical turbulence using numerical wave propagation with new validation analysis. *Optical Engineering*, 56(7):1 – 16, 2017. doi: 10.1117/1.OE.56.7.071502. URL <https://doi.org/10.1117/1.OE.56.7.071502>.
- B. P. Hayden and R. A. Pielke. Planetary boundary layer. *Encyclopedia Britannica*, 2021. URL <https://www.britannica.com/science/planetary-boundary-layer>.
- G. C. Holst. *Electro-optical imaging system performance*. JCD Publishing, 5th edition, 2008. ISBN 978-0-8194-7406-3.
- Y. Ito. Errors in Wind Measurements Estimated by Five-Beam Phased Array Doppler Sodar. *Journal of Atmospheric and Oceanic Technology*, 14(4):792, Jan. 1997. doi: 10.1175/1520-0426(1997)014<textless{ }0792:EIWMEB<textgreater{ }2.0.CO;2.
- W. Jeong and J. Seong. Comparison of effects on technical variances of computational fluid dynamics (CFD) software based on finite element and finite volume methods. *International Journal of Mechanical Sciences*, 78:19–26, Jan. 2014. ISSN 0020-7403. doi: 10.1016/j.ijmecsci.2013.10.017. URL <https://www.sciencedirect.com/science/article/pii/S002074031300297X>.
- D. Kamenetsky, M. Zucchi, G. Nichols, D. Booth, and A. Lambert. Interactive atmospheric turbulence mitigation. In *2016 International Conference on Digital Image Computing: Techniques and Applications (DICTA)*, pages 1–8, Nov 2016. doi: 10.1109/DICTA.2016.7797055.
- M. A. Khalighi and M. Uysal. Survey on free space optical communication: A communication theory perspective. *IEEE Communications Surveys Tutorials*, 16(4):2231–2258, Fourthquarter 2014. ISSN 1553-877X. doi: 10.1109/COMST.2014.2329501.
- D. P. Kingma and J. Ba. Adam: A method for stochastic optimization. *CoRR*, abs/1412.6980, 2014. URL <http://arxiv.org/abs/1412.6980>.

- M. Koerber, D. Wegner, B. Schwarz, G. Ritt, S. Kessler, and B. Eberle. Testbed for thermal imager characterization using an infrared scene projector. *Proc.SPIE*, 10795:10795 – 10795 – 14, 2018. doi: 10.1117/12.2325106. URL <https://doi.org/10.1117/12.2325106>.
- R. C. L. C. Andrews, R. L. Phillips. Propagation of a gaussian-beam wave in general anisotropic turbulence. volume 9224, pages 9224 – 9224 – 12, 2014. doi: 10.1117/12.2061892. URL <http://dx.doi.org/10.1117/12.2061892>.
- R. G. Lane, A. Glindemann, and J. C. Dainty. Simulation of a kolmogorov phase screen. *Waves in Random Media*, 2(3):209–224, 1992. doi: 10.1088/0959-7174/2/3/003. URL <http://dx.doi.org/10.1088/0959-7174/2/3/003>.
- M. Laslandes, K. Patterson, and S. Pellegrino. Optimized actuators for ultrathin deformable primary mirrors. *Appl. Opt.*, 54(15):4937–4952, May 2015. URL <http://ao.osa.org/abstract.cfm?URI=ao-54-15-4937>.
- F. Lei and H. J. Tiziani. Atmospheric influence on image quality of airborne photographs. *Optical Engineering*, 32(9):2271–2280, Sept. 1993. ISSN 0091-3286, 1560-2303. doi: 10.1117/12.147156. URL <https://www.spiedigitallibrary.org/journals/optical-engineering/volume-32/issue-9/0000/Atmospheric-influence-on-image-quality-of-airborne-photographs/10.1117/12.147156.full>.
- J. Mann, J.-P. Cariou, M. S. Courtney, R. Parmentier, T. Mikkelsen, R. Wagner, P. Lindelöw, M. Sjöholm, and K. Enevoldsen. Comparison of 3D turbulence measurements using three staring wind lidars and a sonic anemometer. *IOP Conference Series: Earth and Environmental Science*, 1:012012, May 2008. ISSN 1755-1315. doi: 10.1088/1755-1315/1/1/012012. URL <https://doi.org/10.1088/1755-1315/1/1/012012>.
- T. S. McKechnie. Atmospheric turbulence and the resolution limits of large ground-based telescopes. *J. Opt. Soc. Am. A*, 9(11):1937–1954, Nov 1992. doi: 10.1364/JOSAA.9.001937. URL <http://josaa.osa.org/abstract.cfm?URI=josaa-9-11-1937>.
- K. J. Miller, B. Preece, T. W. Du Bosq, and K. R. Leonard. A data-constrained algorithm for the emulation of long-range turbulence-degraded video, 2019. URL <https://doi.org/10.1117/12.2519069>.
- F. Moll, J. Horwath, A. Shrestha, M. Brechtelsbauer, C. Fuchs, L. A. Martín Navajas, A. M. Lozano Souto, and D. Díaz González. Demonstration of High-Rate Laser Communications From a Fast Airborne Platform. *IEEE Journal on Selected Areas in Communications*, 33(9):1985–1995, Sept. 2015. ISSN 1558-0008. doi: 10.1109/JSAC.2015.2433054.

- R. D. Neidinger. Introduction to Automatic Differentiation and MATLAB Object-Oriented Programming. *SIAM Review*, 52(3):545–563, Jan. 2010. ISSN 0036-1445. doi: 10.1137/080743627. URL <https://epubs.siam.org/doi/10.1137/080743627>.
- R. Nieuwenhuizen and K. Schutte. Deep learning for software-based turbulence mitigation in long-range imaging, 2019. URL <https://doi.org/10.1117/12.2532603>.
- R. J. Noll. Zernike polynomials and atmospheric turbulence\*. *J. Opt. Soc. Am.*, 66(3):207–211, Mar 1976. doi: 10.1364/JOSA.66.000207. URL <http://www.osapublishing.org/abstract.cfm?URI=josa-66-3-207>.
- V. Nosov, V. Lukin, E. Nosov, A. Torgaev, and A. Bogushevich. Measurement of Atmospheric Turbulence Characteristics by the Ultrasonic Anemometers and the Calibration Processes. *Atmosphere*, 10(8):460, Aug. 2019. doi: 10.3390/atmos10080460. URL <https://www.mdpi.com/2073-4433/10/8/460>.
- J. C. Owens. Optical refractive index of air: Dependence on pressure, temperature and composition. *Appl. Opt.*, 6(1):51–59, Jan 1967. doi: 10.1364/AO.6.000051. URL <http://ao.osa.org/abstract.cfm?URI=ao-6-1-51>.
- B. Owren. Werner Romberg Vereinfachte numerische Integration. *Det Kongelige Norske Videnskabers Selskabs Skrifter*, 2011. ISSN 0368-6310. URL [https://www.ntnu.no/ojs/index.php/DKNVS\\_skrifter/article/view/1458](https://www.ntnu.no/ojs/index.php/DKNVS_skrifter/article/view/1458).
- B. C. Platt and R. B. Shack. History and principles of shack-hartmann wavefront sensing. *Journal of refractive surgery*, 17 5:S573–7, 2001.
- V. Rapoport, N. Mityakov, V. Zinichev, and Y. Sazonov. The study of atmospheric turbulence with an acoustic locator. *IEEE Transactions on Geoscience and Remote Sensing*, 40(2):247–250, Feb. 2002. ISSN 1558-0644. doi: 10.1109/36.992780.
- E. Repasi and R. Weiss. Analysis of image distortions by atmospheric turbulence and computer simulation of turbulence effects. volume 6941, 2008. doi: 10.1117/12.775600. URL <https://doi.org/10.1117/12.775600>.
- L. F. Richardson. *Weather Prediction by Numerical Process*. Cambridge Mathematical Library. Cambridge University Press, Cambridge, 2 edition, 2007. ISBN 9780521680448. doi: 10.1017/CBO9780511618291. URL <https://www.cambridge.org/core/books/weather-prediction-by-numerical-process/209AB84257409CF1BB624F97EC9CCA79>.
- F. Roddier. Curvature sensing and compensation: a new concept in adaptive optics. *Appl. Opt.*, 27(7): 1223–1225, Apr. 1988. URL <http://ao.osa.org/abstract.cfm?URI=ao-27-7-1223>.

- V. V. Samarkin, A. Alexandrov, and A. V. Kudryashov. Bimorph mirrors for powerful laser beam correction and formation, 2002. URL <https://doi.org/10.1117/12.454722>.
- J. D. Schmidt. Numerical simulation of optical wave propagation with examples in matlab. *SPIE Digital Library*, 2010.
- P. Thunis and R. Bornstein. Hierarchy of Mesoscale Flow Assumptions and Equations. *Journal of the Atmospheric Sciences*, 53(3):380–397, Feb. 1996. ISSN 0022-4928, 1520-0469. doi: 10.1175/1520-0469(1996)053<0380:HOMFAA>2.0.CO;2. URL [https://journals.ametsoc.org/view/journals/atsc/53/3/1520-0469\\_1996\\_053\\_0380\\_homfaa\\_2\\_0\\_co\\_2.xml](https://journals.ametsoc.org/view/journals/atsc/53/3/1520-0469_1996_053_0380_homfaa_2_0_co_2.xml).
- I. Toselli and V. F. Larry C. Andrews, Ronald L. Phillips. Angle of arrival fluctuations for free space laser beam propagation through non kolmogorov turbulence, 2007. URL <http://dx.doi.org/10.1117/12.719033>.
- I. Toselli, B. Agrawal, and S. Restaino. Light propagation through anisotropic turbulence. *J. Opt. Soc. Am. A*, 28(3):483–488, Mar 2011. doi: 10.1364/JOSAA.28.000483. URL <http://josaa.osa.org/abstract.cfm?URI=josaa-28-3-483>.
- A. Tunick and H. Rachele. Estimating effects of temperature and moisture on Cn2 in the damp unstable boundary layer for visible, infrared, radio, and millimeter wavelengths. In *Atmospheric Propagation and Remote Sensing*, volume 1688, pages 465–476. SPIE, Aug. 1992. doi: 10.1117/12.137914. URL <https://www.spiedigitallibrary.org/conference-proceedings-of-spie/1688/0000/Estimating-effects-of-temperature-and-moisture-on-Cn2-in-the/.full>.
- USA National Weather Service. Turbulence, 2021. "[https://www.weather.gov/source/zhu/ZHU\\_Training\\_Page/turbulence\\_stuff/turbulence/turbulence.htm](https://www.weather.gov/source/zhu/ZHU_Training_Page/turbulence_stuff/turbulence/turbulence.htm) and [http://web.archive.org/web/20210616065134/https://www.weather.gov/source/zhu/ZHU\\_Training\\_Page/turbulence\\_stuff/turbulence/turbulence.htm](http://web.archive.org/web/20210616065134/https://www.weather.gov/source/zhu/ZHU_Training_Page/turbulence_stuff/turbulence/turbulence.htm)" retrieved on 12/16/2021.
- A. M. Vorontsov, P. V. Paramonov, M. T. Valley, and M. A. Vorontsov. Generation of infinitely long phase screens for modeling of optical wave propagation in atmospheric turbulence. *Waves in Random and Complex Media*, 18(1):91–108, 2008. doi: 10.1080/17455030701429962. URL <https://doi.org/10.1080/17455030701429962>.
- M. A. Vorontsov and G. W. Carhart. Anisoplanatic imaging through turbulent media: image recovery by local information fusion from a set of short-exposure images. *J. Opt. Soc. Am. A*, 18(6):1312–1324, June 2001. URL <http://josaa.osa.org/abstract.cfm?URI=josaa-18-6-1312>.
- B. Xue, L. Cui, W. Xue, X. Bai, and F. Zhou. Generalized modified atmospheric spectral model for optical wave propagating through non-kolmogorov turbulence. *J. Opt. Soc. Am. A*, 28(5):912–916,

May 2011. doi: 10.1364/JOSAA.28.000912. URL <http://josaa.osa.org/abstract.cfm?URI=josaa-28-5-912>.

L. Yatcheva, R. Barros, M. Segel, D. Sprung, E. Sucher, C. Eisele, and S. Gladysz. Ultimate turbulence experiment: simultaneous measurements of  $C_n^2$  near the ground using six devices and eight methods. In K. U. Stein and J. D. Gonglewski, editors, *Optics in Atmospheric Propagation and Adaptive Systems XVIII*, volume 9641, pages 28 – 35. International Society for Optics and Photonics, SPIE, 2015. doi: 10.1117/12.2195029. URL <https://doi.org/10.1117/12.2195029>.

X. Zhu and P. Milanfar. Removing atmospheric turbulence via space-invariant deconvolution. *IEEE Transactions on Pattern Analysis and Machine Intelligence*, 35(1):157–170, 2013.

## B. List of Figures

1.1	Dual use scheme: 1. An image based simulation can be used for turbulence model improvements. 2. Simulated image sequences with turbulence degradation can be used for applications that rely on image assessment (digital turbulence mitigation, lab-based imager assessment) . . . . .	4
2.1	Illustration of turbulence near ground: 1. Solar heating of the earth’s surface forms convection cells: Warm air rises and cools down, while cold air descends and warms up. 2. Obstacles and the uneven surface of the earth cause friction between air currents and the ground. 3. Different types of terrain absorb sun radiation to different degrees, which leads to temperature inhomogeneities. . . . .	7
2.2	Kolmogorov cascade theory of turbulence. $L_0$ denotes the outer scale and $l_0$ the inner scale. Eddies between scale sizes $l_0$ and $L_0$ form the inertial subrange (Adaptation of a figure in Andrews and Phillips [2005]). . . . .	9
2.3	Effects of outer scale $L_0$ and inner scale $l_0$ on spectrum: . . . . .	13
2.4	Measured mean values and models of outer scale $L_0$ and turbulence strength $C_n^2$ depending on altitude $h$ (data extracted from Abahamid et al. [2004]) . . . . .	15
3.1	Image degradation process: Final PSF results from subsequent convolution with PSFs related to single degradation effects. Final OTF results from subsequent pixelwise multiplication of OTFs related to same single degradation effects. Gray scale images encode values in $[0, 1]$ , with black = 0, and white = 1 . . . . .	19
3.2	Illustration of two point sources projected onto a camera. The angle of arrivals $\sigma_x(\mathbf{r})$ and $\theta_x(\mathbf{r} + \mathbf{d})$ fluctuate around time-averaged center positions. . . . .	27
3.3	$\log_{10}(\Delta q)$ for relative errors $\Delta q = (q(N) - q(5000))/q(5000)$ of different quantities $q$ depending on number of integral subdivisions $N$ . 95%-confidence bands are shown. Min and max values are shown as dashed lines. $\log_{10}(\text{Mean computation time in ms})$ for single calls are shown on the right vertical axis (black line). . . . .	33
4.1	Single split step: Input beam profile $U_n$ at $z = z_n$ is converted to output profile $U_{n+1}$ at $z = z_n + \Delta z$ . Images show corresponding intensity profiles $I =  U ^2$ of complex fields $U$ . . . . .	38

4.2	A discrete (I)FFT spectrum can only represent a turbulence spectrum at a limited number of equidistant spatial frequencies. Most models for turbulence spectra have high contributions at low frequencies, which cannot be represented by the (I)FFT spectrum . . . . .	39
4.3	Beam propagation along a distance $L$ : A final complex field $U_n(x,y)$ is calculated by multiple iterations of the single step (4.22). For the phase screen operators $\{S_{P,i}\}_{i=1..n}$ a sequence of varying phase screens $\{\varphi_i(x,y)\}_{i=1..n}$ is used. . . . .	40
4.4	Subharmonic division: The zero component $\kappa = 0$ is subdivided by an integer fraction in horizontal and vertical direction, here by 3. Weights of the subharmonics of level $p$ are calculated depending on the extend in Fourier space $\Delta\kappa_{x/y}^{(p)} = \Delta\kappa_{x,y}/3^p$ . $\Delta\kappa_{x/y}$ are the smallest spatial frequencies in the discrete Fourier transform . . . . .	41
4.5	Phase screens for varying outer scale $L_0$ and GMVKS: (a) $L_0 = 0.1$ m, (b) $L_0 = 1$ m, (c) $L_0 = 10$ m, (d) $L_0 = 100$ m. The outer scale $L_0$ limits low frequency contributions. A decreasing outer scale $L_0$ is related to decreased low frequency contributions. . . . .	45
4.6	Phase screens for varying inner scale $l_0$ and GMVKS: (a) $l_0 = 0.001$ m, (b) $l_0 = 0.01$ m, (c) $l_0 = 0.02$ m, (d) $l_0 = 0.1$ m. . . . .	46
4.7	Phase screens for varying exponent $\alpha$ and GMVKS: (a) $\alpha = 3.1$ , (b) $\alpha = 3.4$ , (c) $\alpha = 11/3$ , (d) $\alpha = 3.9$ . . . . .	47
4.8	Comparison of analytical phase structure functions $D_\varphi(r,0)$ and sample structure function $D(x,0)$ and $D(0,y)$ based on horizontal/vertical separations for varying outer scale $L_0$ and GMVKS: (a) $L_0 = 0.1$ m, (b) $L_0 = 1$ m, (c) $L_0 = 10$ m, (d) $L_0 = 100$ m. Colored regions are 95%-confidence bands of the sample structure functions $D_{hor/vert}$ . The analytical Markov structure function (black line) is mainly in the confidence bands of the numerical structure functions (red and blue line). . . . .	49
4.9	Analytical Markov phase structure function $D_\varphi^{(MA)}(r,0)$ for varying turbulence parameters $l_0$ (a), $L_0$ (b), and $\alpha$ (c) based on the model GMVKS. Default values are $C_n^2/m^{3-\alpha} = 10^{-13}$ , $l_0 = 0.01$ m, $L_0 = 1.0$ m, $\alpha = 11/3$ and $L = 150$ m. . . . .	50
4.10	Phase structure function for varying inner scale $l_0$ and GMVKS: (a) $l_0 = 0.001$ m, (b) $l_0 = 0.005$ m, (c) $l_0 = 0.01$ m, (d) $l_0 = 0.1$ m. . . . .	51
4.11	Phase structure function for varying exponent $\alpha$ and GMVKS: (a) $\alpha = 3.1$ , (b) $\alpha = 3.4$ , (c) $\alpha = 11/3$ , (d) $\alpha = 3.9$ . . . . .	52
4.12	Comparison of phase screens for varying phase screen thickness $\Delta z$ and number of plane waves $N_{waves}$ . . . . .	56
4.13	Phase screens for varying outer scale $L_0$ and GMVKS: (a) $L_0 = 0.1$ m, (b) $L_0 = 1$ m, (c) $L_0 = 10$ m, (d) $L_0 = 100$ m. The outer scale $L_0$ limits low frequency contributions. A decreasing outer scale $L_0$ is related to decreased low frequency contributions. . . . .	58
4.14	Phase screens for varying exponent $\alpha$ and GMVKS: (a) $\alpha = 3.1$ , (b) $\alpha = 3.4$ , (c) $\alpha = 11/3$ , (d) $\alpha = 3.9$ . . . . .	59

4.15	Comparison of analytical transversal Non-Markov phase structure function $D^{(NM)}(r,0)$ and sample phase structure function $D_\phi(r,0)$ for varying outer scale $L_0$ and GMVKS: (a) $L_0 = 0.1$ m, (b) $L_0 = 1$ m, (c) $L_0 = 10$ m, (d) $L_0 = 100$ m. Colored regions are 95%-confidence bands of the sample structure functions $D_{hor/vert}$ . The analytical Non-Markov structure function (black line) is mainly in the confidence bands of the numerical structure functions (red and blue line). . . . .	61
4.16	Longitudinal phase structure function $D_\phi(0, m\Delta z)$ for varying outer scale $L_0$ and GMVKS: (a) $L_0 = 0.1$ m, (b) $L_0 = 1$ m, (c) $L_0 = 10$ m, (d) $L_0 = 100$ m. . . . .	62
4.17	Analytical radial Non-Markov phase structure function $D_\phi^{(NM)}(r,0)$ for varying turbulence parameters $l_0$ (a), $L_0$ (b), and $\alpha$ (c) based on the model GMVKS. Default values are $C_n^2 = 10^{-13} \text{ m}^{3-\alpha}$ , $l_0 = 0.01$ m, $L_0 = 1.0$ m, $\alpha = 11/3$ and $L = 150$ m . . . . .	64
4.18	Analytical longitudinal Non-Markov phase structure function $D_\phi^{(NM)}(0, m \cdot \Delta z)$ for varying turbulence parameters $l_0$ (a), $L_0$ (b), and $\alpha$ (c) based on the model GMVKS. Default values are $C_n^2 = 10^{-13} \text{ m}^{3-\alpha}$ , $l_0 = 0.01$ m, $L_0 = 1.0$ m, $\alpha = 11/3$ , $L = 150$ m and $\Delta z = 15$ m. . . . .	65
4.19	Phase structure function for varying exponent $\alpha$ and GMVKS: (a) $\alpha = 3.1$ , (b) $\alpha = 3.4$ , (c) $\alpha = 11/3$ , (d) $\alpha = 3.9$ . . . . .	66
4.20	Example of rippling effects in beam profile $I_n(x,y) =  U_n(x,y) ^2$ for a propagated point source. Aperture masking filters only pixels in the aperture area. . . . .	67
4.21	Workflow of PSF calculation: 1. A beam profile emulating a point source is propagated through a sequence of phase screens. 2. The resulting profile $U_n(x,y)$ is masked by a circular aperture. 3. Fourier optics gives the point spread function $P(u,v)$ . 4. A rescaling of frequencies $x = u/(\lambda f)$ and $y = v/(\lambda f)$ gives the point spread function $P(x,y)$ in the sensor plane . . . . .	69
4.22	Spatial subsampling of phase screens: PSFs for different viewing angles are calculated by subsampling of different regions of interest (colored boxes) of same phase screens $\phi_n(x,y)$ via bilinear interpolation . . . . .	70
4.23	Example of PSF interpolation for 13x13 image. $PSF(1,2, \Delta x, \Delta y)$ is calculated based on four adjacent point spread functions $PSF_{0,0}, PSF_{0,1}, PSF_{1,0}$ and $PSF_{1,1}$ according to equation 4.80 . . . . .	72
4.24	Turbulence-degraded frames of radial sinusoidal pattern with varying pattern period in pixel and varying turbulence strengths $C_n^2/(m^{-2/3})$ . Color range is set uniquely to [0,65535]. . . . .	73
5.1	Long-exposure MTF for varying turbulence strengths $C_n^2$ and GMVKS: (a) $C_n^2 = 10^{-16} \text{ m}^{-2/3}$ , (b) $C_n^2 = 10^{-15} \text{ m}^{-2/3}$ , (c) $C_n^2 = 10^{-14} \text{ m}^{-2/3}$ , (d) $C_n^2 = 10^{-13} \text{ m}^{-2/3}$ . The cutoff frequency $\nu_{cutoff}$ is shown as vertical line. . . . .	77
5.2	Short-exposure MTF for varying turbulence strengths $C_n^2$ and GMVKS: (a) $C_n^2 = 10^{-16} \text{ m}^{-2/3}$ , (b) $C_n^2 = 10^{-15} \text{ m}^{-2/3}$ , (c) $C_n^2 = 10^{-14} \text{ m}^{-2/3}$ , (d) $C_n^2 = 10^{-13} \text{ m}^{-2/3}$ . . . . .	79

5.3	Image section with 10x10 PSFs for two turbulence strengths: (a) $C_n^2 = 10^{-13} \text{ m}^{-2/3}$ , (b) $C_n^2 = 10^{-12} \text{ m}^{-2/3}$ . Shapes of PSFs vary spatially. PSFs are correlated between different positions depending on distance. . . . .	81
5.4	Differential tilt variance (DTV) for varying turbulence strengths $C_n^2$ and GMVKS with 95%-confidence bands: 1. Parallel: $DTV_x(\Delta x, 0)$ , 2. Perpendicular $DTV_y(\Delta x, 0)$ , (a) $C_n^2 = 10^{-15} \text{ m}^{-2/3}$ , (b) $C_n^2 = 10^{-14} \text{ m}^{-2/3}$ , (c) $C_n^2 = 10^{-13} \text{ m}^{-2/3}$ , (d) $C_n^2 = 10^{-12} \text{ m}^{-2/3}$ . . . . .	83
5.5	Aperture-averaged scintillation $\sigma_I^2(D)$ dependent on turbulence strengths $C_n^2$ for the turbulence spectrum GMVKS . . . . .	85
5.6	Strehl ratio $S$ dependent on turbulence strength $C_n^2$ for the turbulence spectrum GMVKS . . . . .	86
5.7	Long-exposure MTF for varying turbulence strengths $C_n^2$ and GMVKS: (a) $C_n^2 = 10^{-16} \text{ m}^{-2/3}$ , (b) $C_n^2 = 10^{-15} \text{ m}^{-2/3}$ , (c) $C_n^2 = 10^{-14} \text{ m}^{-2/3}$ , (d) $C_n^2 = 10^{-13} \text{ m}^{-2/3}$ . . . . .	88
5.8	Short-exposure MTF for varying turbulence strengths $C_n^2$ and GMVKS: (a) $C_n^2 = 10^{-16} \text{ m}^{-2/3}$ , (b) $C_n^2 = 10^{-15} \text{ m}^{-2/3}$ , (c) $C_n^2 = 10^{-14} \text{ m}^{-2/3}$ , (d) $C_n^2 = 10^{-13} \text{ m}^{-2/3}$ . . . . .	89
5.9	Differential tilt variance (DTV) for varying turbulence strengths $C_n^2$ and GMVKS: (a) $C_n^2 = 10^{-15} \text{ m}^{-2/3}$ , (b) $C_n^2 = 10^{-14} \text{ m}^{-2/3}$ , (c) $C_n^2 = 10^{-13} \text{ m}^{-2/3}$ , (d) $C_n^2 = 10^{-12} \text{ m}^{-2/3}$ . . . . .	91
5.10	Aperture-averaged scintillation index dependent on turbulence strengths $C_n^2$ for the turbulence spectrum GMVKS . . . . .	92
5.11	Strehl ratio dependent on turbulence strengths $C_n^2$ for the turbulence spectrum GMVKS . . . . .	93
6.1	Lumitronix LED spectrum measured by QWave spectrometer and weighted by ASICAM 290MM Mono spectral responsivity . . . . .	98
6.2	Experimental scene at 48°59'55"N 8°17'05"E: A telezoom objective Wallimex Pro 650 mm-1300 mm is plugged to a monochrome telescope camera ZWO ASI290MM. For data acquisition the camera is connected to a laptop via USB3. The camera is pointing to a target of 56x18 LEDs in about 150 m . . . . .	100
6.3	Example images of the (2*28)*18 LED target degraded by air turbulence at ground: 1. Warm summer day at 8/22/2020 (Top) at 30° C, 2. Cold winter day 12/18/2020 at 6° C(Bottom) . . . . .	101
6.4	Calculation of ROIs . . . . .	103
6.6	Close capture of a single LED at distance $R \sim 1 \text{ m}$ by using a Tamron objective and ZWO ASICAM 290 MM Mono(left). Normalized log magnitude of 2D FFT of the close capture. The DC coefficient is centered. White is associated with maximum and black with minimum (right). Min/max/mean values and 95% confidence band of 1D profiles from the 2D FFT of the image depending on object-plane spatial frequency (bottom). . . . .	105

6.7	log ratio $R$ for a single video sequence at 8/22/2020 based on $N_f = 100$ frames. Mean values and its 95%-confidence bands are calculated by averaging over $N_{ROI} = 28 \times 18 = 504$ ROIs. Expected log ratio $R$ based on Fried MTFs at the orange average frequency $\bar{\lambda}_{orange} = 593$ nm are shown color-coded for varying turbulence strengths $\log_{10} C_n^2$ . . . . .	107
6.9	Cummulative distribution function of relative deviation $\Delta R$ with 95%-confidence bands for $N = 100$ video sequences at 3/8/2021. Theoretical deviation $\Delta R_{theo}$ is shown as vertical line. . . . .	109
6.11	Example of centroids $\tilde{c}_{00k}$ for the top left region of interest for a single video sequence with 100 frames . . . . .	111
6.12	The camera and objective are placed on a wooden plate about 20 cm above ground. The worst case vibration in terms of angle of arrival fluctuations occurs when one end is fixed and the other is freely movable. . . . .	112
6.13	$\log MTF_{motion}$ dependent on different subtense amplitudes $\theta_0$ . Only strong subtense amplitudes $\theta_0 \sim 10^{-5}$ rad lead to significant degradation in the relevant frequency range $\nu < 2.5 \cdot 10^4 \text{ m}^{-1}$ . . . . .	113
6.14	Differential tilt variances $DTV_{hor/vert}(\Delta x, \Delta y, 0)/\text{rad}^2$ depending on horizontal and vertical separations $\Delta x/\text{m}$ and $\Delta y/\text{m}$ . . . . .	114
6.16	Example of Differential tilt variance (DTV) fit to experimental data for a single video sequence with 100 frames . . . . .	116
6.17	1D grid scans of the loss function $f(\mathbf{z} \mathbf{x})$ (DTV fitting function) for single turbulence parameters parameters $L_0, l_0, C_n^2$ and $\alpha$ for a single video sequence based on the spectrum GMVKS. 95%-confidence intervals of parameters (vertical black lines) and modal values $f(z_{min} x) = f_{min}$ (red dashed lines) are shown. The upper bound for outer scale $L_0$ is cutoff for better illustration. . . . .	118
6.18	DTV relative errors of simulations based on turbulence model parameters of 15 video sequences and single examples for two recording dates 2020/08/22 and 2021/03/06 . . . . .	120
6.19	Box plots of relative errors of $DTV$ simulated versus analytical for several recording dates. $DTV$ values are calculated for $N = 50$ simulations based on retrieved model parameter sets from DTV fits, one per video sequence. Each simulation generates $N_s = 200$ frames of perturbed 9x9 point grids. . . . .	121
6.20	Box plots of relative errors of $DTV$ simulated versus experimental for several recording dates. $DTV$ values are calculated for $N = 50$ simulations based on retrieved model parameter sets from DTV fits, one per video sequence. Each simulation generates $N_s = 200$ frames of perturbed 9x9 point grids. . . . .	122

6.21	Box plots of relative errors of $MTF$ simulated versus analytical for several recording dates. $MTF$ values are calculated for $N = 50$ simulations based on retrieved model parameter sets from DTV fits, one per video sequence. Each simulation generates $N_s = 1000$ frames of single perturbed point sources. . . . .	123
6.22	Box plots of relative errors of $MTF$ simulated versus experimental for several recording dates. $MTF$ values are calculated for $N = 50$ simulations based on retrieved model parameter sets from DTV fits, one per video sequence. Each simulation generates $N_s = 200$ frames of perturbed $9 \times 9$ point grids. . . . .	125
6.23	Interquartile ranges for $MTF_{residual}$ for long-exposure and short-exposure $MTF$ values in horizontal and vertical direction. . . . .	126
6.24	Box plots of relative errors of the log aperture-averaged scintillation index $\ln \sigma_I^2(D)$ simulated versus analytical (left) and experimental (right) for several recording dates. $\sigma_I^2(D)$ values are calculated for $N = 50$ simulations based on retrieved model parameter sets from DTV fits, one per video sequence. Each simulation generates $N_s = 1000$ frames of single perturbed point sources. . . . .	129
6.25	Effective scintillation index $\sigma_{I,eff}^2(D)$ for different real scintillation indices $\sigma_I^2(D)$ depending on signal-to-noise ratio $SNR[dB]$ associated with detector noise. A low $SNR$ leads to biases of the effective scintillation index $\sigma_{I,eff}^2(D)$ towards larger values. . . . .	131
6.26	Signal-to-noise ratio $SNR[dB]$ , peak $P_{max}$ and noise level $\sigma_{\epsilon,exp}$ depending on binning factor/ROI size for different recording dates. . . . .	132
6.27	Sample cumulative distribution function of turbulence parameter resulting from $N = 1112$ DTV data fits based on the spectrum GMVKS. 95%-confidence bands based on the Dvoretzky–Kiefer–Wolfowitz inequality (Dvoretzky et al. [1956]) are shown. . . . .	134
6.28	Cummulative distribution function of ratio vertical/horizontal of turbulence parameters resulting from $N = 1112$ DTV data fits based on the spectrum GMVKS. . . . .	136
6.29	Cummulative distribution function of turbulence parameters resulting from $N = 1112$ DTV data fits based on the spectrum GMAS. . . . .	138
6.30	Cummulative distribution function of ratio vertical/horizontal of turbulence parameters resulting from $N = 1112$ DTV data fits based on the spectrum GMAS. . . . .	139
6.31	Correlation matrix of daytime hour, temperature, relative humidity, wind strength, and turbulence parameters for horizontal and vertical direction based on DTV fits on $N = 1112$ video sequences with nominal frame number of 100 and a framerate $f = 7\text{ Hz}$ : $C_{n,hor/vert}^2$ , $\alpha_{hor/vert}$ , $L_{0,hor/vert}$ and $l_{0,hor/vert}$ . . . . .	142
6.32	Means of turbulence parameters versus date for horizontal and vertical direction based on DTV fits for GMVKS on $N = 1112$ video sequences with nominal frame number of 100 and a framerate $f = 7\text{ Hz}$ : $C_{n,hor/vert}^2$ , $\alpha_{hor/vert}$ , $L_{0,hor/vert}$ and $l_{0,hor/vert}$ . . . . .	144

6.33 Means of turbulence parameters versus date for horizontal and vertical direction based on DTV fits for GMAS on  $N = 1112$  video sequences with nominal frame number of 100 and a framerate  $f = 7\text{ Hz}$ :  $C_{n,hor/vert}^2$ ,  $\alpha_{hor/vert}$ ,  $L_{0,hor/vert}$  and  $l_{0,hor/vert}$  . . . . . 145



## C. List of Tables

4.1	Default simulation parameters for single wave propagation . . . . .	44
5.1	Computation times of the generation of 10 SS phase screens with 2048x2048 pixels on a GTX 1080 Ti depending on number of waves $N_{waves}$ . . . . .	94
5.2	Other durations for 2D uncorrelated phase screens and simulation on a GTX 1080 Ti . . .	94
6.1	Device specifications . . . . .	99
6.2	Record information about captured video sequences . . . . .	102
6.3	Sample means and standard deviations of turbulence parameters based on spectrum GMVKS135	
6.4	Sample means and standard deviations of turbulence parameters based on spectrum GMAS140	



## Symbols

$\alpha$	Turbulence spectrum exponent, confidence level
$\beta$	GMAS turbulence parameter
$\beta_0$	Spherical wave Rytov variance
$\delta(\mathbf{K} - \mathbf{K}')$	Kronecker delta
$\Delta q$	Relative deviation to numerical integration with $N = 5000$ intervals
$\Delta q_{x/y}$	Horizontal/vertical separation of point sources
$\Delta z$	Phase screen thickness
$\varepsilon$	Permittivity, camera noise
$\varepsilon_0$	Vacuum permittivity
$\Gamma(x)$	Euler gamma function
$\Gamma(\mathbf{r}_1, \mathbf{r}_2, L)$	Mutual coherence function
$\kappa$	1D spatial frequency
$\kappa_x$	1D horizontal spatial frequency
$\kappa_y$	1D vertical spatial frequency
$\lambda$	Wavelength
$\bar{\lambda}$	Average wavelength
$\bar{\lambda}_{orange}$	Averaged wavelength of the "orange" spectrum
$\bar{\lambda}_{blue}$	Average wavelength of the "blue" spectrum
$\mu$	Permeability
$\mu_0$	Vacuum permeability
$\nu$	1D spatial frequency in the sensor plane
$\nu_{cutoff}$	Optical cutoff frequency
$\nu_{x/y}$	Horizontal/vertical spatial frequency
$\varphi_n(x, y)$	$n$ -th phase screen
$\Phi_n(\kappa)$	1D refractive index power spectrum
$\Phi_{n,GMAS}(\kappa)$	GMAS refractive index power spectrum
$\Phi_{n,GMVKS}(\kappa)$	GMVKS refractive index power spectrum
$\Phi_{n,Kolmogorov}(\kappa)$	Kolmogorov refractive index power spectrum
$\Phi_n(\mathbf{K})$	3D refractive index power spectrum

$\Phi_\varphi(\boldsymbol{\kappa})$	1D phase power spectrum
$\theta_0$	Isoplanatic angle
$\theta_{x/y}(r)$	Tip/tilt angle of arrival at position $r$
$\theta$	Viewing angle
$\theta_{SH}(x,y)$	Subharmonics phase contribution
$\sigma_I^2(x,y)$	Scintillation index
$\sigma_I^2(D)$	Aperture-averaged scintillation index
$\sigma_{I,sp}^2$	Spherical wave scintillation index
$\sigma_{I,pl}^2$	Plane wave scintillation index
$\sigma_R^2$	Rytov variance
$\sigma_{\parallel}^2$	Parallel differential tilt variance
$\sigma_{\perp}^2$	Perpendicular differential tilt variance
$\sigma_\varepsilon$	Camera noise level (standard deviation)
$a$	GMAS turbulence parameter
$A_0(x,y)$	2D rippling effect correction field
$A(\alpha)$	Turbulence spectrum prefactor
$b$	GMAS turbulence parameter
<b>B</b>	Magnetic flux density
$B_n(x,y,z)$	3D covariance
$Cov(\mathbf{R})$	Covariance
$\tilde{c}_x$	Set horizontal centroid
$\tilde{c}_y$	Set vertical centroid
$c_{x,n}$	Horizontal centroid of frame $n$
$c_{y,n}$	Vertical centroid of frame $n$
$c_{x,ijk}$	Horizontal centroid of frame $k$ in region of interest $(i, j)$
$c_{y,ijk}$	Vertical centroid of frame $k$ in region of interest $(i, j)$
$C_n^2$	Turbulence strength
$C_n^2(z)$	Turbulence strength (path dependent)
$D$	Aperture diameter
<b>D</b>	Electrical flux density
$D_\varphi^{(MA)}(r)$	Markov phase structure function
$D_\varphi^{(NM)}(r, 0)$	Non-Markov transversal phase structure function
$D_\varphi^{(NM)}(0, m \cdot \Delta z)$	Non-Markov longitudinal phase structure function
$D(\mathbf{R}), D(\mathbf{r}_1, \mathbf{r}_2, L)$	3D structure function
$D_{sp}(\rho, L)$	Spherical wave structure function
$D_{pl}(\rho, L)$	Plane wave structure function
$D_\chi(\rho, L)$	Log-amplitude structure function

$D_S(\rho, L)$	Phase structure function
$D_{S,GMVKS}(\rho, L)$	GMVKS phase structure function
$D_{S,GMAS}(\rho, L)$	GMAS phase structure function
$D_{phi}(\mathbf{r})$	Phase structure function
$DOC(\mathbf{r}_1, \mathbf{r}_2, L)$	Complex degree of coherence
$DTV_{(x/y)}$	Differential tilt variance
$dv(\mathbf{K})$	Stieltjes differential
<b>E</b>	Electrical field
$f$	Frame rate
$fl$	Focal length
$f_{hor/vert}(\mathbf{x} \mathbf{z}_{hor/vert})$	Differential tilt variance loss functions
<b>H</b>	Magnetic field
$I$	Electrical current
$I(x, y)$	2D point source profile
$I_n(x, y)$	Frame $n$
$I_1(z)$	Integral function for differential tilt variance
$I_T(z)$	Integral function for differential tilt variance
$I_{n,shifted}(x, y)$	Centroid corrected frame $n$
$I_{FOV_{x,y}}$	Instantaneous field of view horizontal/vertical
$J_\nu(x)$	Bessel function of first kind
$k$	Wave number
<b>K</b>	3D spatial frequency
$K_\nu(x)$	Modified Bessel function of second kind
$l_0$	Inner scale
$L_0$	Outer scale
$L$	Range
$L_\nu(x)$	Laguerre function
<b>M</b>	Magnetization
$MTF$	Modulation transfer function
$MTF_{LE,sp/pl}(u)$	Spherical wave/ plane wave long-exposure modulation transfer function
$N_{ps}$	Number of samples or simulated frames
$N_x$	Number of columns
$N_y$	Number of rows
$N_z$	Number of phase screens for single beam propagation
$n$	Refractive index
$n_1$	Refractive index (turbulence contribution)

$n(\mathbf{r}_1), n(\mathbf{r}_2)$	Refractive indices at coordinates $\mathbf{r}_1$ and $\mathbf{r}_2$
$OTF(v_x, v_y)$	2D optical transfer function
$OTF_{aperture}(v_x, v_y)$	2D aperture optical transfer function
$OTF_{detector}(x, y)$	2D detector optical transfer function
$OTF_{stabilization}(x, y)$	2D stabilization optical transfer function
$OTF_{atm}(x, y)$	2D atmospheric optical transfer function
$OTF_0(\mathbf{v})$	System optical transfer function (without turbulence)
$OTF_{LE}(\mathbf{v}), OTF_{LE}(v_x, v_y)$	Long-exposure optical transfer function
$OTF_{SE}(\mathbf{v}), OTF_{SE}(v_x, v_y)$	Short-exposure optical transfer function
$OTF_{L,total}(\mathbf{v})$	Total long-exposure optical transfer function
$OTF_{S,total}(\mathbf{v})$	Total short-exposure optical transfer function
$O(i, j)$	2D output image
<b>P</b>	Polarization
$P$	Aperture-averaged optical power
$p_n$	Sparse spectrum wave vector component in x direction
$P_n(K)$	Sparse spectrum probability distribution for interval $n$
$p_{x,y}$	Pixel pitch
$P(\mathbf{R})$	Pressure
$PhTF$	Phase transfer function
$PSF(x, y)$	2D point spread function
$PSF_{turb}(x, y)$	2D turbulence point spread function
$PSF_0(x, y)$	2D zero-turbulence point spread function
$PSF_{aperture}(x, y)$	2D aperture point spread function
$PSF_{detector}(x, y)$	2D detector point spread function
$PSF_{stabilization}(x, y)$	2D stabilization point spread function
$PSF_{atm}(x, y)$	2D atmospheric point spread function
$q_n$	Sparse spectrum wave vector component in y direction
<b>R</b>	3D spatial coordinates
$r_0$	Fried parameter
$SNR$	Signal-to-noise ratio
$s_n$	Sparse spectrum wave vector component in z direction
$s_{x/y}$	Horizontal/vertical phase screen shift
$s_{wind,x/y}$	Horizontal/vertical phase screen shift due to wind
$S_F$	Free space operator
$S_{P,n}$	Phase screen operator of phase screen $n$
$SR$	Strehl ratio
$T$	Temperature

$U$	AC/DC Voltage
$U_n(x, y)$	Complex field after phase screen $n$
$\mathbf{U}, U(x, y, z)$	Longitudinally slowly varying envelope of electrical field
$U(\mathbf{r}_1), U(\mathbf{r}_1)$	Complex electrical field
$W$	Correlation factor
$w_n$	Sparse spectrum weight
$w_{x/y}$	Physical dimensions of simulation field
$\mathcal{F}$	Fourier transform



## Acronyms

CDF	Cummulative distribution function
Cov	Covariance
CUDA	Compute Unified Device Architecture (NVIDIA software framework for parallel computing on graphics processing units)
DTV	Differential tilt variance
FFT	Fast Fourier transform
GMAS	Generalized modified atmospheric spectrum
GMVKS	Generalized modified Von Karman spectrum
GPU	Graphics processing unit
IFFT	Inverse Fast Fourier transform
LE	Long-exposure
LED	Light emitting diode
MTF	Modulation transfer function
OTF	Optical transfer function
pl	Plane wave
PSF	Point spread function
PhTF	Phase transfer function
SE	Short-exposure
SI	Scintillation index
sp	Spherical wave
SS	Sparse spectrum
UPS	Uninterruptible power supply



## **Acknowledgements**

First I want to thank my PhD supervisor Prof. Peter Braesicke and co-supervisor Dr. Michael Höpfner for very constructive feedback and fruitful discussions.

Secondly, I want to thank my day-to-day supervisor Dr. Katrin Braesicke for organizational support and patience.

Then I want to thank my family and my partner Sabine Heimbach for moral support and encouragements.

Thanks also goes to my colleague Szymon Gladysz for helpful advices for literature research in the fields of turbulence simulation and turbulence measurements.

Finally, thanks are also due to my colleagues Endre Repasi and Frank Willutzki for technical support and advice for the experimental setup.